Syntheses of TiO_2 Powders via Sol-Gel Process with Different Precursors and Their Photocatalytic Properties

Cheewita Suwanchawalit

A Thesis Submitted in Fulfillment of the Requirements
for the Degree of Doctor of Philosophy in Chemistry
Prince of Songkla University
2009

Thesis Title Syntheses of TiO_2 Powders via Sol-Gel Process with Different Precursors and Their Photocatalytic Properties
Author Miss Cheewita Suwanchawalit
Major Program Chemistry

Major Advisor	**Examining Committee**
....	....Chairperson
(Assoc. Prof. Dr. Sumpun Wongnawa)	(Assoc. Prof. Dr. Supasarote Muensit)
	....
	(Assoc. Prof. Dr. Sumpun Wongnawa)
	....
	(Assoc. Prof. Dr. Lek Sikong)
	....
	(Assoc. Prof. Dr. Apisit Songsasen)

The Graduate School, Prince of Songkla University, has approved this thesis as fulfillment of the requirements for the Doctor of Philosophy Degree in Chemistry

....
(Assoc. Prof. Dr. Krerkchai Thongnoo)
Dean of Graduate School

ชื่อวิทยานิพนธ์ การสังเคราะห์ผงไทเทเนียมไดออกไซด์ด้วยกระบวนการโซล-เจลโดยใช้สารตั้งต้นต่างชนิดและศึกษาสมบัติการเป็นโฟโตคะตะลิสต์

ผู้เขียน นางสาวชีวิตา สุวรรณชวลิต

สาขาวิชา เคมี

ปีการศึกษา 2551

บทคัดย่อ

วิทยานิพนธ์นี้แบ่งงานวิจัยออกเป็นสองส่วน ส่วนแรกศึกษาการเตรียมผงไทเทเนียมไดออกไซด์ (TiO_2) และปรับปรุงประสิทธิภาพการเป็นโฟโตคะตะลิสต์ ในส่วนที่สองเป็นการนำผง TiO_2 ที่เตรียมได้ไปขึ้นรูปเพื่อความสะดวกในการนำไปประยุกต์ใช้งาน

การเตรียมผง TiO_2 ในส่วนแรกแบ่งเป็น 2 วิธี วิธีแรกเป็นการเตรียมผง TiO_2 ด้วยกระบวนการโซล-เจลโดยใช้โพแทสเซียมออกซาเลต (KOX) เป็นสารโด๊ป และใช้เฮกสะเมทิลีนเตตระมีน (HMT) เป็นเบสคะตะลิสต์ ศึกษาสมบัติทางกายภาพและทางเคมีของ TiO_2 ที่เตรียมได้โดยใช้เทคนิค XRD, SEM, BET, FT-IR, PL และ UV-Vis พบว่าผง KOX-TiO_2 ที่สังเคราะห์ได้อยู่ในรูปอสัณฐานที่มีผลึกแบบอนาเทสปนเล็กน้อยและมีพื้นที่ผิวสูง 337 m^2/g และผลจากการศึกษาความสามารถในการเป็นโฟโตคะตะลิสต์ในการสลายเมทิลีนบลู (methylene blue) พบว่า KOX-TiO_2 ที่สังเคราะห์ได้สามารถฟอกสีเมทิลีนบลูได้เนื่องจากอาศัยการดูดซับบนพื้นผิวมากกว่าสมบัติโฟโตคะตะไลติก ดังนั้นจึงปรับปรุงสมบัติโฟโตคะตะไลติกของ KOX-TiO_2 ที่สังเคราะห์ได้โดยการเผาที่อุณหภูมิต่างๆ คือ 400, 600, 800, 1000°C พบว่าอุณหภูมิของการเผามีผลต่อเฟส พื้นที่ผิว รูปร่าง และสมบัติโฟโตคะตะไลติกของ KOX-TiO_2 ที่สังเคราะห์ได้ นั่นคือ เผาที่อุณหภูมิ 800°C แสดงสมบัติโฟโตคะตะไลติกได้ดีเทียบเท่ากับ Degussa P25 ซึ่งเป็น TiO_2 ที่นิยมใช้ในเชิงการค้า นอกจากนี้ยังได้เสนอวิธีการนำกลับมาใช้ใหม่ (regeneration method) ด้วย

ส่วนวิธีที่สองเป็นการเตรียมผง mesoporous TiO_2 ด้วยกระบวนการโซล-เจลโดยใช้สารลดแรงตึงผิวแบบไม่มีประจุ (Pluronic P123) เป็นสารแม่แบบ และใช้สารตั้งต้นสองตัวคือ ไทเทเนียมเตตระคลอไรด์ ($TiCl_4$) และไทเทเนียมออกซีซัลเฟต ($TiOSO_4$) และใช้กรดเป็นคะตะลิสต์โดยกรดที่ใช้ ได้แก่ กรดไฮโดรคลอริก (HCl) กรดไนตริก (HNO_3) กรดฟอร์มิก (HCOOH) กรดอะซิติก (CH_3COOH) กรดซัลฟิวริก (H_2SO_4) กรดฟอสฟอร์ริก (H_3PO_4) จาก

การศึกษาสมบัติทางกายภาพและทางเคมีของไทเทเนียมไดออกไซด์ที่เตรียมได้ (mesoporous TiO_2_$TiCl_4$, mesoporous TiO_2_$TiOSO_4$) พบว่า mesoporous TiO_2_$TiCl_4$ จะได้ไทเทเนียมไดออกไซด์อสัณฐานที่มีผลึกแบบอนาเทสและรูไทล์ปนอยู่ด้วย ส่วนตัวอย่าง mesoporous TiO_2_$TiOSO_4$ จะได้ไทเทเนียมไดออกไซด์อสัณฐานที่มีผลึกอนาเทสปนอยู่ด้วย รวมทั้งมีการเสนอกลไกอธิบายการเกิดผลึกไทเทเนียมไดออกไซด์ ผลจากการศึกษาความสามารถในการเป็นโฟโตคะตะลิสต์ของไทเทเนียมไดออกไซด์ที่เตรียมได้จากสารตั้งต้นทั้งสองชนิด สามารถสลายสีย้อมอินดิโกคาร์มีน (indigo carmine) ได้และสามารถนำไปใช้งานซ้ำได้ดี

ส่วนที่สองเป็นการนำผง TiO_2 ที่เตรียมได้ไปขึ้นรูปเพื่อความสะดวกในการนำไปประยุกต์ใช้งาน เน้นทางด้านคะตะไลซิสต์ ซึ่งการขึ้นรูปผง TiO_2 นั้นแบ่งเป็นสองส่วน คือส่วนแรกนำผง TiO_2 ไปฝังในแผ่นยาง ซึ่งทำได้ง่ายโดยนำผง TiO_2 มาผสมโดยตรงกับน้ำยาง ทิ้งให้แห้งจะได้แผ่นยาง CS/TiO_2 (TiO_2-rubber sheets) แล้วนำไปใช้สลายเมทิลีนบลูพบว่า TiO_2-rubber sheets ที่เตรียมขึ้นสามารถสลายสีย้อมได้ และสามารถใช้งานซ้ำได้ ส่วนที่สองนำผง TiO_2 ไปขึ้นรูปเป็น TiO_2 scaffolds ที่มีโครงสร้างแบบ macroporous เตรียมด้วยวิธี ice-templating ซึ่งได้ทำการศึกษาปัจจัยต่างๆ ได้แก่ อัตราส่วนระหว่าง TiO_2 ต่อไคโตซาน อัตราการจุ่ม ขนาดของกระบอกฉีดยา และชนิดของ TiO_2 จากนั้นนำไปสลายสีย้อมออร์เรนจ์ II (orange II) และเมทิลีนบลู พบว่า CS/TiO_2 scaffolds สามารถสลายสีย้อมทั้งสองได้

Thesis Title Syntheses of TiO_2 Powders via Sol-Gel Process with Different Precursors and Their Photocatalytic Properties
Author Miss Cheewita Suwanchawalit
Major Program Chemistry
Academic Year 2008

Abstract

This thesis consists of two parts. The first part involves titanium dioxide (TiO_2) preparation and improving photocatalytic activity. The second part focuses on applying the as-prepared TiO_2 powders to other forms for convenient use in many applications.

The preparation of TiO_2 in the first part can be divided of two methods. The first method is a preparation of TiO_2 powders by basic-catalyzed sol-gel method using potassium oxalate (KOX) as doping agent and hexamethylenetetramine as basic catalyst. The physicochemical properties of the powders were investigated by XRD, SEM, BET, FT-IR, PL, and UV-vis techniques. The results showed that the product, designated as KOX-TiO_2, was a mixture of mainly amorphous TiO_2 with small amount of anatase phases with high surface area of 337 m^2/g. The photocatalytic investigations revealed that the as-prepared KOX-TiO_2 powders decolorized methylene blue mainly by adsorption more than the photocatalytic property. The calcinations at various calcination temperatures (400, 600, 800, 1000°C) were used to improve the photocatalytic property. The results showed that calcination changed the crystal structure, crystallite size, surface area, morphology, and photocatalytic activity of the as-prepared TiO_2 samples. The photocatalytic activity was also increased with increasing calcination temperature. When the calcination temperature was 800 °C, the photocatalytic activity of the calcined sample was comparable to that of Degussa P25, the prevailing commercial photocatalyst. In addition, the regeneration method was also proposed.

The second method is the preparation of mesoporous TiO_2 via surfactant-mediated sol-gel process using non-ionic surfactant, Pluronic P123, as templating agent and $TiCl_4$ and $TiOSO_4$ as precursors, with acid catalysts (hydrochloric acid (HCl), nitric acid (HNO_3), formic acid (HCOOH), acetic acid (CH_3COOH), sulfuric acid (H_2SO_4), and phosphoric acid (H_3PO_4)). The physicochemical investigations of the resulting TiO_2 powders, designated as mesoporous TiO_2_$TiCl_4$ and mesoporous TiO_2_$TiOSO_4$, showed that mesoporous TiO_2_$TiCl_4$ were mainly amorphous TiO_2 with small amount of anatase and rutile phases while mesoporous TiO_2_$TiOSO_4$ were mainly amorphous TiO_2 with small amount of anatase phase. Mechanism of growth from basic units to nanocrystalline was also proposed. For the photocatalytic studies (indigo camine degradation) it was found that as-prepared mesoporous TiO_2 from both precursors could degrade indigo camine and could be reused in the next cycle.

The second part was devided into two methods. In the first method, the as-prepared TiO_2 powders were embeded into rubber sheet by directly mixing TiO_2 powders with rubber latex (60% HA) and distilled water. These impregnated TiO_2 rubber sheets could degrade MB solution under UV-light irradiation. In the second method, the macroporous CS/TiO_2 scaffolds were prepared via ice-templating method. The parameters studied for preparing the ordered structure are: the ratio of TiO_2/chitosan, freezing rate, size of syringe, and type of TiO_2. All types of CS/TiO_2 scaffolds could be used as photocatalyst to degrade both methylene blue and orange II dyes.

Acknowledgements

The completion of this thesis would be impossible without the help of many people, whom I would like to thank.

I am very grateful to Associate Professor Dr. Sumpun Wongnawa for allowing me to work on very interesting and challenging projects, for all the help and guidance over the past years, for putting up with me for so long, for never failing to answer those annoying questions I kept asking and for all the excellent teaching and supervision.

I would like to thank Professor Dr. Stephen Mann, Dr. Avinash Patil for giving me a chance to do the research, advice and support conducted on part of my research at the school of Chemistry, Bristol University, Bristol, UK.

Thanks are also extended to examination committee members of this thesis for their valuable time.

I am deeply indebted to the Royal Golden Jubilee Ph.D. Program (RGJ) of the Thailand Research Fund (TRF) for scholarship (Grant No.PHD/0197/2548), the Center for Innovation in Chemistry: Post Graduate Education and Research Program in Chemistry (PERCH-CIC), and the Graduate School, Prince of Songkla University, for the partial supports of the research fund.

My acknowledgements are extended to all of my collaborators who helped create an enjoyable atmosphere to be working in and for their many helpful in many countless ways throughout the years.

I would like to express my great debt of gratitude and dedication to my beloved parents, brother, and grandparent who help me walk through the path of life to reach this stage.

Cheewita Suwanchawalit

The Relevance of the Research Work to Thailand

Semiconductor-mediated photocatalytic oxidation has been accepted as a promising method for water and air purification and remediation. Among the semiconductors employed, TiO_2 is known as a good photocatalyst because of its high photosensitivity, non-toxicity, easy availability, friendly, and low cost. In order to maximize photocatalytic activity, TiO_2 particles should be small enough to offer a high number of active sizes by unit mass. The mesoporous TiO_2 materials have attracted much attention in the field of separation and catalysis because of their high specific surface areas, narrow pore size distributions, and offers more active sites for carrying out catalytic reaction. However, many researchers have focused on the synthesis of TiO_2 by annealing to improve its photocatalytic activity and its applicability to wastewater treatment. The purpose of this work is to study the effect of precursor on the preparation of the mesoporous TiO_2 powders using modified sol-gel process. The synthesized-TiO_2 photocatalyst could be used to degrade methylene blue, orange II and indigo carmine, a model dye compound, in wastewater.

Due to the rapid growth of textile and clothing productions in Thailand in the past few decades, several textile industries produce products urgently and also release a lot of dye pollutants into natural systems. Therefore, dye-contaminant wastewater should be carefully managed and controlled. We hope that the prepared TiO_2 powders in this work could be used in Thailand as a cheaper catalyst material for the destruction of dye pollutants in the textile industries or the others organic pollutants before releasing wastewater into the natural system.

Contents

Page

Contents (Continued)

Contents (Continued)

Page

Contents (Continued)

List of Tables

List of Tables (Continued)

List of Figures

List of Figures (Continued)

List of Figures (Continued)

Figure **Page**

List of Figures (Continued)

List of Figures (Continued)

List of Figures (Continued)

List of Figures (Continued)

List of Figures (Continued)

List of Figures (Continued)

List of Figures (Continued)

List of Figures (Continued)

List of Schemes

List of Abbreviations

eV = Electron volt
g = Gram
hr = Hour
IC = Indigo Carmine
nm = Nanometer
min = Minute
mL = Milliliter
mol/L = Mole per liter
^{o}C = Degree celcius
λ_{max} = Maximum wavelength
BET = Brunauer-Emmett-Teller
DRS = Diffused reflectance spectroscopy
EDX = Energy dispersive X-ray
FT-IR = Fourier-transformed infrared spectroscopy
MB = Methylene blue
JCPDS = Joint Committee on Powder Diffraction Standards
OII = Orange II
PL = Photoluminescence
SEM = Scanning electron microscope
TEM = Transmission electron microscope
XRD = X-ray diffraction
UV-Vis = Ultraviolet-Visible

CHAPTER 1

Introduction

1.1 Introduction

Metal oxide semiconductors, such as TiO_2, ZnO, ZnS and SnO_2, have been applied as photocatalysts for the removal of highly toxic and non-biodegradable pollutants commonly present in air and wastewater. Among them titania is believed to be the most promising one, because of its high photocatalytic activity, chemical stability, stable in various solvents under photoirradiation, has potential ability to induce various types of redox reaction, available commercially, ease of handling, low cost and without risks for the environment or humans (Ohtani, *et al.*, 1997; Yang, *et al.*, 2006; Chen, *et al.*, 2006; Baiju, *et al.*, 2007). Moreover, TiO_2 could be used in many applications such as a white pigment in paints, plastic, paper, textile, phamaceuticals (tablet coating, toothpastes, and as a UV absorber in sunscreen cream with high sun protection factors and other cosmetic products), anti-reflection coating in silicon solar cell and thin film in optical devices, gas sensor, biomaterial (as bone substituent and reinforcing mechanical supports), and anti-bacterial agents (Carp, *et al.*, 2004). Titania exists in three crystal structures (anatase, rutile, brookite) and each behaves differently. It is well-known that the anatase phase is suitable for catalysis and supports, while rutile phase is used for optical and electronic purposes because of it highdielectric constant and high refractive index. Brookite has no practical importance owing to its low stability. It has been well demonstrated that the crystalline phase of TiO_2 plays a significant role in catalytic reactions, especially photocatalysis. Some studies have claimed that the anatase phase was more active than the rutile phase in photocatalysis (Zhang, *et al.*, 2006; Hadjiivanov, *et al.*, 1996). In addition, a mixed anatase-rutile phase demonstrates better photocatalytic activity than it does in pure anatase or rutile phase (Cao, *et al.*, 1999; Hurum, *et al.*, 2006; Sun, *et al.*, 2008).

Extensive researches on the photochemistry and photophysics of TiO_2 have shown that the effective performance of a TiO_2 photocatalyst depends on a number of factors such as the crystal structure, the crystallinity, crystallite size, surface functionality, and most importantly, the surface area and the surface accessibility of the catalyst (Chen, *et al.*, 2006; Zhang, *et al.*, 2006; Peng, *et al.*, 2005; Bakardjieva, *et al.*, 2005). Many researchers have focused on the preparation of various phase of TiO_2 powder to improve its photocatalytic activity and its applicability to environmental treatment. It has been reported that the different methods for the syntheses of TiO_2 result in products with different structures (anatase or rutile), crystallinity, and contaminants. As a consequence, the surface properties of TiO_2 strongly depend on the preparation techniques (Zhang, *et al.*, 1999; Reddy, *et al.*, 2001). In order to maximize photocatalytic activity, TiO_2 particles should be small enough to offer a high number of active site by unit mass. Several methods have been reported to improve the photocatalytic efficiency. These include increasing the surface area of TiO_2, generation of defect structures to induce space-charge separation, and modification of the TiO_2 with metal or other semiconductors. The mesoporous TiO_2 is a highly photocatalytically active photocatalyst because it has a high surface-to-volume ratio and offer moreactive sites for carrying out catalytic reactions (Kluson, *et al.*, 2001; Dai, *et al.*, 2002; Yu, *et al.*, 2003; Yoo, *et al.*, 2005; Zhang, *et al.*, 2005). Various techniques of surfactant templating have been employed on preparing mesoporous TiO_2. The solvent extraction or thermal treatment at low temperature was often used to remove the surfactant templating agent.

This research focused on the preparation of mesoporous TiO_2 powders via surfactant templating sol-gel method with different precursors. In addition, potassium oxalate (KOX) was used as the doping agent to enhance surface area by forming an open framework structure. Due to high adsorption property of KOX-TiO_2 sample, the calcination method was used to improve its properties from the as-prepared TiO_2 samples. In order to solve the separation problem of TiO_2 powders from water, we try to prepare TiO_2 impregnated in the rubber sheets (by direct mixing of TiO_2 powder with latex and distilled water) and TiO_2 scaffolds (by ice-templating method). We hope these methods should have potential applications in environmental business.

1.2 Review of Literatures

1.2.1 Titanium dioxide

Titanium dioxide (TiO_2) or titania is a polymorphic compound, having three polymorphous structures: anatase, brookite, and rutile. These polymorphic forms of titanium dioxide are shown in Figure 1. Crystallographic data on the three oxide modifications are summarized in Table 1. Both anatase and rutile are tetragonal, whereas brookite is orthorhombic. In all three oxide modifications, each titanium atom is coordinated to six almost equidistant oxygen atoms, and each oxygen atom to three titanium atoms (Clark, *et al.*, 1968). In the case of anatase, the TiO_6 octahedron is slightly distorted, with two Ti-O bonds slightly greater than the other four, and with some of the O-Ti-O bond angles deviating from 90°. The distortion is greater in anatase than rutile. The structures of anatase and rutile crystals have been described frequently in terms of chains of TiO_6 octahedral having common edges. Two or four edges are shared in rutile and anatase, respectively. The third form of titanium dioxide; brookite, the interatomic distances and the O-Ti-O bond angles are similar to those of rutile and anatase. The essential difference is that there are six different Ti-O bonds ranging from 1.87 to 2.04 Å. Accordingly, there are 12 different O-Ti-O bond angles ranging from 77° to 105°. Brookite is formed by joining together the distorted TiO_6 octahedral sharing three edges. All three oxide modifications are birefringent; anatase is uniaxial negative, brookite is biaxial positive and rutile is uniaxial positive. Further data are given in Table 2.

(a) Anatase

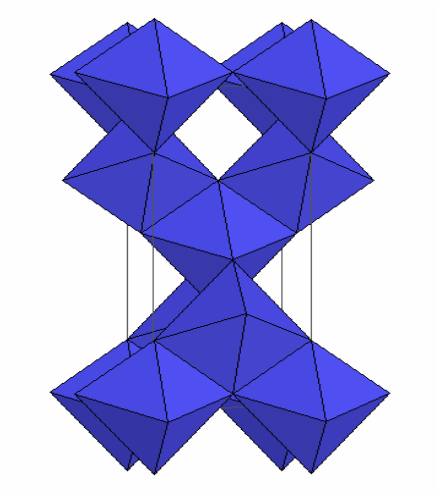

(b) Rutile

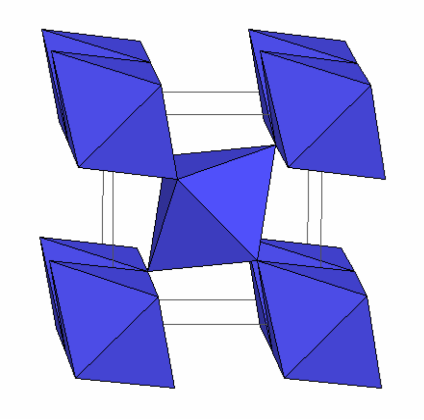

(c) Brookite

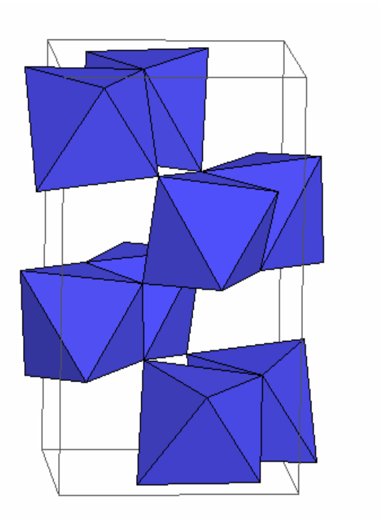

Figure 1. Crystal structures of TiO_2; (a) anatase, (b) rutile, and (c) brookite (http://ruby.colorado.edu/~smyth/min/tio2.html).

Table 1. X-ray data on TiO_2 modifications (Clark, *et al.*, 1968).

	Space group	Z	Cell parameters (Å)			Ti-O
			A	*B*	*C*	(Å)[a]
Anatase	$D_{4h}^{19} = C4/\mathrm{amc}$	8	5.36		9.53	1.91(2) 1.95(4)
Brookite	$D_{2h}^{15} = Pbca$	8	9.15	5.44	5.14	1.84-2.03
Rutile	$D_{4h}^{14} = 4_2/mnm$	2	4.95		2.96	1.94(4) 1.99(2)

Table 2. Properties of the three modifications of titanium dioxide (Clark, *et al.*, 1968).

	Anatase	*Brookite*	*Rutile*
Density (g/cc)	3.90	4.13	4.27
Hardness (Mohs' scale)	5.5-6.0	5.5-6.0	6.0-6.5
Melting Point (°C)	change to rutile	change to rutile	1840 ± 10
Entropy, $S^{\circ}_{298.16}$ (cal/deg/m)	11.93	-	12.01
Refractive Index (25 °C) (λ = 5893 Å)	n_{ω} 2.56 n_{ε} 2.49	n_{α} 2.58 n_{β} 2.58 n_{γ} 2.70	n_{ω} 2.61 n_{ε} 2.89
Dielectric Constant	$\varepsilon = 48$ (powder)	$\varepsilon = 78$	$\varepsilon_{av} \approx 110$ $\varepsilon_{II} = 180$ at 3 x 10^5 c/s 25 °C $\varepsilon_{\perp} = 89$, at 3 x 10^5 c/s 25 °C

---

[a] The numbers in parentheses refer to the number of equivalent oxygen atoms at the stated distance from a titanium atom.

Titanium dioxide is extensively used as a white permanent pigment with good covering power in paint, paper, printing ink, plastic, polymer, cosmetic products, dielectric materials, catalyst supports and photocatalyst. The most common phase used are anatase and rutile since brookite is rather unstable. The anatase form has the problems of poor light, heat resistance, and gradually decreasing in whiteness due to weather. It also has drawbacks for applications involving adsorption technology owing to its low surface energy. The rutile form has outdoor applicability because of its good light resistance and can be applied to surfaces by the use of adsorption technology without advanced skills or sophisticated equipment (Yanqing, *et al.*, 2001; Zhang, *et al.*, 2006).

In industry, it is well known that TiO_2 pigments are produced by the sulfate or chloride processes. The economics of the two processes are very much dependent upon the raw material available. The starting materials for TiO_2 production are ilmenite and titaniferous slag in the case of the sulfate process (Figure 2) and leucoxene, rutile, synthetic rutile, and in the future possibly also anatase, for the chloride process (Figure 3) (Büchner, *et al.*, 1968).

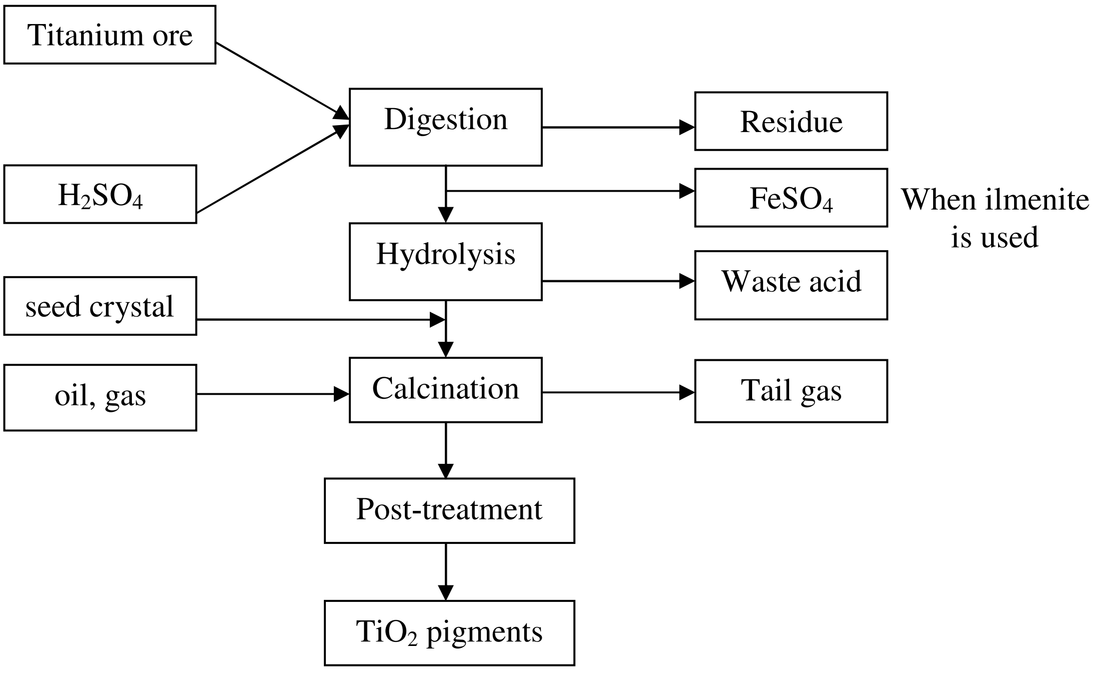

Figure 2. TiO_2 pigment manufactured by the sulfate process (Büchner, *et al.*, 1989).

The sulfate process started from digestion of ilmenite with sulfuric acid at temperatures higher than 95°C, and then calcined at temperature between 800-1,000 °C. The obtained TiO_2 usually has the structure of anatase, and it would be transform to obtain rutile TiO_2 at high temperature (about 1,000°C) (Hadjiivanov, *et al.*, 1996; Wang, *et al.*, 2000; Yang, *et al.*, 2002). In chloride process started from mixing $TiCl_4$ with HCl gas at high temperature to obtain high-purity rutile TiO_2 powders. Usually, TiO_2 prepared from this process has the mixture structure of anatase and rutile. This chloride process requires extra protection devices because of the use of corrosive HCl and Cl_2 gas, lead to high production costs. The obtained products from two process cannot be controlled the particle shape and size, which lead to limitation of their applications (Wang, *et al.*, 2000).

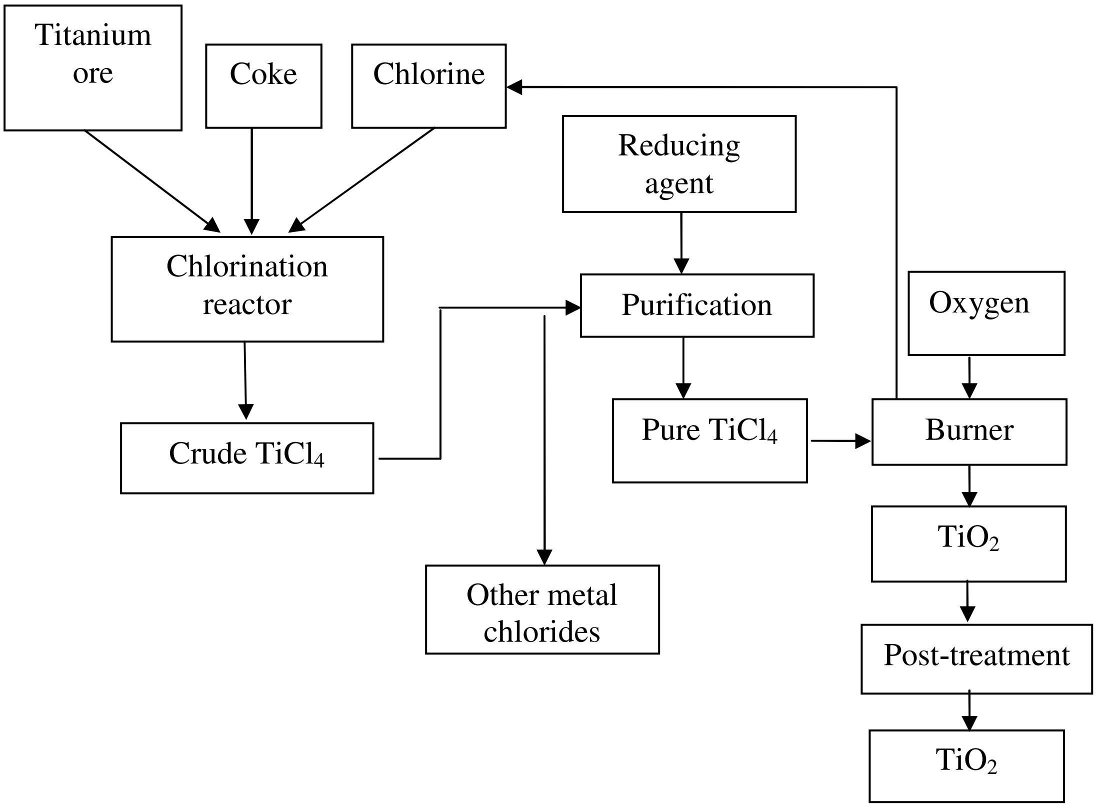

Figure 3. TiO_2 pigment manufactured by the chloride process (Büchner, *et al.*, 1989).

On a laboratory scale, TiO_2 has been prepared by various methods, such as sol-gel method, hydrothermal method, coprecipitation method, microemulsion, combustion synthesis, and so on. The different preparation route and the experiment conditions of TiO_2 result in products with different structures, morphology, particle size and contaminants (Hadjiivanov, *et al.*, 1996; Reddy, *et al.*, 2001). The metal alkoxide is usually used as a precursor on a laboratory scale to prepare TiO_2 powders. The reaction condition is required to control because of the intense hydrolysis of alkoxide in the air and the alkoxide also expensive cost. So, the commercial inorganic compounds such as titanium tetrachloride ($TiCl_4$) and titanium oxysulfate ($TiOSO_4$) are commonly used in the preparation of titanium dioxide than the metal alkoxide.

1.2.2 Sol-gel process

Sol-gel method is a typical wet chemical method to make nanostuctured particles by a chemical reaction in solution starting with metal oxides as a precursor. In general, the sol-gel method involves the transition of system from a liquid “sol” into solid “gel” phase. An overview of the sol-gel product is presented in Figure 4. The starting materials in the preparation of the “sol” are usually inorganic metal salts or metal organic compounds. In a typical sol-gel method, the precursor is subjected to a series of hydrolysis and polymerization (condensation) reactions to form a colloidal suspension or a “sol”. Further processing of the “sol” enables one to make ceramic materials in different forms. Thin films can be prepared on a piece of substrate by spin coating or dip-coating. When the “sol” is cast into a mold, a wet “gel” will form. With further drying and heat-treatment, the “gel” is converted into dense ceramic or glass articles. If the liquid in a wet “gel” is removed under a supercritical condition, a highly porous and extremely low density material called “aerogel” is obtained. As the viscosity of a “sol” is adjusted into a proper viscosity range, ceramic fibers can be drawn from the “sol”. Ultra-fine and uniform ceramic powders are formed by precipitation, spray pyrolysis, or emulsion techniques (Chemat Technology, Inc., 1998).

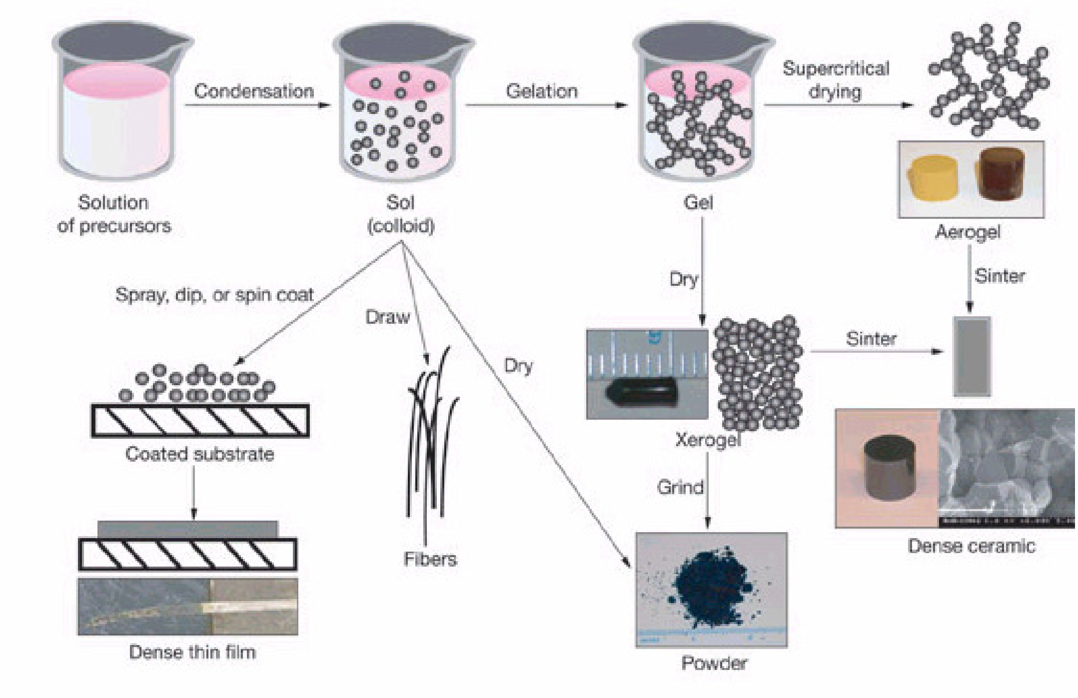

Figure 4. An overview of products prepared by sol-gel methods (http://www.llnl.gov/str/May05/Satcher.html).

The sol-gel process has received more attention due to the ease of controlling various material parameters such as the powder morphology, the surface area, the average nanocrystallite size, the crystallinity, and the phase structure, which significantly affect the photocatalytic activity of nanocrystalline TiO_2 (Yoo, *et al.*, 2005; Baiju, *et al.*, 2007). In sol-gel synthesis, two simultaneous reactions, hydrolysis and condensation, take place when an alkoxide precursor reacts with water as shown in the following eqeuations (1)-(4).

Hydrolysis:

$$M(OR)_z + xH_2O \overset{\text{partially hydrolyzed}}{\rightarrow} (HO)_x - M(OR)_{z-x} + xROH;\ 0 < x < z \qquad (1)$$

$$M(OR)_z + zH_2O \overset{\text{completely hydrolyzed}}{\rightarrow} M(OH)_z + zROH \qquad (2)$$

Condensation:

$$(RO)_{z-1}M - OH + HO - M(OR)_{z-1} \rightarrow (RO)_{z-1}M - O - M(OR)_{z-1} + H_2O \qquad (3)$$

$$(RO)_{z-1}M - OR + HO - M(OR)_{z-1} \rightarrow (RO)_{z-1}M - O - M(OR)_{z-1} + ROH \qquad (4)$$

where R is typically an alkyl group, M is the required metallic cations and z is the valence of cations. The above reactions can be controlled by adjusting the process parameters, such as $H_2O/M(OR)_x$ molar ratios, pH conditions, reaction temperatures, acid or basic catalysts used and composition of raw materials (Yu, *et al.*, 2000; Caruso and Antonietti, 2001; Yoo, *et al.*, 2005; Alapi, *et al.*, 2006).

The sol-gel method offers many advantages in good homogeneity, ease of composition control, low processing temperature, accessibility of nanocrystalline materials, chemical purity, low equipment cost and strongly influenced by the synthesis conditions (Liu, *et al.*, 2005; Venkatachalam, *et al.*, 2007). Strick control on synthesis parameters is necessary to obtain reproducibility in sample with the desired characteristics and high level of chemical purity (Suresh, *et al.*, 1998).

The metal alkoxide is commonly used as precursor for the sol-gel preparation of TiO_2 particles. However, as with other transition metal alkoxides, it hydrolyses rapidly and precipitates. Hydrolysis and polycondensation start immediately in the presence of water (even when in contact with atmospheric moisture) (Kluson, *et al.*, 2001). Since the precipitated particles are usually quite large and their structure inhomogeneous it is desireable to slow down this process as much as possible. The surfactant-mediated sol-gel provides a good control of the hydrolysis and condensation rate. The rate of hydrolysis can also be controlled through the structure-dependent water content of the surfactant. Moreover, the different shape and size of products depend on the surfactant structure (Kluson, *et al.*, 2001).

In this research, titanium tetrachloride ($TiCl_4$) and titanium oxysulfate ($TiOSO_4$) were used as precursor for preparation TiO_2 powders due to their less costly than titanium alkoxide. The potassium oxalate doped TiO_2 samples were prepared from $TiCl_4$ employing HMT to provide slow and controllable precipitation. In another part, the nonionic triblock copolymer, Pluronic P123, was used as surfactant template employed $TiCl_4$ and $TiOSO_4$ as starting materials and NH_4OH as basic catalyst. The parameters including reaction temperatures, water content, TiO_2 concentration, and types of acid catalyst (hydrochloric acid (HCl), nitric acid (HNO_3), acetic acid (CH_3COOH), phosphoric acid (H_3PO_4), sulfuric acid (H_2SO_4), formic acid (HCOOH)) were investigated.

1.2.3 Dye and treatment of dye pollutant

Dyestuffs give color to the material onto which they have been anchored, by selectively retaining some of the wavelengths out of the light falling upon the surface. If, therefore, a dye absorbs strongly at the red end of the spectrum the light which is reflected will be of a bluish hue. Only a limited number of organic molecules possess this property of absorbing light selectively. In 1876, Witt suggested that groups such as nitro, nitrito, azo, and carbonyl conferred upon a substance the potentiality of becoming colored. To these groups he gave the name chromophores (Trotman, 1975).

Table 3. The wavelength of light absorbed and reflected visible color (Trotman, 1975).

Wavelength of light absorbed (nm)	Absorbed light	Visible color
400 – 435	Violet	Yellowish-green
435 – 480	Blue	Yellow
480 – 490	Greenish-blue	Orange
490 – 500	Bluish-green	Red
500 – 560	Green	Purple
560 – 580	Yellowish-green	Violet
580 – 595	Yellow	Blue
595 – 605	Orange	Greenish-blue
605 – 750	Red	Bluish-green

A dye can generally be described as a colored substance that has a chemical affinity to the substrate to which it is being applied. The dye is generally applied in an aqueous solution, and may require a mordant to improve the fastness of the dye on the fiber. Dyeing is the process of imparting color to a textile material in loose fiber, yarn, cloth or garment form, by treatment with a dye (http://www.newworldencyclopedia.org/entry/Dye).

Classification of dyes

Dyes are classified according to their chemical constitution on the basis of their dyeing properties. Thus members of the great group classified constitutionally as azo dyes are found amongst several of the classes based on application. The practical dyer is primarily interested in classification according to application. The constitutional groups will therefore only be classified briefly.

- *Acid dyes*

Acid dye is a member of a class of dye that is applied from an acidic solution. In textiles, acid dyes are effective on protein fibers, i.e. animal hair fibers like wool, alpaca and mohair. They are also effective on silk. They are effective in dyeing the synthetic fiber nylon but of minimal interest in dyeing any other synthetic fibers. Acid dyes are thought to fix to fibers by hydrogen bonding, Van der Waals forces and ionic bonding. Animal protein fibers and synthetic Nylon fibers contain many cationic sites therefore there is an attraction of anionic dye molecule to a cationic site on the fiber. The chemistry of acid dyes is quite complex. Dyes are normally very large aromatic molecules consisting of many linked rings. Acid dyes usually have a sulfo or carboxy group on the molecule making them soluble in water. Water is the medium in which dyeing takes place (http://en.wikipedia.org/wiki/Acid_dye).

- *Basic dyes*

Basic dye is a class of dyes, usually synthetic, that act as bases, and which are actually aniline dyes. Their color base is not water soluble but can be made so by converting the base into a salt. The basic dyes, while possessing great tinctorial strength and brightness, are not generally light-fast; therefore their use in the dyeing of archival materials is largely restricted to those materials not requiring this characteristic. Some examples of basic dyes are crystal violet, safranin, basic fuchsin and methylene blue. It’s applied to wool, silk, cotton and modified acrylic fibres. Basic dyes perform poorly on natural fibres, but work very well on acrylics. Basic dyes are also used in the coloration of paper (http://www.jagson.com/paper_dyes.htm).

- *Direct dyes*

Direct dyes are a class of hot water dyes for use on cellulose fibers, such as cotton, rayon, and linen, but they will also color silk and wool. Direct dyes are applied in hot water, typically between 175°F and 200°F. They can be applied in the same boiling-water dyebath with acid dye. Direct dyes are only loosely associated with the fiber molecule through the property called substantivity, which is the tendency of the dye to associate with the dye without strong bonds that used the relatively weak Van der Waals forces and some hydrogen bonding (http://www.pburch.net/dyeing/directdye.shtml).

- *Mordant dyes*

Mordant dyes require a mordant, which improves the fastness of the dye on the fibre such as water, light and perspiration fastness. Mordants are substances of organic or inorganic origin which combine with the coloring matter and are used to fix the same in the production of the color. The mordant substances include such acids as tannic acid, sumac, gall nuts, bark extracts, oleic and stearic acids, and metallic substances such as various combinations or soluble salts of chromium, aluminum, iron, copper, and tin. The latter, the metallic mordants, are more used than the acid mordants. The choice of mordant is very important as different mordants can change the final colour significantly.

The most commonly used mordant dyes have hydroxyl and carboxyl groups and are negatively charged, i.e. anionic. It is convenient to view these as a specialised subgroup of acid dyes. Some other mordant dyes may possess amino groups, and are cationic overall. Despite this, they must still have hydroxyl or carboxyl groups, since lake formation requires it. Mordant dyes can usually stain by ionic interaction in the same way as other ionisable dyes (http://www.jagson.com/mordant_dyes.htm).

In addition, these dyes have no natural affinity for texiles but are applied to cellulosic or protein fibers which have been mordanted previously with a metallic oxide. The acid mordant dyes are a special class of dyes applied to wool or polyamide fibers as if they were acid dyes, and then given very high wet-fastness by subsequent mordanting (Trotman, 1975).

- *Vat dyes*

Vat dyes are an ancient class of dyes, based on the natural dye, indigo, which is now produced synthetically. Most vat dyes are less suitable than fiber reactive dyes, as they are difficult to work with; they require a reducing agent to solubilize them. The dye is soluble only in its reduced (oxygen-free) form. (http://en.wikipedia.org/ wiki/Vat_dye).

Vat dyes are used in cotton dyeing where high wash and boil fastness required. Because of the high alkali concentration in the dye bath, pure vat dyes cannot be used on animal fibres (wool, natural silk, and various hairs) (http://www.dyeman.com/Dye%20summary.html).

- *Reactive dyes*

In a reactive dye a chromophore contains a substituent that is activated and allowed to directly react to the surface of the substrate. Reactive dyes are used to dye cellulosic fibres. The dyes contain a reactive group, either a haloheterocycle or an activated double bond, that, when applied to a fibre in an alkaline dye bath, forms a chemical bond with an hydroxyl group on the cellulosic fibre. Reactive dyes can also be applied on wool and nylon; in the latter case they are applied under weakly acidic conditions (http://en.wikipedia.org/wiki/Reactive_dye).

- *Disperse dyes*

Disperse dyes were originally developed for the dyeing of cellulose acetate, and are substantially water insoluble. The dyes are finely ground in the presence of a dispersing agent and then sold as a paste, or spray-dried and sold as a powder. Their main use is to dye polyester but they can also be used to dye nylon, cellulose triacetate, and acrylic fibres (http://en.wikipedia.org/wiki/Dye).

- *Azoic dyes*

A dye in which the azo group (N=N) is the chromophore and joins benzene or naphthalene rings. These dyes are insoluble pigments built up within the fibre by padding with a soluble coupling component and then treating with a diazotized base. They are used for dyeing colours on cellulosic fibres when comparatively good wet-fastness combined with brightness of shade is required at a reasonable cost (Trotman, 1975).

- *Sulfur dyes*

Sulphur dyes are dyed from a dye bath containing sodium sulphide and common or Glauber's salt, and are oxidized by airing or with some oxidizing agents (sodium bichromate or hydrogen peroxide) in a fresh bath. The main advantage lays in their cheapness, ease of application and good wash-fastness. In their normal state sulphur dyes are insoluble in water but are readily soluble in the solution of sodium sulphide. In this form they have high affinity to the all cellulose fibres (http://www.dyeman.com/Dye%20summary.html).

In the present work, methylene blue as cationic dye, orange II and indigo carmine as anionic dye were selected as a model of dye pollutant with which the degradation efficiencies of the as-prepared catalysts are to be investigated. The structures of three dyes were shown in Figure 5.

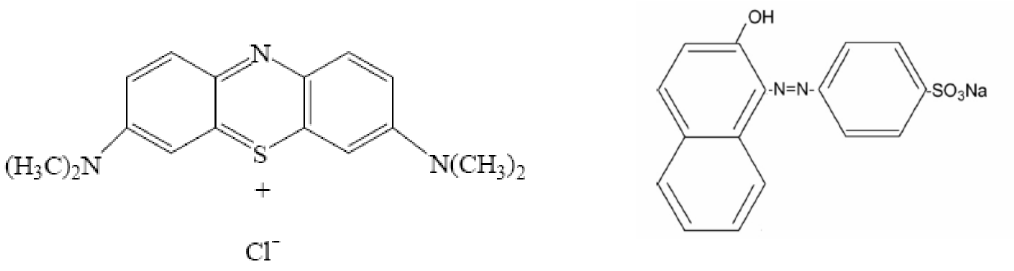

(a) Methylene blue (b) Orange II

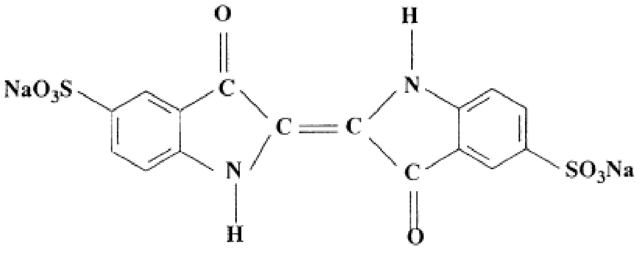

(c) Indigo carmine

Figure 5. Structure of Methylene blue (a), Orange II (b), Indigo carmine (c).

Methylene blue

Methylene blue (MB), (3,7-bis(dimethylamino)phenothiazin-5-ium chloride), $C_{16}H_{18}ClN_3S$, is a brightly colored blue cationic thiazine dye, with λ_{max} values at 665, 614 and 292 nm. It appears as a solid, odorless, dark green powder that yields a blue solution when dissolved in water. It has many uses in a range of different fields such as biology and chemistry. The uses of MB include being an antidote for cyanide poisoning in humans, antiseptic in veterinary medicine and, most commonly, in vitro diagnostic in biology, cytology, hematology and histology, it used as redox indicators in analytical chemistry. (Mills and Wang, 1999).

Methylene blue has been used in several research articles. Xu, *et al*., (1999) reported the influence of particles size of TiO_2 on the photocatalytic degradation of MB in a suspended aqueous solution. Mills and Wang (1999) studied the photobleaching of MB in an aqueous solution in the absence and presence of oxygen. Houas, *et al*., (2001) investigated the TiO_2/UV photocatalytic degradation of methylene blue (MB) in water. Epling and Lin (2002) studied the photoassisted bleaching of MB utilizing TiO_2 and visible light. Awati, *et al*., (2003) studied the photocatalytic decomposition of MB using nanocrystalline anatase titania prepared by ultrasonic technique. Randorn, *et al*., (2004) reported the bleaching of methylene blue by hydrated titanium dioxide. Senthikumaar, *et al*., (2006) investigated the effect of silver doped titania and effect of anions on the degradation of MB. Yang, *et al*., (2006) studied the MB decomposition using nano titania particles embedded in mesoporous SBA-15 silica. Tryba, *et al*., (2007) studied the effect of OH radical formation on TiO_2 in the relation to crystallinity of MB decomposition. Suwanchawalit and Wongnawa, (2008) studied the influence of calcination temperature on microstructures of potassium oxalate dope TiO_2 powder and MB degradation.

A detailed reaction mechanism was presented from the initial step of adsorption involving the cationic functional group of methylene blue molecule, which was probably adsorbed perpendicularly to the surface down to the final products (CO_2, SO_4^{2-}, NH_4^+, and NO_3^-). The degradation pathway of MB has been determined by a careful identification of intermediate products, shown in Scheme 1, in particular aromatics, whose successive hydroxylation lead to the aromatic ring opening (Houas, *et al.*, 2001).

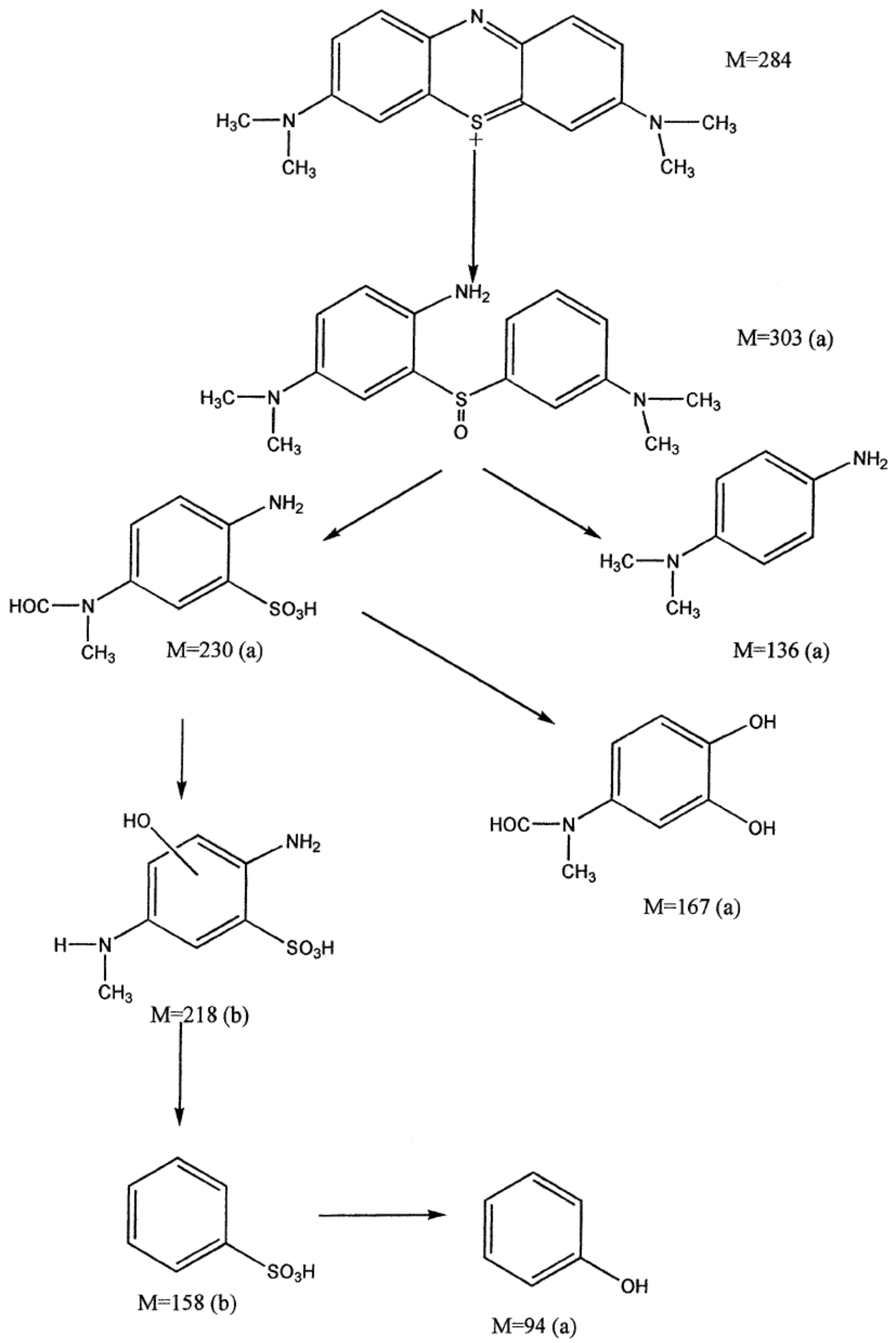

(a) detected by GC/MS (extraction of ions)
(b) detected by LC / MS

Scheme 1. Photocatalytic degradation pathway of methylene blue using TiO_2 as photocatalyst under UV irradiation (Houas, *et al.*, 2001).

Orange II

Orange II (O-II) or also called acid orange 7 (AO 7), (4-(2-hydroxy naphthylazo) benzenesulfonic acid sodium salt), $C_{16}H_{11}N_2NaO_4S$, is a molecule with N=N bonds that is widely used in the dyeing of textiles and cosmetics, and thus found in the wastewaters of the related industries.

Acid orange has been used in several research articles. Stylidi, *et al.* (2003) studied photocatalytic degradation of Acid Orange 7 in TiO_2 suspensions using solar light simulating source. Konstantinou, *et al.*, (2004) investigated kinetic and mechanistic of photocatalytic degradation of AO 7 using TiO_2 as photocatalyst. Fernández, *et al.* (2004) investigated the effect of pH and the H_2O_2 addition using TiO_2-coated glass rings as immobilised photocatalyst. Azam and Hamid (2006) investigated effects of the reactor gap size and UV dosage on decolorization of AO 7 using UV/H_2O_2 process. Hammami, *et al.* (2008) studied the degradation of AO 7 aqueous solutions by electro-Fenton process using Pt or boron-doped diamond (BDD) anode. Zhang, *et al.* (2008) investigated the roles of active oxygen species in photodegradation of AO7 in TiO_2 photocatalysis illuminated by microwave electrodeless lamp**.**

The degradation pathway of AO 7 using TiO_2 as photocatalyst under UV irradiation has been determined by a careful identification of intermediate products, shown in Scheme 2. The oxidative attack of AO 7 leads to benzene sulfonate and naphthoquinone as primary degradation products. The obtained quinone forms are unstable in the oxidative medium of the experience and undergo ring opening reactions leading to the formation of shortchain aliphatic acids such as succinic, formic, maleic, oxalic and acetic acids which are the last by-products before mineralization. Mineralization of AO 7 leads to the conversion of nitrogen and sulphur heteroatoms present in the molecule into inorganic ions, such as nitrate, ammonium and sulphate ions (Konstantinou, *et al.*, 2004; Hammami, *et al.*, 2008).

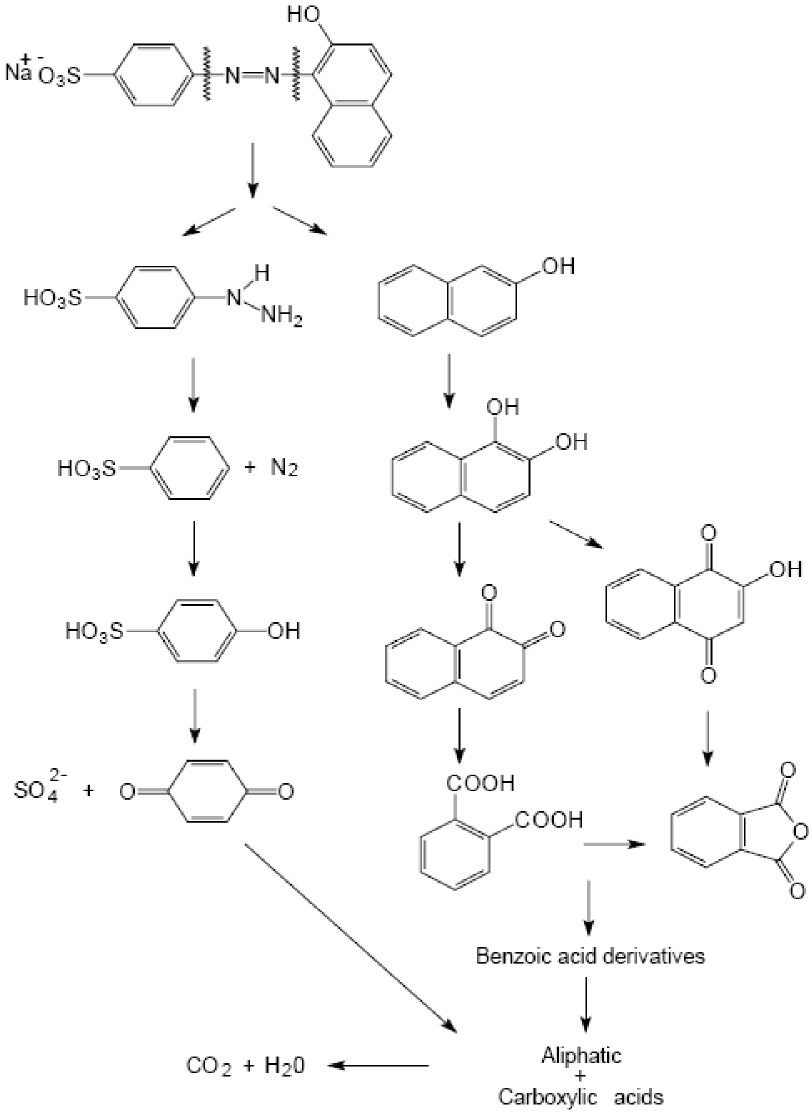

Scheme 2. Photocatalytic degradation pathway of Orange II (or acid orange 7). (Konstantinou, *et al*., 2004)

Indigo carmine

Indigo carmine (IC), disodium salt of 3,3-dioxobi-indolin-2,2-ylidine-5,5-disulfonate, $C_{16}H_8N_2Na_2O_8S_2$, is one of the oldest dyes and still one of the most important used. Its major industrial application is the dyeing of clothes (blue jeans) and other blue denim. It has also been employed as redox indicator in analytical chemistry and as a microscopic stain in biology (Vautier, *et al*., 2001; Gemeay, *et al*., 2003; Barka, *et al*., 2008).

Indigo carmine has been used in several research articles. Vautier, *et al.*, (2001) studied the photocatalytic degradation of indigo and indigo carmine using TiO_2 photocatalyst under UV irradiation. Gemeay, *et al.*, (2003) studied photocatalytic degradation of indigo carmine with H_2O_2 catalyzed by supported transition metal complexes. Barka, *et al.*, (2008) investigated the photocatalytic paremeters: adsorption in the dark, initial concentration of dye solution, temperature, pH using TiO_2 coated non-woven fibres as photocatalyst.

The degradation pathway of IC used Degussa P25-TiO_2 as photocatalyst under UV irradiation has been determined as shown in Scheme 3. In the present case, the OH radicals can break the various C–N and C–C bonds of the chromophore group, thus accounting for the various metabolites identified. The aromatic intermediates found (anthranilic acid, nitrobenzaldehyde, nitrobenzoic acid, and nitrobenzene) undergo successive attacks by OH radicals, giving hydroxylations and/or substitutions generally leading to hydroxy- hydroquinone known as the last aromatic molecule found before the aromatic ring opening. The total degradation leads to the conversion of organic carbon into gaseous CO_2, whereas nitrogen and sulfur heteroatoms are converted into inorganic ions, such as nitrate and ammonium, and sulfate ions, respectively (Vautier, *et al.*, 2001).

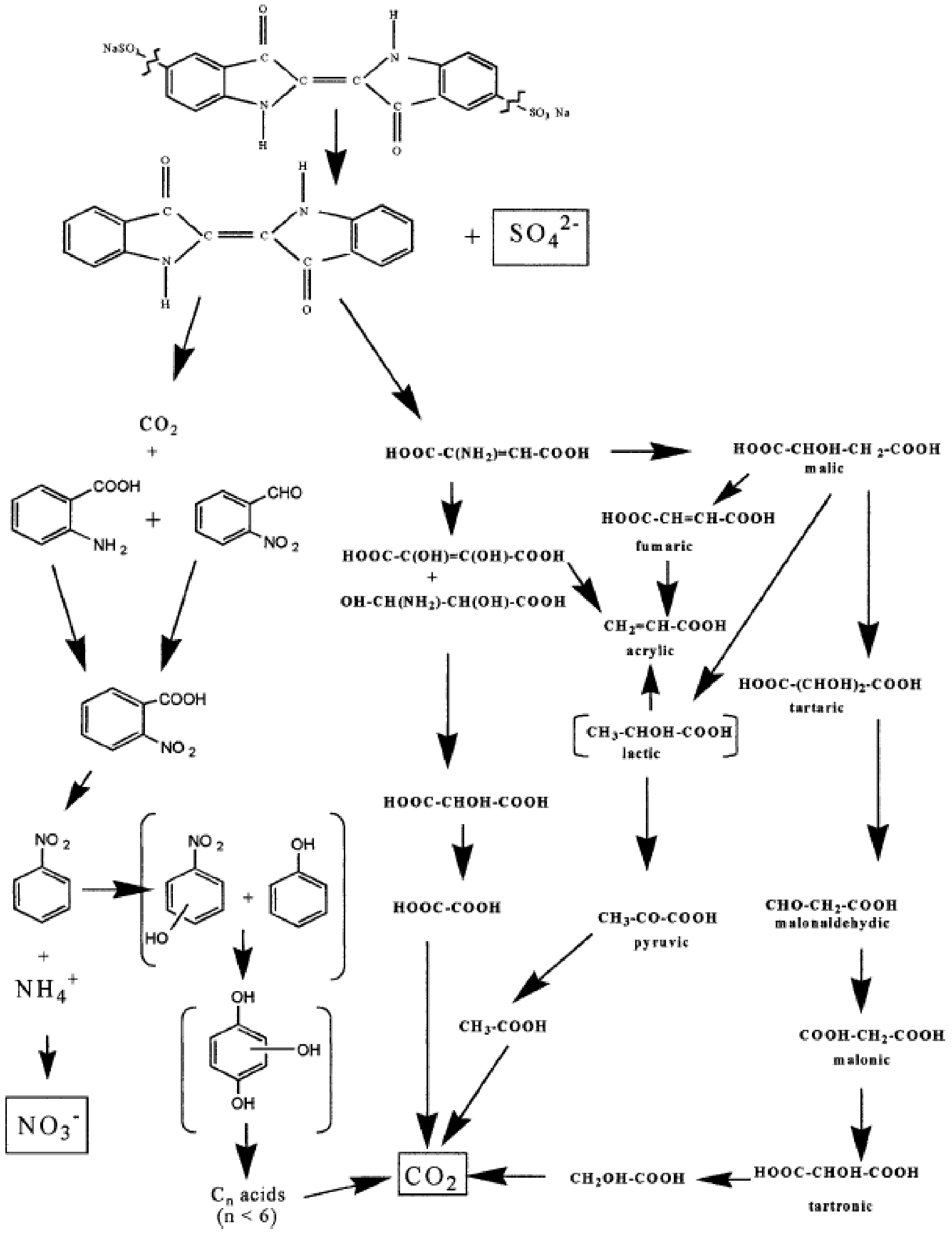

Scheme 3. Photocatalytic degradation pathway of indigo carmine. (Vautier, *et al.*, 2001)

Treatment of dye pollutant

Textile dyes and other industrials dyestuffs constitute one of the largest groups of organic compounds that represent an increasing environmental danger. About 15% of the total world production of the synthetic textile dyes is lost during the dyeing process and is released in the textile effluents. The release of these colored wastewaters in the eco system is a dramatic source of aesthetic pollution, eutrophication and perturbations in aquatic life. Therefore it is important to develop effective wastewater remediation technologies for these compounds (Houas, *et al.*, 2001; Konstantinou, *et al.*, 2004; Senthilkumarr, *et al.*, 2006).

A variety of physical, chemical and biological methods are presently available for treatment of textile wastewater. Biological treatment is a proven technology and is cost-effective. However, it has been reported that the majority of dyes are only adsorbed on the sludge and are not degraded. Physical methods such as ion-exchange, adsorption, air stripping, *etc.*, are also ineffective on pollutants which are not readily adsorbable or volatile, and have the further disadvantage that they simply transfer the pollutants to another phase rather than destroying them (Senthilkumarr, *et al.*, 2006). This leads to search for highly effective method to degrade the dyes into environmentally compatible products. It has been revealed from several literatures that the heterogeneous photocatalysis can be used to destroy the dyes using semiconductor catalyst under light irradiation (Muruganandham, *et al.*, 2005).

Among the semiconductors used, TiO_2 has been successfully used to decolorize and mineralize many organic pollutants including several dyes and their intermediates present in aqueous systems using both artificial light and under sunlight using solar technology. TiO_2 is the most widely used photocatalyst because of its good activity, chemical stability, commercial availability and inexpensiveness. It is generally used as a photocatalyst for environmental applications such as air purification, water disinfection, hazardous waste remediation and water purification (Houas, *et al.*, 2001; Nagaveni, *et al.*, 2004; Muruganandham, *et al.*, 2005).

The major advantages of this heterogeneous photocatalysis are as follows. (i) Photocatalysis offers a good substitute for the energy-intensive conventional treatment methods with the capacity for using renewable and pollution-free solar energy. (ii) Unlike conventional treatment measures, which transfer pollutants from one medium to another, photocatalysis leads to the formation of innocuous products. (iii) This process can be used to destroy a variety of hazardous compounds in different wastewater streams. (iv) It can be applied to aqueous and gaseous-phase treatments, as well as solid- (soil-) phase treatments to some extent. (v) The reaction conditions for photocatalysis are mild, the reaction time is modest, and a lesser chemical input is required. (vi) Secondary waste generation is minimal. (vii) The option for recovery can also be explored for metals, which are converted to their less-toxic/nontoxic metallic states (Kabra, *et al.*, 2004).

The basic principles of heterogeneous photocatalysis can be summarized shortly as follow. The semiconductor is characterized by an electronic band structure in which the highest occupied energy band, called valence band, and the lowest empty band, called conduction band, are separated by a band gap (a region of forbidden energies in a perfect crystal) (Litter, 1999). Absorption of a photon by semiconduction solids excites an electron (e^-) from the valence band to the conduction band if the photon energy, hν, equals or exceeds the band gap of the semiconductor/photocatalyst. Simultaneously, an electron vacancy or a positive charge called a hole (h^+) is also generated in the valence band as shown in Figure 6. Ultraviolet (UV) or near-ultraviolet photons are typically required for this kind of reaction (Kabra, *et al.*, 2004). Recently, many works have been reported on the degradation of organic dyes induced by visible light by photosensitization. The interest is to use solar visible light which is free and inexhaustible (Houas, *et al.*, 2001). The electron-hole pair (e^--h^+ pair) thus created migrates to the photocatalyst surface where it either recombines, producing thermal energy, or participates in redox reactions with the compounds adsorbed on the photocatalyst. The lifetime of an e^--h^+ pair is a few nanoseconds, but this is still long enough for promoting redox reactions in the solution or gas phase in contact with the semiconductor (Kabra, *et al.*, 2004).

Generally, the hole oxidizes water to hydroxyl radicals (which subsequently initiate a chain of reactions leading to the oxidation of organics), or it can be combined with the electron from a donor species, depending on the mechanism of the photoreaction. Similarly, the electron can be donated to an electron acceptor such as an oxygen molecule (leading to formation of superoxide radical) or a metal ion (with a redox potential more positive than the band gap of the photocatalyst). This metal ion can be reduced to its lower valence states and deposited on the surface of the catalyst. The electron-transfer process is more efficient if the species are preadsorbed on the catalyst surface (Kabra, *et al.*, 2004). The heterogeneous photocatalytic oxidation processes is illustrated in Figure 6.

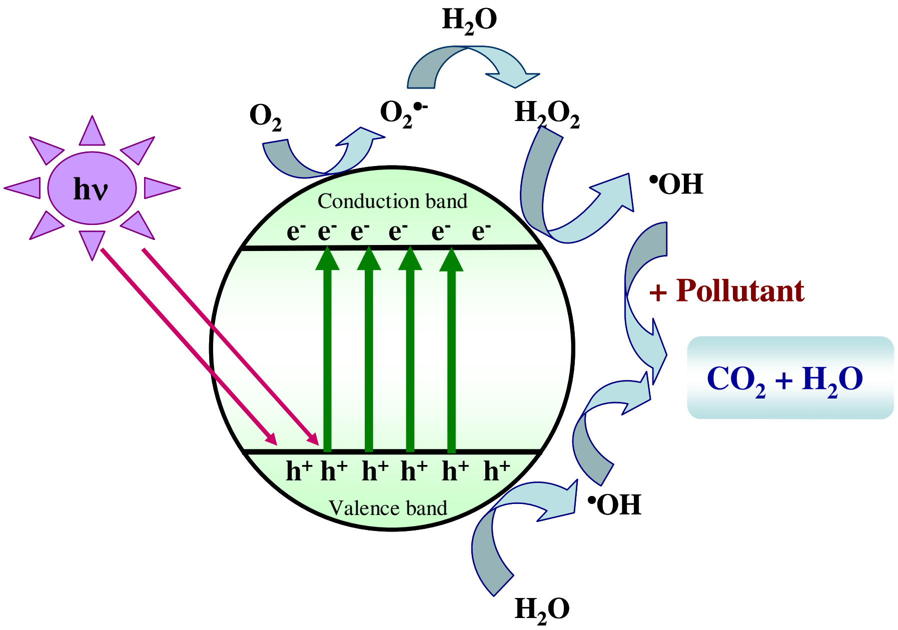

Figure 6. The photocatalytic oxidation processes of TiO_2 photocatalyst. (Adapted from Daneshvar, *et al.*, 2004)

The mineralization of most of the organic pollutants could be degraded following the usually proposed mechanism as following equations.

1. Absorption of efficient photons ($h\nu > E_g = 3.2$ eV) by titania

$$TiO_2 + h\nu \rightarrow e_{CB}^{-} + h_{VB}^{+} \quad (5)$$

2. Oxygen ionosorption (first step of oxygen reduction; oxidation state of oxygen changes from 0 to -1/2)

$$(O_2)_{ads} + e_{CB}^{-} \rightarrow O_2^{\bullet -} \quad (6)$$

3. Neutralization of OH^- groups by photoholes which produces $OH^\bullet$ radicals

$$(H_2O \leftrightarrow H^+ + OH^-)_{ads} + h_{VB}^+ \rightarrow H^+ + OH^\bullet \qquad (7)$$

4. Neutralization of $O_2^{\bullet -}$ by protons

$$O_2^{\bullet -} + H^+ \rightarrow HO_2^\bullet \qquad (8)$$

5. Transient hydrogen peroxide formation and dismutation of oxygen

$$2\,HO_2^\bullet \rightarrow H_2O_2 + O_2 \qquad (9)$$

6. Decomposition of H_2O_2 and second reduction of oxygen

$$H_2O_2 + e^- \rightarrow OH^\bullet + OH^- \qquad (10)$$

7. Oxidation of the organic reactant via successive attacks by $OH^\bullet$ radicals

$$R + OH^\bullet \rightarrow R^\bullet + H_2O \qquad (11)$$

8. Direct oxidation by reaction with holes

$$R + h^+ \rightarrow R^{+\bullet} \rightarrow \text{degradation products} \qquad (12)$$

As an example of the last process, holes can react directly with carboxylic acid generating CO_2

$$RCOO^- + h^+ \rightarrow R^\bullet + CO_2 \qquad (13)$$

The efficiency of advanced oxidation processes for degradation of recalcitrant compounds has been extensively documented. Photochemical processes are used to degrade toxic organic compounds to CO_2 and H_2O without the use of additional chemical oxidants, because the degradation is assisted by high concentrations of hydroxyl radicals ($OH^\bullet$) generated in the process. The hydroxyl radicals and superoxide anion can act as oxidants leading to the mineralization of organic compounds (Gome de Moraes, *et al.*, 2000).

Many studied revealed that heterogeneous photocatalytic oxidation processes can be used for removing coloring material from dye effluent. Zhang, *et al.*, (1998) demonstrated the TiO_2-assisted photodegradation of dye pollutants under illumination by visible light. Kiriakidou, *et al.*, (1999) reported the effect of operational parameters and TiO_2-doping on the photocatalytic degradation of Acid Orange 7 (AO7). Zhang, *et al.*, (2000) investigate the effect of calcination on the photocatalytic properties of nanosized TiO_2 powders prepared by $TiCl_4$ hydrolysis. Zhu, *et al.*, (2000) studied the photocatalytic degradation of azo dyes by supported

TiO_2 + UV in aqueous solution. Hachem, *et al.*, (2001) studied the photocatalytic degradation of various dyes (Orange II, Orange G, Congo Red, Indigo Carmine, Crystal Violet, Malachite Green, Remazol Blue and Methyl Yellow), using P25 Degussa as catalyst. Grzechulska, *et al.*, (2002) investigated the effect of operational parameters, i.e., pH, photocatalyst content, initial dye concentration on the photocatalytic decomposition of azo-dye acid black 1 in water over modified titanium dioxide. Zhao, *et al.*, (2002) studied the influence of Pt doping on photodegradation of sulforhodamine-B dye under visible irradiation. Sauer, *et al.*, (2002) studied the kinetics of photocatalytic degradation of reactive dyes in a TiO_2 slurry reactor. Fernándea, *et al.*, (2002) reported photo-discolouration of Orange II solutions at different concentrations irradiated with a 254 nm mercury lamp (125 W) in the presence of Degussa P-25-TiO_2 dispersions. Daneshvar, *et al.*, (2003) studied the photocatalytic degradation of azo dye acid red 14 in water and investigated the effect of operational parameters. Gomes da Silva and Faria (2003) investigated effect of kinetic on photodegradation of azo dye (Solophenyl Green: SG) by TiO_2 under UV irradiation. Xie and Yuan (2003) reported the photocatalytic activity and recycle application of titanium dioxide sol for X-3B photodegradation. Konstantinou, *et al.*, (2004) investigated the effect of kinetic on the photocatalytic degradation of azo dye in an irradiated titanium dioxide aqueous suspension. Chen, *et al.*, (2005) reported the role of primary active species and TiO_2 surface characteristic in UV-illuminated photodegradation of acid orange 7. Zhang, *et al.*, (2006) revealed the effect of Pt doped on the TiO_2 thin film possessed the higher photocatalytic activity than the undoped TiO_2 thin film under visible irradiation. Venkatachalam, *et al.*, (2007) reported the varied reaction parameters: hydrolyzing agent, molar ratio, aging time, calcination during the synthesis of nano size TiO_2 and revealed its photocatalytic activity higher than P25-TiO_2 on photocatalytic oxidation of bisphenol-A.

1.3 Objectives

The objectives of this research are as follows:

(1) To prepare KOX-TiO_2 powders by the sol-gel method using hexamethylenetetramine (HMT) as basic reagent and $TiCl_4$ as precursor.

(2) To prepare TiO_2/rubber sheets by directly mixing TiO_2 powders with rubber latex and distilled water.

(3) To prepare macroporous chitosan/TiO_2 scaffolds via ice-templating method.

(4) To prepare mesoporous TiO_2 powders via surfactant mediated sol-gel process using $TiCl_4$ ang $TiOSO_4$ as precursors.

(5) To characterize the physical properties of TiO_2 products using XRD, BET, DRS, PL, SEM, TEM, and FT-IR techniques.

(6) To investigate the photocatalytic activity of dye degradation by these synthesized TiO_2 products, and compared with comercial P25 TiO_2 catalyst under the same conditions and evaluated their reclyclability.

CHAPTER 2

EXPERIMENTAL AND CHARACTERIZATION TECHNIQUES

2.1 Experimental

2.1.1 Synthesis of potassium oxalate-doped TiO_2 (KOX-TiO_2) powders

2.1.1.1 Materials

(1) Hexamethylenetetramine, $C_6H_{12}N_4$, A.R., code no. 52710, purity 99%, Fluka, South Korea.

(2) Potassium oxalate, $((COOK)_2.H_2O$, A.R., code no. A413, purity 98.5-101.0%, Ajax Finechem, Australia.

(3) Silver nitrate, $AgNO_3$, A.R. code no. 102333J, BDH, England.

(4) Titanium tetrachloride, $TiCl_4$, A.R. code no. 488407, purity $\geq$ 99%,Carlo Erba, France.

2.1.1.2 Method

A. Synthesis of TiO_2 powder

All chemicals used in this work were of analytical grade and were used without further purification. Titanium tetrachloride was used as starting material to produce titanium dioxide particles by sol-gel method. For the preparation, 20 mL of $TiCl_4$ was added slowly to 100 mL of cold distilled water to obtain the titanium tetrachloride aqueous solution. Then 70 mL of potassium oxalate (1.3 M) was added into this solution and refluxed at 90 ^{o}C for 13 h under vigorous stirring. The resulting solution was then treated with hexamethylenetetramine ($C_6H_{12}N_4$) until the pH value was 7 and maintained at the same temperature for 13 h. The white precipitate formed was filtered and then washed with distilled water until no chloride ion was found by $AgNO_3$ solution test. The washed samples were dried at 105 °C for a day and ground to fine powder to give final products designated as *0.5KOX-*TiO_2*_non calcined*. This product was subsequently calcined at 400, 600, 800, and 1000 °C for 3 h and designated as *0.5KOX-*TiO_2*_**x**c*, where ***x*** is the calcination temperature.

B. Characterization of samples

The crystallization and phase formation of the resulting TiO_2 samples were studied with the Philips PW 3710 powder diffractometer (PHILIPS X'Pert MPD, the Netherlands) using Cu K_α radiation and equipped with a Ni filter in the range 5-90° 2θ. The crystallite size was calculated using the Scherrer's equation;

$$L = \frac{K\lambda}{\beta \cos\theta} \tag{14}$$

where, L is the average crystallite size in nm, λ is the wavelength of the X-ray radiation (0.154056 nm), K is a constant usually taken as 0.9, β is the corrected band broadening (full width at half-maximum (FWHM)) after substraction of equipment broadening in radians, and θ is the diffraction angles (Yan, *et al*., 2005).

The specific surface area and pore size distribution of TiO_2 samples were characterized by analyzing the N_2 adsorption isotherms obtained at 77 K using SA 3100 (Coulter, U.S.A.) equipment.

The surface features and morphologies of the as-prepared TiO_2 samples were investigated by using a scanning electron microscope (SEM) model JSM-5800 LV (Jeol Apparatus, Japan).

The infrared spectra were recorded using PerkinElmer model Spectrum Gx (Bruker, Germany) spectrophotometer in diffused reflectance mode at 400-4000 cm^{-1} with KBr as reference material.

The band gap energies of the TiO_2 samples were determined using two methods: UV-Vis DRS and photoluminescence spectroscopy. For the UV-Vis method, a Shimadzu UV-2401 spectrophotometer (Shimadzu, Japan) was used. The spectra were recorded in diffused reflectance mode using $BaSO_4$ as a reference. For the photoluminescence method, the samples were analyzed with a luminescence spectrometer (LS 55, Perkin Elmer Instrument, U.K.). The band gap energies (E_g) of the catalyst were calculated according to equation (15):

$$E_g = h\frac{c}{\lambda} \qquad (15)$$

where E_g is the band gap energy (eV), h is the Planck's constant, c is the light velocity (m/s), and λ is the wavelength (nm).

2.1.1.3 Photocatalytic test

A. Materials

(1) Methylene blue, $C_{16}H_{18}N_3SCl$; A.R., code no. 1137, purity 96.0-101.0 %, Ajax Finechem, Australia.

(2) Hydrogen peroxide, H_2O_2; A.R., code no. 307701005, Carlo Erba, Italy.

(3) Titanium dioxide P25, code no. D-60287, Degussa AG, Frankfurt, Germany.

B. Photocatalytic procedures

The photocatalytic activity of TiO_2 samples were tested for the degradation of methylene blue solution. The experiments were performed in a closed compartment (0.9 m × 0.9 m × 0.9 m) containing 5 fluorescence blacklight (20 W) tubes. The 1.0 g/L TiO_2 sample was dispersed in 75 mL methylene blue solution (2.5×10^{-4} M) in each experiment. Prior to the illumination, the suspension was stirred for 1 h to reach the adsorption equilibrium. Then the mixture was irradiated using 5 tubes of fluorescence blacklight 20 W (λ_{max} 366 nm). In all studies, the mixture was magnetically stirred, before and during illumination. At given irradiation time intervals (every 1 h), 5 mL of the sample was collected and centrifuged to separate TiO_2 powders prior to the absorbance measurement. The residual concentration of MB was monitored by observing the change in absorbance at 665 nm using UV-Vis spectrophotometer (Specord S100, Analytik Jena GmbH, Germany). Controlled experiments, without light or without TiO_2, were performed to demonstrate that the degradation of the dye was dependent on the presence of both light and TiO_2.

2.1.2 Preparation of TiO_2/rubber sheets

2.1.2.1 Materials

(1) Hexamethylenetetramine, $C_6H_{12}N_4$, A.R., code no. 52710, purity 99%, Fluka, South Korea.
(2) Latex; 60% HA, Chana Latex Co. Ltd, Songkhla, Thailand.
(3) Potassium oxalate, $((COOK)_2.H_2O$, A.R., code no. A413, purity 98.5-101.0 %, Ajax Finechem, Australia.
(4) Silver nitrate, $AgNO_3$, A.R., code no. 102333J, BDH, England.
(5) Titanium tetrachloride, $TiCl_4$, A.R., code no. 488407, purity ≥ 99%, Carlo Erba, France.
(6) Titanium dioxide (P25), A.R., code no. D-60287, Degussa AG, Frankfurt, Germany.
(7) Titanium dioxide (Anatase), A.R., code no. 488257, Carlo Erba, Italy.

2.1.2.2 Method

A. Synthesis of KOX-doped TiO_2 powders

A 20 mL of $TiCl_4$ was added slowly to 100 mL of cold distilled water to obtain the titanium tetrachloride aqueous solution. Then solution of potassium oxalate (1.3 M) was added into this solution and refluxed at 90 ^{o}C for 13 h under vigorous stirring. The resulting solution was then treated with hexamethylenetetramine ($C_6H_{12}N_4$) until the pH value was 7 and maintained at the same temperature for 13 h. The white precipitate formed was filtered and then washed with distilled water until no chloride ion was found by $AgNO_3$ solution test. The washed samples were dried at 105 °C for a day and ground to fine powder to give final products designated as *K1-TiO*$_2$ (for 0.5 mol% K-doped) and *K2-TiO*$_2$ (for 4.0 mol% K-doped).

B. Preparation of TiO_2-impregnated rubber sheets

From the previous study (Sriwong, *et al.*, 2008), The Imp-TiO_2 sheets were prepared by mixing 0.1 g of each TiO_2 in 3 ml distilled water (anatase, Carlo Erba Milano, Italy) and in 5 ml distilled water (P25 Degussa AG, Frankfurt, Germany), stirred for 3 min after which 5 ml of rubber latex (60% HA) was added and then stirred for another 5 min. The Imp-commercial TiO_2 sheets were designated as *Imp-Ana* and *Imp-P25* for impregnated anatase TiO_2 and P25 TiO_2, respectively. In this work, the Imp-synthesized TiO_2 sheets were prepared using the same method as the Imp-commercial TiO_2 sheets but using 0.1 g of the synthesized TiO_2 powders in 1 ml distilled water. The Imp-synthesized TiO_2 sheets were designated as *Imp-K1* and *Imp-K2* for impregnated K1-doped TiO_2 and K2-doped TiO_2, respectively. The mixture was poured into a petri dish (3.5 in. diameter) and left to dryness at room temperature for 15 h after which it was taken out (from petri dish), reversed, and dried at room temperature about 2 h. The preparation process for preparing TiO_2/rubber sheet is shown in Figure 7.

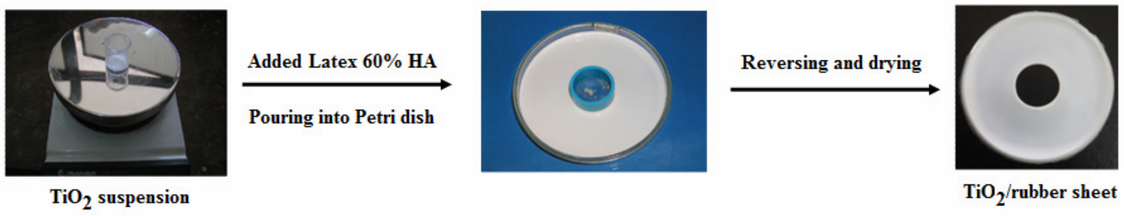

Figure 7. The preparation process for TiO_2/rubber sheet.

2.1.2.3 Characterization of TiO_2/rubber sheets

The crystallization and phase formation of the resulting TiO_2 samples was studied with the Philips PW 3710 powder diffractometer (PHILIPS X'Pert MPD, the Netherlands) using Cu K_α radiation and equipped with a Ni filter in the range 5-90° 2θ. All data were acquired by the Scientific Equipment Center, Prince of Songkla University, Hat Yai, Songkhla, Thailand.

The surface features and morphologies of the as-prepared TiO_2 samples were investigated by using a scanning electron microscope (SEM) model JSM-5800 LV (Jeol Apparatus, Japan).

The band gap energies of the TiO_2 samples were determined using UV-Vis DRS technique. A Shimadzu UV-2401 spectrophotometer (Shimadzu, Japan) was used for recording the DRS spectra in diffused reflectance mode using $BaSO_4$ as a reference.

2.1.2.4 Photocatalytic test

A. Materials

(1) Methylene blue, $C_{16}H_{18}N_3SCl$; A.R., code no. 1137, purity 96.0-101.0 %, Ajax Finechem, Australia.

(2) Hydrogen peroxide, H_2O_2; A.R., code no. 307701005, Carlo Erba, Italy.

B. Construction of calibration graph

In this work, the concentrations of standard methylene blue solutions were in the range 2.5×10^{-6} M to 3.0×10^{-5} M. The standard calibration curve of methylene blue was constructed from five working concentrations: 2.5×10^{-6} M, 5.0×10^{-6} M, 1.0×10^{-5} M, 2.0×10^{-5} M and 3.0×10^{-5} M. The calibration graph was a straight line with $R^2 = 0.9983$.

C. Photocatalytic studies

The photocatalytic activities of the impregnated TiO_2 rubber sheets were tested for the degradation of methylene blue solution. The experiments were performed in a closed compartment (0.9 m × 0.9 m × 0.9 m) containing 5 fluorescence blacklight (20 W, F20T12-BLB, GE, USA) tubes. The impregnated rubber sheets were placed in a petri dish (4 in. diameter) containing 60 mL of MB solution (2.5×10^{-5} M) in each experiment. Prior to the illumination, the solution was stirred in the dark for 1 h to reach the adsorption and desorption equilibrium. Then the solution was irradiated using 5 tubes of fluorescence blacklight 20 w (λ_{max} 366 nm) (Randorn, *et al.*, 2004). In all studies, the solution was magnetically stirred, before and during illumination. At given irradiation time intervals (every 1 h), 4 mL of the sample was collected and measured for the residual concentration of MB by observing the change in absorbance at 665 nm using UV-Vis spectrophotometer (Specord S100, Analytik Jena GmbH, Germany). The concentration of MB solution was determined quantitatively through the calibration graph constructed above. Controlled experiments, without light or without TiO_2, were performed to demonstrate that degradation of the dye was dependent on the presence of both light and TiO_2.

The effect of various initial MB dye concentrations were investigated in the range of 1.0×10^{-5} M to 3.0×10^{-5} M. The pH of MB dye solutions were studied in the range of 3 to 9 by adding dilute aqueous solution of HCl or NaOH. In addition, the reclyclability test and regeneration process were also studied. The regeneration process was successfully done by treating the used rubber sheet in 50 mL of H_2O_2 solution (0.2 M) with stirring overnight under UV light irradiation.

2.1.3 Preparation of Chitosan/TiO_2 scaffolds

2.1.3.1 Materials

(1) Hexamethylenetetramine, $C_6H_{12}N_4$, A.R., code no. 52710, purity 99%, Fluka, South Korea.

(2) Chitosan (low molecular weight), A.R., code no. 448869, Aldrich, Germany.

(3) γ-glycidoxypropyltrimethoxysilane (GPTMS; $C_9H_{20}O_5Si$), A.R., ABCR.

(4) Potassium oxalate, $((COOK)_2.H_2O$, A.R., code no. A413, purity 98.5-101.0 %, Ajax Finechem, Australia.

(5) Silver nitrate, $AgNO_3$, A.R., code no. 102333J, BDH, England.

(6) Titanium tetrachloride, $TiCl_4$, A.R., code no. 488407, purity ≥ 99%, Carlo Erba, France.

(7) Titanium dioxide (P25), A.R., code no. D-60287, Degussa AG, Frankfurt, Germany.

(8) Titanium (IV) isopropoxide, $Ti(OPr)_4$, A.R., code no. 377996, Aldrich, Germany.

2.1.3.2 Method

A. Synthesis of KOX-doped TiO_2 powders

A 20 mL of $TiCl_4$ was added slowly to 100 mL of cold distilled water to obtain the titanium tetrachloride aqueous solution. Then solution of potassium oxalate (1.3 M) was added into this solution and refluxed at 90 ^oC for 13 h under vigorous stirring. The resulting solution was then treated with hexamethylenetetramine ($C_6H_{12}N_4$) until the pH value was 7 and maintained at the same temperature for 13 h. The white precipitate formed was filtered and then washed with distilled water until no chloride ion was found by $AgNO_3$ solution test. The washed samples were dried at 105°C for a day and ground to fine powder and calcined at 400°C (3 h) to give final products designated as *KOX-*TiO_2.

B. Preparation of Dialyzed-TiO_2 sol

The stable sol were prepared by precipitation from titanium(IV) isopropoxide aqueous solution acidified with nitric solution, a white suspension was formed, and then peptized at 85°C for 12 h under vigorous stirring to give light blue solution. The resulting colloid was then dialyzed using dialysis membrane for two days to give the stable solution called dialyzed-TiO_2 sol.

C. Preparation of crosslinked-chitosan gel

Chitosan was dissolved in acetic acid 0.2 M aqueous solution to form a 2.5 wt% chitosan solution. The solution was added a certain amount of GPTMS to give the 5wt% GPTMS-chitosan gel.

D. Preparation of crosslinked chitosan-TiO_2 scaffold

Each type of TiO_2 sol (50 mg/mL) mixed with crosslinked-chitosan (5wt% GPTMS-CS) in the 1:1 ratio. The obtained gel were put in the 2 mL syringe size (diameter 0.8 cm, length 4 cm) and then immerged into liquid N_2 cold bath at a constant freezing rate of 5.9 mm/min. The samples were freeze-dried using LABNOCO freeze-drier overnight. The resulting scaffolds remained intact in both shape and size of the syringes as shown in Figure 8. In this study, we investigated the ratio of TiO_2 sol/chitosan gel, freezing rate, and size of syringe to produced ordered porous structure materials.

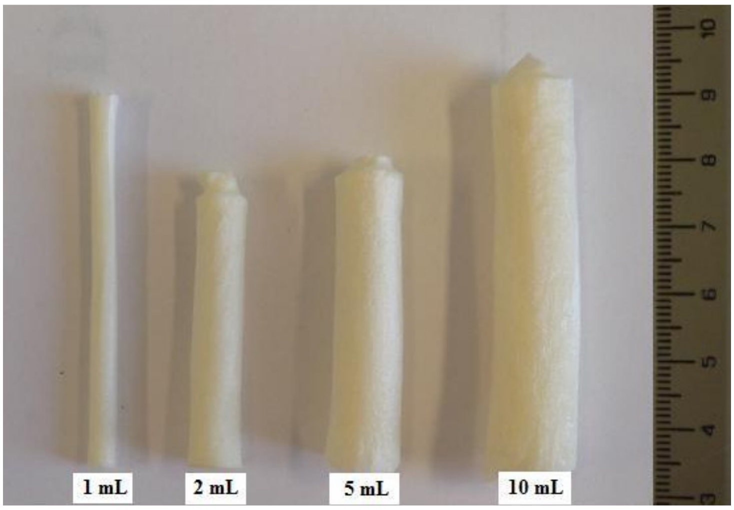

Figure 8. The feature of CS/TiO_2 scaffolds with different size of syringe used.

2.1.3.3 Characterization of crosslinked chitosan-TiO_2 scaffold

The crystallization and phase formation of the TiO_2 powders were studied with the Siemens D500 diffractometer using Cu K_α radiation and equipped with a Ni filter in the range 5-90° 2θ. The crystalline size was calculated using the Scherrer's equation. The feature and estimated size of TiO_2 powders were measured using TEM technique (JEOL: JEM-1200EXII electron microscope). The surface features and morphologies of the TiO_2 powders and CS/TiO_2 scaffolds were investigated by using a scanning electron micrometer model JSM-5600 LV (JEOL apparatus). The surface functional groups of CS/TiO_2 scaffolds were determined using FT-IR technique (a Perkin Elmer Spectrum/ FT-IR spectrometer).

2.1.3.4 Photocatalytic activity of CS/TiO_2 scaffolds

A. Materials

(1) Methylene blue, $C_{16}H_{18}N_3SCl$; A.R., code no. 1137, Ajax Finechem, Australia.

(2) Orange II sodium salt, $C_{16}H_{11}N_2NaO_4S$; A.R., code no. O8126, SIGMA, Germany.

B. Photocatalytic procedures

The photocatalytic activities of the CS/TiO_2 scaffolds were tested for the degradation of methylene blue (as cationic dye model) and orange II (as anionic dye model). The experiments were performed using UV lamp (365 nm, model UVLS-28, U.S.A.). The CS/TiO_2 scaffolds were cut into pieces and placed in a petri dish (2 inch diameter) containing 20 ml of dye solution (2.5×10^{-5} M) in each experiment. Prior to the illumination, the solution was kept in the dark for 1 h to reach the adsorption and desorption equilibrium. Then the solution was irradiated using UV lamp. At given irradiation time intervals (every 1 h), 2 mL of the sample was collected and measured the residual concentration of dye by observing the change in absorbance at 665 nm (for MB) and 484 nm (for OII) using UV-Vis spectrophotometer (a Perkin Elmer Lambda 25 UV-Visible spectrophotometer). The concentration of dye solution was determined quantitatively through the calibration graph constructed from solutions of dye at various concentrations. Controlled experiments, without light or without TiO_2, were performed to demonstrate that degradation of the dye was dependent on the presence of both light and TiO_2.

2.1.4 Synthesis of mesoporous TiO_2 powders with different precursors

2.1.4.1 Materials

(1) Ammonium hydroxide (Ammonia solution) 28.0-30.0%, NH_4OH; A.R., code no. 9721-03, J.T. Baker, U.S.A.

(2) Barium chloride, $BaCl_2.2H_2O$, A.R., purity 99 %, Ajax Finechem, Australia.

(3) Dichloromethane, CH_2Cl_2, A.R., code no. A3508L, purity 99.5 %, LAB-SCAN analytical science, Ireland.

(4) Pluronic P123, $PEO_{20}PPO_{70}PEO_{20}$ ($M_{av} = 5800$), A.R., code no. 435365, Batch#02602TC, Aldrich, Germany.

(5) Silver nitrate, $AgNO_3$, A.R., code no. 102333J, BDH, England.

(6) Titanium (IV) oxysulfate hydrate, $TiOSO_4.nH_2O$, A.R., code no. 14023, Riedel-de Haen, Germany.

(7) Titanium tetrachloride, $TiCl_4$, A.R., code no. 488407, purity $\geq$ 99%, Carlo Erba, France.

(8) Acetic acid, CH_3COOH, A.R., code no. 2789, purity 99.9%, LAB-SCAN, Ireland.

(9) Hydrochloric acid, HCl, A.R., code no. 9535-03, J.T. Baker, U.S.A.

(10) Nitric acid 69.0-70.0%, HNO_3; A.R. code no. 9601-04, purity 69.3 %, J.T. Baker, U.S.A.

(11) Formic acid, HCOOH, A.R., code no. 06460, purity 85 %, Fluka, Switzerland.

(12) Orthophosphoric acid 85% (%w/v), H_3PO_4; A.R. code no. 7664-38-2, Carlo Erba, France.

(13) Sulfuric acid, H_2SO_4, A.R. code no. 9681-03, purity 96.6 %, J.T. Baker, U.S.A.

2.1.4.2 Method

A. Synthesis of TiO_2 powders with $TiCl_4$ as precursor

In a typical preparation, a 0.5 g/L Pluronic P123 aqueous solution was mixed with $TiCl_4$ aqueous solution under stirring and heated the mixed solution up to 60°C and refluxed for 1 h. The resulting solution was then treated with concentrated ammonium hydroxide solution until the pH value was 7 and maintained at the same temperature for a day. The white precipitate formed was extracted with dichloromethane twice then filtered and washed with distilled water until no chloride ion was found by $AgNO_3$ solution test. The washed samples were dried at 105°C for a day and ground to fine powder to give final products that called ***P123-TiO₂_TiCl₄***. In this study, we investigated the effect of reaction temperatures (40°C, 60°C, 90°C), amount of water (60w, 100w, 200w, 300w), and types of acid catalyst (HCl, HCOOH, HNO_3, CH_3COOH, H_2SO_4, H_3PO_4) on the morphologies of mesoporous TiO_2 materials and their photocatalytic property.

B. Synthesis of TiO_2 powders with $TiOSO_4$ as precursor

In a typical preparation, a 0.5 g/L Pluronic P123 aqueous solution was mixed with 3 M $TiOSO_4$ aqueous solution under stirring and heated the mixed solution up to 90°C and refluxed for 1 h. The resulting solution was then treated with concentrated ammonium hydroxide solution until the pH value was 7 and maintained at the same temperature for a day. The white precipitate formed was extracted with dichloromethane twice then filtered and washed with distilled water until no sulfate ion was found by $BaCl_2$ solution test. The washed samples were dried at 105°C for a day and ground to fine powder to give final products that called ***P123-TiO₂_TiOSO₄***. In this study, we investigated the effect of reaction temperatures

(40°C, 60°C, 90°C), concentrations of $TiOSO_4$ (0.5 M, 1 M, 3 M, 5M), and types of acid catalyst (HCl, HCOOH, HNO_3, CH_3COOH, H_2SO_4, H_3PO_4) on the morphologies of mesoporous TiO_2 materials and their photocatalytic property.

2.1.4.3 Characterization of mesoporous TiO_2 powders

The crystallization and phase formation of the resulting TiO_2 samples was studied with the Philips PW 3710 powder diffractometer (PHILIPS X'Pert MPD, the Netherlands) using Cu K_α radiation and equipped with a Ni filter in the range 5-90° 2θ.

The specific surface area and pore size distribution of TiO_2 samples were characterized by analyzing the N_2 adsorption isotherms obtained at 77 K using SA 3100 (Coulter, U.S.A.) equipment.

The surface features and morphologies of the as-prepared TiO_2 samples were investigated by using a scanning electron micrometer model JSM-5800 LV, Jeol Apparatus, Japan.

The transmission electron microscopy image was obtained on a JEOL JSM 2010 electron microscope operating at 120 kV. The TEM sample prepared by dipping an aqueous suspension of sample powders on a Formvar coated copper grid and dried at room temperature.

The Fourier-transformed infrared spectra were recorded on PerkinElmer model Spectrum Bx (Bruker, Germany) spectrophotometer at the range 400-4000 cm^{-1} using the pellets of the samples mixed with KBr.

The band gap energies of the calcined TiO_2 samples were determined using Shimadzu UV-2401 spectrophotometer (Shimadzu, Japan). The spectra were recorded in diffused reflectance mode. $BaSO_4$ was used as a reference.

2.1.4.4 Photocatalytic test

A. Materials

(1) Indigo Carmine, $C_{16}H_8N_2Na_2O_8S_2$; A.R., code no. 57000, Fluka, U.S.A.

(2) Hydrochloric acid; HCl, A.R., code no. 9535-03, J.T. Baker, U.S.A.

(3) Sodium hydroxide; NaOH, A.R., code no. K2001, LAB-SCAN analytical science, Ireland.

B. Photocatalytic procedures

The experiments were performed by dispersing 1.0 g/L TiO_2 sample in 50 mL indigo carmine solution (5.0×10^{-5} M). Prior to the illumination, the suspension was stirred for 1 h to reach the adsorption equilibrium onto the surface of sample. Then the mixture was irradiated using 5 tube of black light 20 w (λ_{max} 366 nm). In all studies, the mixture was magnetically stirred, before and during illumination. At given irradiation time intervals (every 15 min), 4 mL of the sample was collected and centrifuged to separate TiO_2 powders. The residual concentration of IC is monitored by using the change in absorbance of dyes at 610 nm using UV-Vis spectrophotometer. A test with a commercial TiO_2, P25, was also conducted under the same experimental conditions. Controlled experiments without light and without TiO_2 were performed to demonstrate that degradation of the dye was dependent on the presence of light and TiO_2. The disappearance of IC was analyzed by UV–Vis spectrophotometer (Specord S100, Analytik Jena GmbH, Germany) over the 200–800 nm range. Calibration plots based on Beer-Lamberts law were established relating the absorbance to the concentration. The decolorization was determined at the maximum 610 nm. % Removal efficiency of IC was measured by applying the following equation;

$$\%\ \ Removal\ efficiency = \frac{C_0 - C}{C_0} \times 100 \qquad (16)$$

where C_o is the original indigo carmine (IC) content and C is the retained IC in solution.

In addition, the photodegadation of methylene blue was also studied. The photocatalytic parameters includings: the effect of various initial dye concentrations, pH, kinetics studies, and recyclability studies were investigated. The pH of dye solutions were studied in the range of 3 to 11 by adding dilute aqueous solution of HCl or NaOH, respectively.

2.2 Characterization techniques

2.2.1 X-ray diffraction (XRD)

X-rays have wavelengths in the Angstrom range, are sufficiently energetic to penetrate solid and are well suited to probe their internal structure. XRD is used to identify bulk phases, to monitor the kinetics of bulk transformations and to estimate particle sizes. The X-ray wavelength commonly employed is the characteristic K_α radiation, λ = 1.5418 Å, emitted by copper. When crystal diffract X-ray, it is the atoms or ions which act as secondary point sources and scatter the X-rays; in the optical grating, it is the lines scratched or ruled on the glass surface which cause scattering.

Historically, two approaches have been used to treat diffraction by crystals are as follows (West, 1987).

1. The Laue equations

Diffraction from a hypothetical 1-dimensional crystal, constituting a row of atoms, may be treated in the same way as diffraction of light by an optical grationg because, in projection, the grating is a row of points. An equation is obtained which relates the separation, a, of the atoms in the row, the X-ray wavelength, λ, and the diffraction angle, ϕ; i.e.

$$a \sin \phi = n\lambda \qquad (17)$$

A real crystal is a three-dimentional arrangement of atoms for which three Laue equations may be written:

$$a_1 \sin \phi_1 = n\lambda$$

$$a_2 \sin \phi_2 = n\lambda$$

$$a_3 \sin \phi_3 = n\lambda$$

Each equation corresponds to the diffraction condition for rows of atoms in one particular direction and three directions or axes are needed in order to represent the atomic arrangement in the crystal. For a diffracted beam to occur, these three equations must be satisfied simultaneously. The Laue equations provide a rigorous and mathematically correct way to describe diffraction by crystals. The drawback is that they are cumbersome to use.

2. Bragg's Law

The Bragg approach to diffraction is to regard crystals as built up in layers or planes such that each acts as a semi-transparent mirror. Some of the X-rays are reflected off a plane with the angle of reflection equal to the angle of incidence, but the rest are transmitted to be subsequently reflected by succeeding planes.

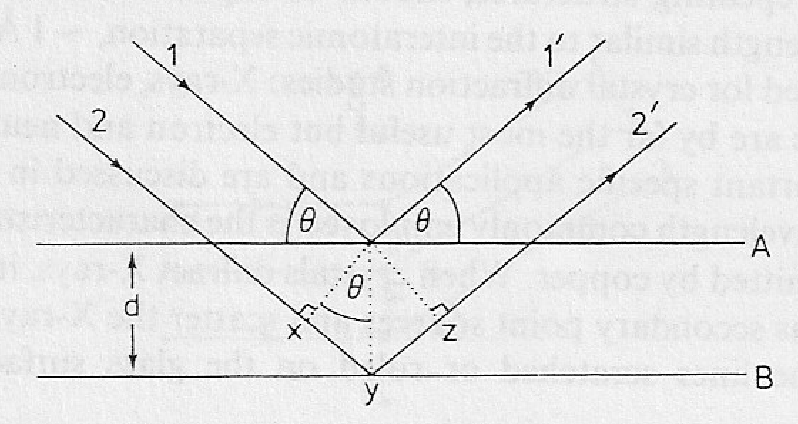

Figure 9. Derivation of Bragg's Law for X-ray diffraction.

The derivation of Bragg's Law is shown in Figure 9. Two X-ray beams, 1 and 2, are reflected from adjacent planes, A and B, within the crystal and would like to know what coditions the reflected beams $1'$ and $2'$ are in phase. Beam $22'$ has to travel the extra distance *xyz* as compared to beam $11'$, and for $1'$ and $2'$ to be in phase, distance *xyz* must equal a whole number of wavelengths. The perpendicular distance between pairs of adjacent planes, the *d-spacing*, *d*, and the angle of incidence, or *Bragg angle*, θ, are related to the distance *xy* by

$$xy = yz = d \sin \theta$$

Thus

$$xyz = 2d \sin \theta$$

But

$$xyz = \mathrm{n}\lambda$$

Therefore

$$2d \sin \theta = \mathrm{n}\lambda \qquad \textit{(Bragg's relation)} \qquad (18)$$

$$(\mathrm{n} = 1, 2, 3, \ldots)$$

The XRD pattern of a powdered sample is measured with a stationary X-ray source and a movable detector, which scans the intensity of the diffracted radiation as a function of the angle 2θ between the incoming and the diffracted beams. When working with powdered samples, and image of diffraction lines occurs because a small fraction of the powder particles will be oriented such that by chance a certain crystal plane is at the right angle θ with the incident beam for constructive interference, as shown in Figure 10.

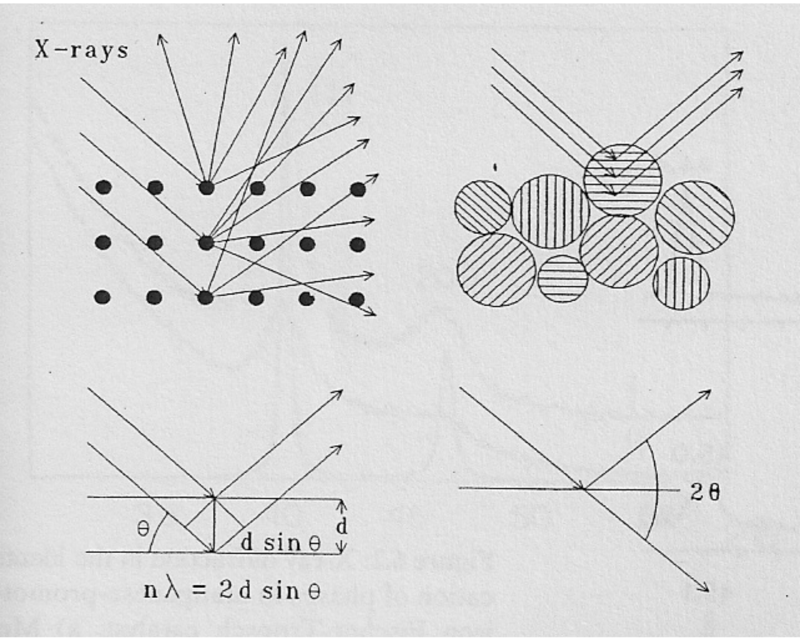

Figure 10. X-ray scattered by atoms in an ordered lattice interfere constructively in directions given by Bragg's Law (Niemantsverdriet, 1993).

The angles of maximum intensity enable one to calculate the spacings between the lattice planes and allow for phase identification. Diffractograms are measured as a function of the angle 2θ. When the sample is a polycrystalline powder, the diffraction pattern is formed by a small fraction of the particle only. Rotation of the sample during measurement enhances the number of particles that contribute to diffraction.

X-ray diffraction has an important limitation: clear diffraction peaks are only observed when the sample possesses suficient long range order. The advancetage of this limitation is that the width of diffraction peaks carries information on the dimensions of the reflecting planes. Diffraction lines from perfect crystals are very narrow. For crystallite size below 100 nm, the linebroadening occurs due to incomplete destructive interference in scattering directions where the X-rays are out of phase.

The Scherrer's equation relates crystal size to line width;

$$L = \frac{K\lambda}{\beta \cos\theta} \tag{14}$$

In addition, amorphous phases and small particles give either broad and weak diffraction lines or no diffraction at all, with the consequence that if catalysts contain particles with a size distribution, XRD may only detect the larger ones.

2.2.2 Surface area and porosity (BET method)

Adsorption is of great technological important. Thus, some adsorbents are used on a large scale as desiccants, catalysts or catalyst supports; others are used for the separation of gases, purification of liquids, pollution control or for respiratory protection. In addition, adsorption phenomena play a vital role in many solid state reactions and biological mechanisms. Another reason for the widespread use of adsorption techniques is the importance now attached to the characterization of the surface properties and texture of fine powders such as pigment, fillers and cements. In particular, gas adsorption has become one of the most widely used procedures for determining the surface area and pore size distribution of a diverse range of powders and porous materials. Adsorption occurs whenever a solid surface is exposed to gas or liquid. There are two types invole in adsorption process including physisorption adsorption in which the van der Waals interactions are involved and chemisorption adsorption in which the adsorbed molecules are attached by chemical bonding (Rouquerol, *et al.*, 1999).

The surface area is an average measurement of the external surface of a large number of particles and expressed in term of the area per unit mass (m^2/g). There are two main analysis techniques for measuring surface area; gas adsorption and gas permeability. In this work gas adsorption surface area analysis was used.

The gas adsorption approach starts with a clean surface achieved through vacuum or inert gas break-out. The clean powder surface is exposed to varying partial pressure of known adsorbing vapors. A measurement is mode of the amount of gas adsorbed on the powder surface versus the partial pressure. The measurement is often referred to as the BET specific surface area after Brunauer, Emmett and Teller who developed the concept in 1938.

Under equilibrium, the rate of adsorption equals the rate of evaporation. Letting P equal the partial pressure of adsorbate, P_0 equal the saturation pressure of adsorbate (which depends on the gas and temperature), X equal the amount of gas adsorbed at a pressure P, X_m equal the monolayer capacity of the powder (the amount of gas nescessary to form a uniform surface coating one atomic layer thick), and C equal a constant relating to the adsorption enthalpy, gives

$$\frac{P}{X(P_0 - P)} = \frac{1}{X_m C} + \frac{C-1}{X_m C}\frac{P}{P_0} \qquad (19)$$

The linear relation between the term on the left of the equal sign and the partial pressure ratio P/P_0 is noted. This is the BET equation, and is generally valid for powders in the range P/P_0 from 0.05 to 0.30. Equation (19) can be rewritten in a general form as,

$$\frac{P}{X(P_0 - P)} = B + \frac{AP}{P_0} \qquad (20)$$

Where

$$X_m = \frac{1}{A+B} \qquad (21)$$

Giving A as the slope and B as the intercept of the linear equation. Finally, the surface area is calculated as

$$S = \frac{X_m N_0 A_0}{wM} \tag{22}$$

using M as the molecular weight of adsorbate, A_o as the average occupational area of an adsorbate molecule, N_o as Avogadro's number, and w as the sample weight.

The porous nature of synthesized titanium dioxide was studied by nitrogen adsorption isotherm. In order to ultilize the information within the adsorption isotherms, it is necessary to consider the shape of physisorption isotherm and the identification of the principle mechanism of adsorption. The majority of physisorption isotherms could be grouped into six types, as shown in Figure 11. The IUPAC classifications of the pore are shown in Table 4.

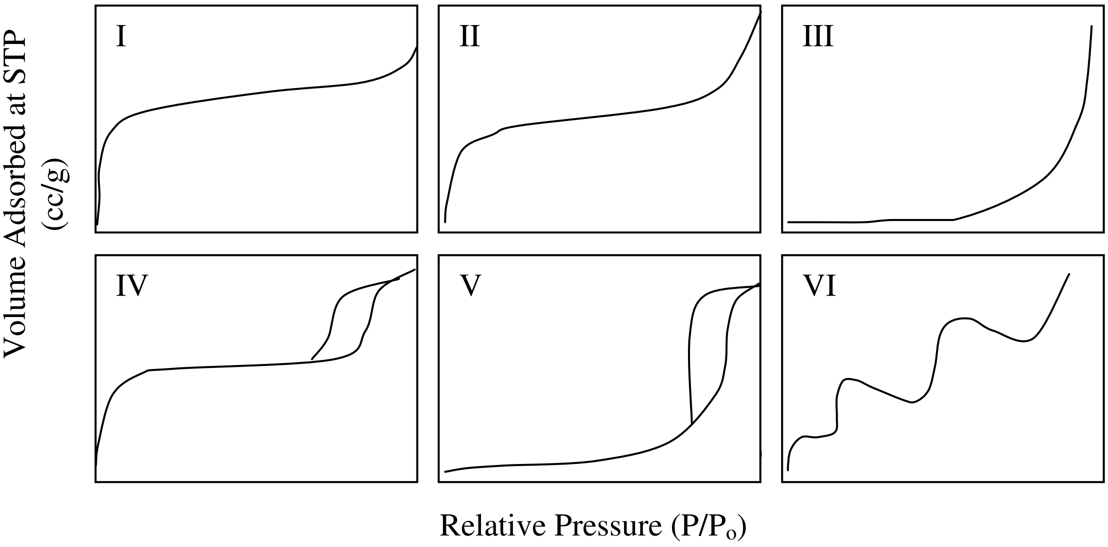

Figure 11. IUPAC classification of adsorption isotherms (Ryu, *et al.*, 1999).

Table 4. IUPAC classification of the pore (Khalil, *et al.*, 2001).

Porosity type	Size (d)
Ultramicropores	< typical molecule diameter of the adsorptive about 0.6 nm
Micropores	d < 2 nm
Mesopores	2 nm < d < 50 nm
Macropores	d > 50 nm

The Type I isotherm is given by microporous solids. The very steep region at low P/P_o is due to the filling of very narrow pores and limiting uptake is dependent on the accessible micropore volume rather than on the internal surface area. The Type II isotherm is normally given by a non-porous solids which unrestricted monolayer-multilayer adsorption can occur. The Type III isotherm is generally associated with weak adsorbent-adsorbate and relatively strong adsorbate-adsorbate interactions. In this case cooperative effects lead to the development of patches of multilayer before a uniform monolayer has been formed. Type IV isotherm with hysteresis loop is the characteristic features of the adsorbate-absorbate interactions which is associated with capillary condensation. Some microporous or mesoporous solids are amongst the few adsorbents to give Type V isotherm. The Type VI isotherm is relatively rare, it presents stepwise multilayer adsorption on a uniform non-porous surface. (Ryu, *et al.*, 1999).

2.2.3 Electron Microscopy

Electron microscopy is a rather straightforward technique to determine the size and shape of supported particles. It can also reveal information on the composition and internal structure of the particles, for example by detecting the characteristic X-rays which are produced by the interaction of the electrons with matter, or by analyzing how the electrons are diffracted.

The electron microscopy techniques used in this work are as follows.

2.2.3.1 Scanning electron microscopy (SEM)

SEM is a type of electron microscope that images the sample surface by scanning it with a high-energy beam of electrons in a raster scan pattern. The electrons interact with the atoms that make up the sample producing signals that contain information about the sample's surface topography, composition and other properties such as electrical conductivity.

The types of signals produced by an SEM include secondary electrons, back scattered electrons (BSE), characteristic x-rays, light (cathodoluminescence), specimen current and transmitted electrons. These types of signal all require specialized detectors for their detection that are not usually all present on a single machine. The signals result from interactions of the electron beam with atoms at or near the surface of the sample. In the most common or standard detection mode, secondary electron imaging or SEI, the SEM can produce very high-resolution images of a sample surface, revealing details about 1 to 5 nm in size. Due to the way these images are created, SEM micrographs have a very large depth of field yielding a characteristic three-dimensional appearance useful for understanding the surface structure of a sample. A wide range of magnifications is possible, from about x 25 (about equivalent to that of a powerful hand-lens) to about x 250,000, about 250 times the magnification limit of the best light microscopes (http://en.wikipedia.org/ wiki/ Scanning_electron_microscope).

Sample preparation in SEM

All samples must also be of an appropriate size to fit in the specimen chamber and are generally mounted rigidly on a specimen holder called a specimen stub. Several models of SEM can examine any part of a 6-inch (15 cm) semiconductor wafer, and some can tilt an object of that size to 45 degrees.

For conventional imaging in the SEM, specimens must be electrically conductive, at least at the surface, and electrically grounded to prevent the accumulation of electrostatic charge at the surface. Metal objects require little special preparation for SEM except for cleaning and mounting on a specimen stub. Nonconductive specimens tend to charge when scanned by the electron beam, and especially in secondary electron imaging mode, this causes scanning faults and other image artifacts. They are therefore usually coated with an ultrathin coating of electrically-conducting material, commonly gold, deposited on the sample either by low vacuum sputter coating or by high vacuum evaporation. Conductive materials in current use for specimen coating include gold, gold/palladium alloy, platinum, osmium, iridium, tungsten, chromium and graphite. Coating prevents the accumulation of static electric charge on the specimen during electron irradiation.

2.2.3.2 Transmission electron microscopy (TEM)

TEM is a microscopy technique whereby a beam of electrons is transmitted through an ultra thin specimen, interacting with the specimen as they pass through. An image is formed from the interaction of the electrons transmitted through the specimen, which is magnified and focused onto an imaging device, such as a fluorescent screen, as is common in most TEMs, on a layer of photographic film, or to be detected by a sensor such as a CCD camera.

TEMs are capable of imaging at a significantly higher resolution than light microscopes, owing to the small de Broglie wavelength of electrons. This enables the instrument to be able to examine fine detail even as small as a single column of atoms, which is tens of thousands times smaller than the smallest resolvable object in a light microscope (http://en.wikipedia.org/wiki/Transmission_electron_microscope).

The TEM is used heavily in material science, metallurgy and the biological sciences. In each case the specimens must be very thin and able to withstand the high vacuum present inside the instrument.

Sample preparation in TEM

TEM specimens are typically hundreds of nanometres thick, as the electron beam interacts readily with the sample, an effect that increases roughly with atomic number. High quality samples will have a thickness that is comparable to the mean free path of the electrons that travel through the samples, which may be only a few tens of nanometres. Preparation of TEM specimens is specific to the material under analysis and the desired information to obtain from the specimen.

In material science and metallurgy the specimens tend to be naturally resistant to vacuum, but still must be prepared as a thin foil, or etched so some portion of the specimen is thin enough for the beam to penetrate. Constraints on the thickness of the material may be limited by the scattering cross-section of the atoms from which the material is comprised. Materials that have dimensions small enough to be electron transparent, such as powders or nanotubes, can be quickly produced by the deposition of a dilute sample containing the specimen onto support grids or films.

TEM versus SEM

Globally, distinction is made between transmission electron microscopy (TEM) to study the inner structure of objects and scanning electron microscopy (SEM) to visualize the surface of tissues, macromolecular aggregates and materials. Instead of light, in TEM as well as in SEM electron bombardment of the sample is applied to produce an image. Like in the light microscope one in EM of a source (here an electron gun) and lenses (here electro-magnetic lenses that deflect electrons), namely a condenser that concentrates the beam, an objective to focus it and components to produce the scan movement in SEM only. The principle of both EM techniques is explained in brief in Figure 12 and Table 5 below.

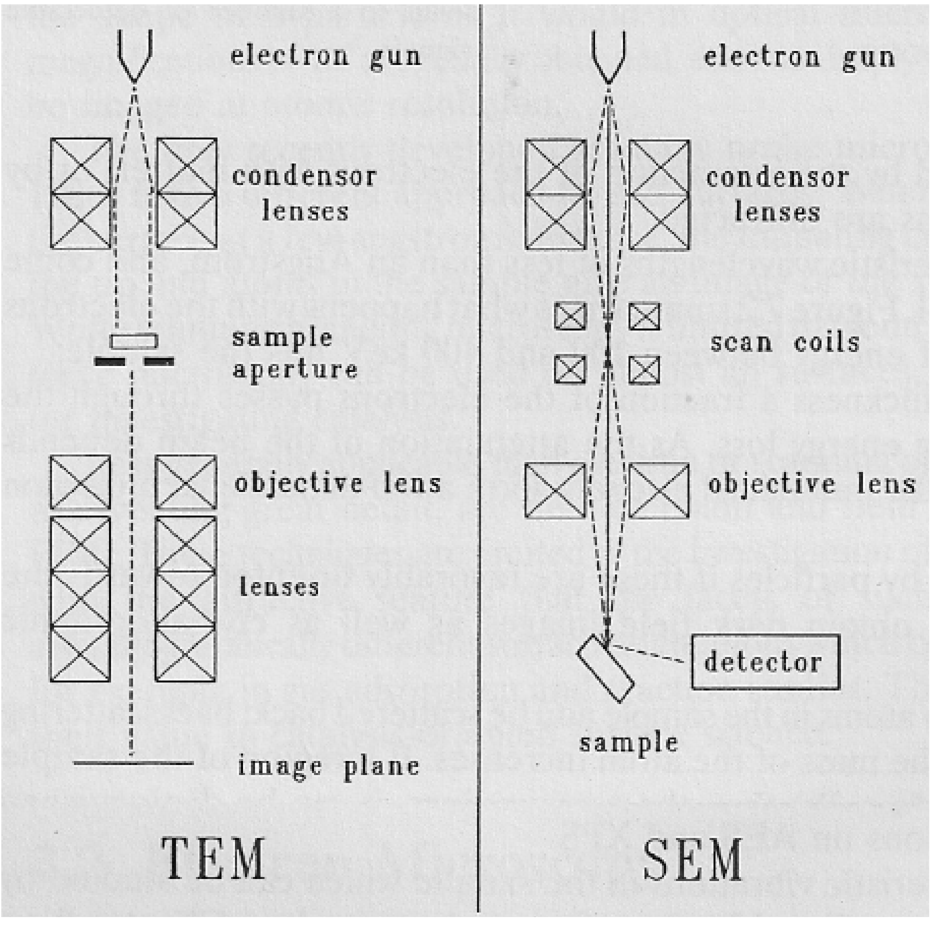

Figure 12. Schematic set up of an electron microscope in the transmission (TEM) and the scanning (SEM) mode (Niemantsverdriet, 1993).

Table 5. The principle of both TEM and SEM techniques
(www.vcbio.science.ru.nl/.../electron/)

<table>
<tr><th>TEM</th><th>SEM</th></tr>
<tr><td>
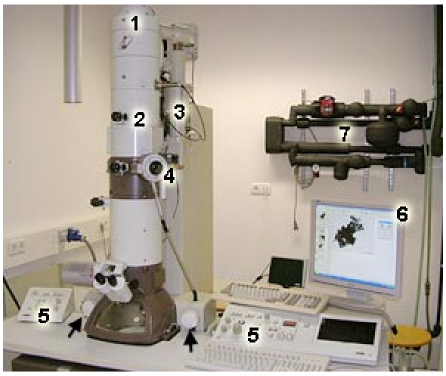

1. Electron cannon in the upper part of the column.
2. Electro-magnetic lenses to direct and focus the electron beam inside the column.
3. Vacuum pumps system.
4. Opening to insert a grid with samples into the high-vacuum chamber for observation.
5. Operation panels (left for alignment; right for magnification and focussing; arrows for positioning the object inside the chamber).
6. Screen for menu and image display.
7. Water supply to cool the instrument.
</td><td>


1. Electron cannon in the upper part of the column (here a so-called field-emission source).
2. Electro-magnetic lenses to direct and focus the electron beam inside the column.
3. Vacuum pumps system.
4. Opening to insert the object into the high-vacuum observation chamber in conventional SEM mode.
5. Operation panel with focus, alignment and magnification tools and a joystick for positioning of the sample.
6. Screen for menu and image display.
7. Cryo-unit to prepare (break, coat and sublimate) frozen material before insertion in the observation chamber in Cryo-SEM mode.
</td></tr>
<tr><td>
TEM makes high-resolution (± 1 nm) views of the inner side of objects.

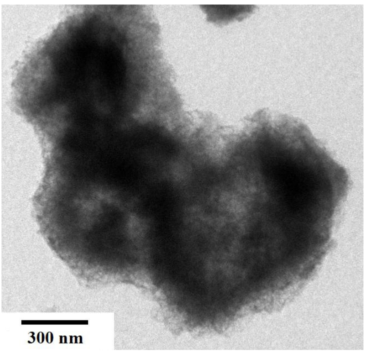

</td><td>
In SEM an image of the surface of the object is made.

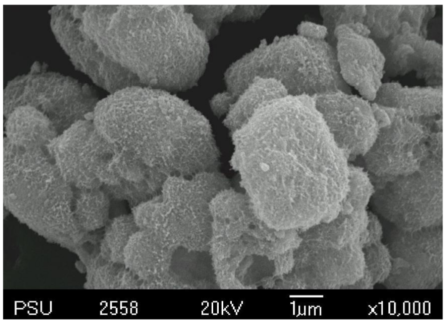

</td></tr>
</table>

2.2.5 Difused reflectance UV-Vis spectroscopy (DRS)

UV-Vis spectroscopy has been used to characterize the bulk structure of crystalline titanium dioxide. Titanium dioxide is a semiconducting oxide with easily measured optical band gap. UV-Vis diffused reflectance spectroscopy is used to probe the band structure or molecular energy levels in the materials since UV-Vis light excitation creates photo-generated electron and holes (Reddy, *et al.*, 2001).

In order to establish the type of band-to-band transition in these synthesized TiO_2 particles, the absorption data were fitted to equation for both indirect and direct band gap transitions (Kumar, *et al.*, 2000).

Direct semiconductors are characterized by the minimum of the lowest conduction band positioned in k space directly under the maximum of the highest valence band. The optical absorption coefficient (α) near the absorption edge for direct interband transitions is given by equation (23);

$$\alpha = B_d (h\nu - E_g)^{1/2} / h\nu \qquad (23)$$

where B_d is the absorption constant for a direct transition.

For indirect semiconductors, the minimum of the lowest conduction band is shifted relative to the maximum of the highest valence band and the lowest-energy interband transition must then be accompanied by phonon excitation. Indirect interband transitions are characterized by the stronger energy dependence of the optical absorption coefficient (α) nearer the absorption edge than is otherwise the case for direct transitions. The equation of indirect transition given by the following equation ;

$$\alpha = B_i (h\nu - E_g)^2 / h\nu \qquad (24)$$

where B_i is the absorption constant for an indirect transition, $h\nu$ is the energy of excitation, E_g is the band gap energy (Serpone, *et al.*, 1995).

The absorption coefficient (α) for reflectivity measurements could be calculated by the following equation (Zhao, *et al.*, 1991);

$$\alpha = A / d_s' \qquad (25)$$

where A is the measured absorbance and d_s' is the thickness of sample in UV-Vis cell (0.4 cm).

2.2.6 Fourier-transformed infrared spectroscopy (FTIR)

Infrared spectroscopy (IR) is a flexible and powerful technique that may be used to characterize materials. It provides direct information about the potential energy surface in the region of the equilibrium position, and thus allows the structural and bonding characteristic of molecules to be probed. IR is the most common form of vibrational spectroscopy. Infrared radiation falls into three categories, as indicated in Table 6. The interested energy of most of these molecular vibrational modes corresponds to that of the IR spectrum between around 400 cm^{-1} and 4000 cm^{-1}.

Table 6. Classifacation of Infrared radiation (Niemantsverdriet, 1993).

Region	Wavenumber (cm^{-1})	Detection of
Infrared	10 -10000	
Far	10-200	Lattice vibrations
Mid	200-4000	Molecular vibrations
Near	4000-10000	Overtones

Infrared spectroscopy exploits the fact that molecules have specific frequencies at which they rotate or vibrate corresponding to discrete energy levels (vibrational modes). These resonant frequencies are determined by the shape of the molecular potential energy surfaces, the masses of the atoms and, by the associated vibronic coupling. In order for a vibrational mode in a molecule to be IR active, it must be associated with changes in the permanent dipole. In particular, in the Born-Oppenheimer and harmonic approximations, i.e. when the molecular Hamiltonian corresponding to the electronic ground state can be approximated by a harmonic oscillator in the neighborhood of the equilibrium molecular geometry, the resonant frequencies are determined by the normal modes corresponding to the molecular electronic ground state potential energy surface. Nevertheless, the resonant frequencies can be in a first approach related to the strength of the bond, and the mass of the atoms at either end of it. Thus, the frequency of the vibrations can be associated with a particular bond type.

There are four types of vibration (Niemantsverdriet, 1993), as illustrated in Figure 7, each with a characteristic symbol:

- stretch vibrations (symbol ν), changing the length of a bond.
- bending vibrations in one plane (symbol δ), changing bond angles but leaving bond lengths unaltered (in larger molecules further divided into rock, twist and wag vibrations).
- bending vibrations out of plane (symbol γ), in which one atom oscillates through a plane defined by at least three neighbouring atoms.
- Torsion vibrations (symbol τ) changing the angle between two planes through atoms.

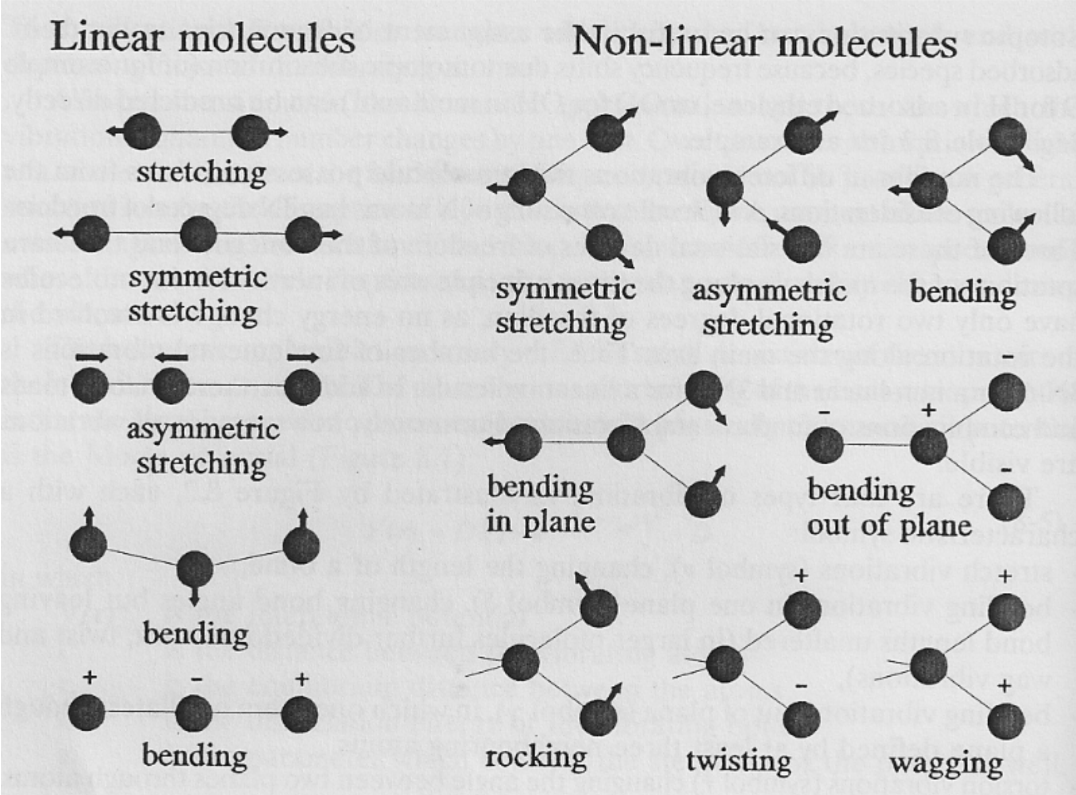

Figure 13. Fundamental vibration of several molecules(Niemantsverdriet, 1993).

Generally, the frequencies of these vibrations decrease in the order $\nu > \delta > \gamma > \tau$. In addition, vibrations are divided into symmetric and asymmetric vibrations (ν_s and ν_{as}).

CHAPTER 3
RESULTS AND DISCUSSION

3.1 Syntheses of potassium oxalate-doped TiO_2 powders and studies on the effect of calcinations on the morphology and their photocatalytic activities

In the present study, TiO_2 powders were prepared by the sol-gel method, using $TiCl_4$ as starting material for its low cost but high content of titanium compared with titanium alkoxide. Hexamethylenetetramine (HMT) was used as the mild basic reagent to control the rate of hydrolysis and condensation reactions. Potassium oxalate (KOX) was used as the doping agent to enhance surface area by forming an open framework structure. Furthermore, the oxalate group when bonded to metal ion will exert a ligand field strength similar to the oxide ion (O^{2-}) in TiO_2, therefore, the intrinsic energy levels within the material bulk is almost unchanged. The use of potassium oxalate creates another advantage over using oxalic acid as acid causes the solution to become too acid. Potassium oxalate can be added in varying amounts: 0.5, 1.0, and 4.0 % by mass. The oxalate anion is a good bidentate ligand that usually interlinks the metal ions into a two or three dimensional networks (Andres, *et al.*, 1999; Vaidhyanathan, *et al.*, 1999; Boudaren, *et al.*, 2003; Lethbridge, *et al.*, 2003; Decurtins, *et al.*, 1996; Coronado, *et al.*, 2000; Evans, *et al.*, 2001; Chaiyapoom, *et al.*, 2006). This property of the oxalate anion may help form aggregates of TiO_2 with a framework of high specific surface area which is one important parameter in the photocatalytic study. Hexamethylenetetramine was used as a homogeneous hydrolyzing agent. The advantage of this reagent lies in its slow hydrolysis that introduces OH^- uniformly and homogeneously into the system, thereby, causing the metal hydroxide to precipitate slowly. The slow precipitation means that morphology, size, and crystallinity of the product can be controlled (Li, *et al.*, 2005; Liu, *et al.*, 2005).

3.1.1 Characterization of the synthesized KOX-doped TiO_2 powders

In general, the sol-gel process consists of the hydrolysis and condensation reactions: the former leads to the formation of original nuclei of titanium dioxide while the latter leads to the growth of network system of original nuclei. When $TiCl_4$ was dissolved in water, the exothermic reaction took place with the formation of orthotitanic acid [$Ti(OH)_4$], eq.(26). When potassium oxalate was added "titanium oxalate complex" was formed in the same hydrolysis solution, eq.(27).

The hydrolysis reaction: $TiCl_4 + 4 H_2O \rightarrow Ti(OH)_4 + 4 H^+ + 4 Cl^-$ (26)

$$y\, Ti(OH)_4 + y\, K_2C_2O_4 \rightarrow y\, K_2[Ti(OH)_4(C_2O_4)] \quad (27)$$

The coefficient y is used in eq.(27) to mean that only small amount of $K_2C_2O_4$ was used (y << 1). The hypothetical "titanium oxalate complex" is loosely represented by $K_2[Ti(OH)_4(C_2O_4)]$. Upon addition of HMT and at 90 °C, NH_3 and formaldehyde were produced, eq.(28) (Zhang, *et al.*, 2007). The presence of NH_3 rendered the solution basic, eq.(29), and catalyzed the condensation reaction to yield the products, eqs.(30)-(31).

$$(CH_2)_6N_4 + H_2O \rightarrow 4 NH_3 + 6 HCHO \quad (28)$$

$$NH_3 + H_2O \rightarrow NH_4^+ + OH^- \quad (29)$$

The condensation reaction:

$$(1\text{-}y)\, Ti(OH)_4 \xrightarrow{OH^-} (1\text{-}y)\, TiO_2 + 2(1\text{-}y)\, H_2O \quad (30)$$

$$y\, K_2[Ti(OH)_4(C_2O_4)] \xrightarrow{OH^-} y\, TiO(C_2O_4) + y\, K_2O + 2y\, H_2O \quad (31)$$

The precipitated product obtained should be the mixture of TiO_2 + y $TiO(C_2O_4)$ + y K_2O. The occurrence of $TiO(C_2O_4)$ was supported by the studies of titanium-oxalate systems (Potdar, *et al.*, 2001; Patil, *et al.*, 2001).

The X-ray diffraction patterns of the as-prepared samples are shown in Figure 14. The patterns of most products consist of mixed phases of potassium acetate hydrate ($C_2H_3KO_2.xH_2O$; JCPDS No. 00-061-0512), potassium titanium oxide ($K_2Ti_4O_9$ $2.2H_2O$; JCPDS No. 00-039-0043), and titanium oxide (Ti_3O_5; JCPDS No. 01-072-0519). Only the 0.5KOX-TiO_2 sample showed the amorphous phase. As expected, with increasing potassium oxalate loading, sharper peaks were observed due to the increased crystalline quality of the mixed titanate products.

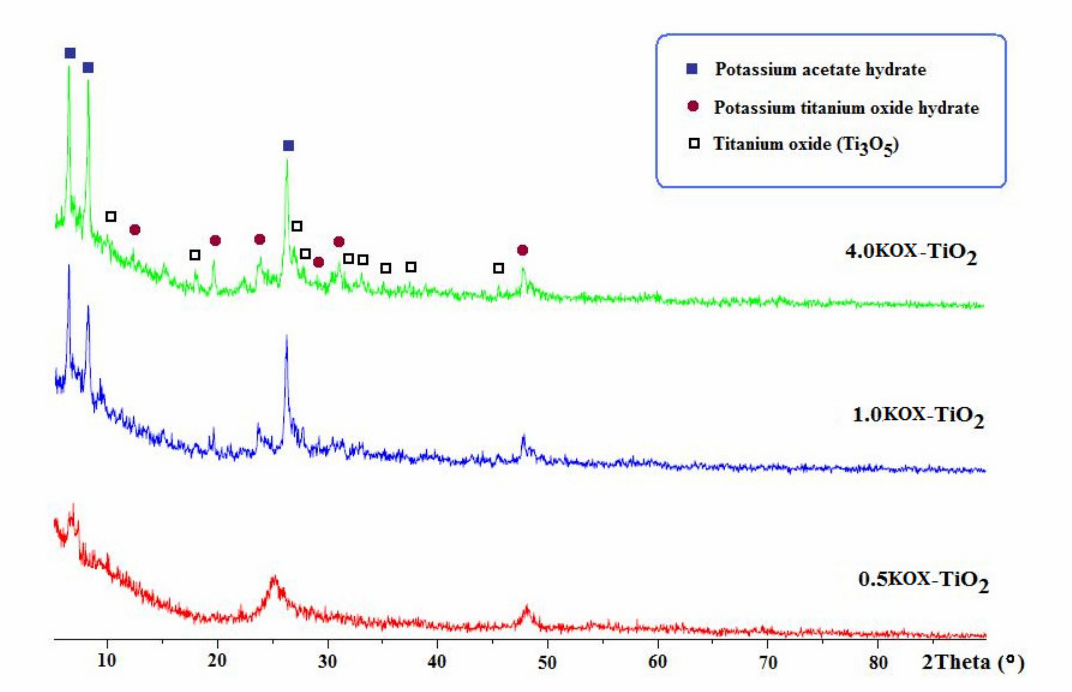

Figure 14. XRD patterns of the as-prepared KOX-TiO_2 samples

The N_2 adsorption isotherms and pore size distributions of the prepared titanate samples are shown in Figures 15 and 16, respectively.

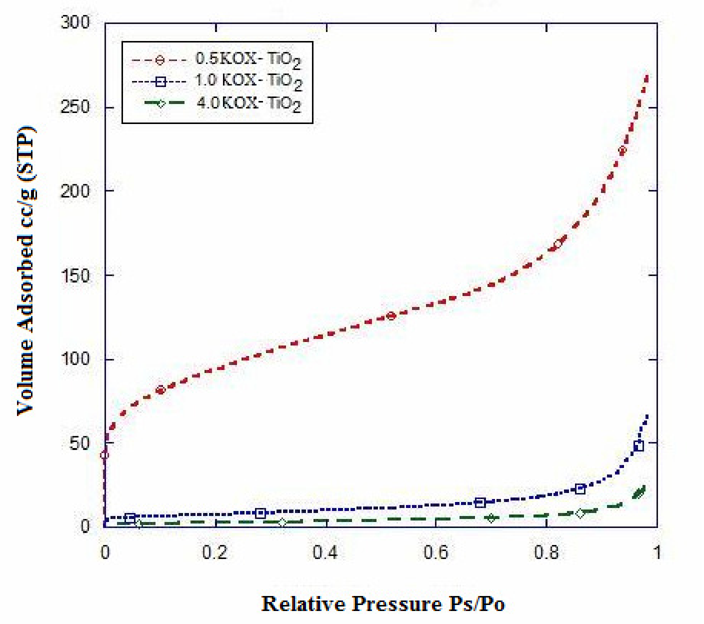

Figure 15. N_2 adsorption isotherms for the as-prepared KOX-doped TiO_2 samples

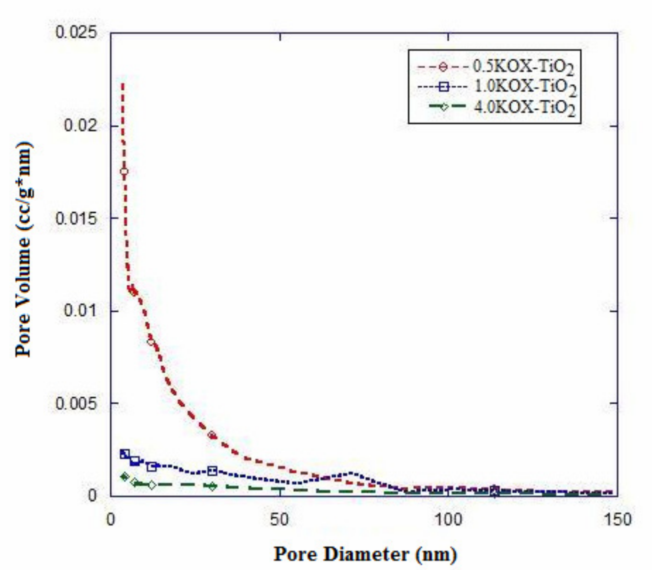

Figure 16. Pore size distributions for the as-prepared KOX-doped TiO_2 samples.

The specific surface area, pore volume, and pore diameter are summarized in Table 7. It is readily seen that BET surface area and pore volume decreased when increasing amount of added potassium oxalate. It can be concluded from these results that increasing crystallinity of sample leads to decreasing specific surface area.

Table 7. Typical physicochemical properties of the as-prepared KOX-doped TiO_2 samples

Sample	Crystallite phase	Surface area (m^2/g)	Total pore volume (cm^3/g)
0.5KOX-TiO_2	Amorphous	336.7	0.2928
1.0KOX-TiO_2	Mixed phases*	26.6	0.1063
4.0KOX-TiO_2	Mixed phases*	8.8	0.0428

* Data from XRD: mixed phases were potassium acetate hydrate ($C_2H_3KO_2.xH_2O$), potassium titanium oxide ($K_2Ti_4O_9$ 2.2H_2O), and titanium oxide (Ti_3O_5).

From the nitrogen adsorption-desorption isotherms, the 0.5KOX-TiO_2 sample showed the isotherm types I and IV (BDDT classification) indicating the presence of micropore and mesopore structure. The other two samples showed type IV isotherm and almost had no hyteresis loop* indicating that all the pores had collapsed and the total pore volume was very small. It could be seen from Figure 16 that the pore size distribution curves of the three samples were different. The 0.5KOX-TiO_2 sample had wide pore size distribution from micropore to mesopore while the 1.0KOX-TiO_2 sample had a mesopore in the range 50-80 nm. The pore size distribution curve of 4.0KOX-TiO_2 sample, turned into a line indicating the disappearance of pores.

Figure 17 shows SEM images of TiO_2 samples prepared from the sol-gel route. Two magnifications, 1500× and 10,000×, were taken for each sample. From the SEM results we can see that morphologies of the samples were affected by the preparation conditions. The particle sizes of samples are in the micrometer range; 4 μm for 0.5KOX-TiO_2, 10-50 μm for 1.0KOX-TiO_2, and 7 μm for 4.0KOX-TiO_2 samples. The 0.5KOX-TiO_2 sample showed almost spherical shape with rough surface and some particles were hollow, and the 4.0KOX-TiO_2 sample showed coral-like structure with high crystallinity. In the case of 1.0KOX-TiO_2 sample, it showed dense features with highly agglomerated particles. The SEM results correspond with TEM results which are shown in Figure 18.

---

*The Coulter SA 3100 equipment could not measure the desorption process, therefore, the hyteresis loop could not be found.

a) 0.5KOX-TiO_2_× 1500 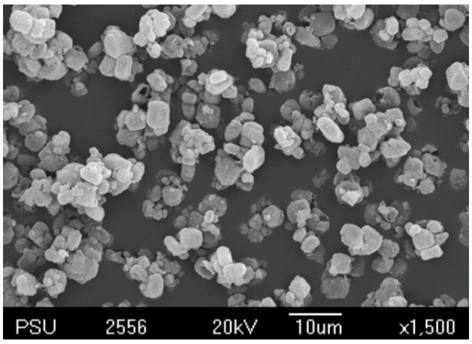 	0.5KOX-TiO_2_× 10000 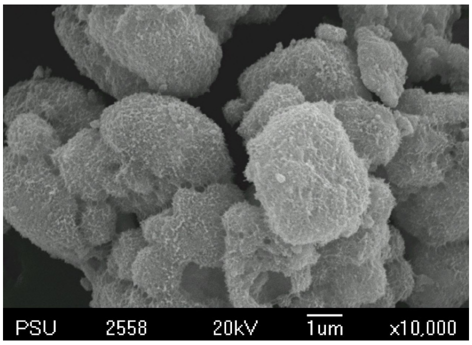
b) 1.0KOX-TiO_2_× 1500 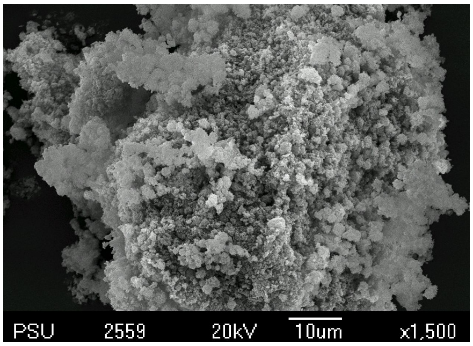 	1.0KOX-TiO_2_× 10000 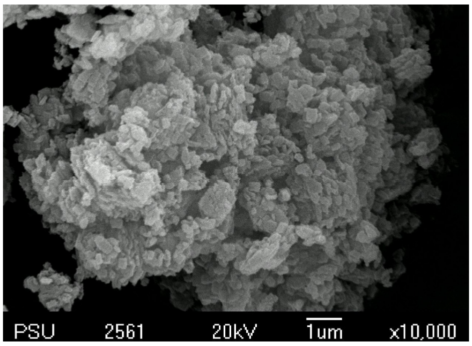
c) 4.0KOX-TiO_2_× 1500 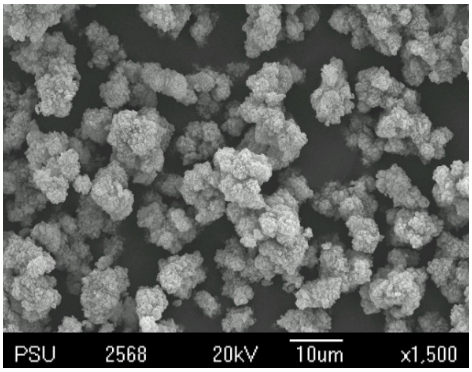 	4.0KOX-TiO_2_× 10000 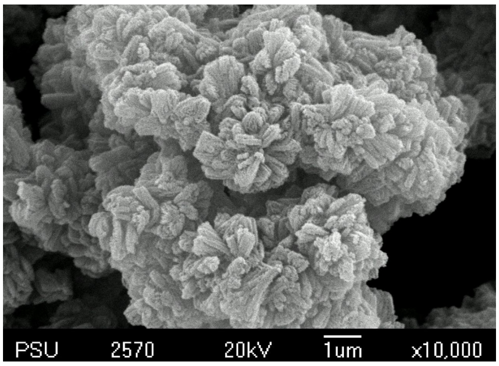

Figure 17. SEM photographs of the as-prepared TiO_2 samples; a) 0.5KOX-TiO_2, b) 1.0KOX-TiO_2, and c) 4.0KOX-TiO_2 sample. Each sample was photographed at low (1,500×) and high (10,000×) magnefication.

a) 0.5KOX-TiO_2

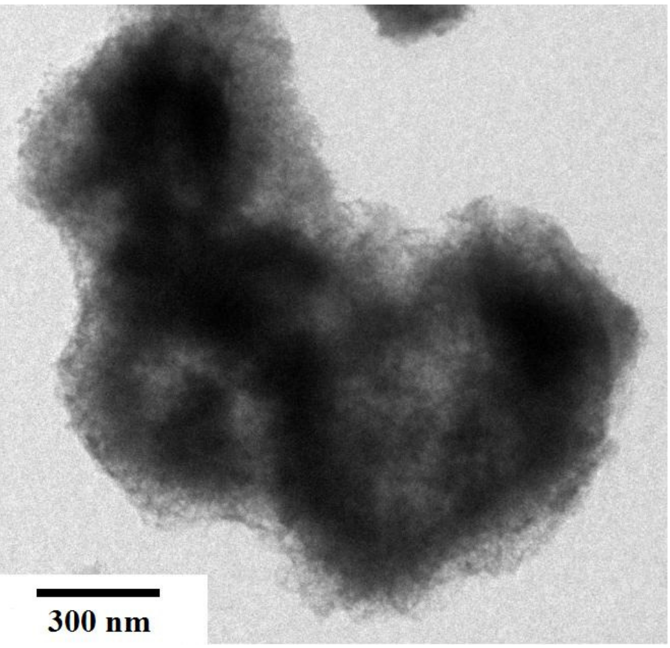

b) 4.0KOX-TiO_2

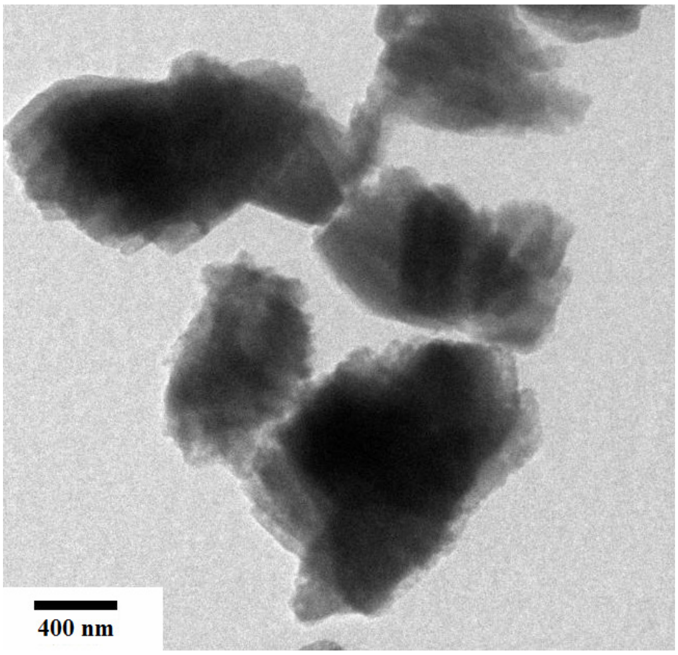

Figure 18. TEM photographs of the as-prepared TiO_2 samples; a) 0.5KOX-TiO_2, and b) 4.0KOX-TiO_2 sample.

Figure 19 shows the FT-IR spectra of the prepared TiO_2 samples in the range of 4000-400 cm^{-1}. From these spectra, we can see strong bands at 3313 cm^{-1}, 1752-1627 cm^{-1}, 1413 cm^{-1}, 1217 cm^{-1}, and in the range of 956 to 447 cm^{-1}. The band at 3313 cm^{-1} can be assigned to both ν_{OH} and ν_{NH} (stretching modes), indicating the presence of hydroxyl group of water in the samples. The C=O and C-O stretching modes appear as intense bands in the range 1752-1627 cm^{-1} and 1413-1217 cm^{-1}, respectively. These bands are characteristic of oxalate ligand from the added potassium oxalate during sol-gel process. The observed band in the same range of 956 cm^{-1} and 447 cm^{-1} is associated with the characteristic vibrational modes of TiO_2 ($\nu_{Ti\text{-}O}$, stretching mode of Ti-O bond) (Zhang, *et al.*, 2002). Consequently, results from FT-IR spectra confirmed the presence of oxalate ligand, Ti-O moiety, and impurities such as NH_4^+ and H_2O at the surface of the synthesized TiO_2.

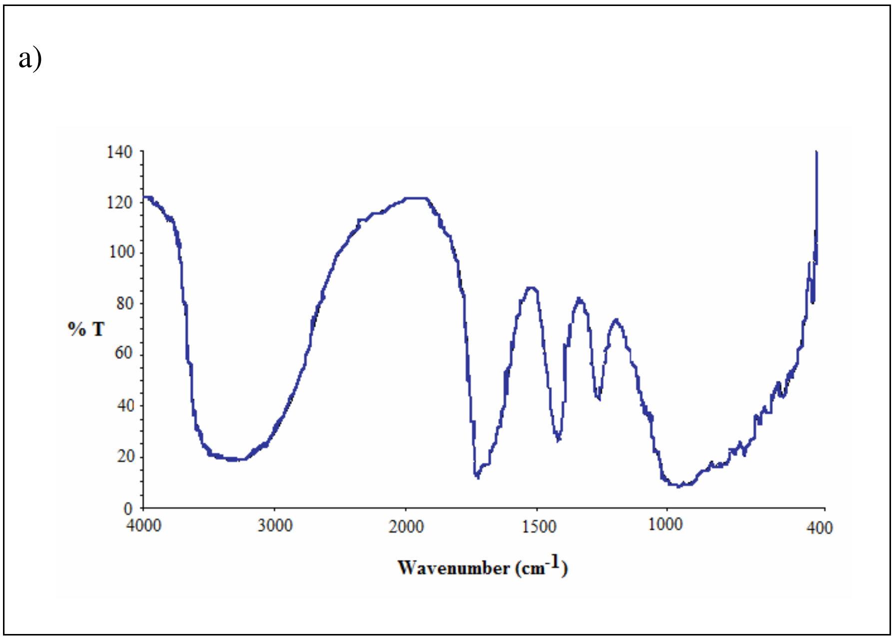

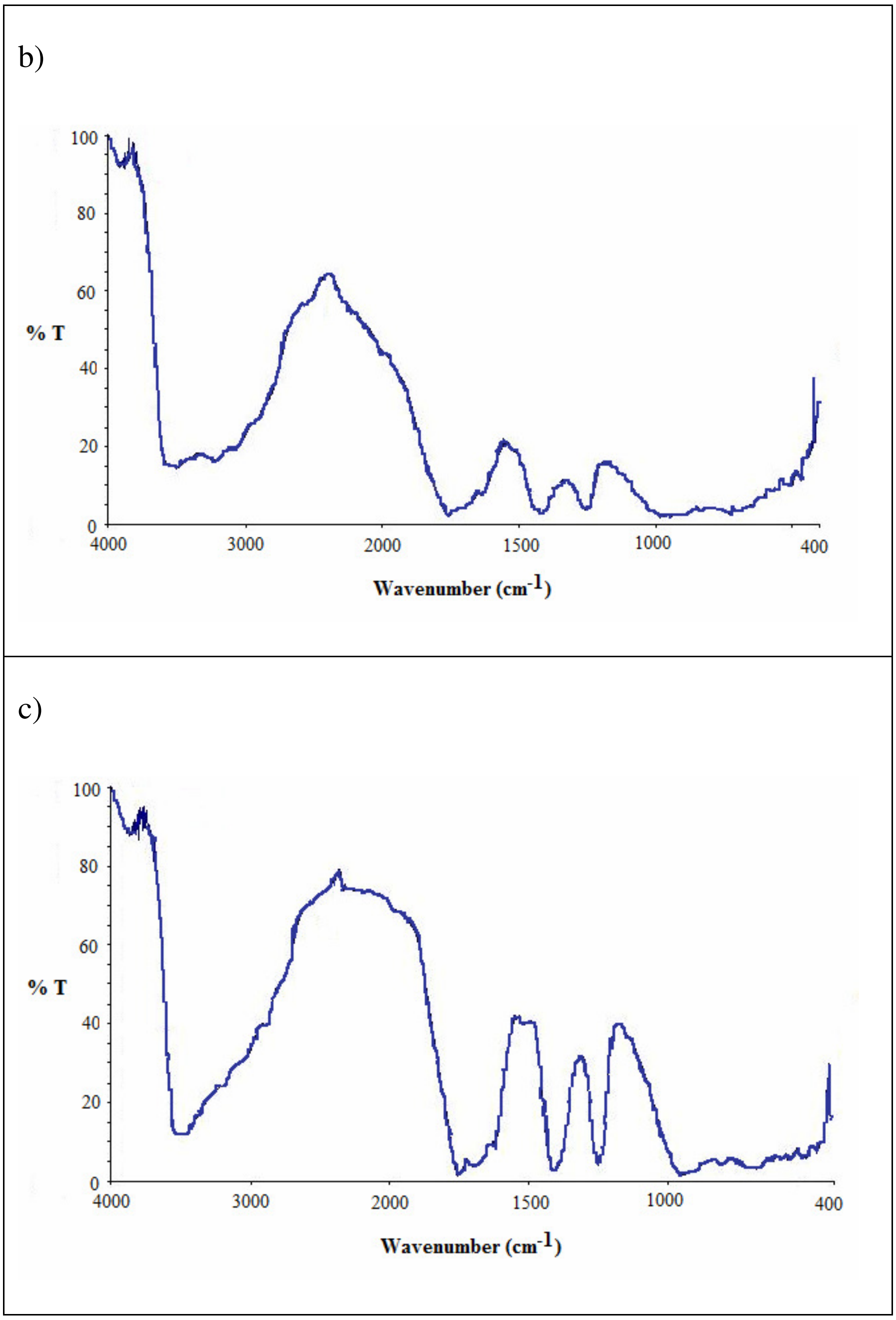

Figure 19. FT-IR spectra of the as-prepared TiO_2 samples; a) 0.5KOX-TiO_2, b) 1.0KOX-TiO_2, and c) 4.0KOX-TiO_2 samples.

In order to evaluate the content of each element (Ti, K) in the as-prepared titanate samples, all samples were analysed for their compositions by using XRF technique. The results are shown in Table 8 which show that the amount of K element increased with increasing the doping content. These results also are comfirm by the EDX spectra as shown in Figure 20.

Table 8. Data from XRF, DRS, and PL techniques of the as-prepared TiO_2 samples

Technique / Sample	XRF		DRS		PL	
	Amount of element (%)		λ_{onset} (nm)	E_g (eV)	Intensity (a.u.)	E_g (eV)
	Ti	K				
0.5KOX-TiO_2	14.08	2.44	385	3.22	391	3.17
1.0KOX-TiO_2	5.43	10.75	384	3.23	386	3.21
4.0KOX-TiO_2	7.67	19.55	385	3.22	390	3.18

UV-Vis diffuse reflectance spectrum was carried out in order to characterize the band gap energy including nature of electronic transition in materials. The absorption edge which determined by the linear extrapolation of the steep part of the UV adsorption toward the baseline and the band gap energy was calculated from equation (15) as mentioned above. Figure 20 shows the UV-Vis absorption spectra of the as-prepared TiO_2 samples. The absorption edges and calculated band gap energies of the synthesized samples are shown in Table 7. The threshold wavelength of TiO_2 samples are nearly of the same values. The absorption intensities at 300 nm of the two samples, 1.0KOX-TiO_2, 4.0KOX-TiO_2 are lower than 0.5KOX-TiO_2 due to the effect of crystal phase and surface area (Chen, *et al.*, 2007). Accordingly, absorption intensity at 300 nm decreased with increasing amount of potassium oxalate loading due to increase in crystallinity and decrease in specific surface area.

a) 0.5KOX-TiO_2

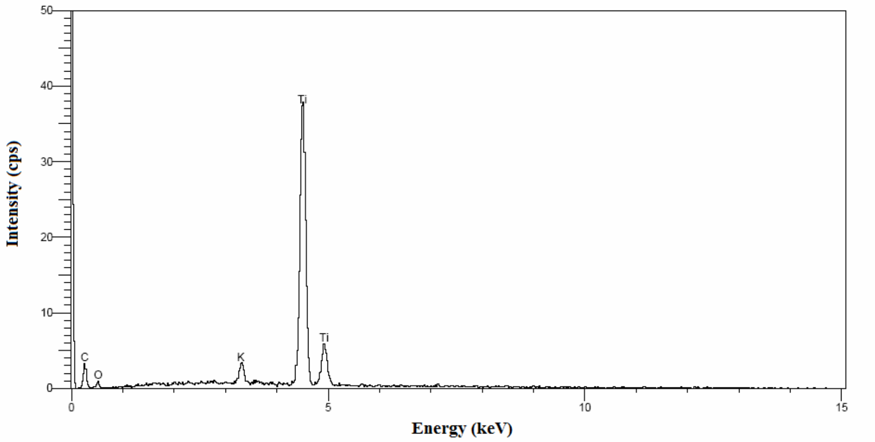

b) 1.0KOX-TiO_2

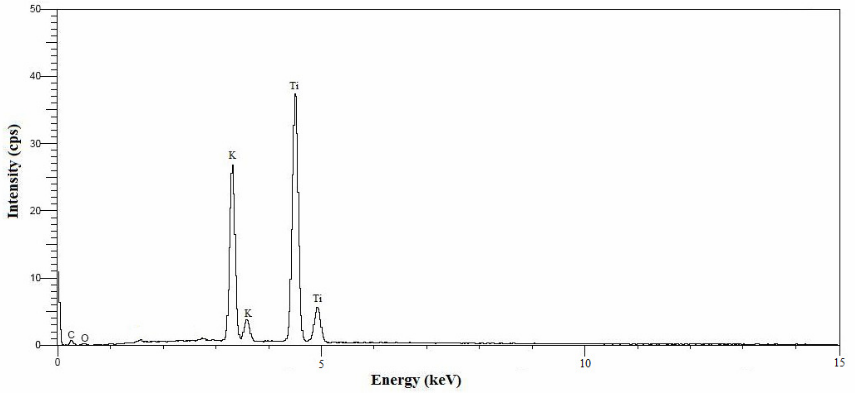

c) 4.0KOX-TiO_2

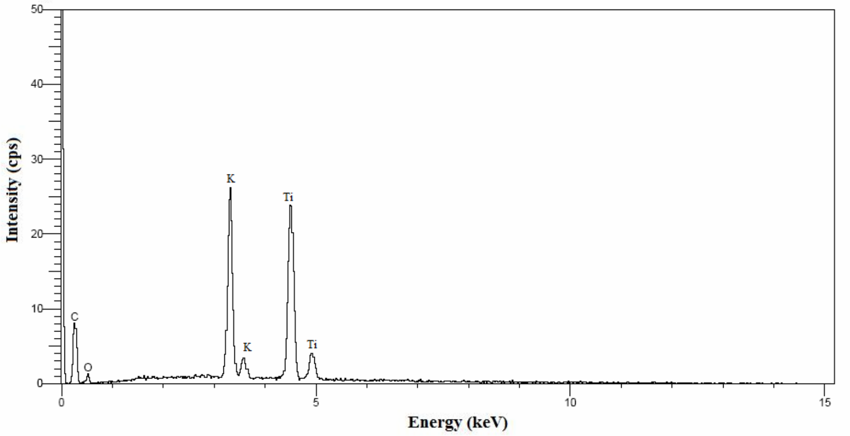

Figure 20. EDX spectra of the as-prepared TiO_2 samples; a) 0.5KOX-TiO_2, b) 1.0KOX-TiO_2, and c) 4.0KOX-TiO_2 samples.

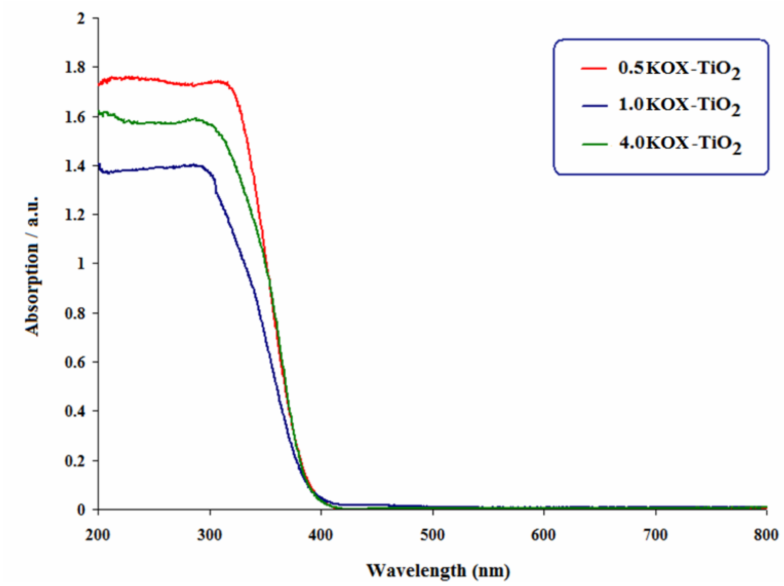

Figure 21. The diffused reflectance UV-vis spectra of the as-prepared TiO_2 samples.

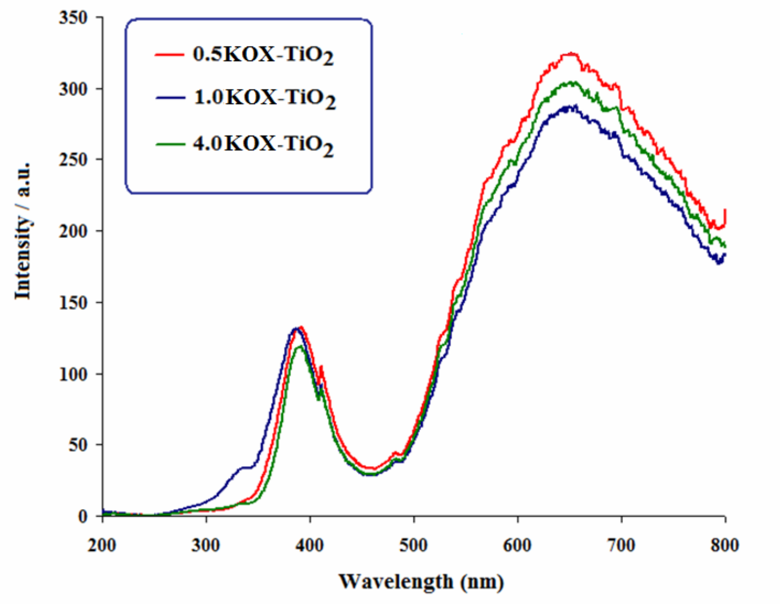

Figure 22. PL spectra of the as-prepared TiO_2 samples.

The photoluminescence spectra of the synthesized TiO_2 samples were recorded at room temperature. PL spectum can provide the information about the surface oxygen vacancies and defects on the electronic structure and optical characteristic (Kumar, *et al*., 2000; Liqiang, *et al*., 2003). Figure 22 shows the PL spectra of the as-prepared TiO_2 samples where one sharp UV emission at 390 nm and one broad high intensity band at 650 nm are observed. The UV band peaking at 390 nm has been attributed to the electronic transition from conduction band (CB) to valence band (VB). In this case, the peaking at 650 nm could be ascribed to electron transition mediated by defects level in the band gap, such as oxygen vacancies formed during sample preparation. Therefore, the stronger PL intensity gives the larger content of oxygen vacancies or defects in samples (Liqiang, *et al.*, 2003).

For the photocatalytic activity test, methylene blue (MB) was employed to evaluate the photocatalytic activity of as-prepared K-doped TiO_2 samples. In photodegradation process, there are two factors resulting in the decreasing of MB concentration: the adsorption of MB onto the surface of photocatalyst, and the photooxidation of MB. In this experiment, the commercial reference material, Degussa P25-TiO_2, was used to compare the efficiency of MB solution decolorization. In the comparision test, the catalyst was used at fixed concentration (1.0 g/L) and the concentration of MB was 2.5×10^{-5} M. At this concentration, the as-prepared titanate samples could decolorize MB solution completely during adsorption MB in the dark. Therefore, the MB solution at the concentration of 2.5×10^{-4} M was chosen as the initial concentration for the photocatalytic experiment. Figure 10 shows the efficiencies of decolorization of MB between commercial TiO_2 sample and as-prepared TiO_2 samples. The results showed that all synthesized titanate samples could decolorize MB solution with higher efficiency than the commercial P25-TiO_2. The order of the efficiencies are 4.0KOX-TiO_2 > 1.0KOX-TiO_2 > 0.5KOX-TiO_2 > P25-TiO_2.

In this part we can see that all synthesized TiO_2 samples show higher decolorizing efficiency than Degussa P25-TiO_2 sample. Besides, they have good adsorption property and low photocatalytic property as shown in Figure 23. Therefore, the decolorizing MB solution results from adsorption property more than photocatalytic property. In the following part, we try to improve the photocatalytic property via calcination.

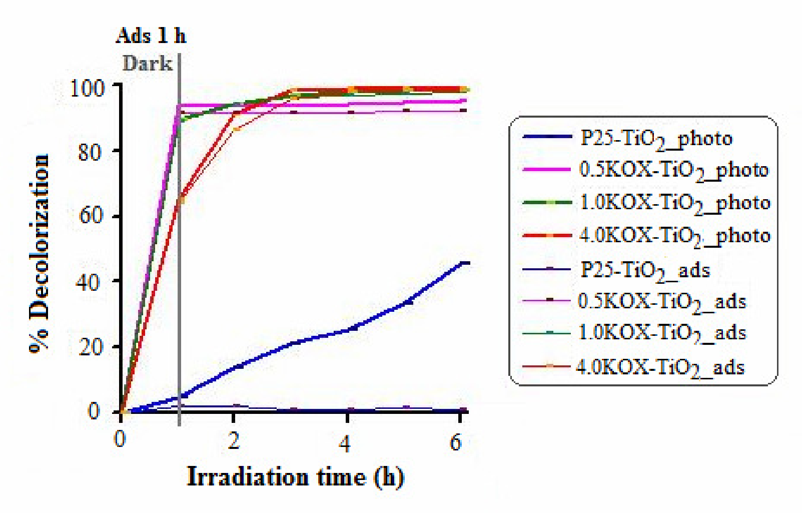

Figure 23. The efficiencies of decolorization of MB solution (2.5×10^{-4} M) under UV light irradiation in the presence of 1.0 g/L TiO_2 sample.

3.1.2 Effect of calcination on the properties of KOX-doped TiO_2 powders

3.1.2.1 Characterization of the calcined-0.5KOX-TiO_2

From all data above, only the 0.5 % concentration (0.5KOX-TiO_2) will be chosen for further studies since it has some interesting properties that make it stands out from the rest. The effect of the calcination temperature on the phase structure, crystallite size, morphology, specific surface area, pore structure, and photocatalytic activity of the as-prepared TiO_2 samples were investigated. Their photocatalytic properties were tested, again, by the methylene blue decolorization in comparision with the commercial Degussa P25 TiO_2. The regeneration of the used catalyst and its reuse were also studied.

The X-ray diffraction spectra of the as-prepared samples are illustrated in Figure 24. The XRD pattern at $2\theta = 25.50$ (101) in the spectrum of TiO_2 is identified as the crystal of anatase form (denoted as “A”) whereas the peak at $2\theta = 27.50$ (110) arises from the crystal of rutile form (denoted as “R”). The patterns apparently revealed the effect of calcination temperature on the phase change of TiO_2 samples. It can be seen that the 0.5KOX-TiO_2_non_calcined sample had the amorphous phase, when samples were calcined at 400 to 800 °C they turned to anatase phase. As the calcination temperature rose to 1000 °C, the crystals completely turned to rutile. According to many reports, the anatase-rutile transformation temperature was observed around 700-800 °C (Arroyo, *et al.*, 2003; Sreethawong, *et al.*, 2005; Yoo, *et al.*, 2005; Yu, *et al.*, 2006; Baiju, *et al.*, 2007; Tryba, *et al.*, 2007). The result in this study indicated that anatase-rutile transformation was significantly retarded. It has been reported that the phase transformation temperature mainly depends on the particles sizes, morphology of crystals, and the addition of additives (Wu, *et al.*, 2002). In this study, the transformation was retarded as indicated by the transformation temperature being raised to 1000 °C. This may be attributed to the addition of potassium oxalate during the sol-gel reaction. TiO_2 was treated with K^+ ion or prepared in the ionic liquid medium exhibited higher anatase-rutile transformation temperature (Yoo, *et al.*, 2005; Chen, *et al.*, 2007) while the treatment with Na^+ appeared to have no effect on the transformation temperature (Yu, *et al.*, 2006). Oxalate group in many complexes ususally decomposes at temperature < 500 °C or at most < 650 °C (House Jr., *et al.*, 1980; Foster, *et al.*, 1983). Therefore, when the temperature reached 700-800 °C all the oxalate ions should have been destroyed leaving the final product in the form of TiO_2 with trace of K_2O. In the sample bulk, the K^+ ion will be surrounded by the oxide ions, its own O^{2-} and also O^{2-} from TiO_2. This is, in fact, the ionic solid and its stability is governed by the lattice energy. The size of K^+ ion is almost equal to that of O^{2-} ion, 133 pm for the former and 140 pm for the latter [J.E. Huheey, 1978]. Theoretically, the comparable sizes of cation and anion give more favorable lattice energy [J.E. Huheey, 1978]. The product at this stage, presumably in the anatase phase, will be quite stable with the presence of K_2O and to transform it to rutile would need higher temperature. (In the presence of Na^+ ion, the effect is less favorable due to the smaller size of Na^+ ion which is only 95 pm, hence a slightly mismatched with O^{2-} ion and less favorable lattice energy compared with the K^+ case.) The phase structure and average crystallite size of the calcined TiO_2 samples calculated using the Scherrer equation for the main diffraction peak are given in Table 9.

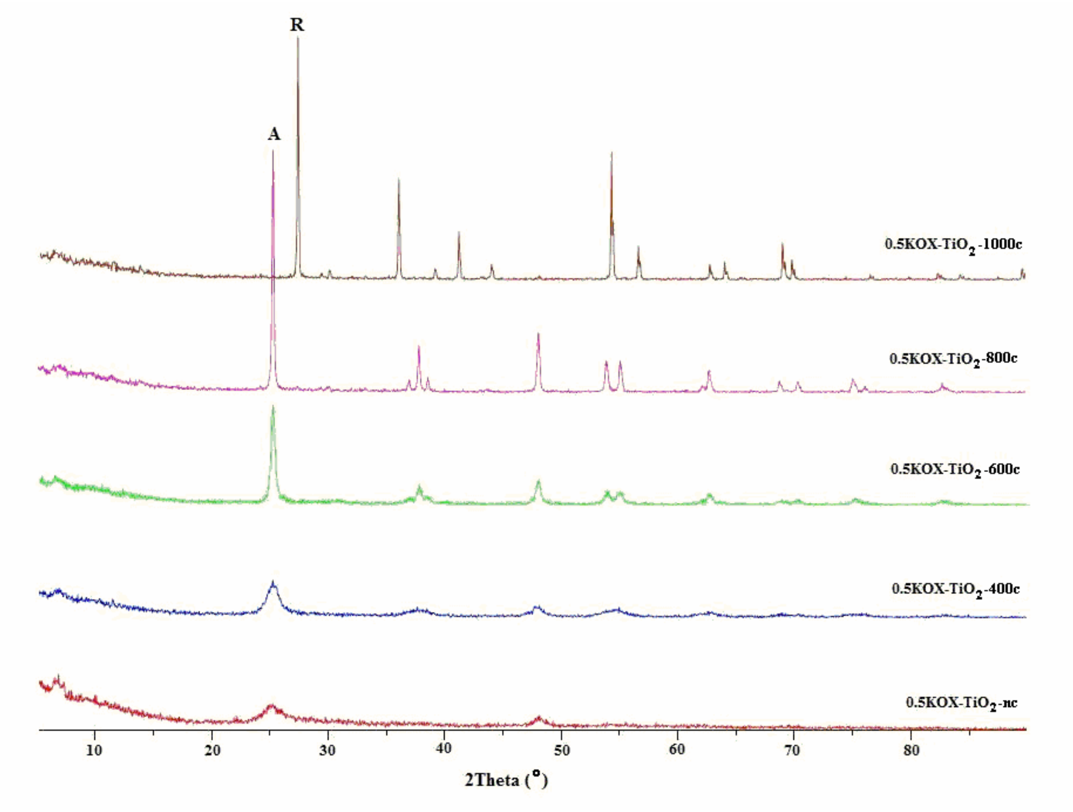

Figure 24. XRD patterns of the as-prepared 0.5KOX-TiO_2 samples at different calcination temperatures.

Table 9. Effect of calcination temperature on phase structure and average crystallite size (nm) of KOX-TiO_2 samples

Sample	Crystallite phase	Crystallite size (nm)*
0.5KOX-TiO_2_non calcined	Amorphous	-
0.5KOX-TiO_2_400c	Anatase	8
0.5KOX-TiO_2_600c	Anatase	24
0.5KOX-TiO_2_800c	Anatase	37
0.5KOX-TiO_2_1000c	Rutile	36

* Calculated from the Scherrer formula

The N_2 adsorption isotherms and pore size distributions before and after calcination at different temperatures are shown in Figures 25 and 26, respectively. The isotherms of types I and IV (BDDT classification) were observed for 0.5KOX-TiO_2_non_calcined and 0.5KOX-TiO_2_400c samples indicating the presence of micropore and mesopore structures. The samples calcined at higher temperature showed isotherm of type IV and almost had no hyteresis loop indicating that all the pores had collapsed during calcination and the total pore volumes were very small.

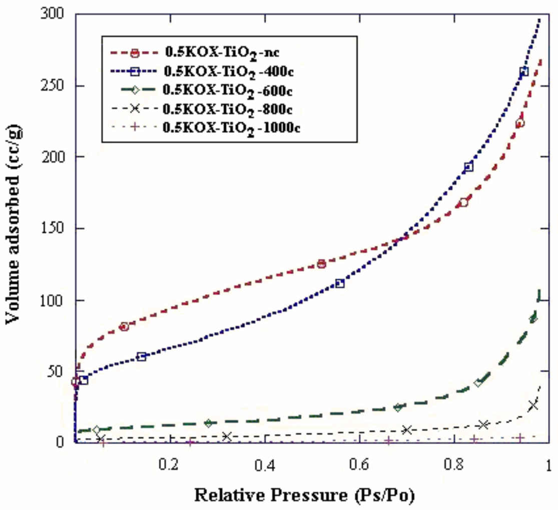

Figure 25. N_2 adsorption isotherms for calcined TiO_2 samples

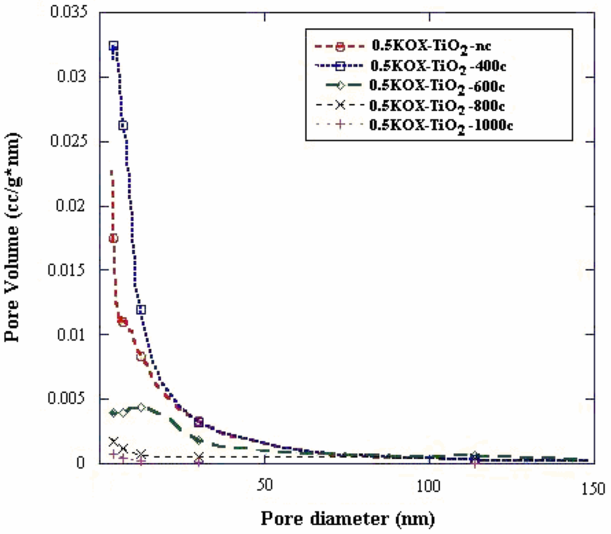

Figure 26. Pore size distributions for calcined TiO_2 samples.

The 0.5KOX-TiO_2_non_calcined and 0.5KOX-TiO_2_400c samples (from Figure 26) have wide pore size distribution from micropore to mesopore. The 0.5KOX-TiO_2_600c sample has mesopore in the range 20-80 nm. However, the pore size distribution curve of 0.5KOX-TiO_2_800c and 0.5KOX-TiO_2_1000c samples appear as a line, indicating the absence of pores. The specific surface area, pore volume, and pore diameter are summarized in Table 10. It is obvious that BET surface area and pore volume decreased with increasing calcination temperatures. As the calcination temperature increased the crystallinity also increased, however, the specific surface area decreased due to the collapse of the pore structure and the growth of TiO_2 crystallites.

Table 10. Effect of calcination temperature on the BET specific surface area (S_{BET}) and pore parameters of calcined-TiO_2 samples

Sample	S_{BET} (m^2/g)	Pore volume (cm^3/g)	Pore diameter (nm)
0.5KOX-TiO_2_non calcined	337	0.29	4
0.5KOX-TiO_2_400c	236	0.41	5
0.5KOX-TiO_2_600c	43	0.18	12
0.5KOX-TiO_2_800c	14	0.08	5
0.5KOX-TiO_2_1000c	2	0.01	6

The agglomerated particle size of 0.5KOX-TiO_2_non_calcined sample is rather large, about 3-5 μm, and showed almost spherical shape with rough surface. Some of these agglomerated lumps were hollow as detected by SEM and TEM techniques (Figure 27). In addition, the TiO_2 modified with potassium oxalate has different morphology compared with unmodified TiO_2 sample as shown in Figure 28. This result is an evidence that potassium oxalate really affects the surface morphology of TiO_2 sample.

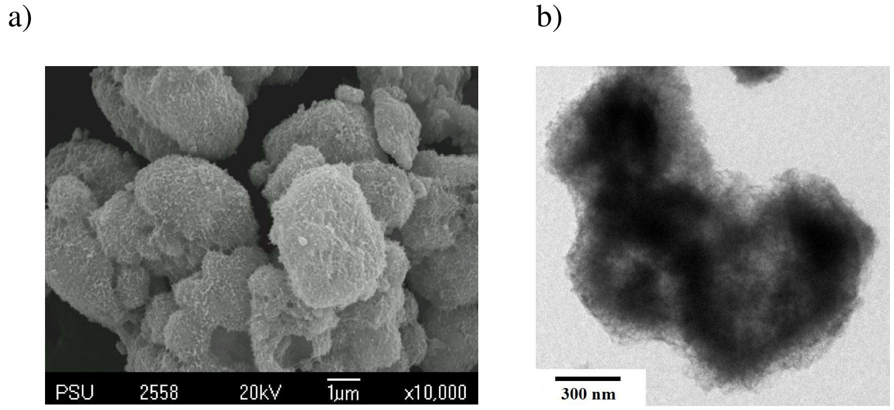

Figure 27. The morphologies of 0.5KOX-TiO_2_non calcined sample: a) SEM image and b) TEM image.

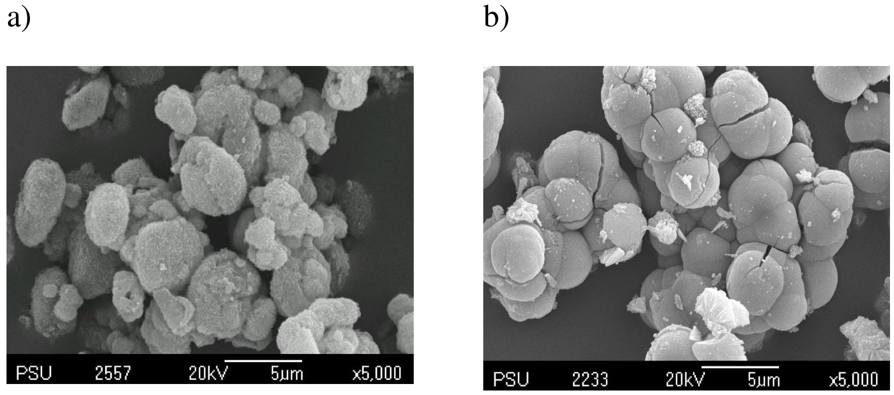

Figure 28. The SEM images of non-calcined samples: a) 0.5KOX-TiO_2 and b) undoped TiO_2.

Figure 29 shows SEM images of the samples after calcination at 400, 600, 800, 1000°C. With increasing calcination temperatures the crystal began to grow and form larger agglomerated particles. From Figures 28(a) and 29(a), it can be seen that the morphology of the non-calcined sample and the one calcined at 400°C had very similar shapes and surface textures. This result agreed with the XRD that both samples consisted mainly of amorphous phase and, thus, large surface area as evidenced from the BET results. As the calcination temperature rose the amorphous phase completely transformed to anatase phase at 600°C which in turn transformed to rutile phase at 1000°C. As the calcination temperature was increased, the sample bulk became denser and more aggregation could be observed (Figures 29(a)-(d)). The very high degree of crystallinity could be seen in the sample calcined at 1000°C (Figure 29(d)) which is the rutile phase. At higher magnification (not shown) the sample of Figure 29(d) appears as compact and well formed crystals with rounded edges/corners and smooth surfaces.

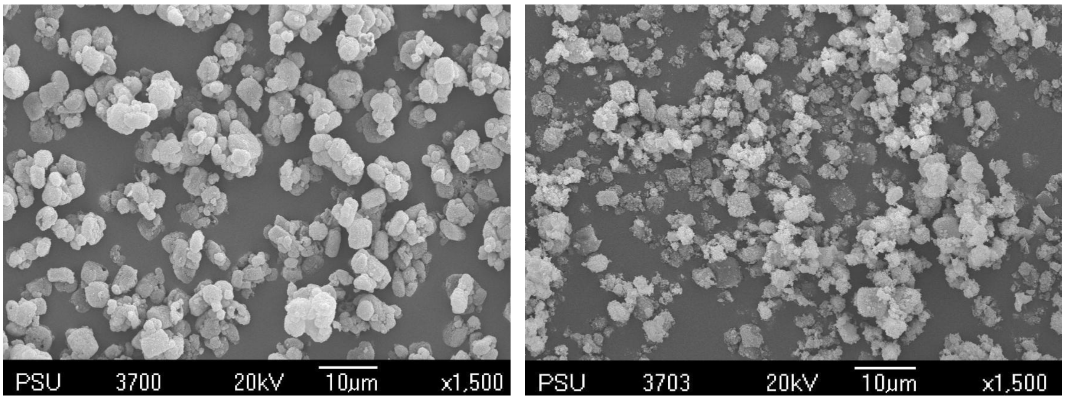

a) 0.5KOX-TiO_2_400c b) 0.5KOX-TiO_2_600c

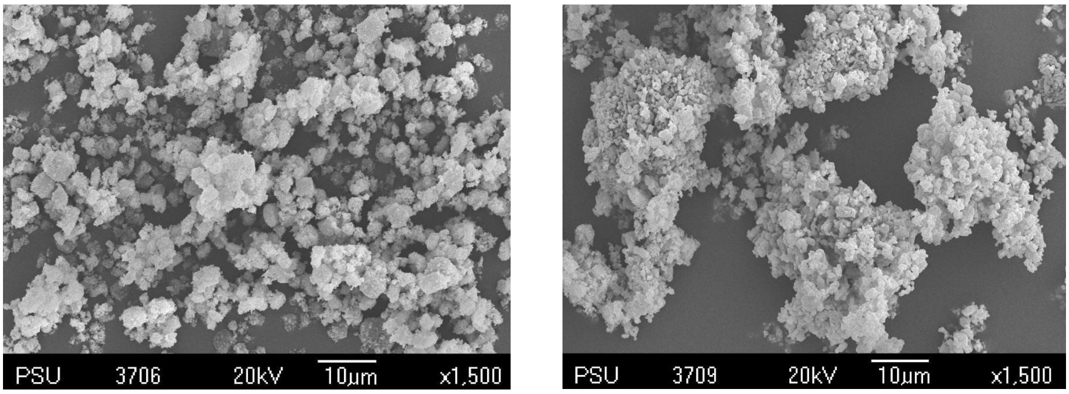

c) 0.5KOX-TiO_2_800c d) 0.5KOX-TiO_2_1000c

Figure 29. SEM images of calcined 0.5KOX-TiO_2 samples at different temperatures.

Figure 30 shows the FT-IR spectra of TiO_2 samples in the range of 4000-400 cm^{-1}. From these spectra, there appeared the strong bands at 3313 cm^{-1}, 1752-1627 cm^{-1}, 1413 cm^{-1}, 1217 cm^{-1}, and in the region of low energy (960 – 420 cm^{-1}). The band at 3313 cm^{-1} can be assigned to both ν_{OH} and ν_{NH} (stretching modes) indicating the presence of hydroxyl group of water in the samples. In the case of 0.5KOX-TiO$_2$_non_calcined sample, the C=O and C-O stretching modes show up as intense bands in the range 1752-1627 cm^{-1} and 1413-1217 cm^{-1}, respectively. These bands indicate the prescence of oxalate ligand resulting from addition of potassium oxalate during the sol-gel process. The bands in the region 960 to 420 cm^{-1} associate with the characteristic vibrational modes of TiO$_2$ ($\nu_{Ti\text{-}O}$, stretching mode of Ti-O bond) (Zhang, *et al.*, 2002). In this study, the Ti-O stretching mode of rutile appears at 450 cm^{-1}, however, the characteristic bands of anatase at 475 and 528 cm^{-1} were not clearly seen. With regards to calcination, the characteristic bands of hydroxyl group of water and of oxalate ligand decreased with increasing calcination temperature. The results from FT-IR spectra, hence, confirmed the presence of oxalate ligand and impurities such as NH_4^+ and H_2O on the surface of the synthesized TiO$_2$.

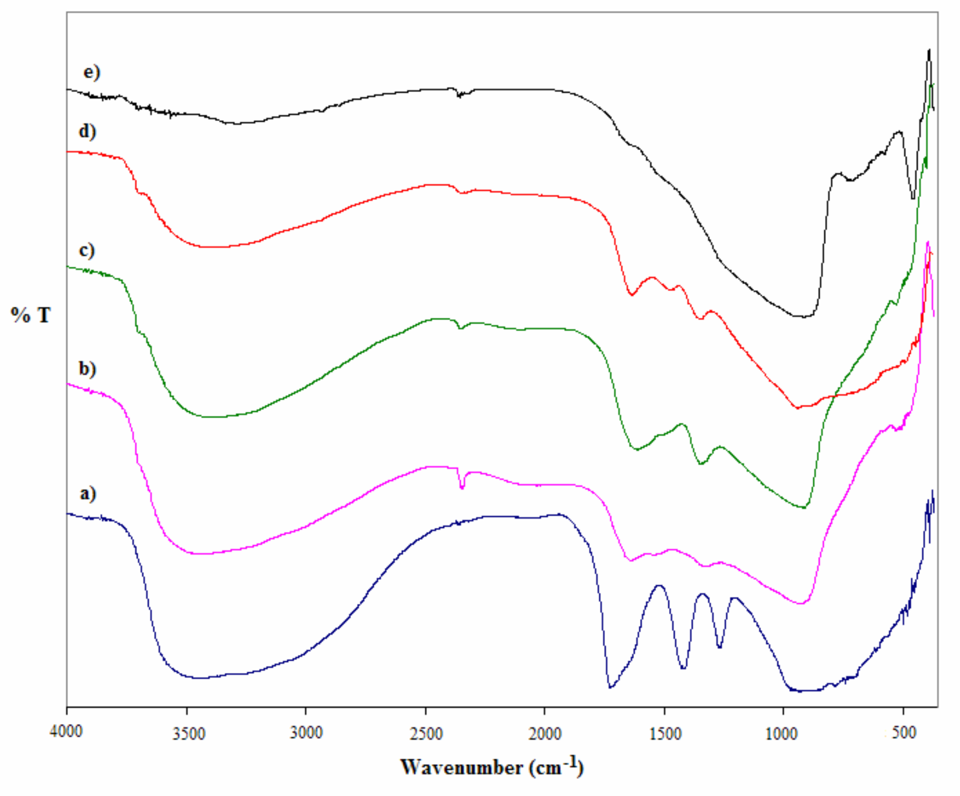

Figure 30. FT-IR spectra of a) 0.5KOX-TiO$_2$_non calcined, b) 0.5KOX-TiO$_2$_400c, c) 0.5KOX-TiO$_2$_600c, d) 0.5KOX-TiO$_2$_800c and e) 0.5KOX-TiO$_2$_1000c samples. [A small sharp band at 2400 cm^{-1} in (b) to (e) is due to the atmospheric CO$_2$].

DRS technique	PL technique
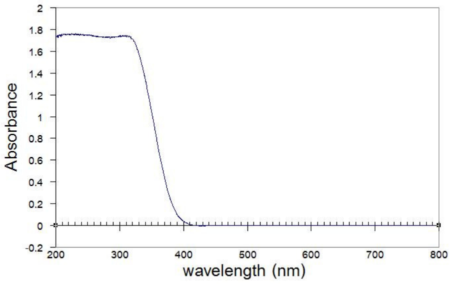 a) 0.5KOX-TiO$_2$_non calcined	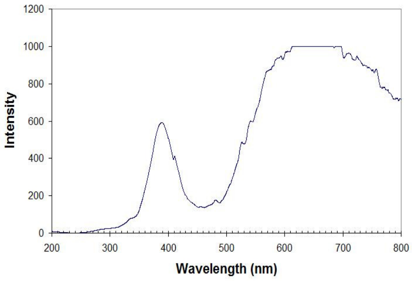 a) 0.5KOX-TiO$_2$_non calcined
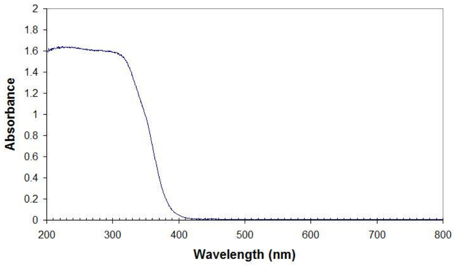 b) 0.5KOX-TiO$_2$_400c	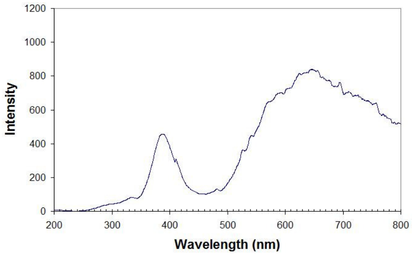 b) 0.5KOX-TiO$_2$_400c
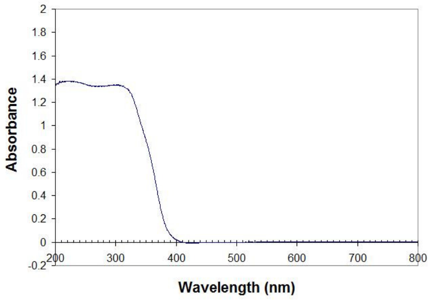 c) 0.5KOX-TiO$_2$_600c	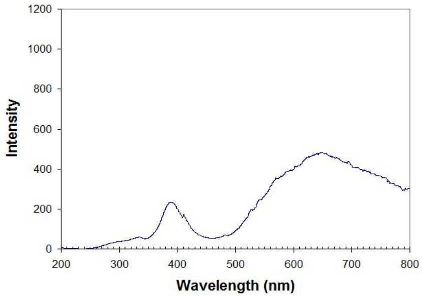 c) 0.5KOX-TiO$_2$_600c
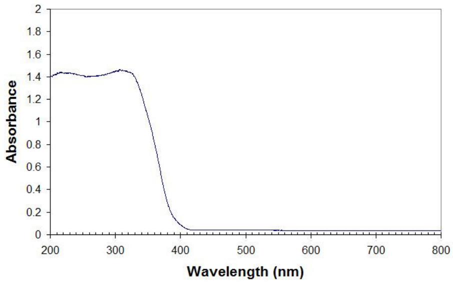 d) 0.5KOX-TiO$_2$_800c	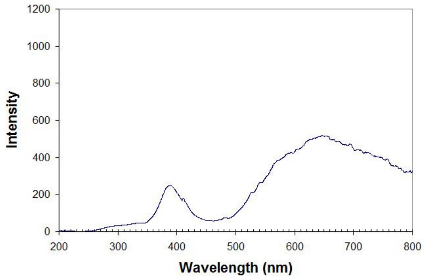 d) 0.5KOX-TiO$_2$_800c
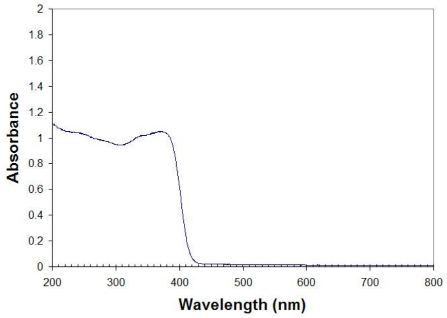 e) 0.5KOX-TiO$_2$_1000c	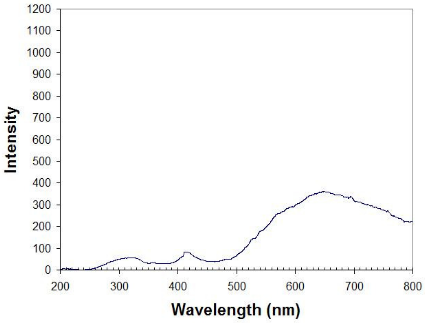 e) 0.5KOX-TiO$_2$_1000c

Figure 31. The diffused reflectance UV-Vis spectra and photoluminescence spectra of the calcined 0.5KOX-TiO_2 samples.

Table 11. Data from DRS and PL techniques of KOX-TiO_2 samples before and after calcinations

Sample	DRS		PL	
	λ_{onset} (nm)	E_g (eV)	λ_{emis}(nm.)	E_g (eV)
0.5KOX-TiO_2_non calcined	385	3.22	390	3.18
0.5KOX-TiO_2_400c	387	3.20	390	3.18
0.5KOX-TiO_2_600c	388	3.19	390	3.18
0.5KOX-TiO_2_800c	389	3.18	390	3.18
0.5KOX-TiO_2_1000c	416	2.98	416	2.98

UV-Vis diffuse reflectance and photoluminescence spectra were measured in order to characterize the band gap energy, shown in Figure 31, including nature of electronic transition in materials. The absorption edge in the UV-Vis DRS and the emission peak in the PL spectra were used to calculate the band gap energy by the Plank's equation ($E_g = 1240/\lambda_{onset}$). The position of the absorption edge (λ_{onset}) and the PL emission peak (λ_{emis}), however, remained rather unchanged, except that of the rutile. The λ_{onset}, the λ_{emis} , and the calculated band gap energy of synthesized samples are shown in Table 11. The band gap energy of TiO_2 can be measured using PL technique. (Gfroerer, 2000; Liqiang, *et al.*, 2006). All the PL spectra are not much different in that they show one sharp UV emission peak at 390 nm and one broad peak with high intensity at 650 nm. The UV band peaking at 390 nm has been attributed to the electronic transition from conduction band (CB) to valence band (VB) for anatase crystal and band at 416 nm for rutile crystal, respectively. Since they are very similar, only some of the representative UV-Vis absorption and PL spectra are shown in Figure 31. The intensity of both UV-Vis DRS and PL decreased steadily as the calcination temperature increased due to high crystallinity, low surface defect, and less oxygen vacancies in these calcined samples. This is because the PL signals of semiconductor materials relate to the recombination rate of electron-hole pair in the material bulk produced after irradiation (Liqiang, *et al.*, 2006). The recombination rate is high for the poor crystallinity with high surface defect materials, and vice versa.

3.1.2.2 Photocatalytic activity and regeneration studies

Methylene blue (MB) was employed to evaluate the photocatalytic activity of the as-prepared titanate samples. Generally, MB could be mineralized into harmless gaseous CO_2, inorganic SO_4^{2-}, NH_4^+, and NO_3^-. The degradation reaction was proposed to start with the cleavage of the $C - S^+=C$ part in MB molecule leading to formation of sulfate ions. Other species were also detected such as leucomethylene blue, sulfoxides, and sulfones. However, at the end of reaction these species vanished and MB appeared to be completely mineralized (Houas, *et al.*, 2001; Gnaser, *et al.*, 2005).

In photodegradation process, the most likely scenario is that the MB molecule is first adsorbed onto the catalyst surface followed by photooxidation to mineralization. The adsorption stage is favored by the attraction force between the positive charge on the MB molecule and the negative charge at the oxygen atom attached to titanium at the catalyst surface. In this experiment, the commercial Degussa P25 was used to compare the efficiency of the decolorization of MB solution with the as-prepared TiO_2 samples. Figure 32 shows a typical absorption spectra of methylene blue (2.5×10^{-5} M) solution which decreased when increasing irradiation time.

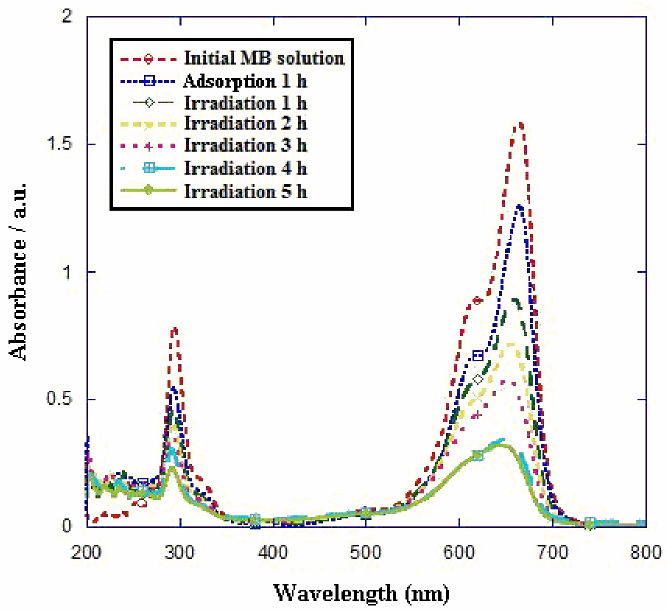

Figure 32. Absorption spectra of methylene blue solution containing titania catalysts (0.5KOX-TiO_2_1000c) under UV light irradiation at different time intervals.

Figures 33 and 34 show the efficiencies of decolorization of MB by the commercial TiO_2 sample and the as-prepared TiO_2 samples before and after being calcined at different calcination temperatures. Figure 33 shows the results when low concentration of MB was used (2.5×10^{-5} M). At this low concentration, P25 and four of the as-prepared TiO_2 (non-calcined, 400c, 600c, and 800c) showed 100 % decolorization by the combined adsorption and photocatalytic processes. The one calcined at 1000 °C, which was converted to rutile, could decolorize only 80 %. The decolorization by P25 (Figure 33(a)) was mainly by photocatalytic process. In the dark, P25 could decolorize by only *ca.* 30 %, presumably by the adsorption process. The non-calcined sample showed very high adsorption power that by adsorption alone it could completely decolorize the solution leaving no trace of color to test for the photocatalytic power. As the samples were calcined at higher temperatures, the adsorption power decreased significantly with increasing calcination temperature (Figures 33(c)-33(f)). When the adsorption was low the photocatalytic power became dominant and the decolorization could be brought up further by the photocatalytic process. In Figure 33(f) the decolorization was not complete even with the help from photocatalytic process. This sample composed mainly of rutile which has been known for its low efficiency in photocatalytic power. However, in other samples, Figures 33(c)-33(e), the decolorizations were all complete by the photocatalytic process. The compositions in these samples were amorphous (Figure 33(c)), mixed amorphous and anatase (Figure 33(d)), and anatase (Figure 33(e)). At this concentration, the non-calcined sample and those calcined at 400, 600, 800°C could decolorize the dye solution as good as using P25. The non-calcined and the low- temperature calcined-samples decolorize by mainly the adsorption process while the higher calcined temperature samples decolorize by combined adsorption and photocatalytic processes. The one with higher calcination temperature showed larger portion of photocatalytic process. This result agrees with other reports studying the effect of calcination temperature on the efficiency of photocatalytic effect (Yu, *et al.*, 2006; Baiju, *et al.*, 2007; Tryba, *et al.*, 2007). The high adsorption power of the non-calcined and low temperature calcined samples stems from large surface area in these samples. As might be expected the added oxalate group should chelate with titanium ion as well as interlinking few units of titanium moieties together to form some open framework, hence, large surface area. The framework, however, should be rather short as evidenced by the low crystallinity. Furthermore, the oxalate group is rich in oxygen atoms which bear partial negative charge. This is another factor that gives rise to strong adsorption power besides the large surface area. Upon calcination, decomposition of the oxalate group took place and, hence, the framework collapsed. The particles aggregation increased with higher crystallinity of the bulk resulting in lower surface area (Table 10). Therefore, the decrease in adsorption ability can be observed with the samples that were calcined at high temperatures. This trend is clearly demonstarted by the data in Figures 33-34. At low temperature calcination (400 ºC) the collapse of oxalate framework was not complete as evidenced by the still high surface area and the FT-IR spectrum showing characteristic bands of oxalate (the region 1752-1627 cm^{-1} in Figure 30(b)), therefore, the adsorption power was still considerably high.

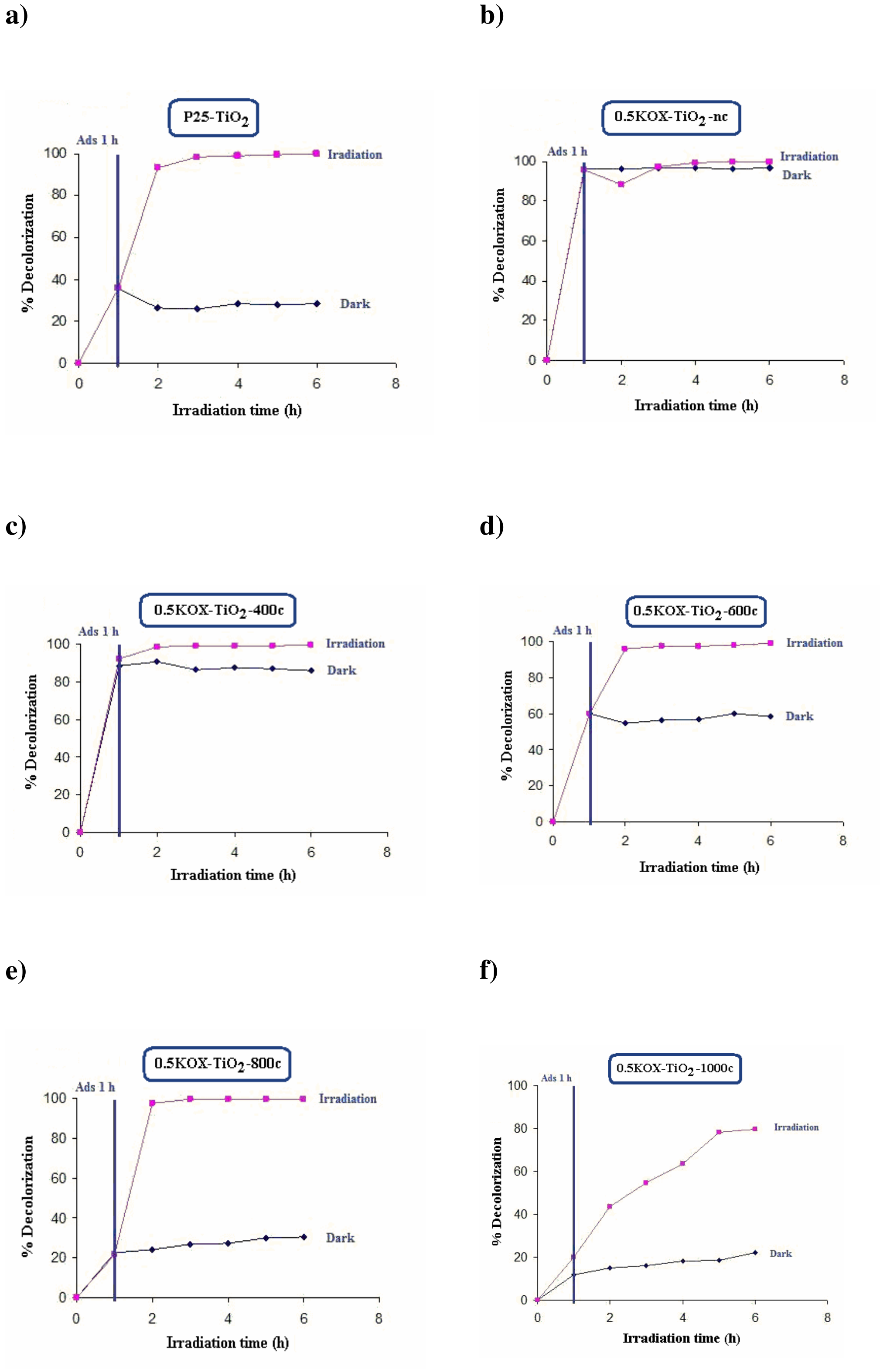

Figure 33. The efficiencies of decolorization of MB solution (2.5×10^{-5} M) under UV light irradiation in the presence of 1.0 g/L KOX-TiO_2 sample.

a) MB 7.5×10^{-5} M

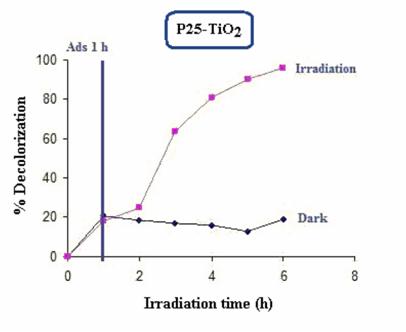

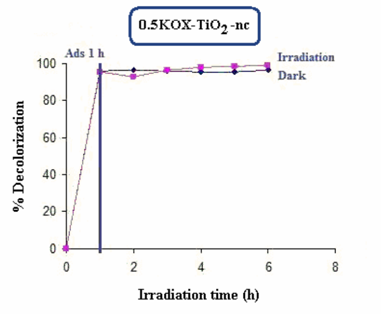

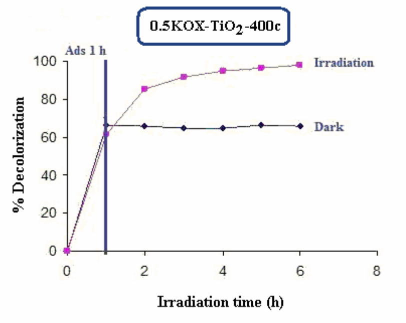

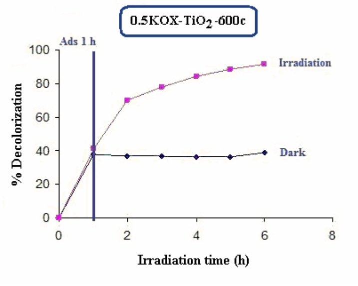

b) MB 1.25×10^{-4} M

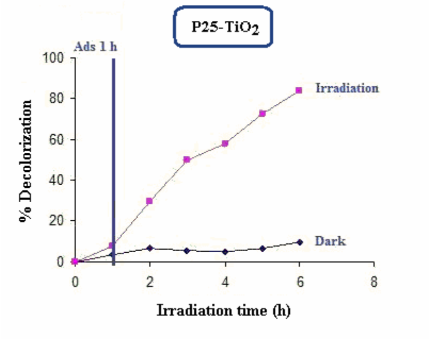

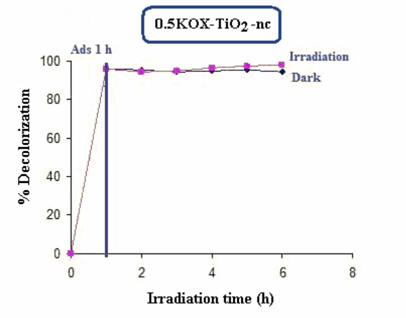

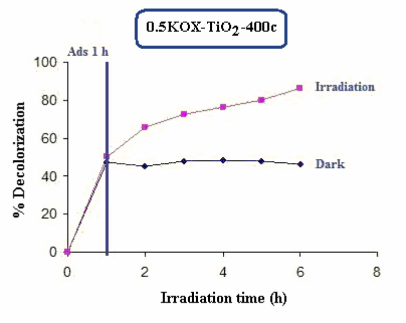

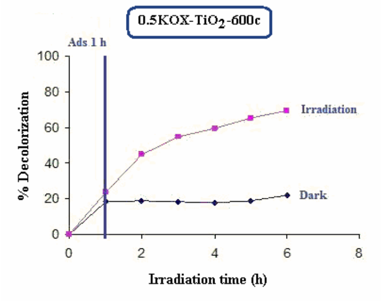

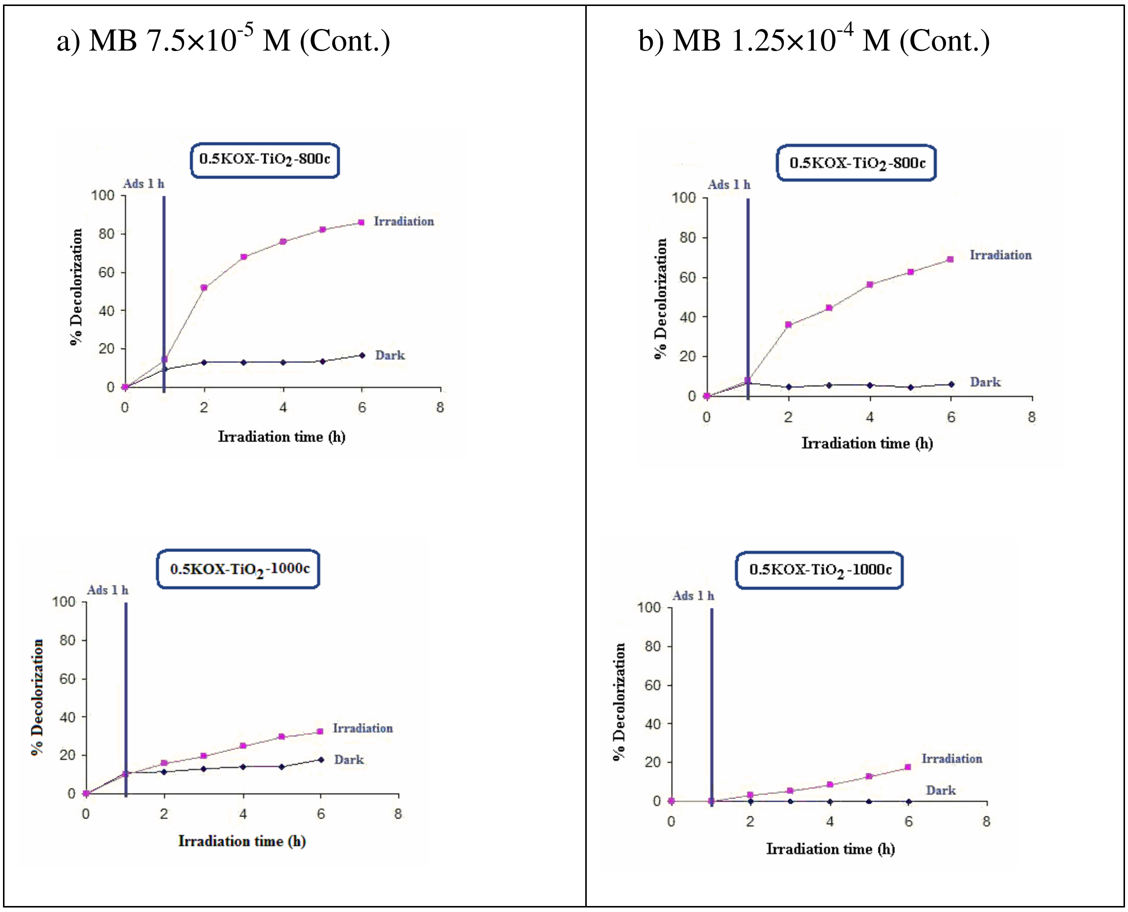

a) MB 7.5×10^{-5} M (Cont.)

b) MB 1.25×10^{-4} M (Cont.)

Figure 34. The efficiencies of decolorization of higher concentrations of MB solution; a) 7.5×10^{-5} M and b) 1.25×10^{-4} M under UV light irradiation in the presence of 1.0 g/L KOX-TiO_2 sample.

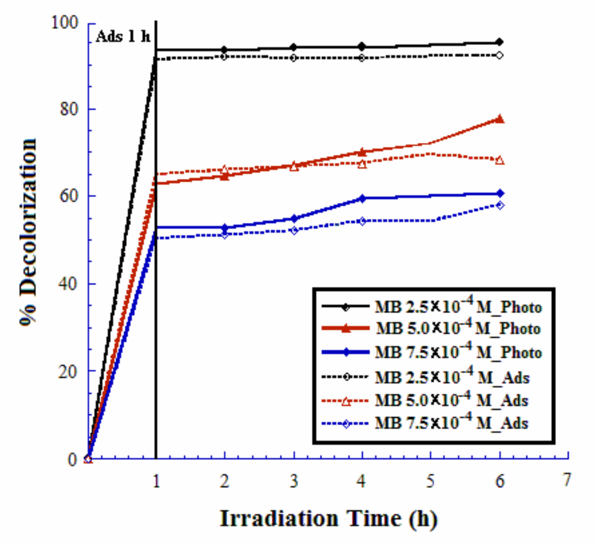

Figure 35. Comparison of decolorization efficiencies at low and high concentrations by the non-calcined KOX-TiO_2 sample.

Results from Figures 33 and 34 showed that the as-prepared 0.5KOX-TiO_2_non calcined sample could decolorize MB solution completely during the adsorption of MB in the dark for concentrations up to 1.25 x 10^{-4} M. Eventhough, the photocatalytic experiments were performed, no conclusion could be drawn whether this complete decolorization resulted from adsorption alone or the combination of both processes. Therefore, further investigations for 0.5KOX-TiO_2_non-calcined were carried out by using higher concentration of MB solutions and studied for its photocatalytic activity. Figure 35 shows that the non-calcined sample could completely decolorize, by adsorption, the MB solutions up to 2.5 x 10^{-4} M. At higher concentrations, 5.0 x 10^{-4} and 7.5 x 10^{-4} M, then the non-calcined sample began to show its limitation by decolorizing only *ca.* 70-80 % and *ca.* 50-60 %, respectively. It is noteworthy to point out the very low, barely detectable, photocatalytic activity exhibited by the non-calcined samples. The decrease in adsorption of MB at higher concentrations (5.0 x 10^{-4} and 7.5 x 10^{-4} M) resulted solely from its adsorption saturation point being reached. The saturation point should lie between 2.5 x 10^{-4} and 5.0 x 10^{-4} M. By taking that at the concentration 5.0 x 10^{-4} M the sample exhibited *ca.* 65 % adsorption, the approximate saturation point would be *ca.* 3.8 x 10^{-4} M corresponding well with *ca.* 55 % adsorption exhibited by the concentration 7.5 x 10^{-4} M (Figure 22). This simple explanation fits with this case where the adsorption is dominant. (In the system where the photocatalytic activity is dominant the decrease of % decolorization, mainly by the photocatalytic activity, when increasing the dye concentration can be explained slightly different from that given above, see for example Ref (Grzechulska, *et al.*, 2007)).

The non-calcined sample had large amount of –OH functional group on its surface as evident by the very strong absorption band at 3300-3400 cm^{-1} in the FT-IR spectrum. This band decreased as the sample was calcined at higher temperature due to the loss of –OH functional group in the form of H_2O. The OH group at the surface acts like surface charge-carrier trapping for both the conduction band electron and the valence band hole as shown in eqs. (32)-(33).

$$e^- + \text{>Ti}^{IV}\text{-OH} \rightarrow (\text{>Ti}^{III}\text{-OH}) \quad (32)$$

$$h^+ + \text{>Ti}^{IV}\text{-OH} \rightarrow (\text{>Ti}^{IV}\text{-}^{\bullet}\text{OH})^+ \quad (33)$$

where $\text{>Ti}^{IV}\text{-OH}$ is the hydrated surface functional group, $(\text{>Ti}^{III}\text{-OH})$ is the surface-trapped conduction band electron, and $(\text{>Ti}^{IV}\text{-}^{\bullet}\text{OH})^+$ is the surface-trapped valence band hole (Baiju, *et al.*, 2007). Since the crystallite size of the samples increase with calcination temperatures, the reverse is true that the crystallite size of the non-calcined samples are the smallest in the series. (As shown in Table 8, the non-calcined sample existed in amorphous phase. The lack of diffraction peaks in XRD prevented the crystallite size calculation by the Sherrer equation.) The effect of small crystallite size means that the two surface charge-carrier traps in eqs. (8) and (9) will be close together on the surface and annihilate. This is called the surface charge-carrier recombination and probably is the main factor for the inactivity of the amorphous or low crystallinity form of TiO_2. For the calcined samples, the one calcined at 800 °C showed the best photocatalytic activity, approximately equal to P25. This could be due to the high crystallinity and the presence of small amount of rutile. There has been a prevailing presumption that small amount of rutile mixed with anatase seems to give a synergistic effect in the photocatalytic process (Ohno, *et al.*, 2003). In the most recent report by Hirakawa, et al., it was shown that pure anatase and mixture of anatase and small amount of rutile efficiently generated $^{\bullet}OH$ radical in the photocatalytic process while the amount of OH-radicals generated was extremely low with pure rutile (Hirakawa, *et al.*, 2007). This indicates that anatase is the active phase in the photocatalytic process. The general trend for the calcined samples, upon comparison data from several reports, is that the higher the calcination temperature the better photocatalytic activity as long as the anatase phase is still present and once the the calcination temperature surpasses the anatase-rutile transformation temperature, the photocatalytic activity drops (Yoo, *et al.*, 2005; Yu, *et al.*, 2006; Baiju, *et al.*, 2007; Tryba, *et al.*, 2007; Chen, *et al.*, 2007). This is because at that temperature the main composition is anatase of high crystallinity with very small amount of rutile begins to form and being mixed in with anatase. Beyond this temperature, the content of rutile increases and the photocatalytic activity decreases.

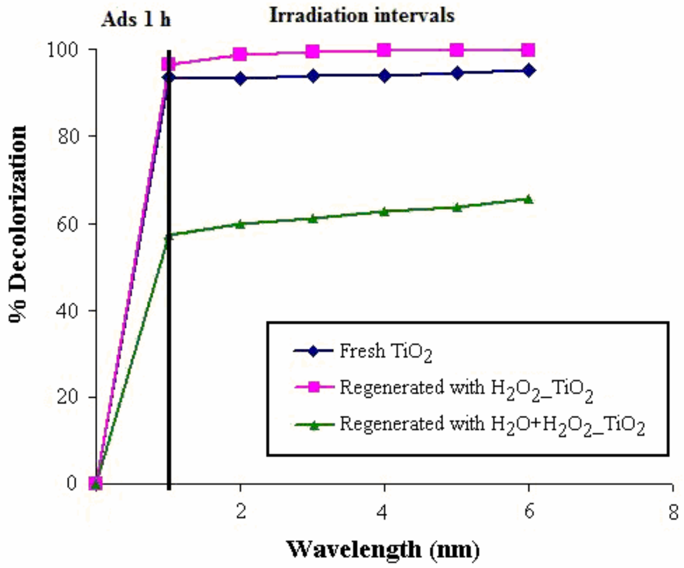

Figure 36. Comparison of the decolorization efficiencies of MB solution (2.5×10^{-4} M) using the regenerated TiO_2 samples under UV irradiation.

After decolorization experiments, the powders were covered with dye molecules due to the high adsorption power. The clean surface, however, could be regenerated for further uses. Two methods of regeneration were attempted. The first was by treating the used powder in 50 mL of distilled water and 5 mL of H_2O_2 solution (1 M) with stirring overnight under UV light irradiation. The second was by using the same method but with 50 mL hydrogen peroxide (H_2O_2, 1 M) solution. The regenerated TiO_2 powders were obtained and separated for reused in the next cycle. The regenerated TiO_2 powders were off-white instead of being "snow" white as freshly prepared. The performance of the two regenerated TiO_2 samples were compared to the freshly prepared TiO_2 sample as shown in Figure 36. It can be seen that the sample regenerated with H_2O_2 showed higher decolorization ability than the freshly prepared sample and much better than the one regenerated with mixed H_2O and H_2O_2 solution. In the regeneration process, the presence of both H_2O_2 and UV light were necessary. In the prescence of UV light alone no regeneration could be observed. With the presence of H_2O_2 alone the regeneration could take place but it took very long time to do so. Furthermore, in the absence of TiO_2 powder, MB pigment was also completely decomposed by H_2O_2 and UV in about the same time as was observed in the regeneration process. These observations could be rationalized based on the increase of the reactive $^{\bullet}OH$ radical in the regeneration setup.

It appears that in the regeneration process, H_2O_2 played the major role to destroy the dye molecules previously adsorbed at the TiO_2 surface. This resulted from the increasing concentration of the $^{\bullet}OH$ radical according to the following equations (Neppolian, *et al.*, 2002).

$$H_2O_2 \rightarrow 2\,^{\bullet}OH \qquad (34)$$

$$H_2O_2 + e^- \rightarrow OH^- + ^{\bullet}OH \qquad (35)$$

$$H_2O_2 + O_2^{\bullet -} \rightarrow OH^- + ^{\bullet}OH + O_2 \qquad (36)$$

Eq (34) represents the homolytic cleavage of H_2O_2 by light while eqs. (35)-(36) are associated with the photocatalytic reaction of TiO_2. Among eqs (35) and (36), the main source of $^{\bullet}OH$ comes from eq. (35) where H_2O_2 is reduced by the conduction band electron. The production of $^{\bullet}OH$ from eq. (36) is negligible as only small amount of $O_2^{\bullet -}$ anion was produced (Hirakawa, *et al.*, 2007). Since in a controlled experiment, the MB pigment was also decomposed by H_2O_2 and UV light without the need of TiO_2 plus the very low photocatalytic property exhibited by the non-calcined sample as depicted in Figure 35, we, therefore, concluded that the regeneration was driven by eq (34). The combined use of UV/H_2O_2 to decolorize and mineralize dyes has been demonstrated recently by using UV light with major wavelength of 254 nm (Shu, *et al.*, 2005; Shu, *et al.*, 2006). In another study to investigate the UV/H_2O_2 oxidation of NO_x emissions, a UV lamp with spectral output range from 200 to 320 nm was used (with an additional spike at 365-370 nm) (Cooper, *et al.*, 2002). However, a small amount of UV spectral in the solar light , *ca.* 5 %, could also initiate the $^{\bullet}OH$ production from H_2O_2 which accounted for 20-25 % degradation of dye by H_2O_2 in the absence of TiO_2 (Neppolian, *et al.*, 2002). In our system, the emission wavelength from the fluorescent UV light was 366 nm which should be sufficient to initiate the $^{\bullet}OH$ radical in the regeneration process.

3.2 Preparation of TiO_2/rubber sheets and their photocatalytic activity

Several studies have dealt with the syntheses of ultrafine TiO_2 nanoparticles and their applications in water purification. However, powder form of TiO_2 photocatalysts have to be separated after water treatment and the process for the separation of ultrafine nanoscale particle is in fact tedious and costly (Neppolian, *et al.*, 2002). The use of powder photocatalysts to photodegrade toxic or non-biodegradable organic compounds in solution is hindered by (a) the separation of the reaction product and catalyst at the end of the reaction and (b) the low quantum efficiency of these processes (Zhiyong, *et al*, 2008; Zhiyong, *et al.*, 2008). These disadvantages could be overcome by using supported photocatalysts fixing TiO_2 on glass (Losito, *et al.*, 2005), ITO glass (Sankapal, *et al.*, 2005), polymer films (Yang, *et al.*, 2006), and plastic (Kwon, *et al.*, 2004). TiO_2 thin films have been prepared by various techniques such as chemical vapor deposition (Ding, *et al.*, 2001), spray pyrolysis deposition (Weng, *et al.*, 2005), flame synthesis (Partsinis, *et al.*, 1996), and sol-gel dip coating (Sen, *et al.*, 2005; Guo, *et al.*, 2005), and however these techniques need expensive equipment and complex procedures.

In the present study, synthesized KOX-doped TiO_2 powders were impregnated in the rubber sheet by direct mixing of TiO_2 powder with latex and distilled water. The synthesized KOX-doped TiO_2 powders were prepared by sol-gel method, using $TiCl_4$ as starting material. Hexamethylenetetramine was used as basic solution to control rate of hydrolysis and condensation reaction. Potassium oxalate was selected as dopant added in varying amounts: 0.5, 1.0, and 4.0 % by mass. The two samples with 0.5 % and 4.0% were selected for preparing rubber sheet due to their outstanding properties. Their photocatalytic properties were tested for the decolorization of methylene blue and compared with commercial (Degussa P25 TiO_2 and anatase) impregnated rubber sheet. The regeneration of the used impregnated rubber sheet and its reuse were also studied.

3.2.1 Characterization of the impregnated TiO_2 rubber sheets

Each of the synthesized KOX-doped TiO_2 samples and two other commercial TiO_2 samples (Degussa P25-TiO_2 and Anatase-TiO_2) was used as an impregnating powder on rubber sheet substrate. The synthesiszed KOX-doped TiO_2 samples were prepared via sol-gel method. The phase structure, surface area, and amount of element of the selected two synthesized KOX-doped TiO_2 samples are given in Table 12.

Table 12. Typical physicochemical properties of as-prepared KOX-doped TiO_2 samples.

Sample	Crystallite phase	Surface area (m^2/g)	Amount of element	
			Ti (%)	K (%)
K1-doped TiO_2	Amorphous	336.7	14.08	2.44
K2-doped TiO_2	Mixed phase*	8.8	7.67	19.55

*Data from XRD: mixed phase were potassium acetate hydrate ($C_2H_3KO_2.xH_2O$), potassium titanium oxide ($K_2Ti_4O_9$ $2.2H_2O$), and titanium oxide (Ti_3O_5).

The effect of parameters such as the amount of distilled water, the amount of rubber latex, and the amount of commercial TiO_2 powder were studied in previous study (Sriwong, *et al.*, 2008), to optimize the preparation of impregnated rubber sheets to give high photocatalytic efficiency. The surface morphology of impregnated rubber sheet sample was governed by the amount of distilled water, rubber latex, and TiO_2 powder. It was found that the effect from varying the amount of distilled water on the viscosity of the mixture, and hence on the surface morphology and roughness of sheet sample, was more pronounced than the effect of varying the amount of latex and TiO_2 powder. The period of time for drying sheet at room temperature also depended on the amount of distilled water, rubber latex, and TiO_2. On increasing either the amount of distilled water or the amount of rubber latex, the drying period was longer in allowing more TiO_2 particles to deposit to bottom of the mixture, hence, increasing the TiO_2 particles at the bottom surface of the dried sheet. However, increasing the amount of TiO_2 showed opposite effect as the drying period became shorter (Sriwong, *et al.*, 2008). Furthermore, when using different types of TiO_2 powders, the morphology of TiO_2 powders will be another factor to affect the characteristic properties of the rubber sheets. Powder with high agglomeration will cause the sheet to have high surface morphology and roughness, and the opposite will result with powder of low agglomeration. This may be due to the faster deposition rate of the highly agglomerated TiO_2 particles at the bottom of the vessel. This point was demonstrated clearly in this work which used synthesized TiO_2 powders comparing with the commercial anatase and Degussa P25 TiO_2.

In addition, the adhesions and stability of all Imp-TiO_2 sheets were also studied by submerging of the films in water and stirred continuously for 6 h. The Imp-TiO_2 sheets prepared this way did not show sign of any deterioration after being submerged in water. Therefore, all Immo-TiO_2 sheets can be used in the actual applications.

3.2.1.1 X-ray powder diffraction (XRD)

The X-ray diffraction spectra of the TiO_2 powders and impregnated TiO_2 rubber sheets are illustrated in Figures 37 and 38. The diffraction peaks for the anatase and rutile phases are marked with ‘A’ and ‘R’, respectively. Figure 37 shows XRD patterns of the synthesized KOX-doped TiO_2 samples and the two commercial TiO_2 samples in the powder form. The phase structure of the synthesized TiO_2 samples showed amorphous and mixed phases (potassium acetate hydrate ($C_2H_3KO_2.xH_2O$), potassium titanium oxide ($K_2Ti_4O_9$ $2.2H_2O$), and titanium oxide (Ti_3O_5)) for the K1-doped TiO_2, and K2-doped TiO_2, respectively. For the two commercial TiO_2 samples, only anatase phase was found in commercial anatase and mixed phase of anatase and rutile phases for the commercial Degussa P25 TiO_2 sample. Figure 38 shows XRD pattern of Imp-TiO_2 rubber sheets. From Figure 38, a well-crystallized anatase form was found in the Imp-Ana sheet as shown in Figure 38e while both anatase and rutile were observed for the Imp-P25 sheet in Figure 38d. The pristine rubber sheet shows a clean base line throughout the spectrum except a large broad peak near $2\theta = 19°$ due to scattering of X-ray beam by low Z matrix of rubber. This broad scattered peak also shows up in the patterns of both the impregnated sheets but at a much smaller intensity due to the inclusion of TiO_2 particles in the impregnated sheets. The surface with high content of TiO_2 particles cause the average matrix of the rubber sheet to increase, therefore, less scattering of X-ray beam (Sriwong, *et al.*, 2008).

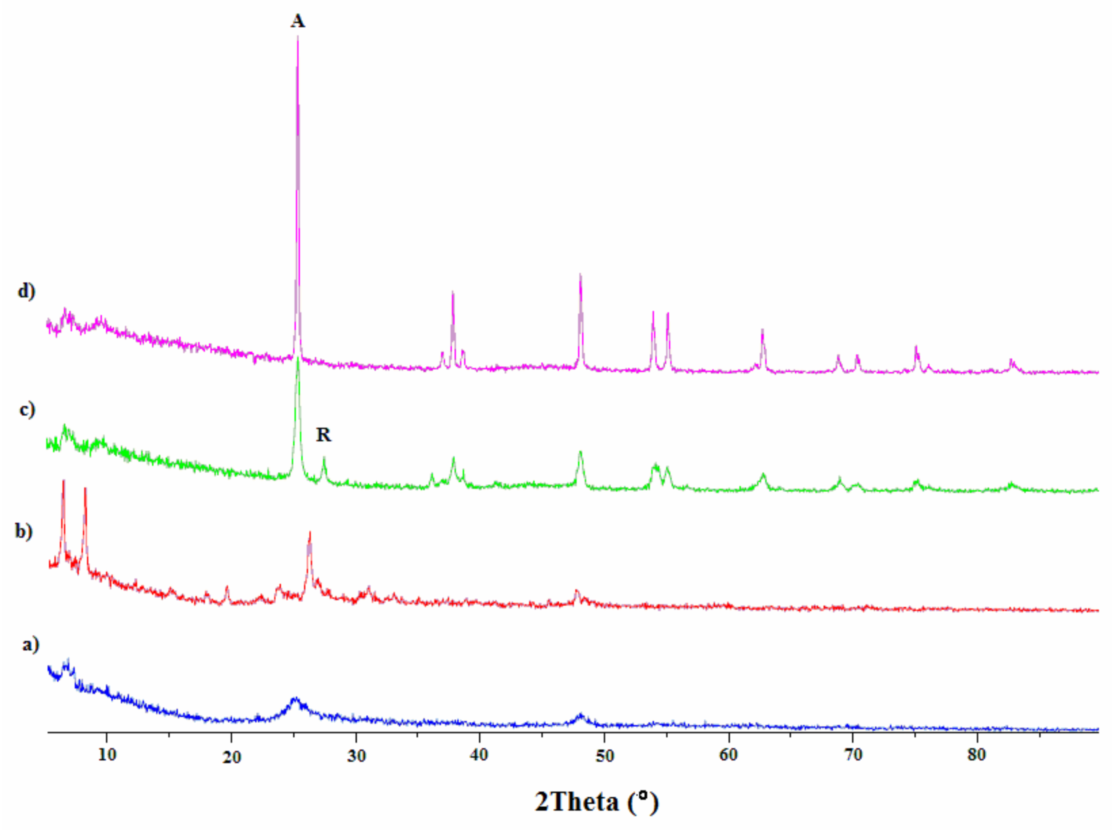

Figure 37. XRD patterns of TiO_2 powders (a) K1-doped TiO_2, (b) K2-doped TiO_2, (c) Degussa P25, and (d) Anatase.

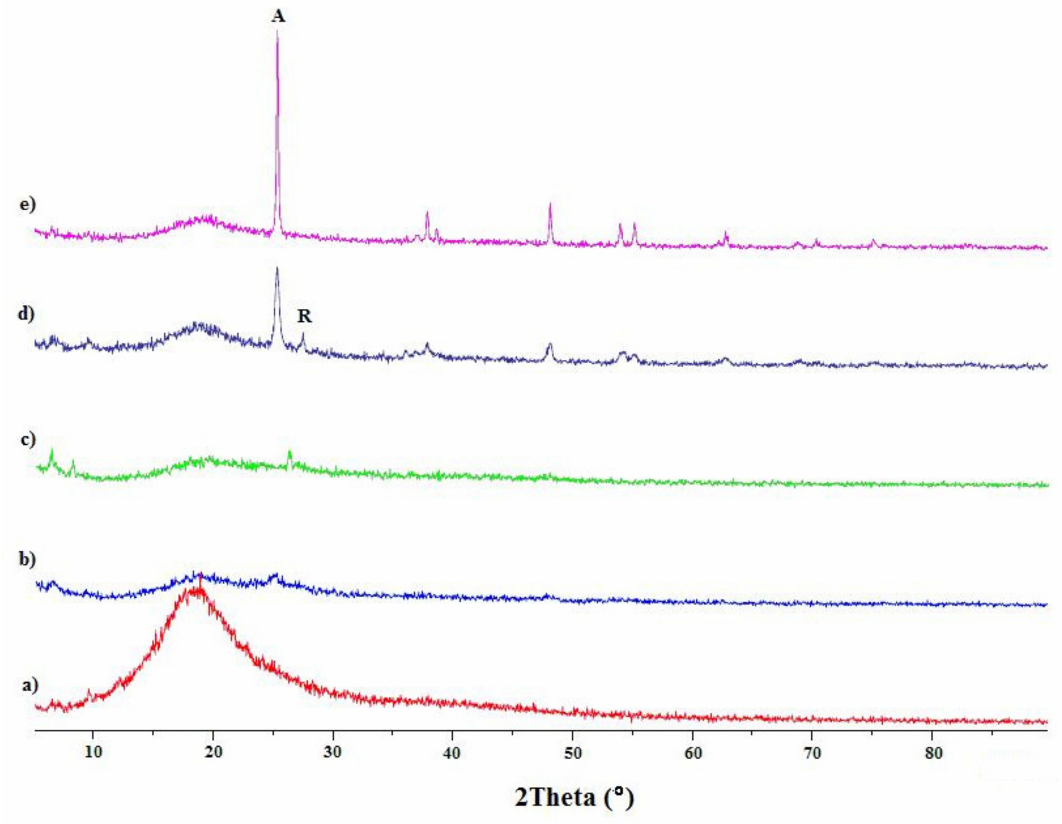

Figure 38. XRD patterns of (a) pristine rubber sheet, (b) Imp-K1 sheet, (c) Imp-K2 sheet, (d) Imp-Ana sheet, and (e) Imp-P25 sheet.

3.2.1.2 Scaning electron microscopy (SEM)

The surface morphology of all Imp-TiO_2 sheets was characterized by scanning electron microscopy (SEM) technique. Figures 39-40 show the SEM micrographs of fresh TiO_2 powders, Imp-TiO_2 sheets, and Imp-TiO_2 cross-section sheets, respectively. It can be seen from Figure 39 that the TiO_2 samples have different morphology and characteristic properties. The microstructures of the impregnated rubber sheets, as revealed in Figures 40 and 41, are a significantly different from each other. It can be seen that the latex in the mixture serves as rubber substrate and adhesively binding of TiO_2 particles to remain on the surface of the dried films. It is noted that the SEM images of Imp-Ana sheet and Imp-K1 sheet show a uniform, small grains with dense structure and well surface coverage more than Imp-K2 and Imp-P25 sheets.

Figure 41 shows SEM cross-section micrographs of Imp-TiO_2 rubber sheets. From these results we can see that most TiO_2 powders gathered at the bottom of petri disk, except the P25 powder that disperses uniformly within the rubber substrate. The case of P25 may be attributed to the light weight and the fluffy-like nature of the P25 TiO_2 powder, making it sinking to the bottom much slower than others. Hence, P25 particles were evenly embedded within the rubber matrix, not at the surface. For K2-doped TiO_2 sample, the particles are more massive and more agglomerated than the others causing it to sink faster to the bottom, so in the cross-section showed good separation between TiO_2 layer and rubber layer as seen in Figure 41b. The order of dense and agglomeration of TiO_2 samples are as follows: K2-doped TiO_2 > K1-doped TiO_2 > anatase TiO_2 > P25 TiO_2. We can conclude that the physical properties of fresh TiO_2 powder, including morphology, particle size, and weight of sample, could affect the morphology and stability of Imp-TiO_2 rubber sheet.

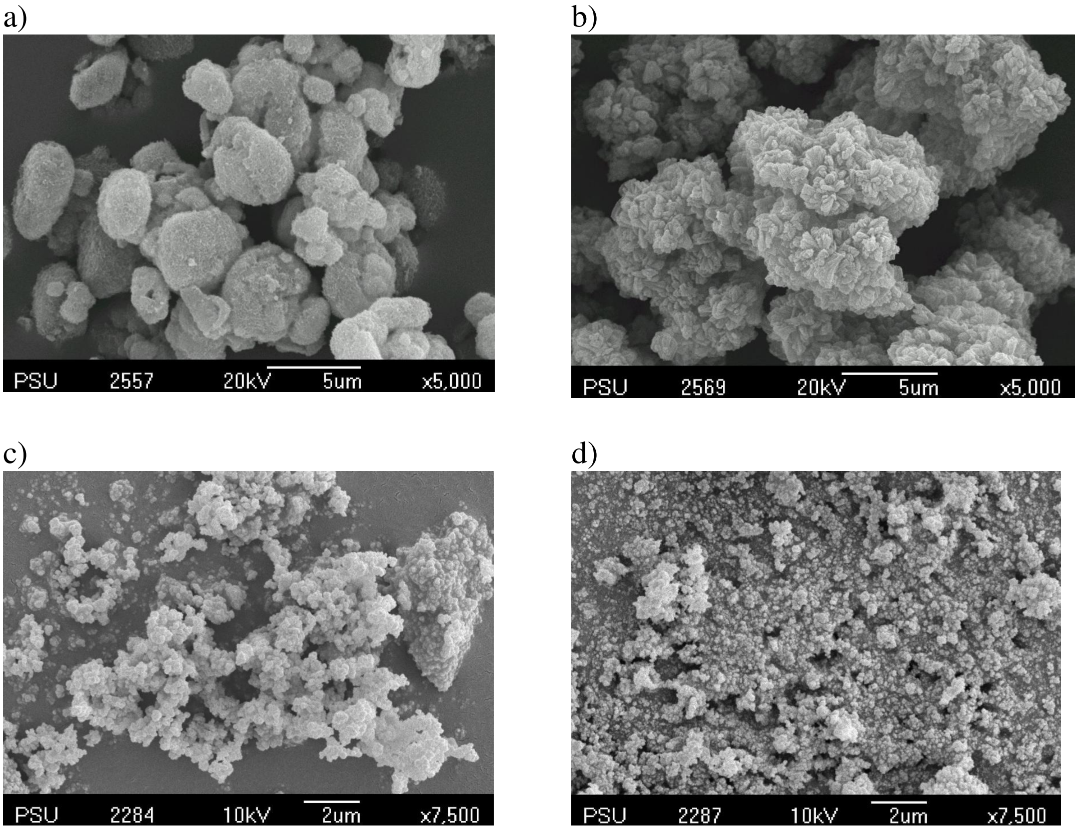

Figure 39. SEM images of TiO_2 powders (a) K1-doped TiO_2, (b) K2-doped TiO_2, (c) Anatase, and (d) P25 Degussa powders.

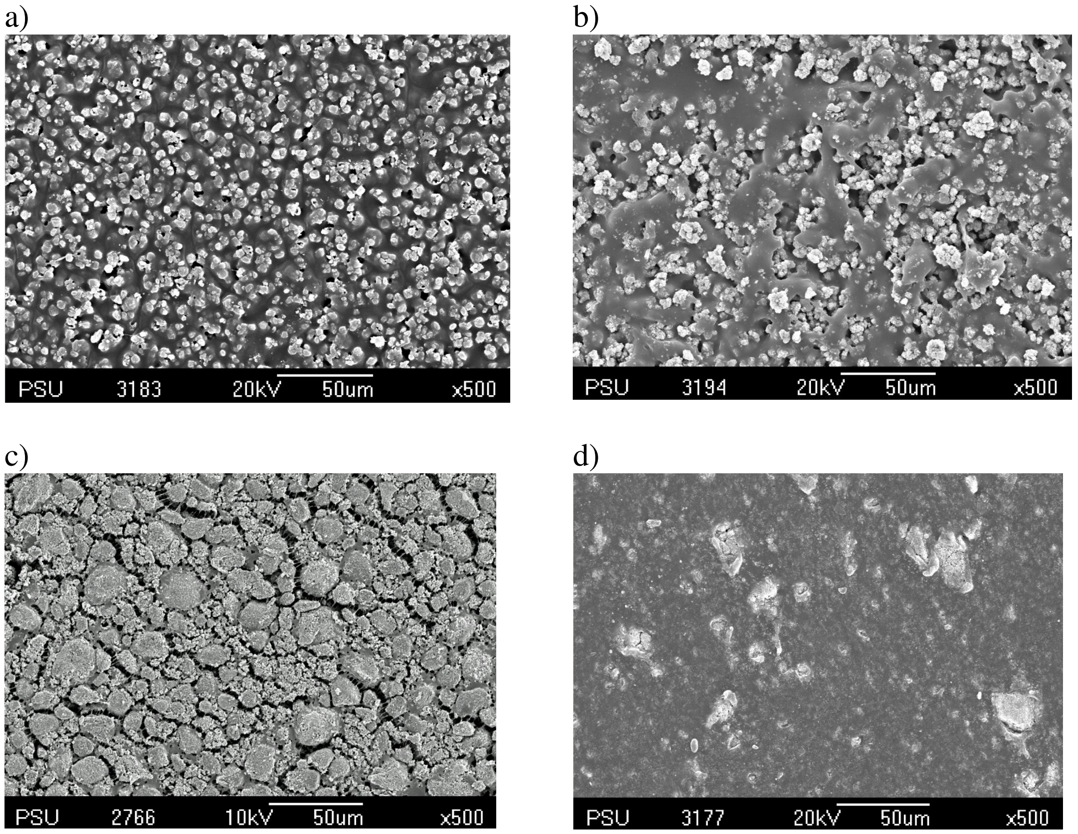

Figure 40. SEM micrographs of Imp-TiO_2 rubber sheets (a) Imp-K1 sheet, (b) Imp-K2 sheet, (c) Imp-Ana sheet, and (d) Imp-P25 sheet.

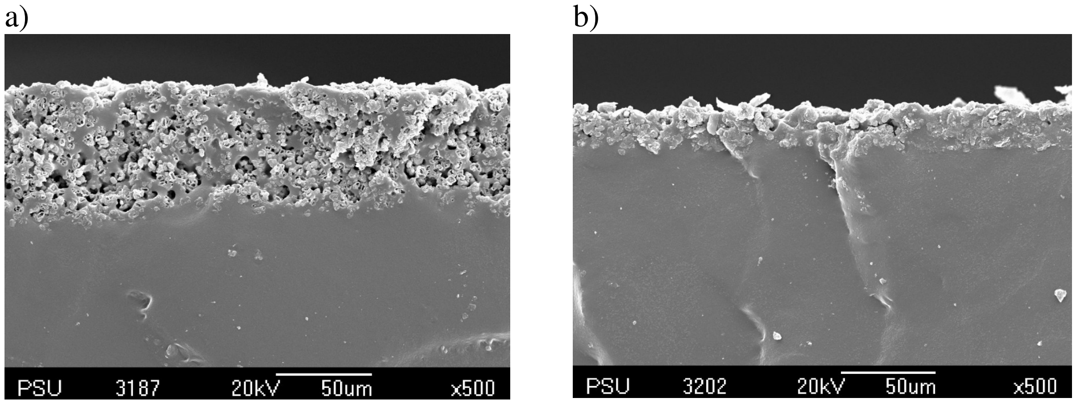

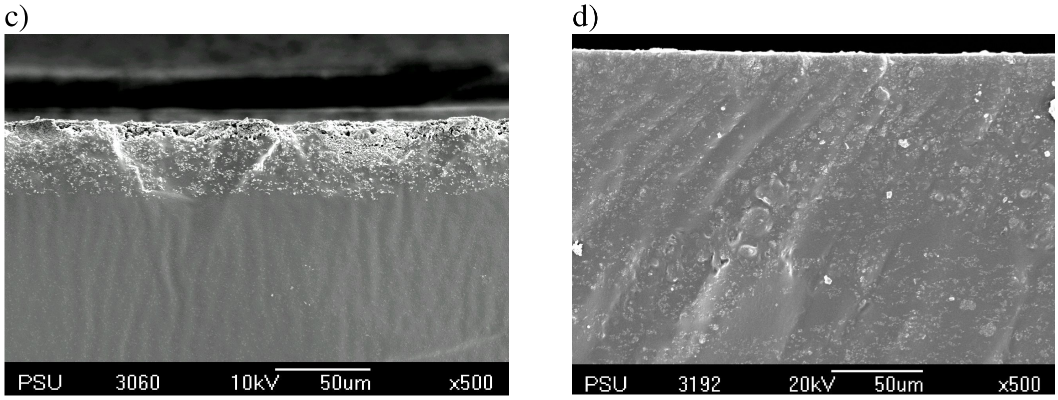
c) d)

Figure 41. SEM cross-section micrographs of Imp-TiO_2 rubber sheets (a) Imp-K1 sheet, (b) Imp-K2 sheet, (c) Imp-Ana sheet, and (d) Imp-P25 sheet.

3.2.1.3 Diffused reflectance UV-vis spectroscopy (DRS)

UV-Vis diffuse reflectance was carried out in order to characterize the band gap energy including nature of electronic transition in materials. The absorption edge in the UV-Vis DRS was used to calculate the band gap energy by the equation (15);

$$E_g = h\frac{c}{\lambda} \qquad (15)$$

where E_g is the band gap energy (eV), h is the Planck's constant, c is the light velocity (m/s), and λ is the wavelength (nm). The calculated band gap energy of the TiO_2 powder samples and Imp-TiO_2 rubber sheets are shown in Table 13.

Table 13. Band gap energy of TiO_2 samples in the forms of powder and Imp-TiO_2 rubber sheets.

Sample	Band gap energy (eV) *Imp-TiO_2 rubber sheet*	Band gap energy (eV) *TiO_2 powders*
P25 TiO_2	3.16	3.03
Ana TiO_2	3.20	3.20
K1-doped TiO_2	3.20	3.22
K2-doped TiO_2	3.18	3.22

a) TiO_2 powder DRS spectra

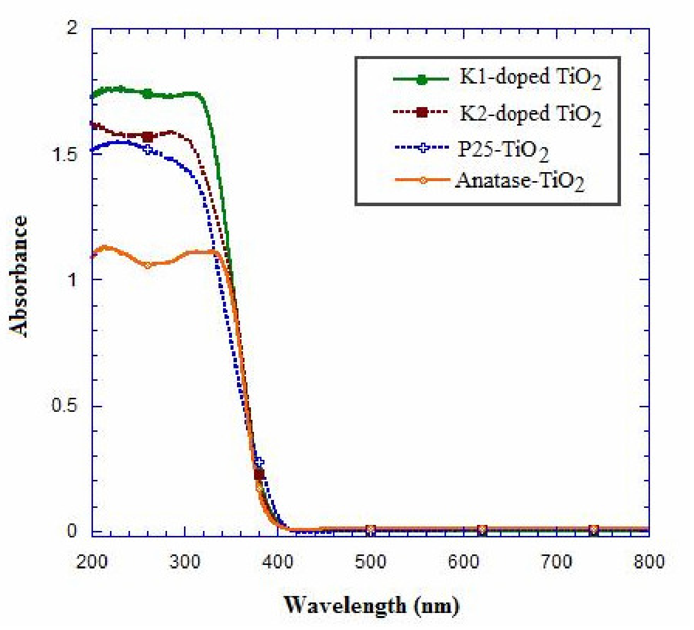

b) Imp-TiO_2 rubber sheet spectra

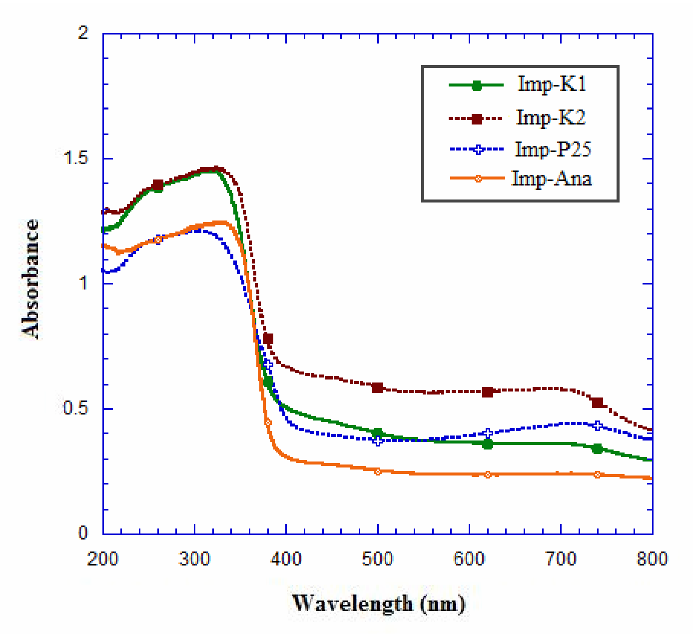

Figure 42. DRS spectra of a) powder TiO_2 and b) Imp-TiO_2 rubber sheets

From the DRS results, the band gap energy of TiO_2 in powder form and in Imp-TiO_2 rubber sheet appeared at the same value. From Figure 42, the DRS spectra of both forms look different in the range 400 to 800 nm as the Imp-TiO_2 rubber sheet shows higher absorption in this region. The absorption in this region could result from the rubber content on the surface of Imp-TiO_2 rubber sheet. In the case of Imp-K2 sheet which shows higher absorption than the other sheets (Figure 42b), indicating that this sheet has more rubber content on the surface in agreement with the SEM and XRD results.

3.2.2 Photocatalytic activity and regeneration studies

3.2.2.1 Photocatalytic activity evalution

Methylene blue (MB) was employed to evaluate the photocatalytic activity of the of Imp-TiO_2 rubber sheets. Two blank experiments were performed, one with only the MB solution, the other with pristine rubber sheet in MB solution, and they showed no significant change in MB solution color (or the absorbances in the spectra). This result confirmed the photocatalytic activity to come from the TiO_2 particles impregnated in the rubber sheets.

The detailed mechanism of the photocatalytic oxidation process has been discussed previously in the literature (Konstantinou, *et al.*, 2004; Houas, *et al.*, 2001; Prevot, *et al.*, 2001; Tanakai, *et al.*, 2000; Saien, *et al.*, 2008; Galindo, *et al.*, 2000; Bandara, *et al.*, 1999; Daneshvar, *et al.*, 2003). Most photocatalytic oxidation processes involve the generation of a very powerful oxidizing agent, the hydroxyl radiacal ($OH^{\bullet}$), which attack and destroy organic pollutants. It is well established that when TiO_2 is illuminated with the light having $\lambda < 390$ nm, electrons are promoted from the valence band to the conduction band of the TiO_2 to give electron-hole pairs. The valence band (h^+_{VB}) potential is positive enough to generate hydroxyl radicals at the surface and the conduction band (e^-_{CB}) is negative enough to reduce the oxygen molecules, present in the solution. The generated hydroxyl radicals are present at the surface of TiO_2 or near it (within 0-500 μm). The resulting $^{\bullet}OH$ radical can oxidize most of azo dye to the mineral end-products. According to this, the relevant reactions at the semiconductor surface causing the degradation of methylene blue can be expresses as follows:

$$TiO_2 + h\nu \longrightarrow TiO_2\,(e^-_{CB} + h^+_{VB}) \qquad (37)$$

$$h^+_{VB} + e^-_{CB} \longrightarrow \text{heat (recombination)} \qquad (38)$$

$$h^+_{VB} + H_2O_{(ads)} \longrightarrow H^+ + {}^{\bullet}OH_{(ads)} \qquad (39)$$

$$h^+_{VB} + OH^-_{(ads)} \longrightarrow {}^{\bullet}OH_{(ads)} \qquad (40)$$

$$e^-_{CB} + O_{2(ads)} \longrightarrow O_2^- \qquad (41)$$

$$O_2^- + H^+ \longrightarrow HO_2 \qquad (42)$$

$$HO_2 + HO_2 \longrightarrow H_2O_2 + O_2 \qquad (43)$$

$$H_2O_2 + h\nu \longrightarrow 2{}^{\bullet}OH \qquad (44)$$

$$H_2O_2 + e^-_{CB} \longrightarrow OH^- + {}^{\bullet}OH \quad (45)$$

$$^{\bullet}OH + \text{dye} \longrightarrow \text{degradation of dye} \quad (46)$$

$$h^+_{VB} + \text{dye} \longrightarrow \text{oxidation of dye} \quad (47)$$

Figure 43 shows the photocatalytic efficiencies of Imp-TiO_2 rubber sheets. The Imp-K1 sheet performed the highest efficiency for decolorization of methylene blue solution. It is not surprising that the Imp-K1 sheet showed higher efficiency than Imp-K2, due to the highly uniform TiO_2 particle distributed on the surface of Imp-TiO_2 rubber sheet including the particularly high surface area of the K1-doped TiO_2 sample. Therefore, the fresh Imp-K1 sheet has better photocatalytic properties than Imp-K2 sheet.

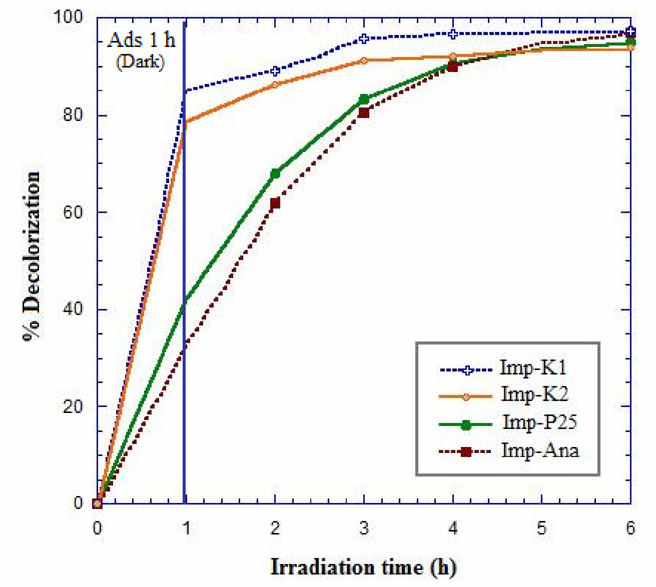

Figure 43. The decolorization of Imp-TiO_2 rubber sheets (including adsorption).

3.2.2.2 Kinetics study

The photocatalytic oxidation kinetics of many organic compounds have often been modeled with the Langmuir-Hinshelwood equation (Houas, *et al.*, 2001; Prevot, *et al.*, 2001; Tanakai, *et al.*, 2000**;** Ibhadon, *et al.*, 2008; Chiou, *et al.*, 2008], which also covers the adsorption properties of the substrate on the photocatalyst surface. The modified L-H equation, where the reaction rate, r, is proportional to the surface coverage, θ, is given by:

$$r = -\frac{dC}{dt} = k_r\theta = \frac{k_r KC}{1+KC} \tag{48}$$

where k_r is the reaction rate constant, K is the adsorption coefficient of the reactant, and C is the reactant concentration at any time, *t*. When C is very small, KC is negligible with respect to unity and Eq. (48) describes a first order kinetics. The integration of Eq. (48) with the limit condition that at the start of radiation, *t*=0, the concentration is the initial one, C=C_0, yields Eq. (49):

$$-\ln\left(\frac{C}{C_0}\right) = k_r Kt = k_{app}t \tag{49}$$

$$\ln\left(\frac{C_0}{C}\right) = k_{app}t \tag{50}$$

where k_{app} = k_rK, k_{app} is the apparent first order rate constant. A plot of ln (C_0/C) versus time represents a straight line, the slope of which upon linear regression equals the apparent first-order rate constant k_{app}.

In this work, the plots of ln (C_0/C) versus time (Figure 44) yielded straight lines for all the materials, indicating that the degradation of methylene blue by these samples are of first order process. The rate constant values resulting from the application of Eq. (50) are summarized in Table 14 for Imp-TiO_2 rubber sheets.

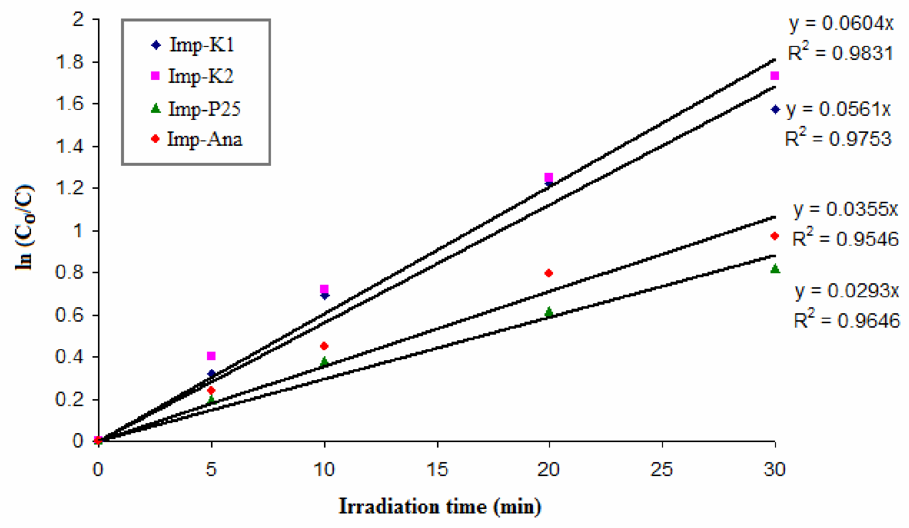

Figure 44. The kinetics plot of methylene blue using Imp-TiO_2 rubber sheets.

Table 14. The rate constant values of Imp-TiO_2 rubber sheets toward MB degradation.

Imp-TiO_2 rubber sheets	k_{app} (min^{-1})	R^2
Imp-K1	5.61×10^{-2}	0.9753
Imp-K2	6.04×10^{-2}	0.9831
Imp-P25	2.93×10^{-2}	0.9546
Imp-Ana	3.55×10^{-2}	0.9646

3.2.2.3 Effect of pH

As the charge of the MB molecules and the surface of the TiO_2 photocatalyst are both pH-dependent, so we studied the influence of pH on the degradation of dye in the range from 3 to 8 including the natural pH of MB solution at 6.8. The pH was adjusted by adding aqueous solution of either HCl or NaOH, respectively. Figure 45 shows the effect of pH on the adsorption of dye on the surface of TiO_2 catalyst and the photodegradation of dye in an aqueous TiO_2 suspension. It is well known that pH would influence both the surface state of titania and the ionization state of ionizable dye molecules. The point of zero charge (pzc) of the TiO_2 (Degussa P25) is at 6.8 (Konstantinou, *et al.*, 2004). Thus, the TiO_2 surface is positively charged in acidic media (pH<6.8), whereas it is negatively charged under alkaline condition (pH>6.8), according to the following reactions (Wen, *et al.*, 2005):

$$\text{pH} < \text{pzc:}\quad \text{Ti-OH} + H^+ \rightarrow TiOH_2^+ \qquad (51)$$

$$\text{pH} > \text{pzc:}\quad \text{Ti-OH} + OH^- \rightarrow TiO^- + H_2O \qquad (52)$$

Since the parent fragment of MB bears positive charge, the adsorption on a positively charged surface of TiO_2 is favored at high pH. Increasing the pH caused the surface of TiO_2 becoming less positive or even turned to negative once the pH exceeded pzc. Hence, we expect the repulsive force to operate stronger at low pH, therefore, less adsorption of dye onto the TiO_2 surface. This fact is borne out as the adsorption trend from pH 3 to 8 of Imp-TiO_2 rubber sheets gradually increased in adsorption capacity as shown in Fig 45a. For the decolorization results (Figure 45b) also showed gradually increased in decolorization when increased pH values, due to high concentration of $^{\bullet}$OH radical, hence, the high decolorization efficiencies. So, the order trend of decolorization of all Imp-TiO_2 rubber sheets is pH 8 > pH 6.8 > pH 3.

a) Adsorption

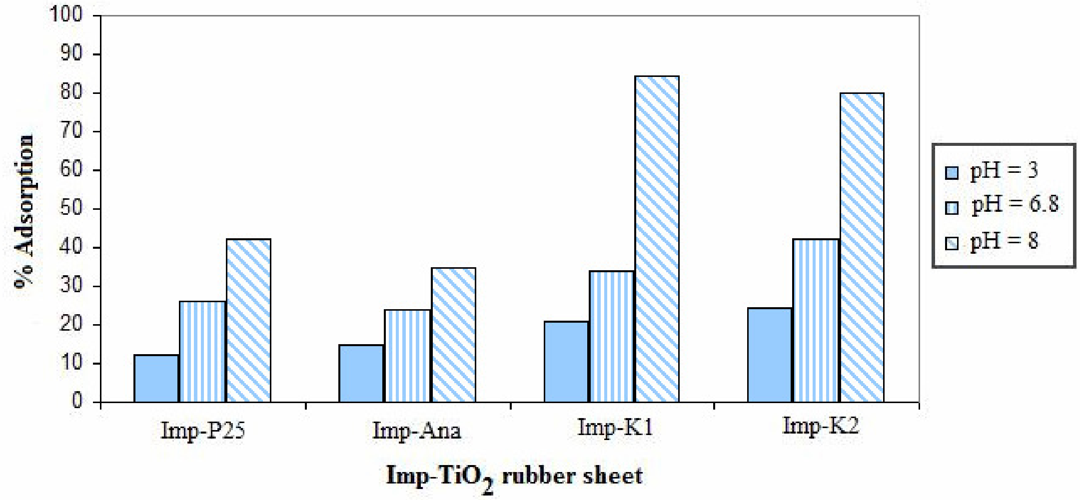

b) Decolorization

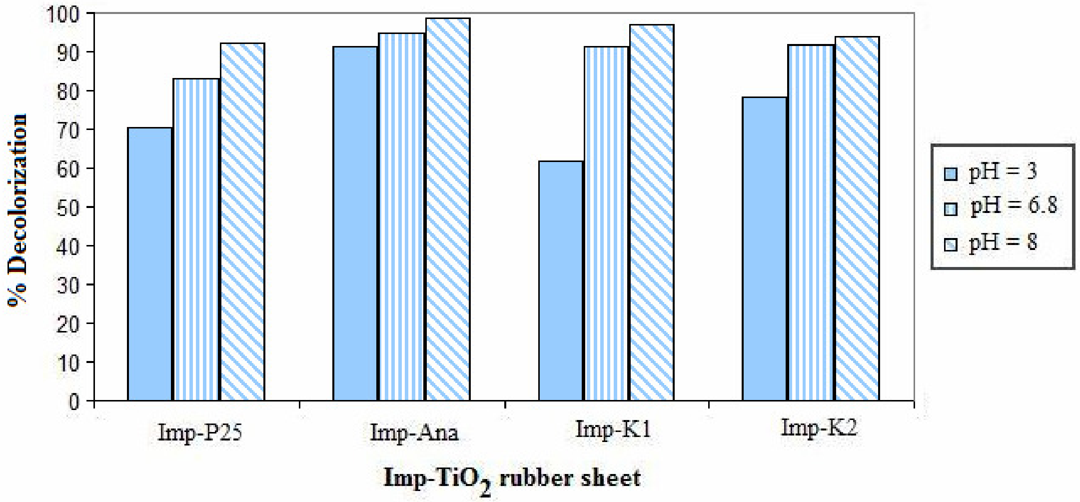

Figure 45. Effect of pH on a) adsoption of MB on the photocatalyst surface and b) the photocatalytic decomposition of MB. (Condition: Imp-TiO_2 sheet, 50 mL MB solution under adsorption in the dark 1 h (a) and under UV irradiation of 5 h. (b)).

3.2.2.4 Reclycle test

To determine the reclyclability of the prepared rubber sheets, all Imp-TiO_2 rubber sheets were used for several photocatalytic runs. After the first photocatalytic reaction, the rubber sheet was separated and used for further runs without any treatment. The results in Figure 46 show that the activity of Imp-commercial TiO_2 rubber sheets decreased greatly and significant deactivation occurred after four runs. On the other hand, the activity of Imp-synthesized TiO_2 rubbber sheets only slightly decreased and still achieved good performance after four runs; thus, Imp-K2 retained its activity with almost no deactivation occurred.

Comparing between Imp-K2 and Imp-K1 sheet, for the freshly prepared Imp-TiO_2 rubber sheet that was used for the first time Imp-K1 showed higher photocatalytic efficiency than Imp-K2 sheet, as shown in Figure 46. However the reclycle study revealed that Imp-K2 showed higher efficiencies than Imp-K1 in the repeated photocatalytic runs. These results might be the high adsorptivity of the Imp- K1 sheet where more methylene blue molecules were attracted to remain on the surface of Imp-K1 sheet as shown in Fig 47a. Figure 47 showed the photographs of the 4th recycled use of all the Imp-TiO_2 rubber sheets (without cleaning).

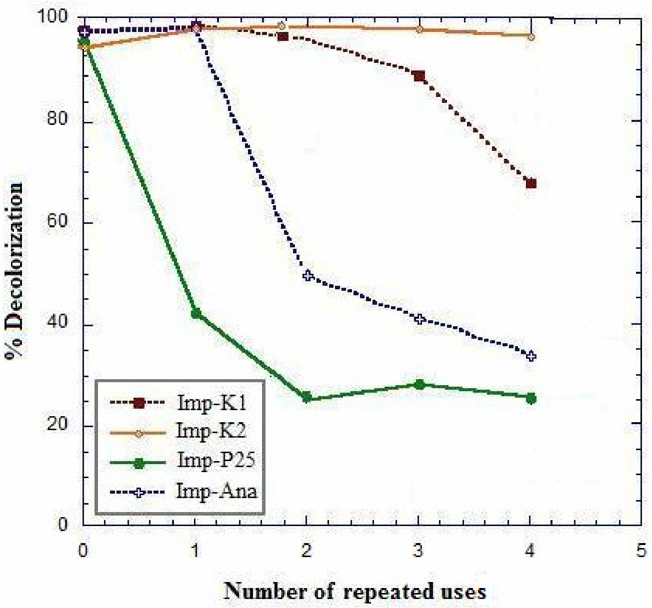

Figure 46. The efficiencies of MB degradation by Imp-TiO_2 rubber sheets the repeated used with no cleaning (including adsorption).

a) Imp-K1 	b) Imp-K2 
c) Imp-Ana 	d) Imp-P25 

Figure 47. The photographs of the 4th recycled use of Imp-TiO_2 rubber sheets(without cleaning): (a) Imp-K1 sheet, (b) Imp-K2 sheet, (c) Imp-Ana sheet, and (d) Imp-P25 sheet.

3.2.2.5 Regeneration process of the TiO_2-impregnated rubber sheets

After decolorization experiments, the Imp-TiO_2 rubber sheets were covered with dye molecules due to the high adsorption power. The clean surface, however, could be regenerated for further uses. The regeneration was successfully done by treating the used rubber sheet in 50 mL of H_2O_2 solution (0.2 M) with stirring overnight under UV light irradiation. The regenerated Imp-TiO_2 sheets were yellownish instead of being “snow” white as freshly prepared for Imp-commercial TiO_2 sheet and being pale yellow for the Imp-synthesized TiO_2 sheets. The performances of the two regenerated Imp-TiO_2 sheets were compared to the freshly prepared Imp-TiO_2 sheets as shown in Figure 48. It can be seen that the sheets regenerated with H_2O_2 showed higher decolorization ability than the freshly prepared TiO_2 rubber sheet.

a1) Used Imp-Ana b1) Regenerated Imp-Ana

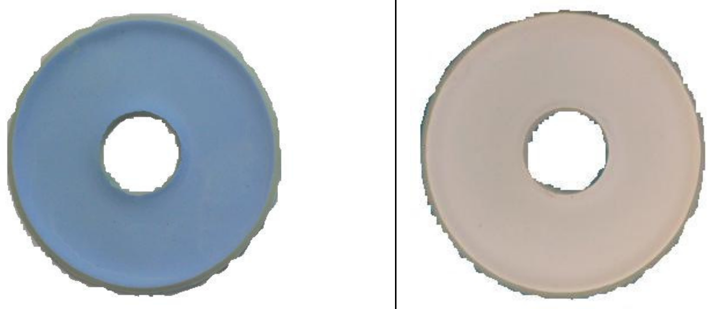

a2) Used Imp-K2 b2) Regenerated Imp-K2

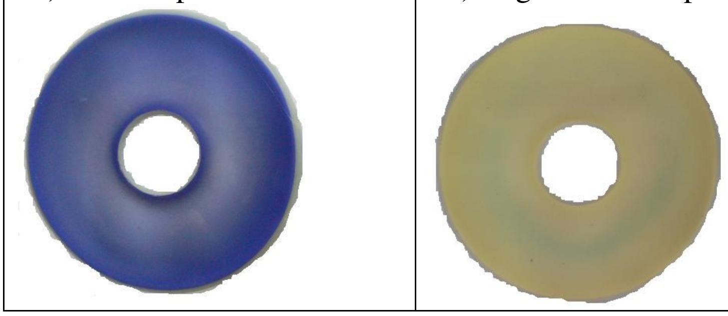

Figure 48. The photographs of Imp-TiO_2 rubber sheets: (a) used Imp-TiO_2 rubber sheets (before treated with H_2O_2) (b) regenerated Imp-TiO_2 rubber sheets (after treated with H_2O_2).

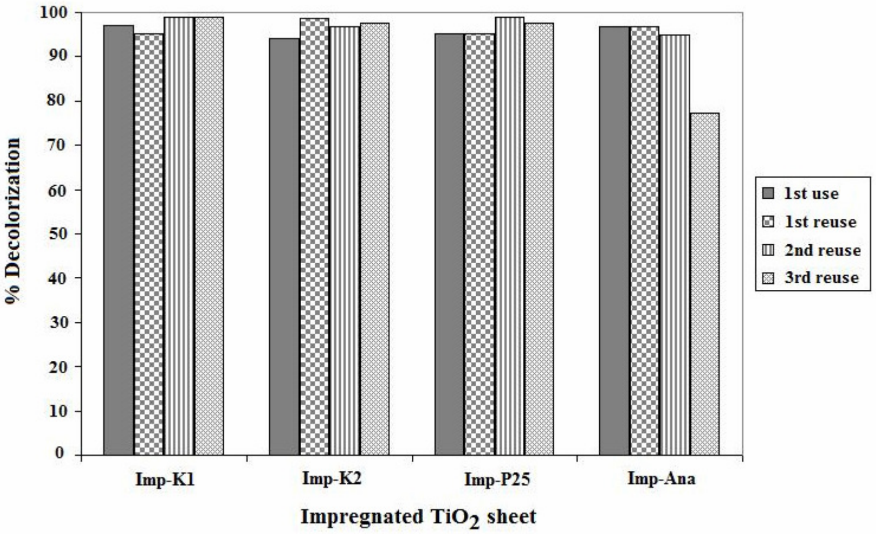

Figure 49. The efficiencies of MB degradation by the regenerated Imp-TiO_2 rubber sheets in the repeated uses (including adsorption).

In the regeneration process, the presence of both H_2O_2 and UV light were necessary as increasing of the reactive $^{\bullet}OH$ radical in the regeneration setup. It appears that H_2O_2 played the major role to destroy the dye molecules previously adsorbed at the TiO_2 surface. This resulted from the increasing in concentration of the $^{\bullet}OH$ radical according to the following equations (Suwanchawalit and Wongnawa, 2008).

$$H_2O_2 \rightarrow 2\,^{\bullet}OH \tag{53}$$

$$H_2O_2 + e^- \rightarrow OH^- + {}^{\bullet}OH \tag{54}$$

$$H_2O_2 + O_2^{\bullet -} \rightarrow OH^- + {}^{\bullet}OH + O_2 \tag{55}$$

Eq (53) represents the homolytic cleavage of H_2O_2 by light while eqs. (54)-(55) are associated with the photocatalytic reaction of TiO_2. Among equations (54) and (55), the main source of $^{\bullet}OH$ comes from eq. (54) where H_2O_2 is reduced by the conduction band electron. The production of $^{\bullet}OH$ from eq. (55) is negligible due to only small amount of $O_2^{\bullet -}$ anion was produced (Baiju, *et al.*, 2007).

3.3 Preparation of Chitosan/TiO_2 scaffolds

Porous materials are attracting much attention as a new class of materials with wide range of application such as high-performance adsorbents, lightweight materials, thermal, acoustic, and electrical insulators in the field of catalysis, photonics, chromatography, and large molecule separation processes (Dabrowski, 2001; Cooper, 2003; Nishihara, *et al.*, 2005). Typically they are formed into shapes such as powders, colloidal spheres, membranes, fibers, honeycomes, monoliths, and so on. Recently, a new class of shape, macroporous monoliths, has drawn attention. Macroporous monoliths with micro/mesopores inside their framework are practical materials with hierarchical pore systems. (Zhang, *et al.*, 2002; Nishihara, *et al.*, 2005; Nishihara, *et al.*, 2006; Deville, *et al.*, 2006; Guitierrez, *et al.*, 2006; Guitierrez, *et al.*, 2007). In such materials, the macropores promote mass transfer and reduce the pressure drop inside the monoliths, and micro/mesopores supply large surface area where reaction or adsorption can occur. Therefore, macroporous monoliths can be used as catalyst supports and adsorbents in applications where high throughput is required.

Macroporous monolith can be prepared through a template synthesis method. First, a template with a desired structure is prepared, and then the skeletal material is formed around the template. Next, the template is removed by physical and/or chemical treatment. Typical templates are phase-separated polymer (Smatt, *et al.*, 2003), colloidal crystals (Velev, *et al.*, 2000), surfactant micelles (Zarur, *et al.*, 2000). The voids which are formed after the removal of the template become the macropores.

Recently, the ice-templating method using ice crystal as the template has attracted considerable attention. Ice crystals have many advantages when used as a template, i.e. they are extremely inexpensive, easy to be removed and allow the production of highly pure materials (Mukai, *et al.*, 2006; Deville, *et al.*, 2007; Zhang, *et al.*, 2007; Gutierrez, *et al.*, 2008). This method is highly biocompatible, economical and environmentally friendly and can produce highly pure materials with interconnected macropores and unique macroporous structure. The ice-templating process involves the submission of an aqueous gel to liquid-nitrogen temperatures. The rapid ice formation (hexagonal form) causes every solute originally dispersed in the aqueous gel to be segregated from the ice phase, giving rise to a hierarchical assembly characterized by fences of matter enclosing empty areas where the ice originally resided (Mukai, *et al.*, 2006; Deville, *et al.*, 2007; Zhang, *et al.*, 2007; Gutierrez, *et al.*, 2008). The ice formation during freezing casting in ice-templating process is shown in Figure 50. The macroporous scaffold obtained after subsequent drying by freeze-drying shows a macroporosity that corresponds to the empty areas where ice crystals originally resided.

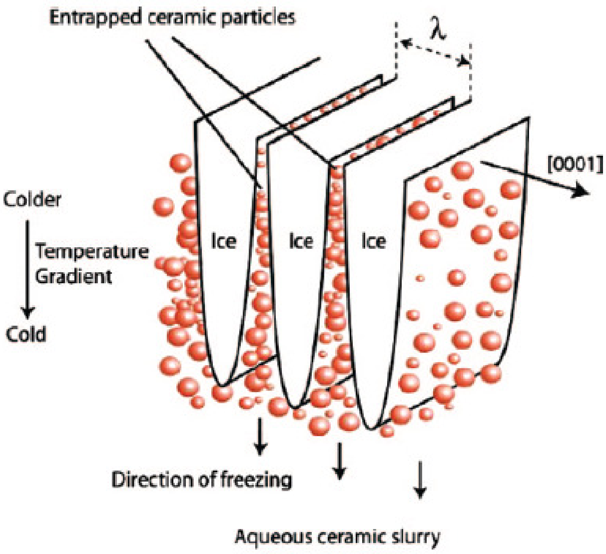

Figure 50. Pattern formation and particle segregation during freeze-casting of ceramic slurries. The ice platelets grow in a direction perpendicular to the *c*-axis of hexagonal ice. The interlamellar separation of the structure is represented by λ. (Deville, *et al.*, 2007; Gutiérrez, *et al.*, 2008).

In this work, we used the ice-template method for the preparation of macroporous crosslinked-chitosan/TiO_2 scaffolds (CS/TiO_2). Herein, we used three types of TiO_2; as-synthesized TiO_2 (Dialyzed-TiO_2), KOX-TiO_2, and commercial P25-TiO_2 as TiO_2 sources to produce macroporous structures and test for photocatalytic decomposition of dye molecules. To achieve the resulting porous materials, the ratio of TiO_2 sol/chitosan gel, freezing rate, and size of syringe are studied. The possible mechanisms for the photodecomposition of dye molecule using CS/TiO_2 scaffolds are also discussed.

3.3.1 Characterization of the starting TiO_2 materials

The X-ray diffraction spectra of the synthesized KOX-doped TiO_2, the dialyzed-TiO_2, and the commercial Degussa P25-TiO_2 samples are illustrated in Figure51. The diffraction peaks for the anatase and rutile phases are marked with ‘A’ and ‘R’, respectively. The phase structure of the synthesized TiO_2 samples showed anatase phase for the two synthesized TiO_2 samples, while the commercial TiO_2 samples showed mixed phase of anatase and rutile phase. The average crystallite sizes of TiO_2 samples calculated using Scherrer formula are shown in Table 15.

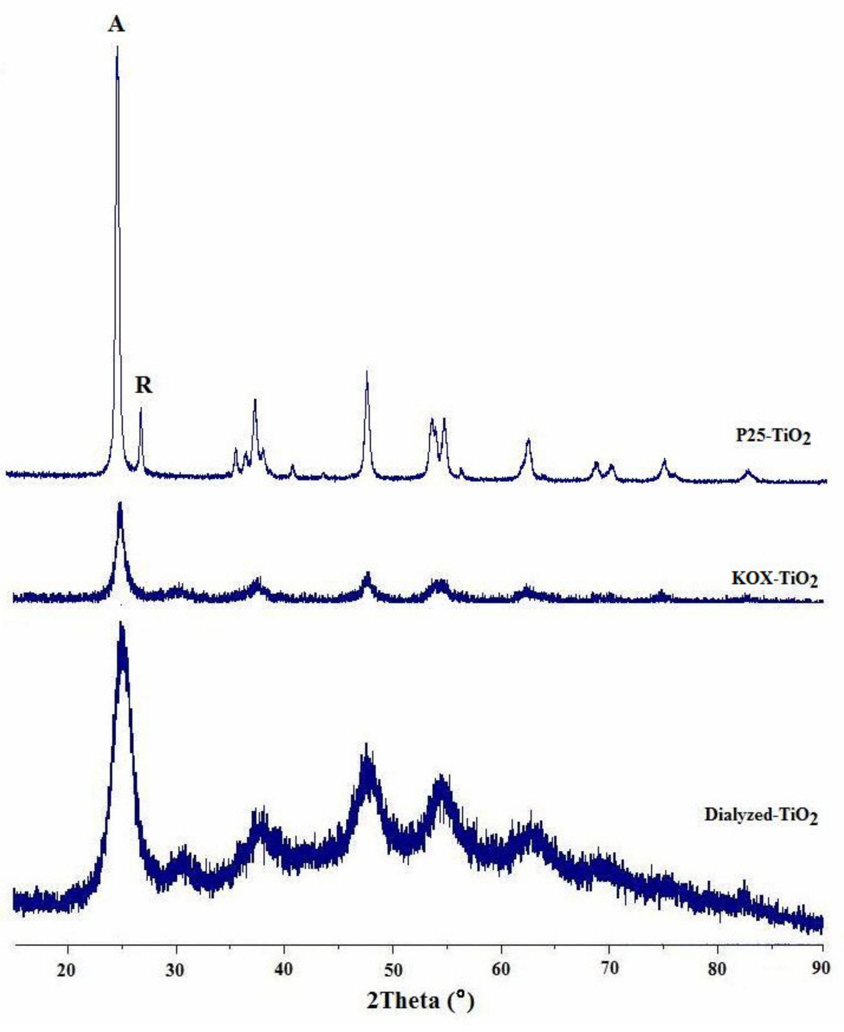

Figure 51. XRD patterns of TiO_2 samples.

Table 15. The average crystallite size of TiO_2 samples.

TiO_2 sample	Crystallite size (nm)	
	Anatase	Rutile
P25-TiO_2	24	33
KOX-TiO_2	27	-
Dialyzed-TiO_2	12	-

The morphologies of all samples were investigated using SEM and TEM techniques. The SEM and TEM images of TiO_2 powders of KOX-TiO_2, Degussa P25-TiO_2, and dialyzed-TiO_2 sol are shown in Figures 52 and 53. TEM results revealed that the particle sizes, calculated using SIS analysis software, of dialyzed-TiO_2, P25-TiO_2, and KOX-TiO_2 sample were approximately 6, 27, 11 nm, respectively. In case of KOX-TiO_2, it showed large particle which consisted of small crystallites as shown in Figures 53b) and 53c).

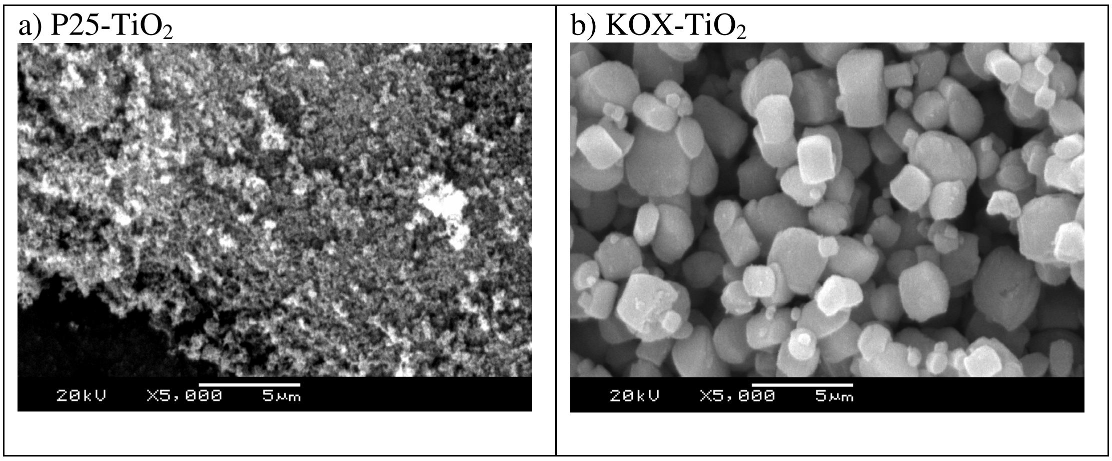
a) P25-TiO_2

b) KOX-TiO_2

Figure 52. SEM images of the TiO_2 powders

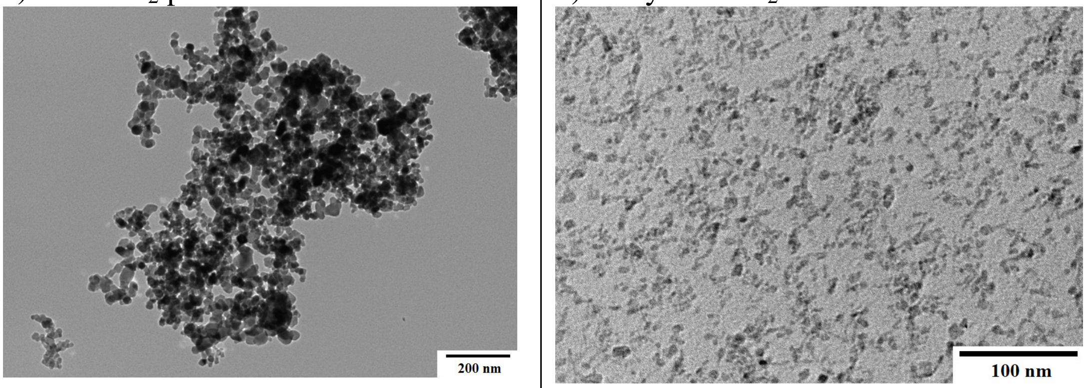

a) P25-TiO_2 powders

b) Dialyzed-TiO_2 sol

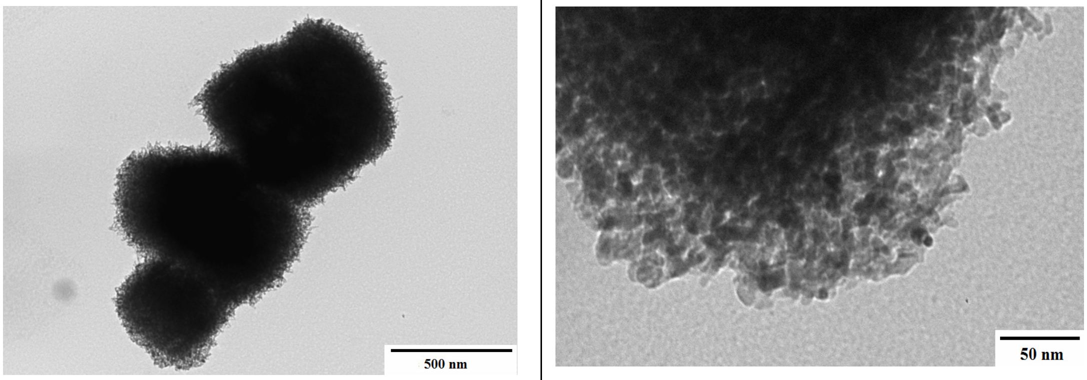

c) KOX-TiO_2 powders

d) KOX-TiO_2 powders (high magnification)

Figure 53. TEM images of the TiO_2 samples.

3.3.2 Characterization of the CS/TiO_2 scaffolds

In this "ice-templating" method, template ice spheres are formed *in situ* and can be easily removed simply through thawing and drying. Needing neither a special template material nor a special removal process of the template, this ice-templating method is inexpensive and environmentally friendly and can produce highly pure materials with interconnected spherical macropores. From these excellent advantages, this method can be used to produce highly pure micro-/mesoporous materials and is popularly used to prepare scaffold materials in tissue engineering. However, as the size of the template, ice spheres, is determined by freezing conditions, such as immersion rate into a cold bath and freezing temperature, and it is impossible to adjust such conditions to be completely uniform throughout the whole sample at the freezing stage, it is difficult to produce well-ordered macropores by using this ice-templating method (Nishihara, *et al*., 2005). The ordered macroporous solids could be prepared by combining pseudo-steady state ice growth which occurs during unidirectional freeze-gelation with a pore-protecting drying method, freeze drying. Freeze-drying is the process whereby water or another solvent is removed from a frozen product by sublimation. Sublimation occurs when a frozen solvent goes directly to the gaseous phase without passing through the liquid phase. As the ice sublimates, it leaves voids in the dry residual material making it easy to re-hydrate (Velardi, *et al*., 2008). Further, the brittleness of porous materials and their tendency to form debris can be reduced by adding a polymer. Chitosan is a biodegradable and nontoxic copolymer. It has a highly reactive amino group and has been regarded as a useful material for various purposes (Liu, *et al*., 2004). However, the poor solubility of chitosan indeed limits its application and processing convenience. Considerable efforts have been done on developing a water-soluble chitosan to improve this drawback. Oneway to overcome this limitation is chemical crosslinking. Since the frequently used crosslinking reagents such as glutaraldehyde (Jameela, *et al*., 1995), epichlorohydrin (Tan, *et al*., 2001), and sulfuric acid (Mukoma, *et al*., 2004), suffer from the drawback of inherent toxic, erosive characteristics, 3-glycidoxypropyltrimethoxysilane (GPTMS), one of the silane-coupling agents with an epoxy group and three methoxysilane groups, may be chosen as a novel and efficient candidate (Liu, *et al.*, 2004; Liu, *et al.*, 2005; Shirosaki, *et al.*, 2005; Jiang, *et al.*, 2006; Chao, 2008). In this work, we choose 3-glycidoxypropyltrimethoxysilane (GPTMS) as crosslinking reagent with chitosan. The structure of chitosan and the crosslinking reagent were shown in Figure 54. Herein, we proposed the mechanism for the formation of CS/TiO_2 scaffold as shown in Figure 55.

a) Chitosan

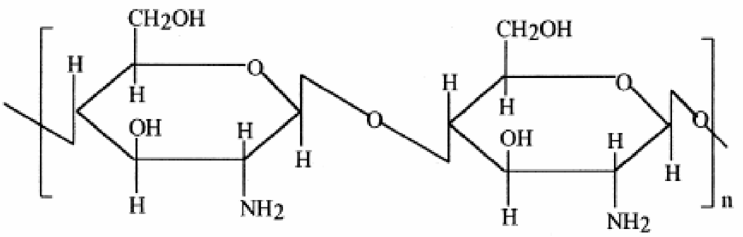

B) 3-glycidoxypropyltrimethoxysilane (GPTMS)

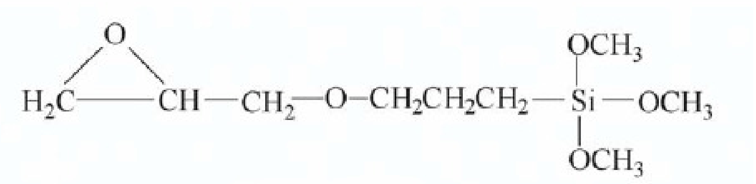

Figure 54. Structure of a) chitosan and b) 3-glycidoxypropyltrimethoxysilane (GPTMS) (Liu, *et al.*, 2004).

In this study, we investigated the ratio of TiO_2 sol/chitosan gel, freezing rate, and size of syringe to produce ordered porous structure materials. These investigations affect the structure and their photocatalytic activity. The CS-TiO_2 scaffolds were cut into pieces before measuring the morphology by SEM and using as the photocatalyst as shown in Figure 56. The effects of the ratio of TiO_2 sol/chitosan gel, freezing rate, and size of syringe on the structure of the scaffolds (vertical section) are shown in Figures 57-59, respectively. All parameters were studied using dialyzed-TiO_2 to obtain the optimum condition, and prepared the others TiO_2 samples.

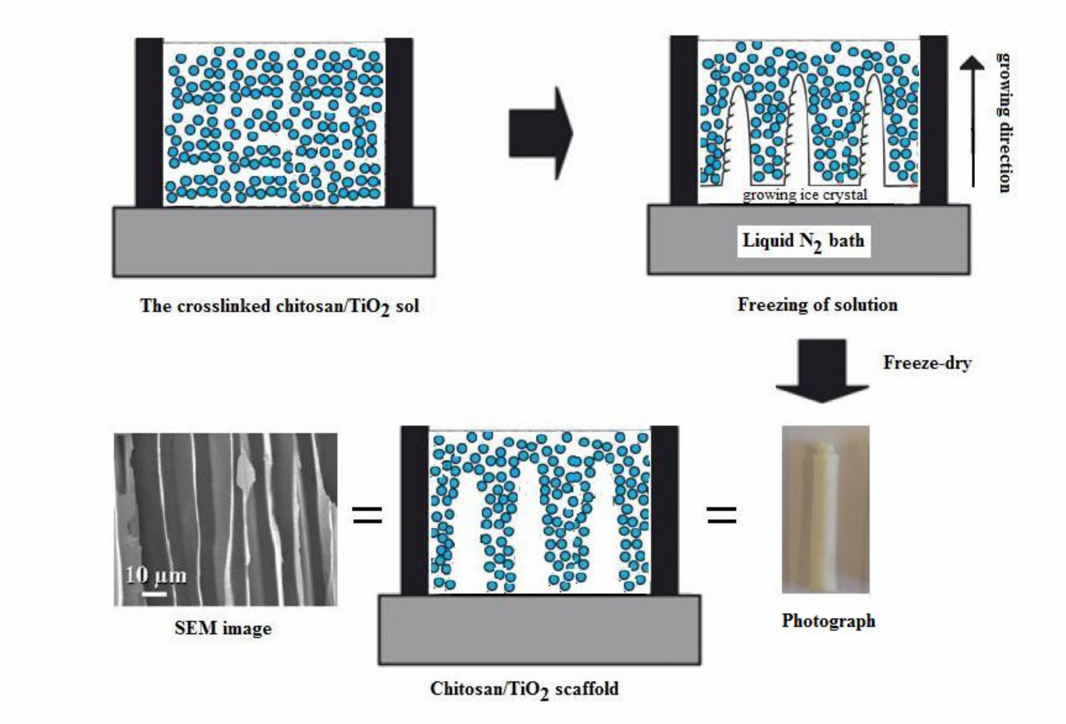

Figure 55. Mechanism for the formation of crosslinked chitosan/TiO_2 scaffold. (Adapted from S. Deville, *et al*., 2006; N. Thongprachan, *et al*., 2008) (Deville, *et al*., 2006; Thongprachan, *et al*., 2008).

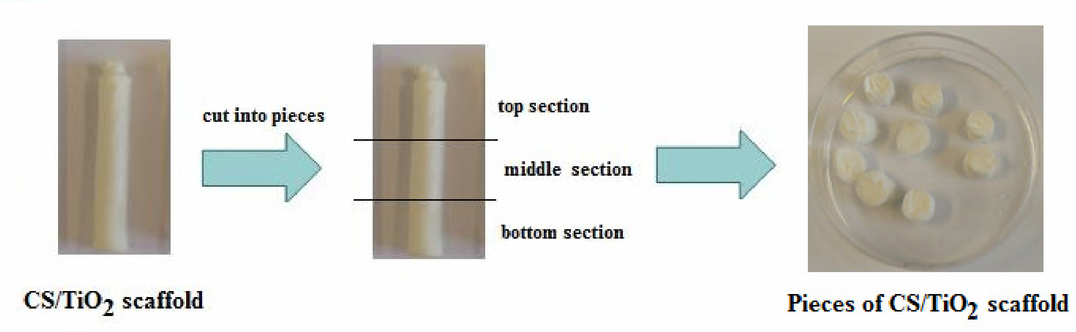

Figure 56. The cut of crosslinked chitosan/TiO_2 scaffold into pieces.

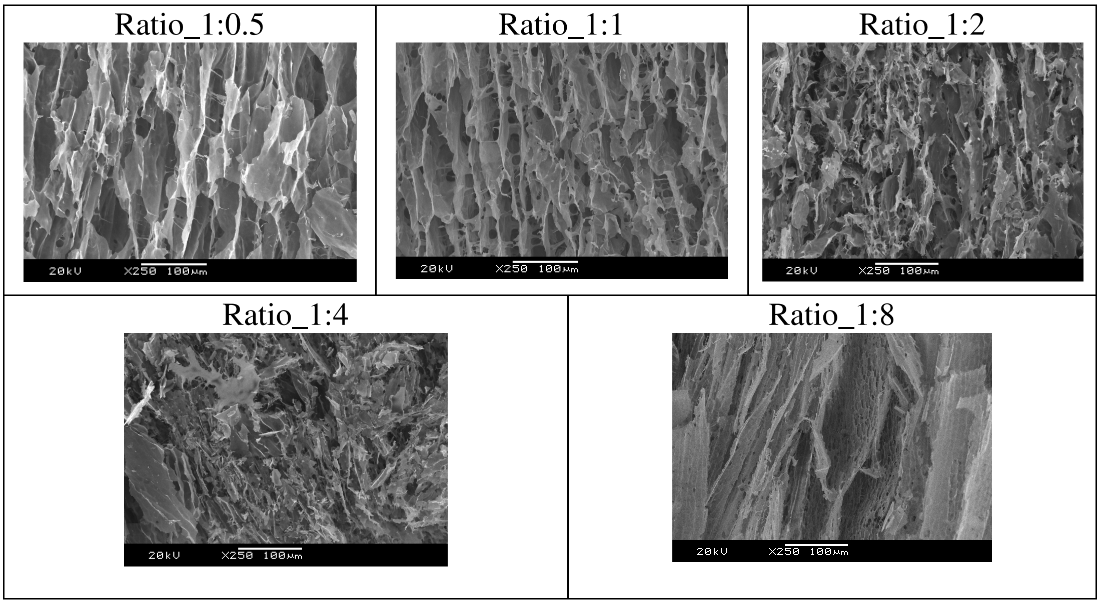

Ratio_1:0.5

Ratio_1:1

Ratio_1:2

Ratio_1:4

Ratio_1:8

Figure 57. SEM images of CS/Dialyzed-TiO_2 samples (middle and long section) showing effect of varying ratio of the TiO_2 sol/chitosan gel.

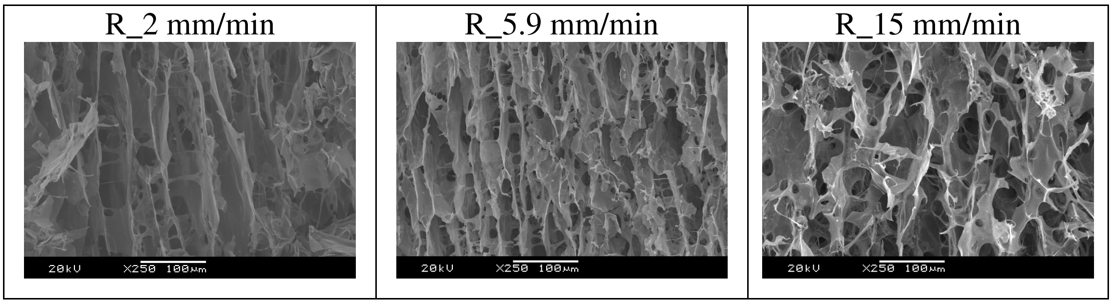

R_2 mm/min

R_5.9 mm/min

R_15 mm/min

Figure 58. SEM images of CS/Dialyzed-TiO_2 samples (middle and long section) showing effect of freezing rate.

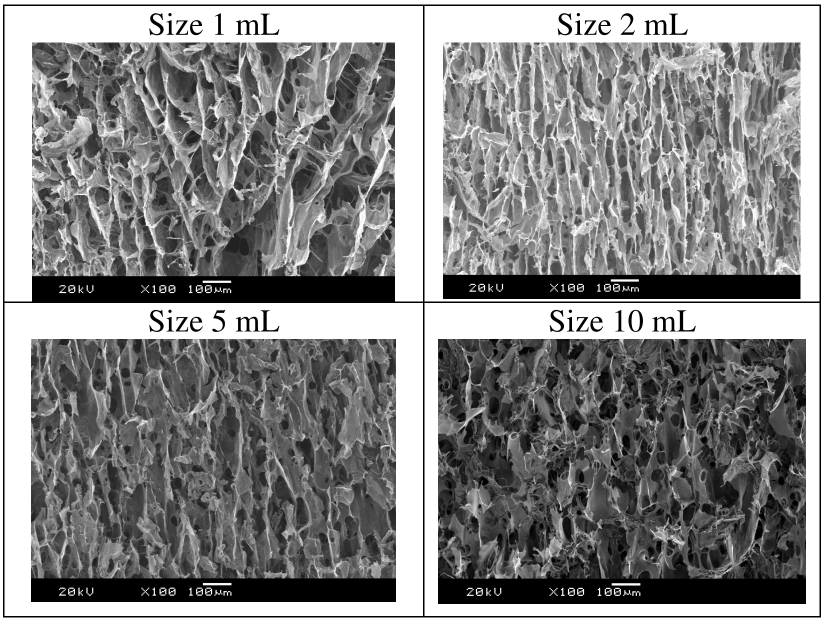

Size 1 mL

Size 2 mL

Size 5 mL

Size 10 mL

Figure 59. SEM images of CS/Dialyzed-TiO_2 samples (middle and long section) showing effect of size of syringe (volume of syringe size): 1 mL, 2 mL, 5 mL, 10 mL (syringe diameter are 0.5, 0.8, 1.2, 1.5 cm).

The SEM results on the ratio of TiO_2 sol/chitosan gel at 1: 1 ratio showed highly ordered porous structure than the other ratios. For the freezing rate and size of syringe studied, the rate 5.9 mm/min and size 2 mL produced uniform macropore structure. Therefore, we chose this condition to obtain the ordered structure as shown in Figures 60 on the cross-section and vertical section, respectively. Figure 61 showed the structure on the high magnification. The results showed that the dialyzed-TiO_2 sol mixed well with chitosan gel giving TiO_2 on the wall of the scaffold, P25-TiO_2 powders coated on the wall of monoliths, and the K-TiO_2 powders embeded on the wall of the scaffold.

a) GPTMS/CS scaffold

Cross section	Vertical section
Bottom 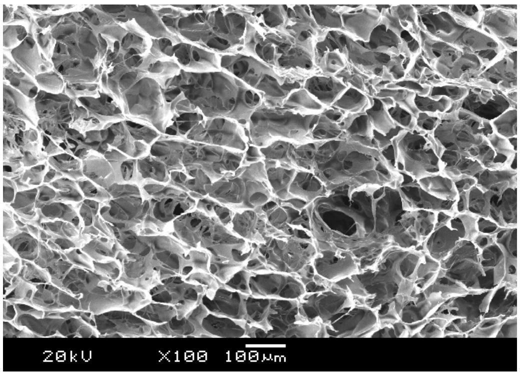	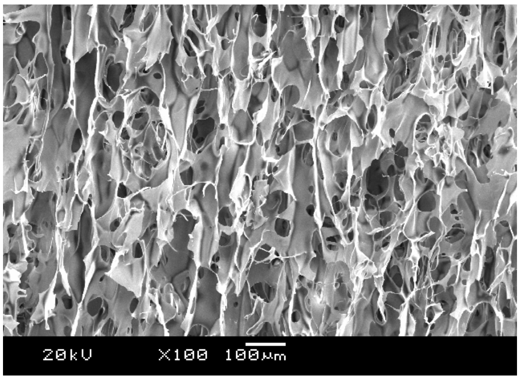
Middle 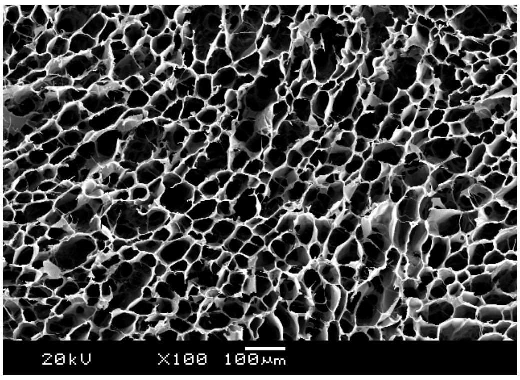	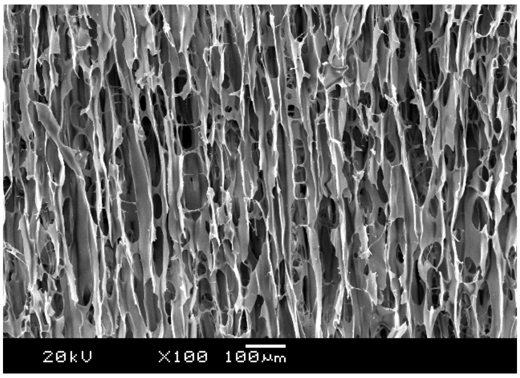
Top 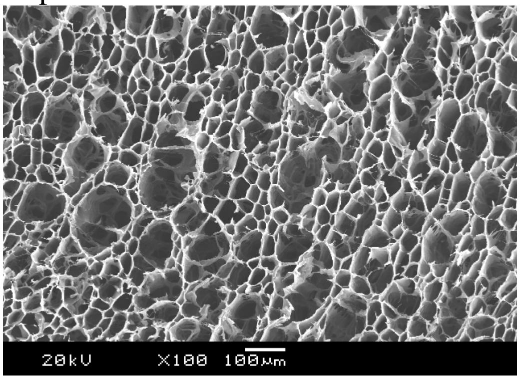	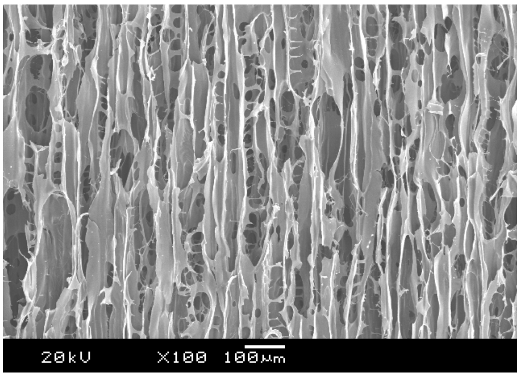

b) Dialyzed-CS/TiO$_2$ scaffold

Cross section	Vertical section
Bottom 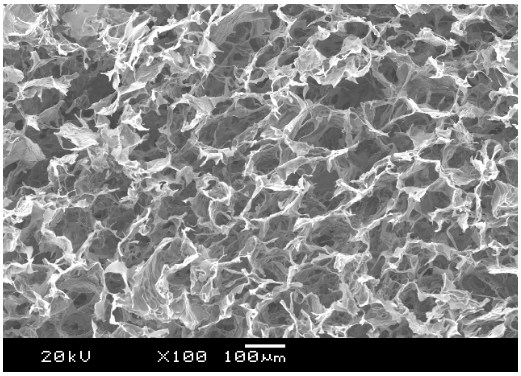 	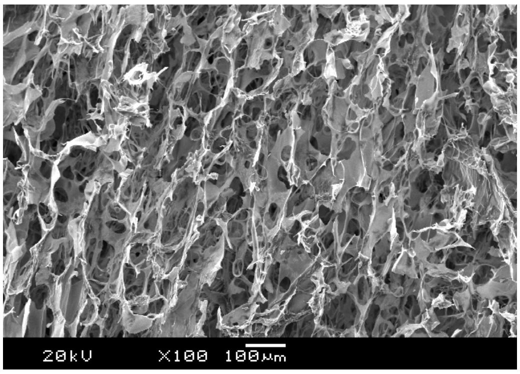
Middle 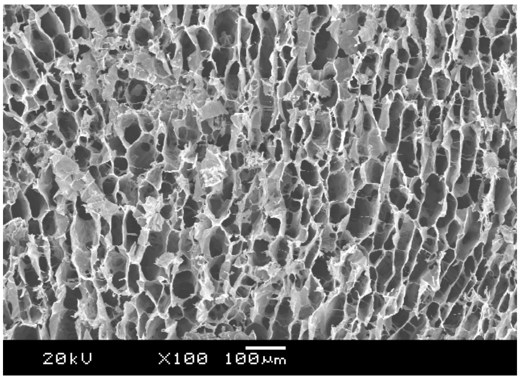 	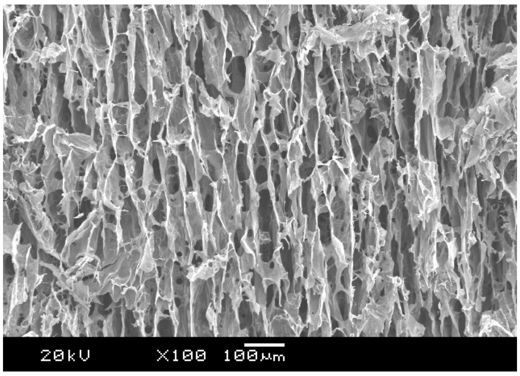
Top 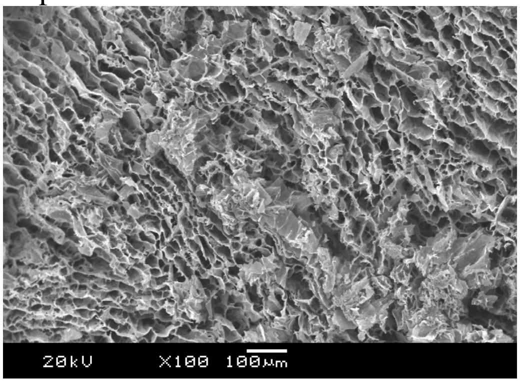 	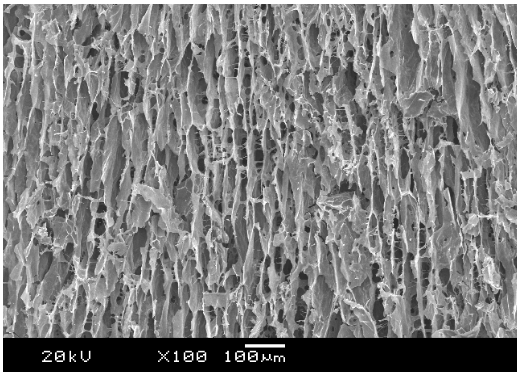

c) P25-CS/TiO_2 scaffold

Cross section	Vertical section
Bottom 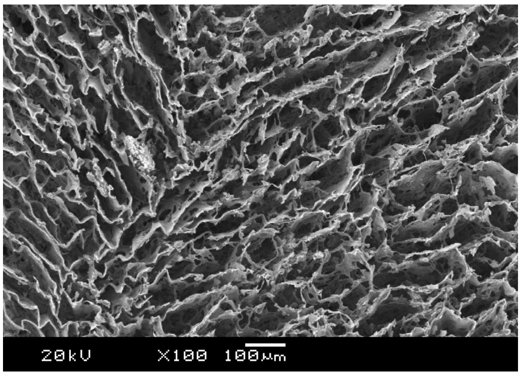 	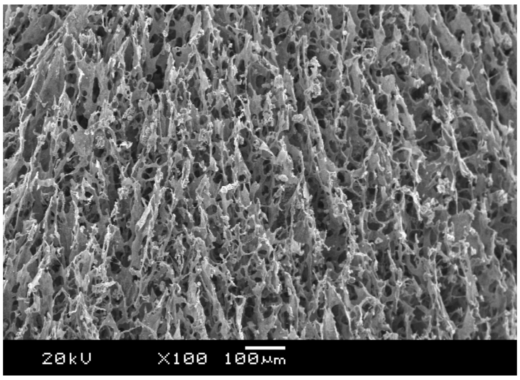
Middle 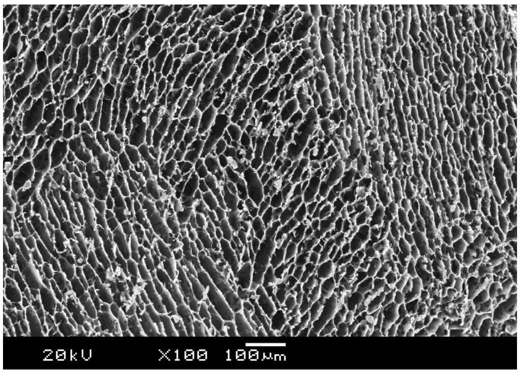 	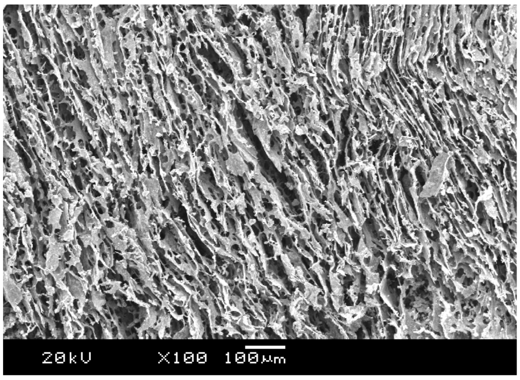
Top 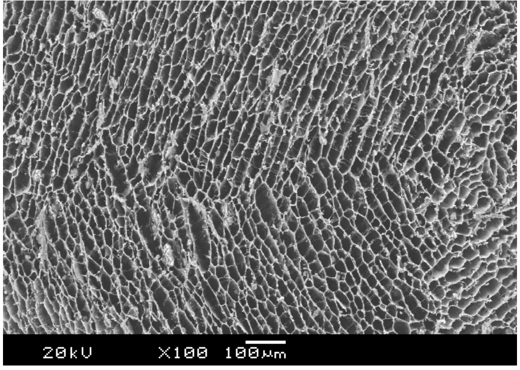 	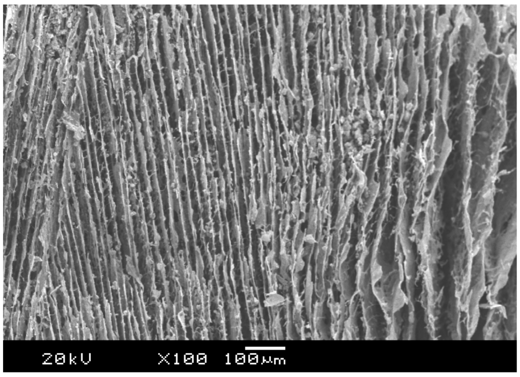

d) KOX-CS/TiO$_2$ scaffold

Cross section	Vertical section
Bottom 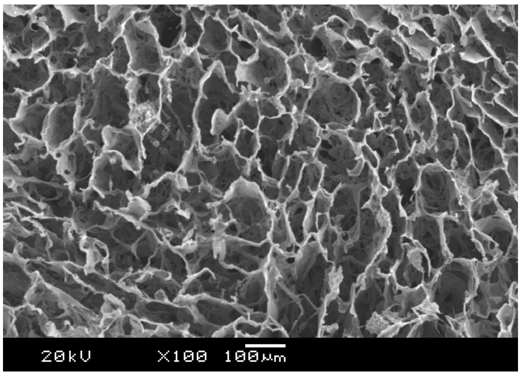 	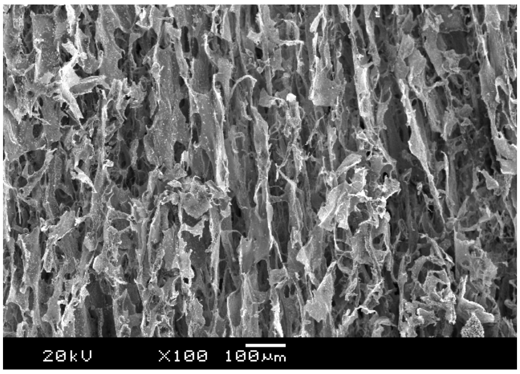
Middle 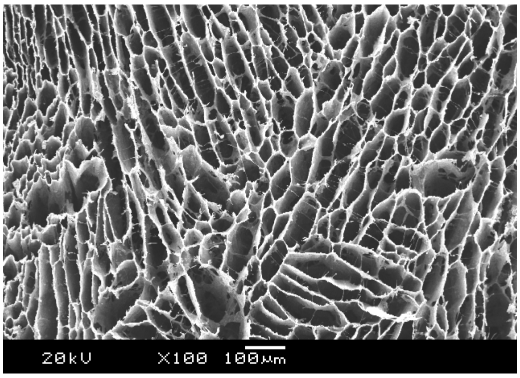 	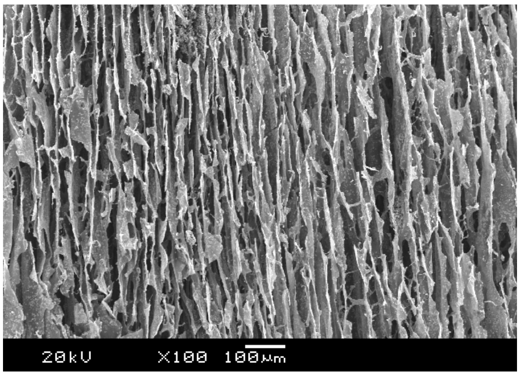
Top 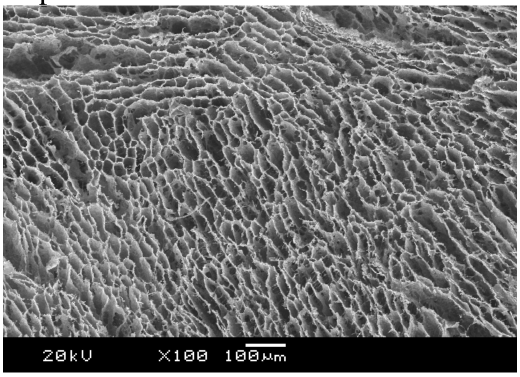 	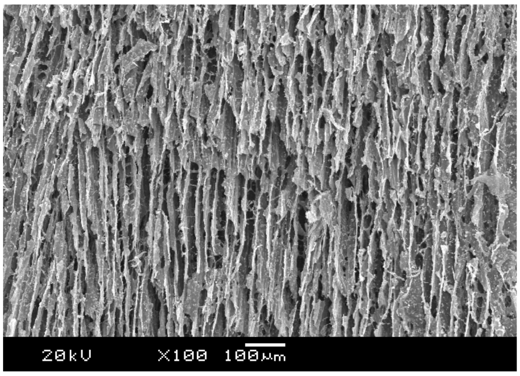

Figure 60. SEM images of the CS/TiO$_2$ scaffolds: a) crosslinked-CS scaffold, b) dialyzed-CS/TiO$_2$ scaffold, c) P25-CS/TiO$_2$ scaffold, d) KOX-CS/TiO$_2$ scaffold

on the bottom, middle and top position on the cross section and vertical section observing on the SEM technique.

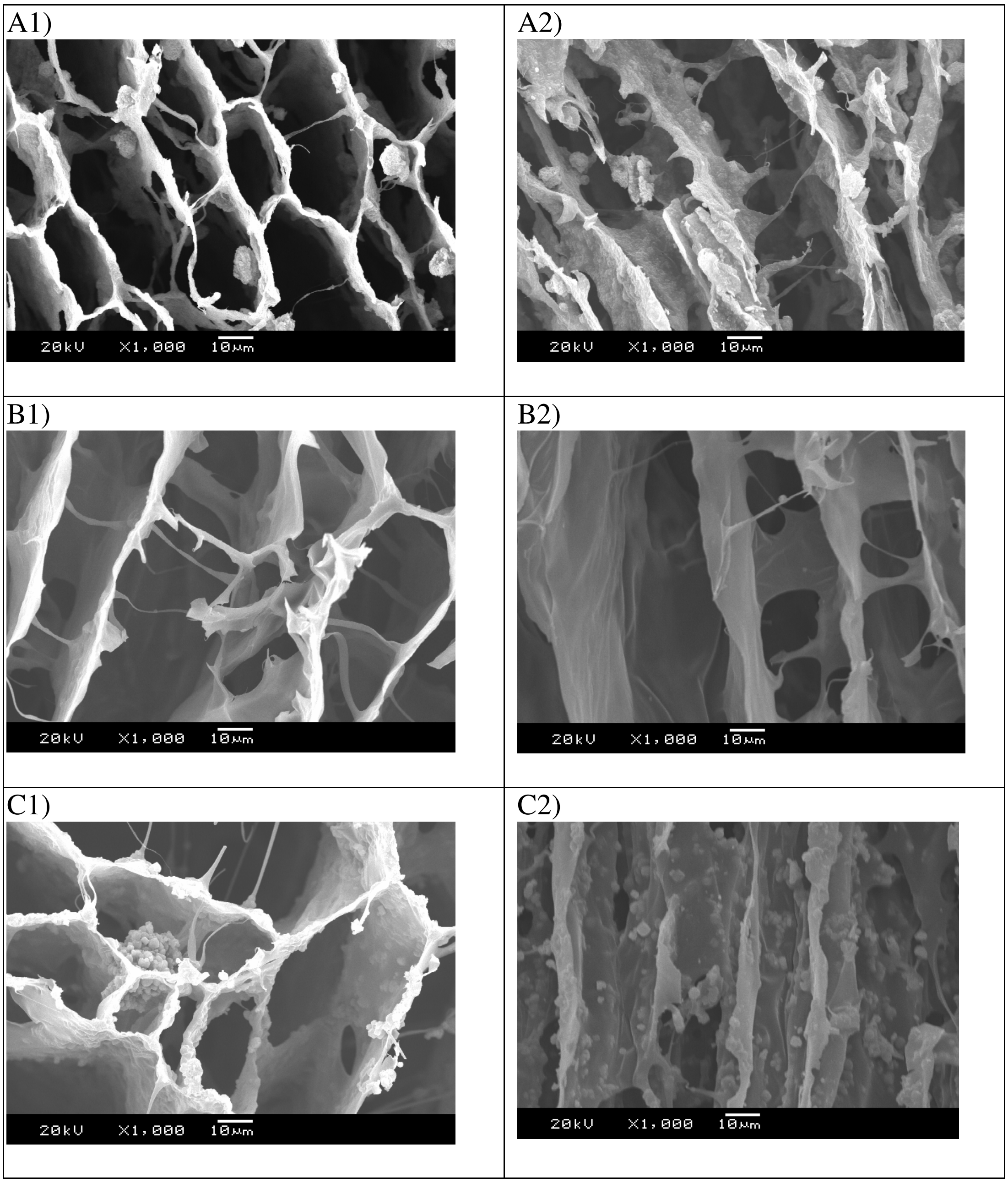

Figure 61. High magnification SEM images of the CS/TiO_2 samples: A) CS/P25-TiO_2 scaffold, B) CS/Dialyzed-TiO_2 scaffold, and C) CS/KOX-TiO_2 scaffold on the cross-section and vertical section.

The morphology of the as-prepared CS/TiO_2 scaffold was also compared with other scaffolds as shown in Figure 62. It could be seen that the morphology of the as-prepared CS/TiO_2 scaffold showed ordered structure like the structure of the porous hybrid silica-chitosan (ChG10) (Shirosaki, *et al.,* 2008) and silica hydrogel (Mukai, *et al.,* 2008). In case of KOX-CS/TiO_2 scaffold, the KOX-TiO_2 powders embeded on the wall of the scaffold, as shown in Figures 63(A1) and 63(A2), are similar to the structure of poly(lactide-co-glycotide) (PLGA) microsphere into gelatin/ chitosan/hyaluronan scaffold (Tan, *et al.,* 2008) shown in Figures 63(B1) and 63(B2).

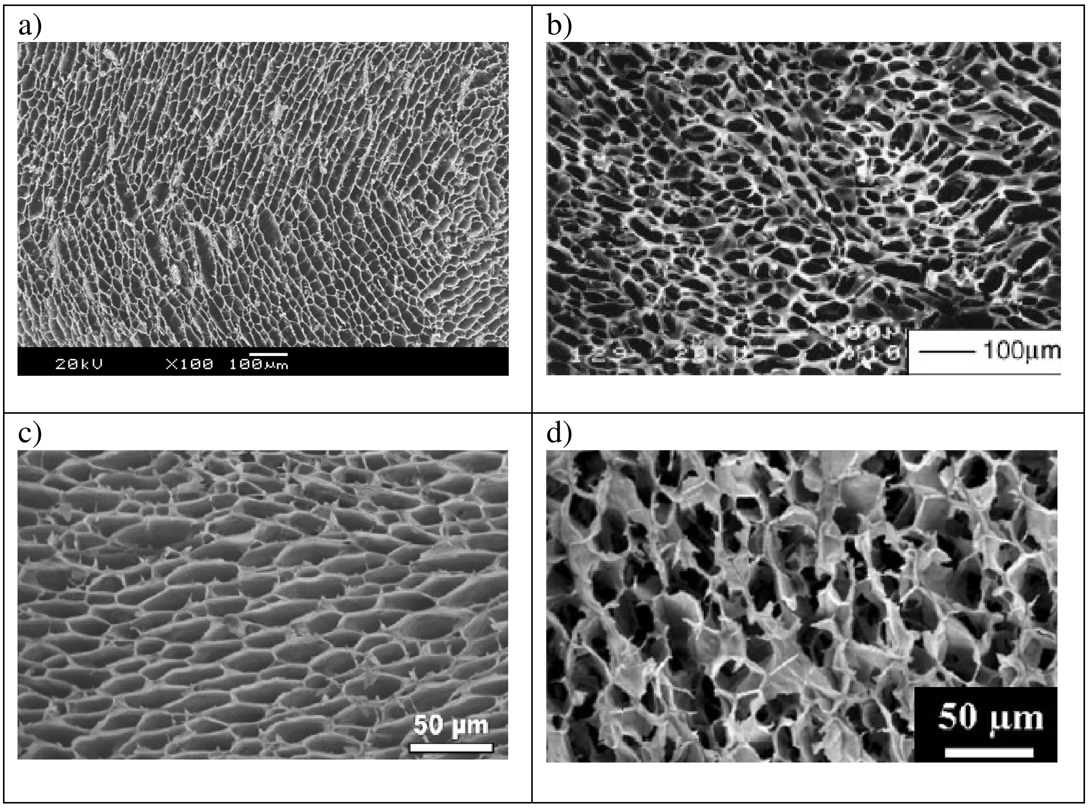

Figure 62. Comparison the cross-section of the as-prepared P25-CS/TiO_2 samples (a), the porous hybrid silica-chitosan (ChG10) (Shirosaki, *et al.,* 2008) (b), silica hydrogel (Mukai, *et al.,* 2008) (c), and SiO_2–Al_2O_3 cryogels (Nishihara, *et al.*, 2006) (d).

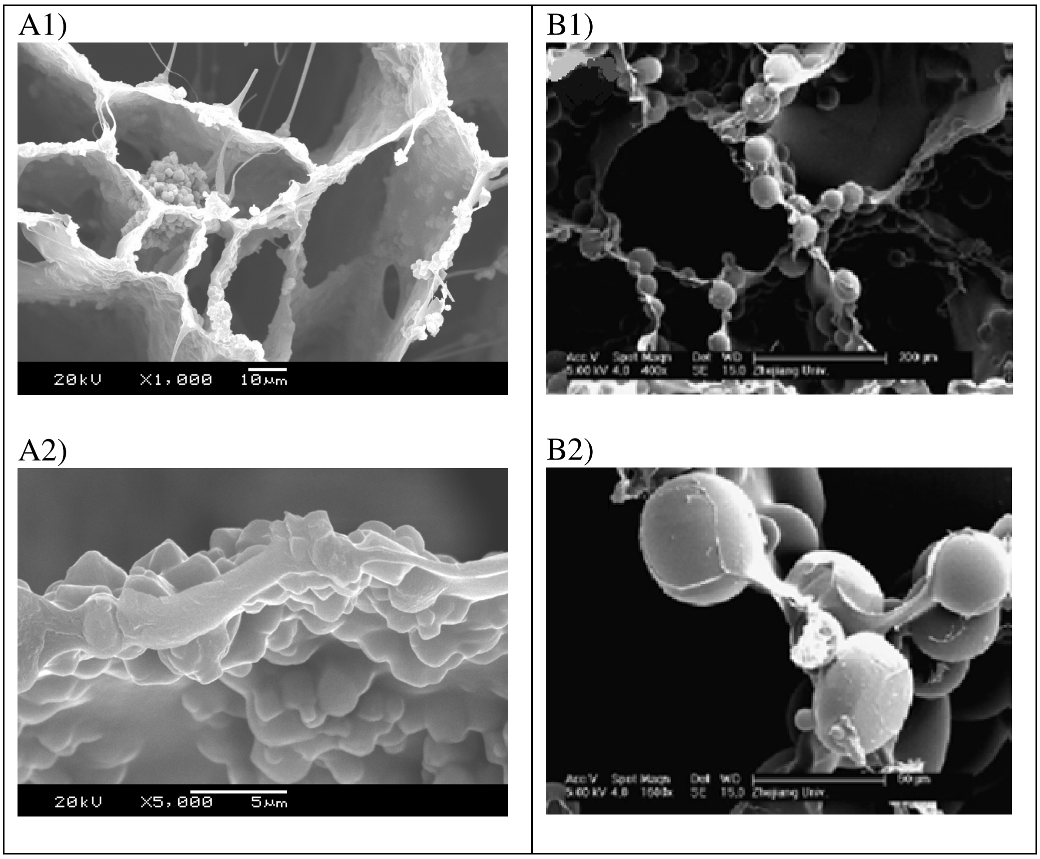

Figure 63. Comparison the cross-section of the as-prepared KOX-CS/TiO_2 samples (A1), magnified image of KOX-CS/TiO_2 samples (A2), the poly(lactide-co-glycotide) (PLGA) microsphere into gelatin/chitosan/hyaluronan scaffold (B1), and magnified image of PLGA- gelatin/chitosan/hyaluronan scaffold (B2) (Tan*, et al.,* 2008).

The EDX spectra and mapping analysis of CS/TiO_2 scaffolds are shown in Figures 64 and 65. The results show that all CS/TiO_2 scaffolds have the Si, Ti element distributed uniformly on the wall of the scaffolds.

a) GPTMS/CS

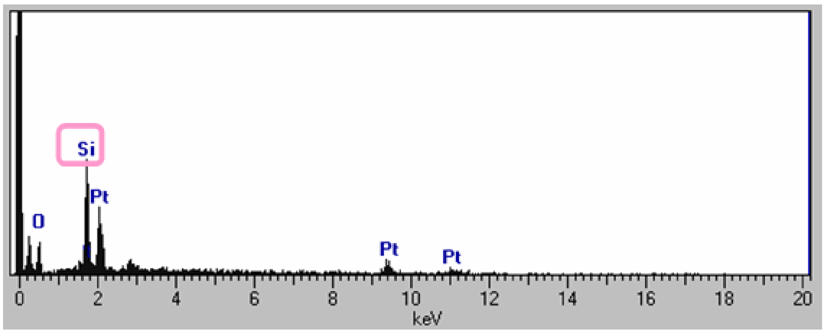

b) Dialyzed-TiO_2

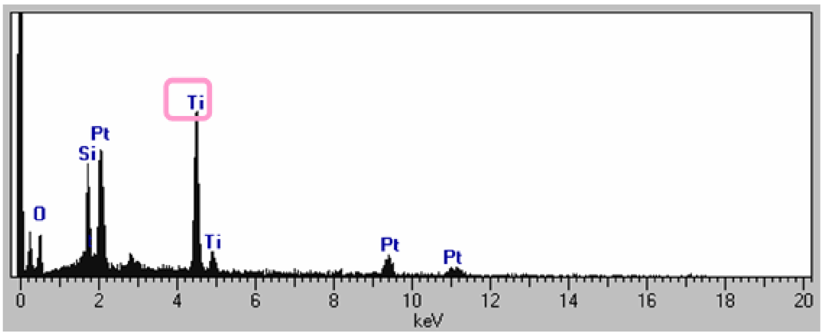

c) P25-TiO_2

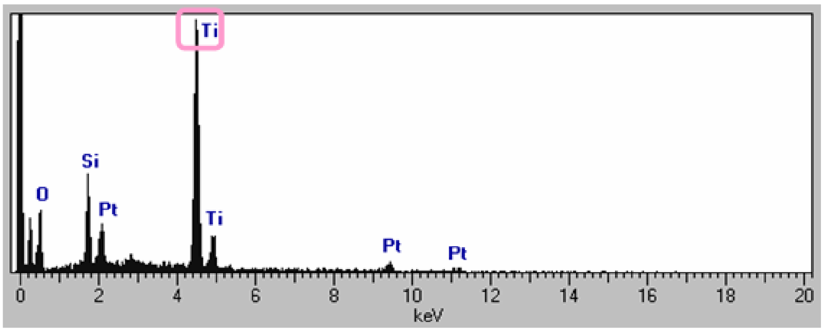

d) K-TiO_2

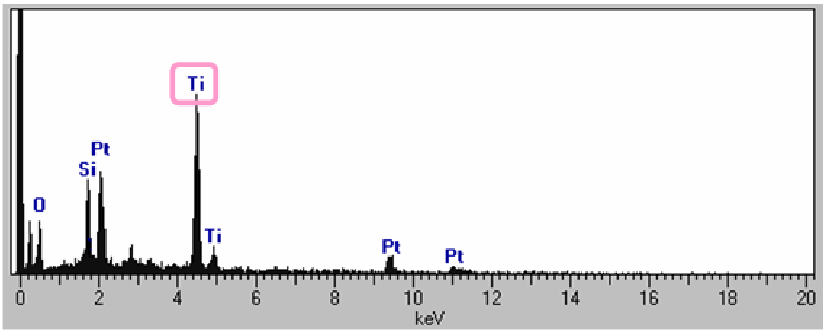

Figure 64. EDX spectra of CS/TiO_2 samples: a) Crosslinked-CS scaffold, b) CS/Dialyzed-TiO_2 scaffold c) CS/P25-TiO_2 scaffold, d) CS/KOX-TiO_2 scaffold.

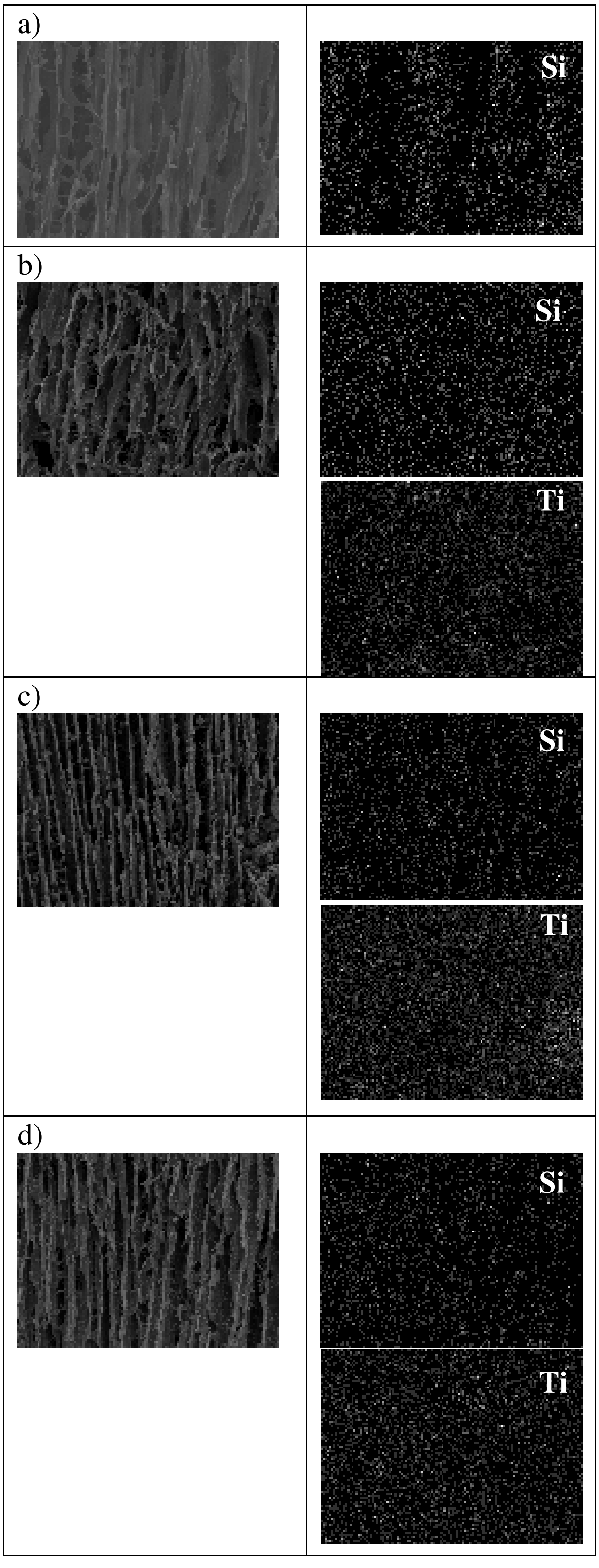

Figure 65. Mapping analysis of CS/TiO_2 samples: a) Crosslinked-CS scaffold, b) CS/Dialyzed-TiO_2 scaffold c) CS/P25-TiO_2 scaffold, and d) CS/K -TiO_2 scaffold.

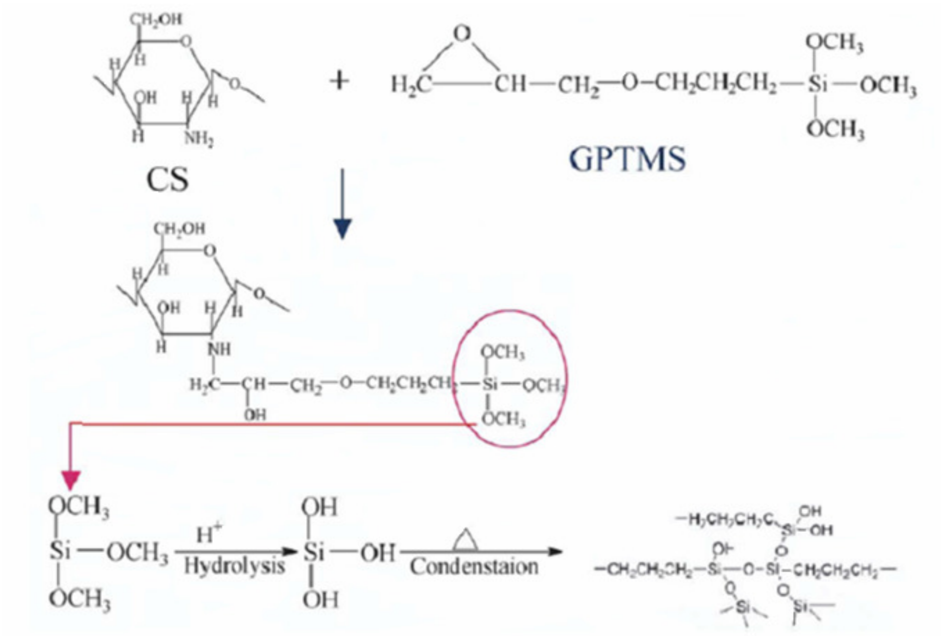

Figure 66. Crosslinking on chitosan and *in situ* formation of chitosan–silica hybrid material (Liu, *et al.*, 2004).

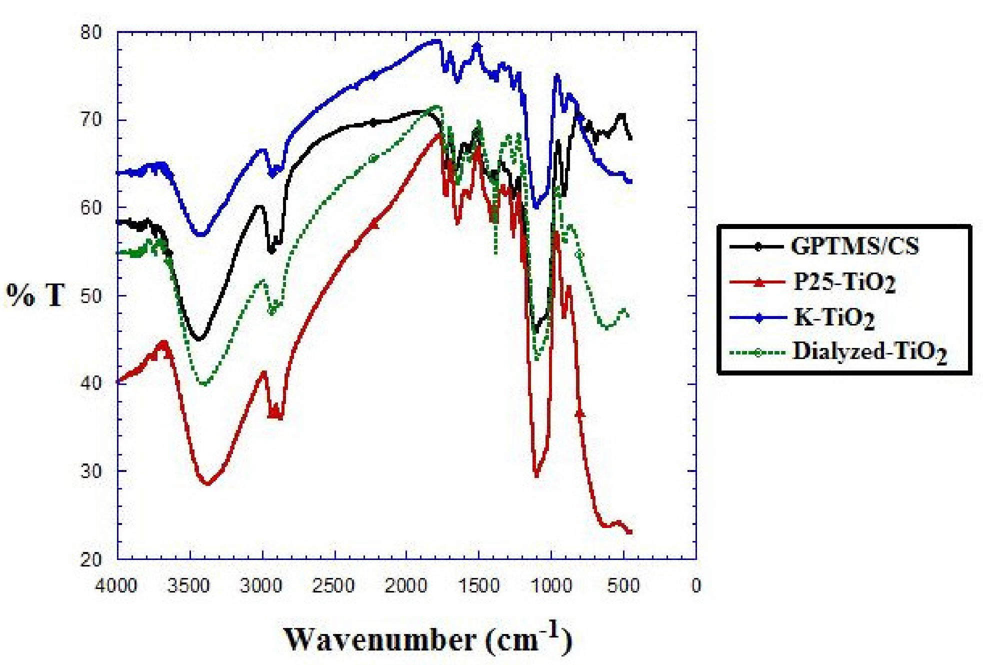

Figure 67. The FT-IR spectra of crosslinked-CS/TiO_2 scaffolds.

Figure 66 shows the crosslinked-chitosan with the 3-glycidoxypropyltrimethoxysilane (GPTMS). The crosslinked-chitosan was confirmed by the FT-IR technique as shown in Figure 67. The FT-IR spectra of all CS/TiO_2 scaffolds were investigated in the range of 4000-400 cm^{-1}. From these spectra, there appear strong bands at 3423 cm^{-1}, 2868 cm^{-1}, 1651 cm^{-1}, 1380 cm^{-1}, 1100 cm^{-1}, and in the range of 906 to 450 cm^{-1}. The absorption at 3423 cm^{-1} can be assigned to ν_{OH} (stretching modes) indicating the presence of hydroxyl group of water in sample. The band at 2868 cm^{-1} is assigned to CH_2 stretching mode. Those bands at 1651 cm^{-1}, 1380 cm^{-1}, 1100 cm^{-1} belong to the N-H bending, and Si-O-C bond indicating the characteristic of crosslinked chitosan. The observed bands in the range of 906 to 450 cm^{-1} are associated with the characteristic vibrational modes of TiO_2 ($\nu_{Ti\text{-}O}$, stretching mode of Ti-O bond) (Zhang, *et al.*, 2002).

3.3.3 Photocatalytic activity test

3.3.3.1 Evaluating the photocatalytic activity

Methylene blue (MB) and orange II (OII) were employed as cationic dye and anionic dye in order to evaluate the photocatalytic activity of the CS/TiO_2 scaffolds. Two blank experiments were performed, one with only the dye solution, the other with pristine crosslinked-CS scaffold in dye solution. The first showed no significant change in dye absorbance, the other showed only absorption property (no photocatalytic oxidation properties). These results confirmed the photocatalytic activity to come from the TiO_2 particles on the wall of scaffolds.

The detailed mechanism of the photocatalytic oxidation process has been discussed previously in the literatures (Konstantinou, *et al.*, 2004; Houas, *et al.*, 2001; Prevot, *et al.*, 2001; Tanakai, *et al.*, 2000; Saien, *et al.*, 2008; Galindo, *et al.*, 2000; Bandara, *et al.*, 1999; Daneshvar, *et al.*, 2003). Most photocatalytic oxidation processes involve the generation of a very powerful oxidizing agent, the hydroxyl radiacal ($OH^{\bullet}$), to attack and destroy organic and hazadardous pollutants.

The resulting $^{\bullet}OH$ radical can oxidize most of azo dye to the complete mineralized end-products.

In this photocatalytic study, all parameters: the ratio of TiO_2 sol/chitosan gel, freezing rate, and size of syringe were also investigated since these parameters also affect the photocatalytic activity. The photocatalytic results of these studies are shown in Figure 68. From these results the 1:1 ratio, 5.9 mm/min, and 2 mL syringe size showed the highest photocatalytic efficiency. In the case of 1:8 ratio, the photocatalytic efficiency was the highest but the scaffold was not strong, so we chose the 1:1 ratio as the higher photocatalytic efficiency. These results corresponded with the SEM results that they also have the unique ordered porous structure.

a) Ratio of TiO_2 sol/chitosan gel

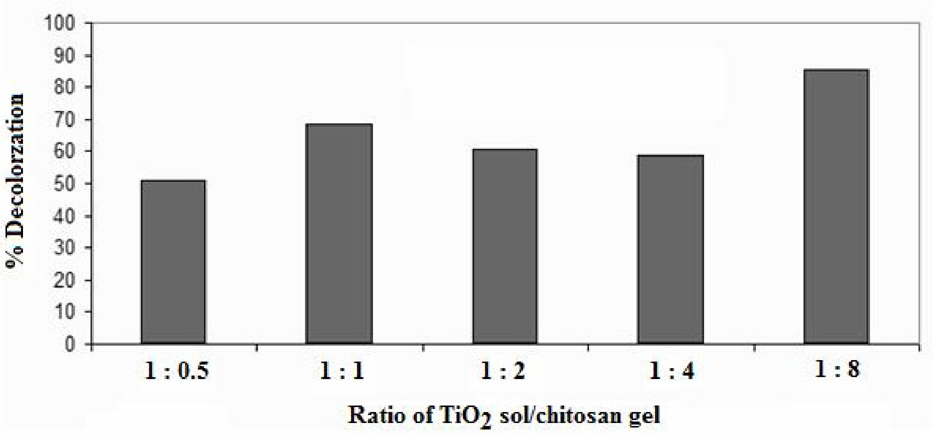

b) Freezing rate

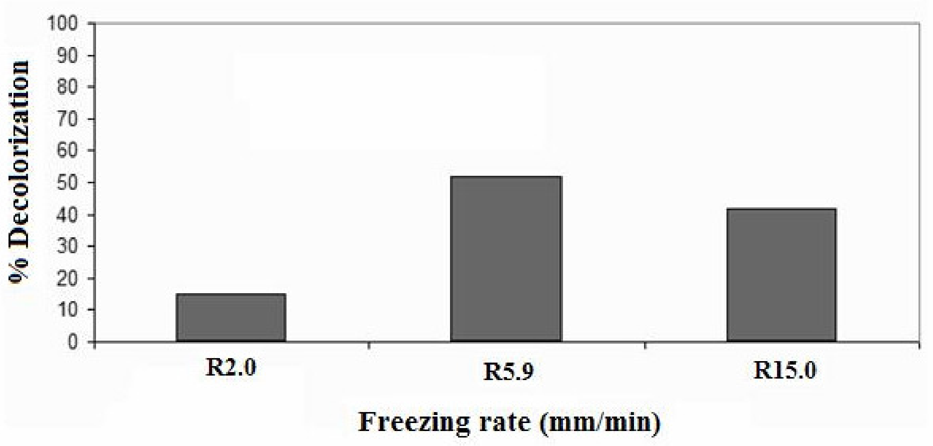

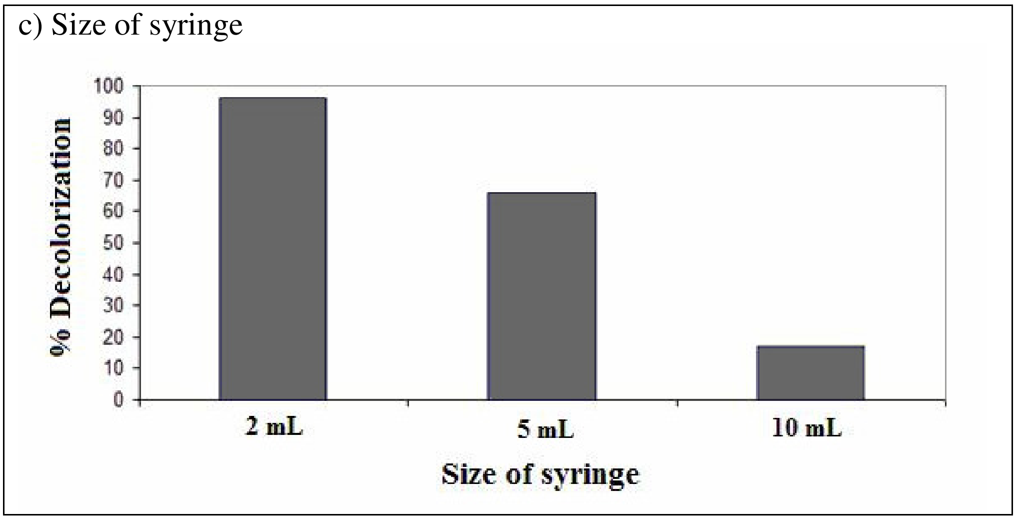

c) Size of syringe

Figure 68. The photocatalytic decolorization of MB (under UV light 20 h) using CS/TiO_2 scaffolds with varying: a) ratio of TiO_2 sol/chitosan gel, b) freezing rate, and c) size of syringe.

Figure 69 shows the photocatalytic efficiencies of CS/TiO_2 scaffolds. The P25-TiO_2 scaffold showed the highest efficiency for decolorization of methylene blue solution. The photocatalytic efficiency falls in the order: P25-TiO_2 > KOX-TiO_2 > dialyzed-TiO_2 as shown in Figure 69a. It is not surprising that the P25-TiO_2 and KOX-TiO_2 scaffold showed higher efficiency than the dialyzed-TiO_2 scaffolds, due to the highly uniform TiO_2 particle distributed on the wall of the scaffold, so the dye molecule could be diffused through the TiO_2 particles and were decomposed by them. The reason that the dialyzed-TiO_2 scaffolds showed low photocatalytic efficiency, despite of fresh dialyzed-TiO_2 sol have high efficiency as well as P25-TiO_2 sol as shown in Figure 70a, because the dialyzed-TiO_2 sol formed in the wall of the scaffold. On the contrary, in the case of orange II degradation, the photocatalytic efficiency falls in the order: dialyzed-TiO_2 > P25-TiO_2 > KOX-TiO_2 as shown in Figure 70b. The high efficiency of dialyzed-TiO_2 is possibly due to the electrostatic interaction between orange II and dialyzed-TiO_2 scaffold. The surface of chitosan has positive charge and orange II which anionic dye, the dye is adsorbed strongly on the surface of scaffold. The CS/TiO_2 scaffolds are covered with dye molecules as shown in Figure 73.

a) Methylene blue degradation

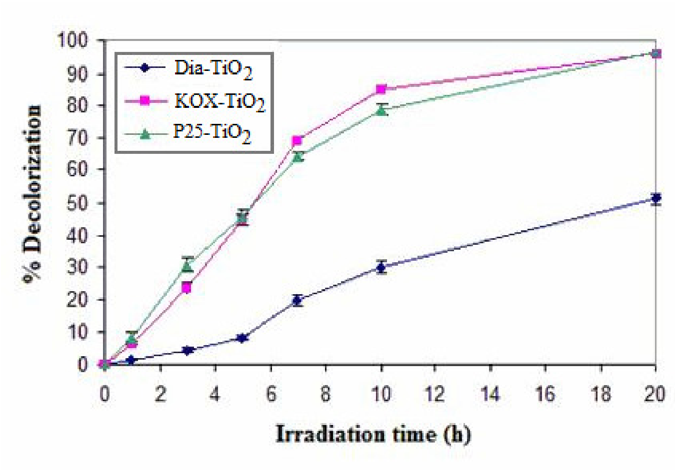

b) Orange II degradation

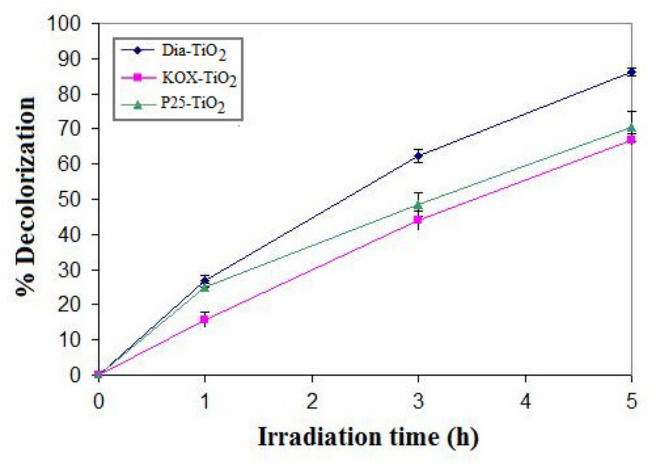

Figure 69. The photocatalytic decolorization of a) MB (20 h), b) OII (5 h) using CS/TiO_2 scaffolds.

a) Degradation of MB

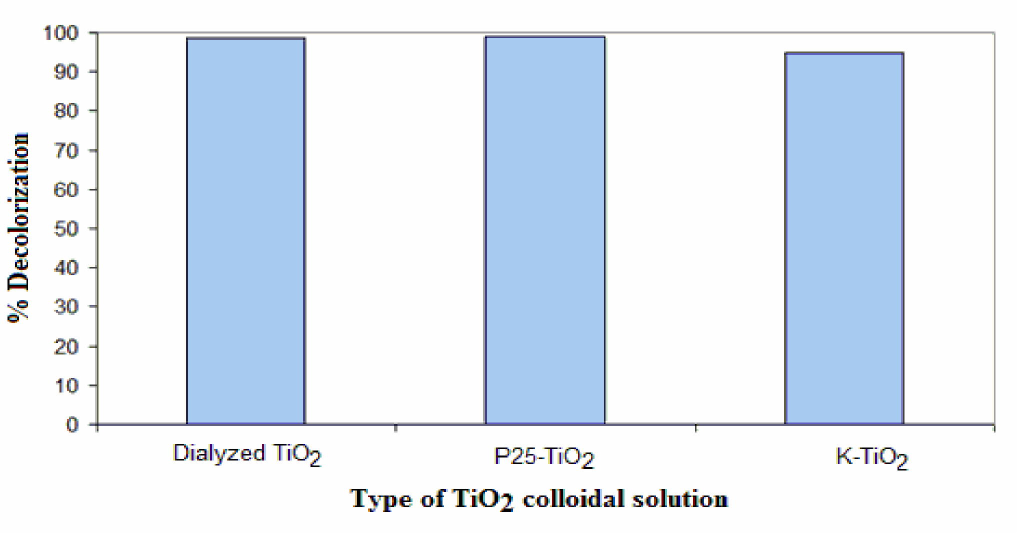

b) Degradation of OII

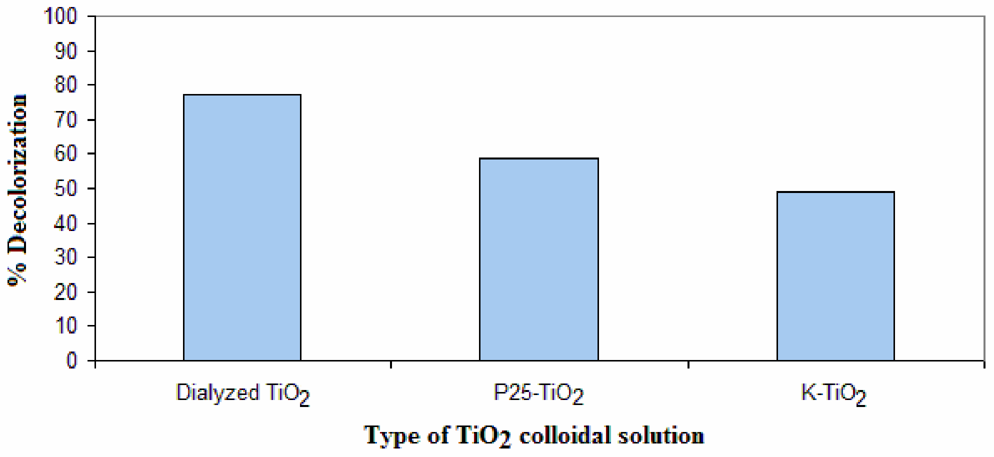

Figure 70. The photocatalytic decolorization of (a) MB (under UV light 20 h) and (b) OII (under UV light 5 h) using 50 mg/mL TiO_2 solutions.

3.3.3.2 Kinetics study

For kinetics study, a plot of ln (C_0/C) versus time represents a straight line, the slope of which upon linear regression equals the apparent first-order rate constant (Houas, *et al.*, 2001; Prevot, *et al.*, 2001; Tanakai, *et al.*, 2000; Ibhadon, *et al.*, 2008; Chiou, *et al.*, 2008) as shown by the equation (26).

For kinetics results, as shown in Figure 71, straight lines were found for all the materials, indicating that the degradation of both methylene blue and orange II are of first order process or pseudo-first order process. The rate constant values are summarized in Table 16 for CS/TiO_2 scaffolds.

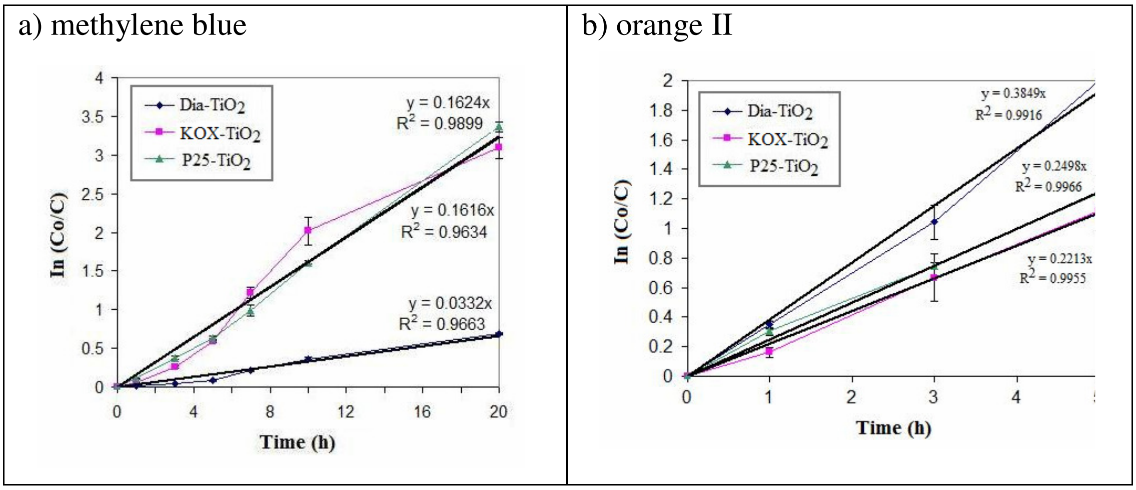

a) methylene blue

b) orange II

Figure 71. The kinetics of disappearance of a) methylene blue, b) orange II using CS/TiO_2 scaffolds.

Table 16. The rate constant values of CS/TiO_2 scaffolds toward MB and OII degradation.

CS/TiO_2 scaffolds	k_{app} (min^{-1})	R^2
a) Methylene blue		
Dialyzed-TiO_2	0.0332	0.9663
K-TiO_2	0.1616	0.9634
P25-TiO_2	0.1624	0.9899
b) Orange II		
Dialyzed-TiO_2	0.3849	0.9916
K-TiO_2	0.2498	0.9955
P25-TiO_2	0.2213	0.9966

3.3.3.3 Reusability of the CS/TiO$_2$ scaffolds.

After finishing the decolorization experiments, the *CS/TiO$_2$ scaffolds* were tested for the next cycle without cleaning. The efficiency of the fresh-TiO$_2$ scaffold and reused-TiO$_2$ scaffold were compared as shown in Figure 72. For both dyes degradation, the photocatalytic efficiency of the reuse decreased slightly compared with the first use.

a) Methylene blue

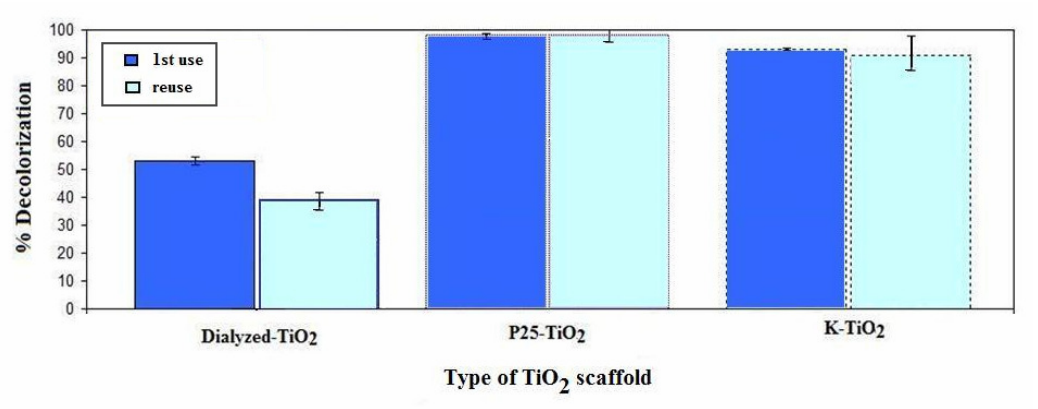

b) Orange II

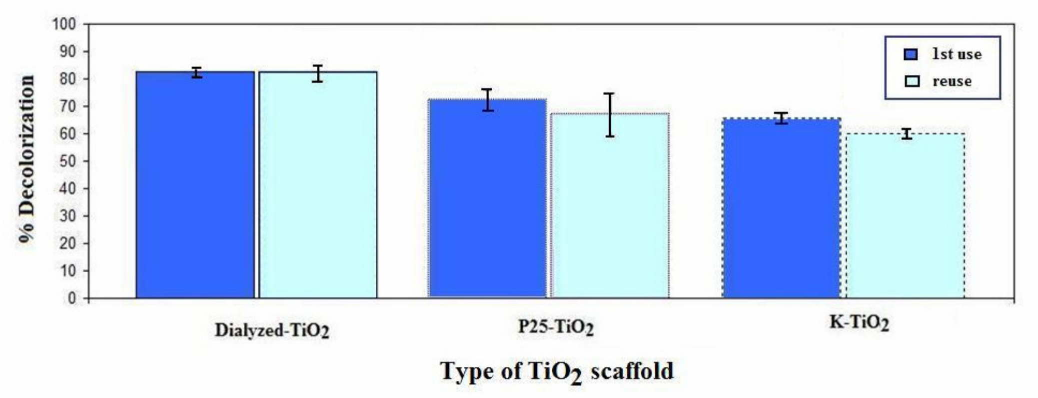

Figure 72. The reuse efficiency of CS/TiO$_2$ scaffolds for decolorized a) methylene blue (under UV light 20 h), b) orange II (under UV light 5 h).

a) Methylene blue

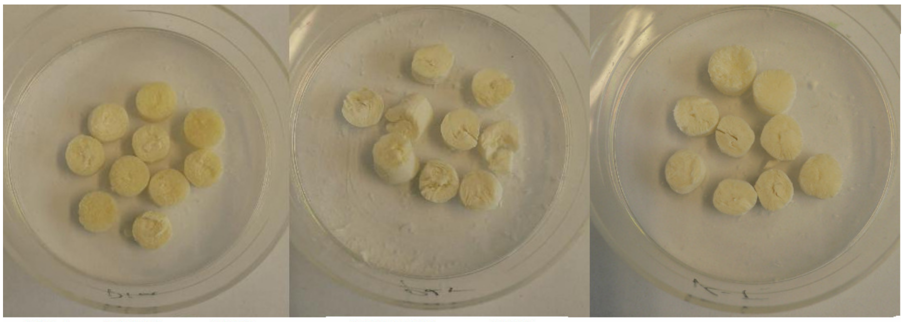

Dialyzed-TiO_2 scaffold **P25-TiO_2 scaffold** **K-TiO_2 scaffold**

b) Orange II

Dialyzed-TiO_2 scaffold **P25-TiO_2 scaffold** **K-TiO_2 scaffold**

Figure 73. The appearance of CS/TiO_2 scaffolds after decolorization experiments a) methylene blue, b) orange II.

3.4 Synthesis of mesoporous TiO_2 powders with different precursors

The mesoporous TiO_2 materials have attracted much attention in the field of separation and catalysis because of their high specific surface areas and pore volumes, as well as narrow pore size distributions which offer more active sites for catalytic reaction to take place (Antonelli, *et al.*, 1995). The first synthesis of mesoporous titania through modified sol-gel reactions in the presence of alkyl phosphate surfactant as template was reported by Antonelli and Ying in 1995 (Antonelli, *et al.*, 1995). Since then many efforts have been devoted to the synthesis of mesoporous titanic powders and films and some synthetic approaches have been developed (Antonelli, 1999; Stone, *et al.*, 1995; Zhang, *et al.*, 2000; Zheng, *et al.*, 2001; Zhao, *et al.*, 2000).

In most cases, ionic and neutral surfactants have been employed as templates to direct the mesoporous structure based on the electrostatic and hydrogen-bonding interactions, respectively. The use of ionic surfactants presents limited potential applications because of their strong interactions with titania walls resulted in the impossibility of completely removing the surfactant by extraction procedures and in the collapse of the inorganic structure when post synthesis thermal treatment is employed for surfactant elimination. Thus, non-ionic surfactants appeared to be a potential alternative given that, in this case, hydrogen bonding mediated the formation of the metal oxide-surfactant composites involved in the inorganic framework organization (Calleja, *et al.*, 2004). Recently, inorganic block copolymers have been studied extensively as structure-directing agents in the synthesis of highly ordered mesostructured materials (Yu, *et al.*, 2001).

There are several ways of preparing mesostructured materials such as sol-gel, hydrothermal, and microemulsion methods. Among them, the sol-gel process is the most popular technique for preparing porous TiO_2 powder (Zheng, *et al.*, 2001; Calleja, *et al.*, 2004; Yoo, *et al.*, 2005; Zhao, *et al.*, 2004; Kluson, *et al.*, 2001). In sol-gel synthesis, hydrolysis and condensation reactions, take place when the alkoxide precursor reacts immediately in the presence of water that leads to formation of the larger and inhomogeneous product (Wang, *et al.*, 2006). So the rate of hydrolysis and condensation reaction could be controlled through the surfactant mediated sol-gel process.

In this work, mesoporous TiO_2 was synthesized from sol-gel process using a nonionic triblock copolymer $(PEO)_{20}$ – $(PPO)_{70}$ - $(PEO)_{20}$, or Pluronic P123, as structure directing agent and studying the effect of precursor using $TiCl_4$ and $TiOSO_4$ as precursors. The P123 template could be totally removed without calcinations. The synthesized TiO_2 material was characterized by various physical techniques. Photocatalytic activity of sample was tested using indigo carmine as the model pollutant and compared with commercial Degussa P25-TiO_2.

3.4.1 Characterization of the mesostructured TiO_2

The XRD patterns of the as-synthesized P123-TiO_2 using $TiCl_4$ as precursor (denoted as P123-TiO_2_$TiCl_4$) and $TiOSO_4$ as precursor (denoted as P123-TiO_2_$TiOSO_4$) are shown in Figures 74 and 75, respectively. The XRD pattern at $2\theta = 25.5$ (101) in the spectrum of TiO_2 is identified as the crystal of the anatase form (denoted as ‘‘A’’) whereas the peak at $2\theta = 27.5$ (110) arises from the crystal of the rutile form (denoted as ‘‘R’’). In this part, we studied the effect of reaction temperature, water content and type of acid catalyst for $TiCl_4$ as precursor and also studied the effect of reaction temperature, Ti content, and type of acid catalyst for $TiOSO_4$ as precursor. As shown in Figure 74, the synthesized P123-TiO_2_$TiCl_4$ samples were mixtures of amorphous TiO_2, anatase, and rutile phase. The amorphous phase was dominant with small amount of anatase or mixed anatase and rutile (as shown in Table 19). In case of P123-TiO_2_$TiOSO_4$ samples were mixtures of amorphous TiO_2 and anatase phase. The amorphous phase was dominant with small amount of anatase phase (as shown in Table 20). It can be seen that the amount of anatase phase of most P123-TiO_2_$TiOSO_4$ samples is higher than the percentage of anatase in the P123-TiO_2_$TiCl_4$ samples. The percentage of each phase existed in sample was determined by the standard addition method employing the standard curve of anatase and rutile as shown in Figures 76 and 77, respectively. The standard curve was constructed from mixed pure amorphous phase with anatase or rutile phase (10%, 20%, and 30% by weight) then measure the phase by XRD technique. The plot of area and percentage of anatase or rutile phase was applied to estimate the percentage of each phase in sample, the rest percentage is the amorphous phase. The average crystallite sizes of anatase and rutile in the sample were calculated by applying the Debye-Scherrer formula. The phase structure and average crystallite size of the P123-TiO_2_$TiCl_4$ samples and P123-TiO_2_$TiOSO_4$ samples are given in Table 17 and Table 18, respectively.

a) Effect of reaction temperature

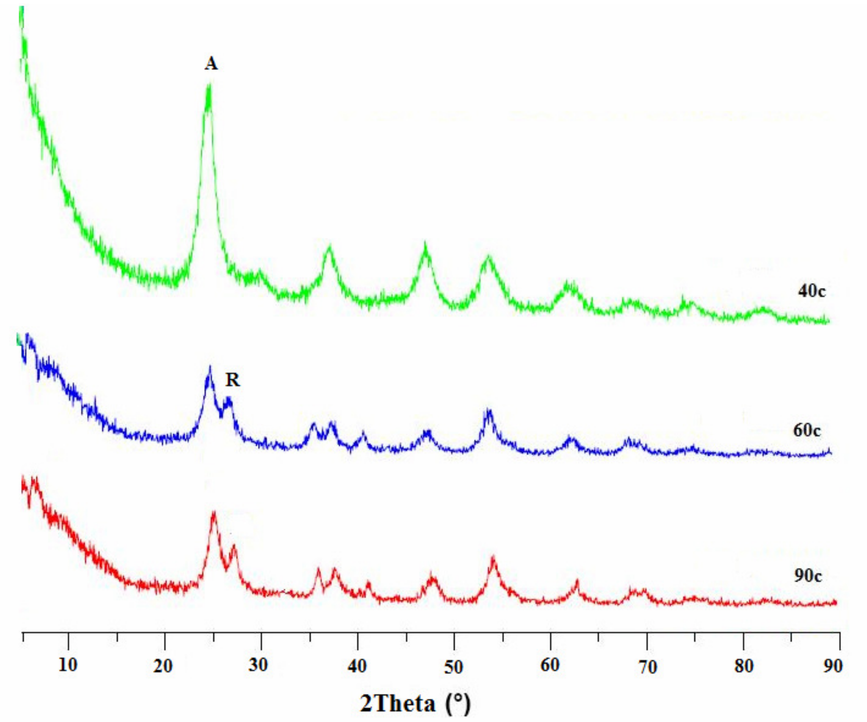

b) Effect of water content

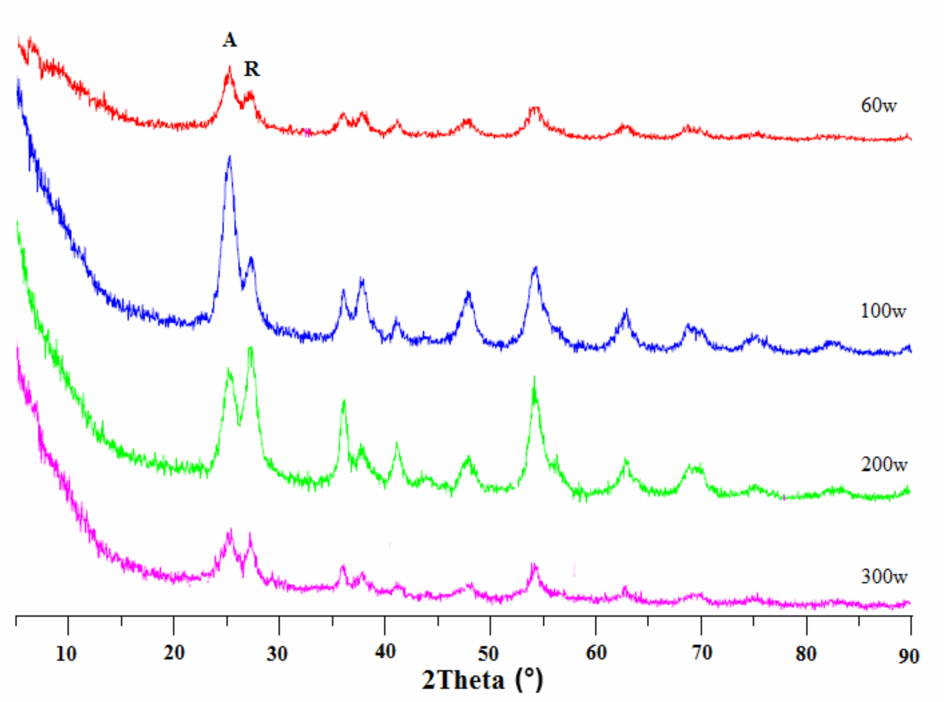

c) Effect of acid

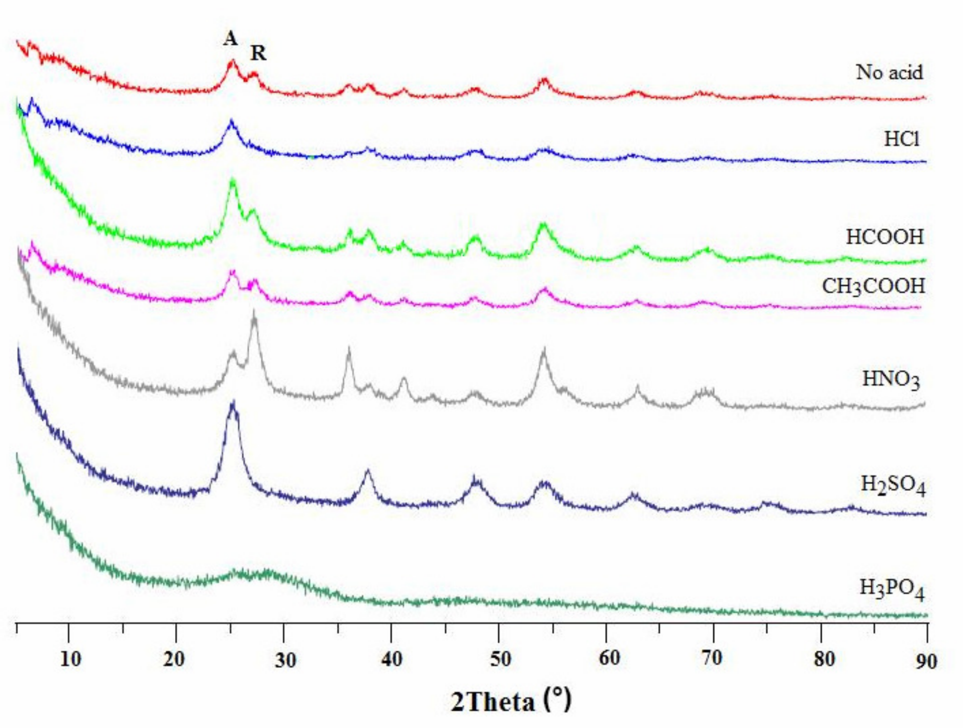

Figure 74. XRD patterns of P123-TiO_2_$TiCl_4$ samples: a) effect of reaction temperature, b) effect of water content, and c) effect of acid catalyst.

a) Effect of reaction temperature

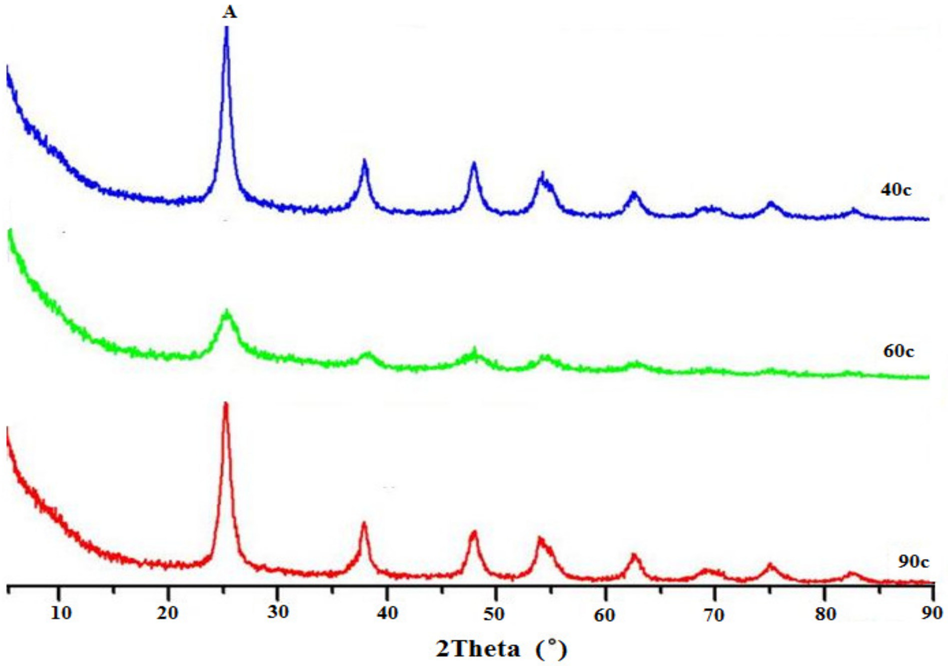

b) Effect of titanium content

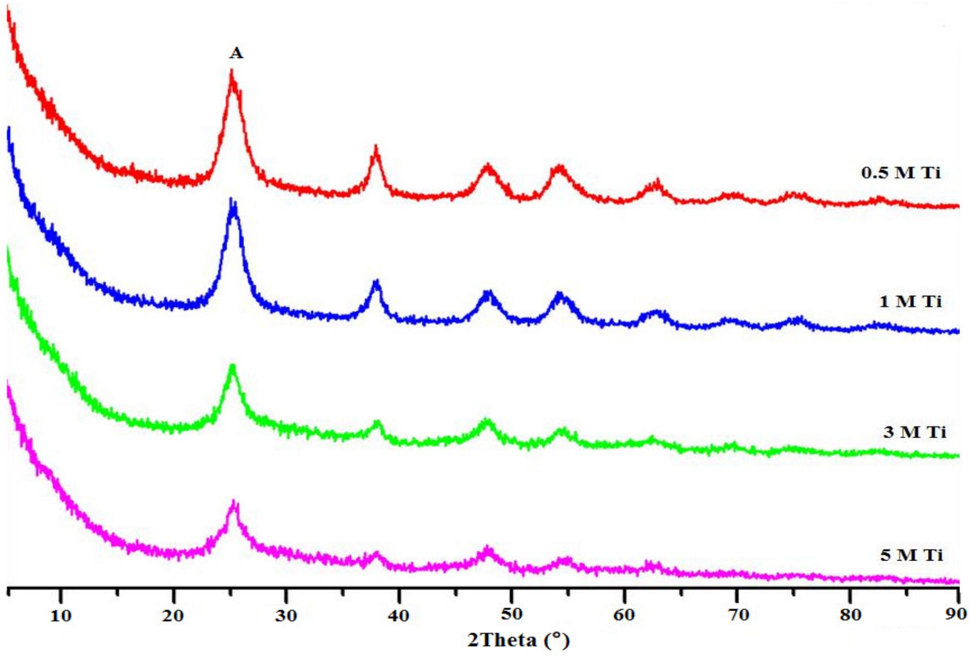

c) Effect of acid

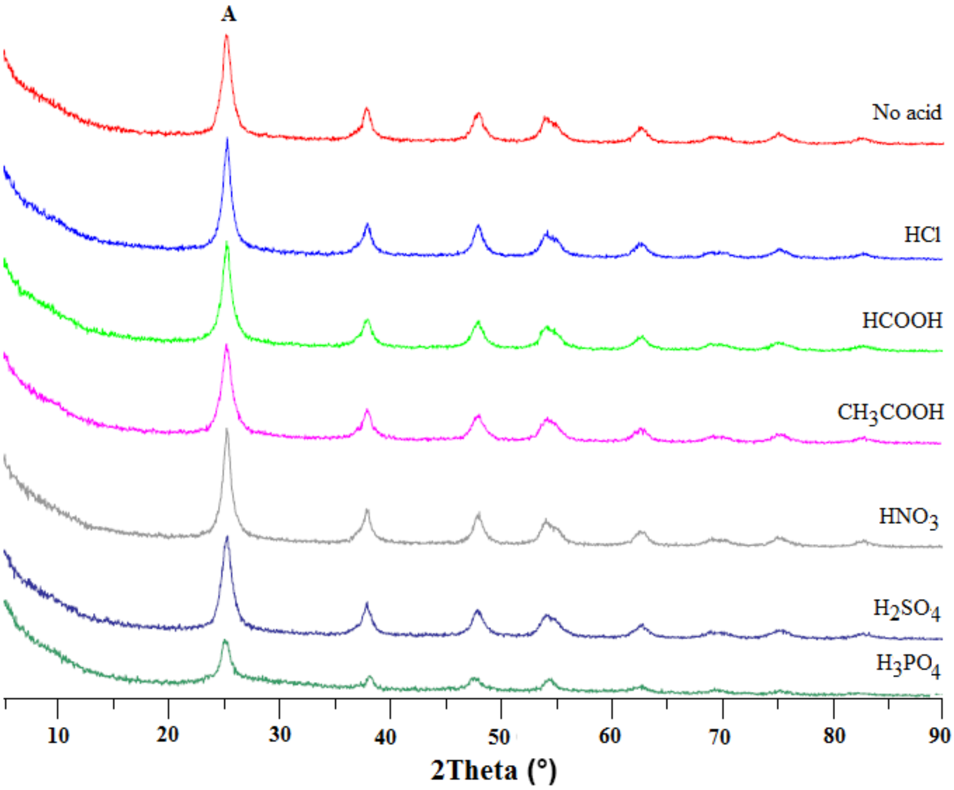

Figure 75. XRD patterns of P123-TiO_2_$TiOSO_4$ samples: a) effect of reaction temperature, b) effect of Ti content, and c) effect of acid catalyst.

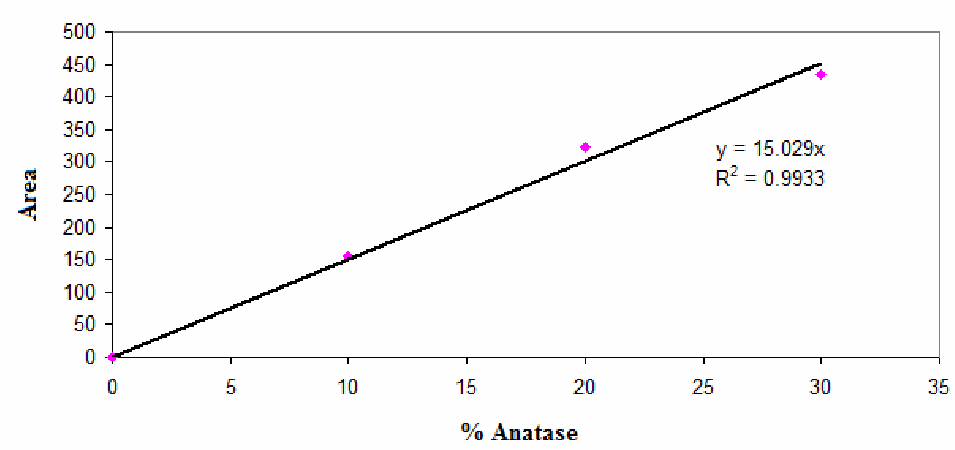

Figure 76. Standard curve for the calculation of % anatase phase in TiO_2 sample.

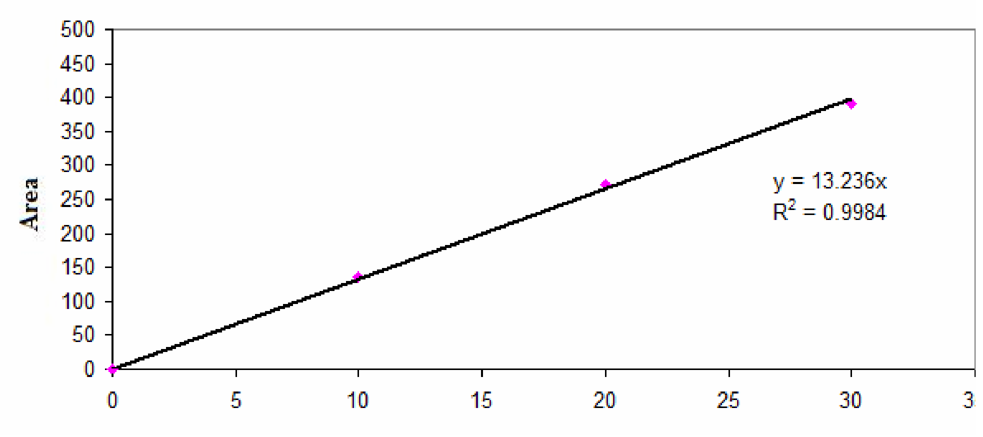

Figure 77. Standard curve for the calculation of % rutile phase in TiO_2 sample.

Table 17. The phase structure, average crystallite size of P123-TiO_2_$TiCl_4$ samples.

P123/TiO_2_$TiCl_4$ sample	Phase structure	Crystallite size (nm)[a]
Effect of reaction temperature		
40c	Anatase	7.22 (A)
60c	Anatase + Rutile	8.27 (A), 13.83 (R)
90c	Anatase + Rutile	9.19 (A), 13.83 (R)
Effect of water content		
60w	Anatase + Rutile	8.27 (A), 13.83 (R)
100w	Anatase + Rutile	9.22 (A), 12.13 (R)
200w	Anatase + Rutile	8.25 (A), 20.73 (R)
300w	Anatase + Rutile	11.81 (A), 13.83 (R)
Effect of acid		
No acid	Anatase + Rutile	8.27 (A), 13.83 (R)
HCl	Anatase	27.09 (A)
HCOOH	Anatase + Rutile	9.18 (A), 9.22 (R)
CH_3COOH	Anatase + Rutile	8.27 (A), 10.38 (R)
HNO_3	Anatase + Rutile	11.81 (A), 10.38 (R)
H_2SO_4	Anatase	7.35 (A)
H_3PO_4	Amorphous	-

[a] calculated by applying the Debye-Scherrer formula

Table 18. The phase structure, average crystallite size of P123-TiO_2_$TiOSO_4$ samples.

P123/TiO_2_$TiOSO_4$ sample	Phase structure	Crystallite size (nm)[a]
Effect of reaction temperature		
40c	Anatase	11.85
60c	Anatase	6.35
90c	Anatase	18.37
Effect of Ti concentration		
0.5 M	Anatase	13.69
1 M	Anatase	8.27
3 M	Anatase	6.35
5 M	Anatase	9.02
Effect of acid		
No acid	Anatase	18.37
HCl	Anatase	27.37
HCOOH	Anatase	23.35
CH_3COOH	Anatase	27.37
HNO_3	Anatase	33.08
H_2SO_4	Anatase	23.35
H_3PO_4	Anatase	13.69

[a] calculated by applying the Debye-Scherrer formula

Table 19. The percentage of each phase of P123-TiO_2_$TiCl_4$ samples.

P123/TiO_2_$TiCl_4$ sample	% Anatase	% Rutile	% Amorphous
Effect of reaction temperature			
40c	30.21	-	69.79
60c	9.25	3.70	87.05
90c	9.45	4.00	86.55
Effect of water content			
60w	9.25	3.70	87.05
100w	25.75	8.16	66.09
200w	16.77	9.67	73.56
300w	3.93	3.70	92.37
Effect of acid			
No acid	9.25	3.70	87.05
HCl	2.86	-	97.14
HCOOH	15.70	9.90	74.40
CH_3COOH	7.39	19.42	87.25
HNO_3	7.72	5.36	72.86
H_2SO_4	28.68	-	71.32
H_3PO_4	-	-	100.00

Table 20. The percentage of each phase of P123-TiO_2_$TiOSO_4$ samples.

P123/TiO_2_$TiOSO_4$ sample	% Anatase	% Rutile	% Amorphous
Effect of reaction temperature			
40c	10.91	-	89.09
60c	30.67	-	69.33
90c	23.02	-	76.98
Effect of Ti concentration			
0.5 M	19.03	-	80.97
1 M	14.57	-	85.43
3 M	30.67	-	69.33
5 M	15.24	-	84.76
Effect of acid			
No acid	30.67	-	69.33
HCl	18.56	-	81.44
HCOOH	17.77	-	82.23
CH_3COOH	13.91	-	86.09
HNO_3	14.57	-	85.43
H_2SO_4	13.11	-	82.10
H_3PO_4	9.38	-	86.89

The N_2 adsorption isotherms of P123-TiO_2_$TiCl_4$ samples and P123-TiO_2_$TiOSO_4$ samples are shown in Figures 78 and 79, respectively. The nitrogen adsorption-desorption isotherms corresponding to these P123-TiO_2_$TiCl_4$ samples and P123-TiO_2_$TiOSO_4$ samples are a combination of isotherm Type I and IV (BDDT classification) (Ryu, *et al.*, 1999) with two distinct regions; at low relative pressure, the isotherm exhibits high adsorption, indicating that the sample contains micropore (Type I) indicating the micropore and mesoporous structure was formed and at high relative presure, the curve exhibits the presence of mesopores (Type IV). In this study, the hysteresis loop in the isotherm could not be determined due to the limited capability of the equipment (SA3100 coulter) which was not able to do the desorption study. The presence of micropore could be checked by plotting the adsorbed layer called "*t*-plot" as seen in Figures 80-81. The *t*-plot data of most P123-TiO_2_$TiCl_4$ samples showed linear part not passing the origin indicating that they contained both mesoporous and microporous structure (Khalil, *et al.*, 2001), except the 40c_P123-TiO_2_$TiCl_4$ sample that showed microporous structure. All P123-TiO_2_$TiOSO_4$ samples showed linear t-plot not passing the origin indicating either mesopore or micropore were presence for all samples. The plots of the pore size distribution determined by the BJH (Barrett-Joyner-Halenda) method are shown in Figures 82-83 for P123-TiO_2_$TiCl_4$ samples and P123-TiO_2_$TiOSO_4$ samples, respectively. The P123-TiO_2_$TiCl_4$ samples show bimodal pore size distribution consisting of intra-particle pores (4-8 nm) and larger inter-particle pores (8-100 nm). Usually, there are two types of pores present in the bimodal pore size distribution. One is made from the intra-aggregated pores at lower P/P_o range (the pores within the hard aggregates) and the other is larger inter-aggregated pores in the higher P/P_o range arising from hard aggregated (the void between hard aggregates) (Yu, *et al.*, 2003). All P123-TiO_2_$TiOSO_4$ samples showed narrow pore size distribution with intra-aggregated pores at lower P/P_o range (the pores within the hard aggregates). The specific surface area, pore volume, pore size of P123-TiO_2_$TiCl_4$ samples and P123-TiO_2_$TiOSO_4$ samples are given in Table 21 and Table 22, respectively.

a) Effect of reaction temperature

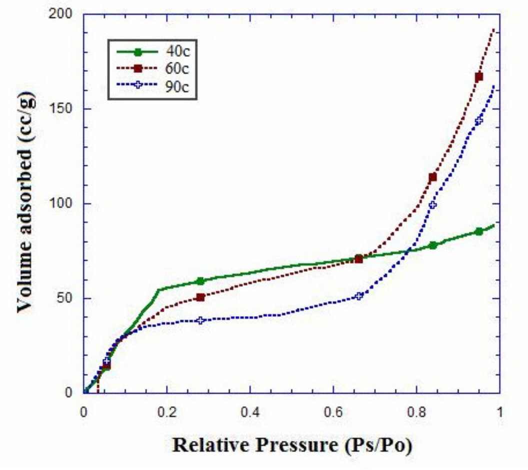

b) Effect of water content

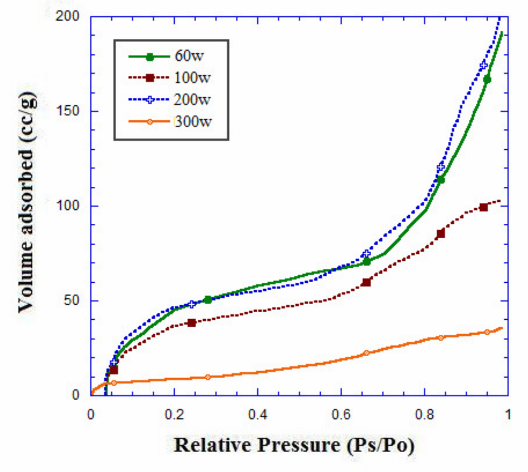

c) Effect of acid

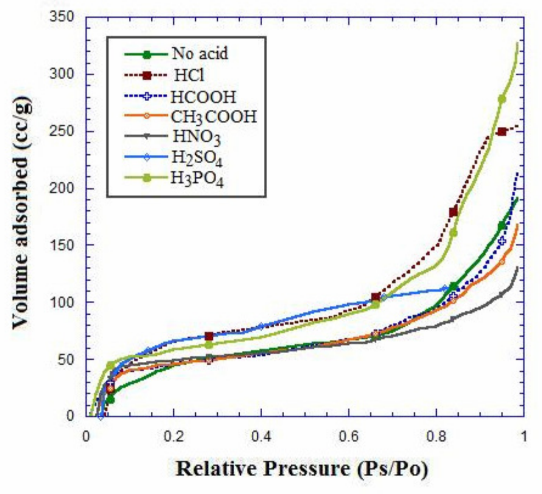

Figure 78. N_2 adsorption isotherm of P123-TiO_2_$TiCl_4$ samples: a) effect of reaction temperature, b) effect of water content, and c) effect of acid catalyst.

a) Effect of reaction temperature

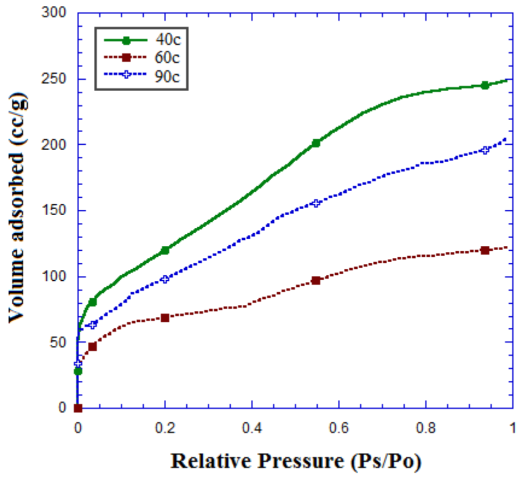

b) Effect of Ti content

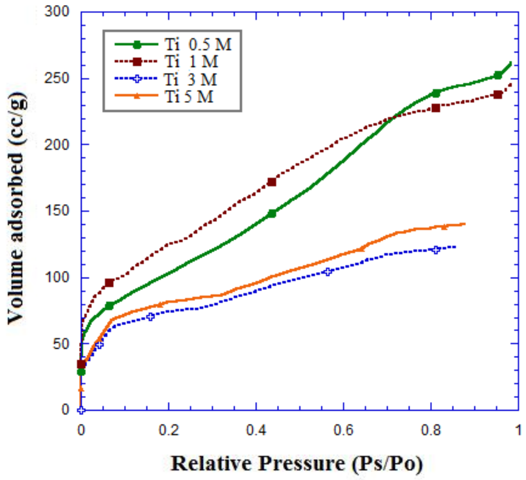

c) Effect of acid

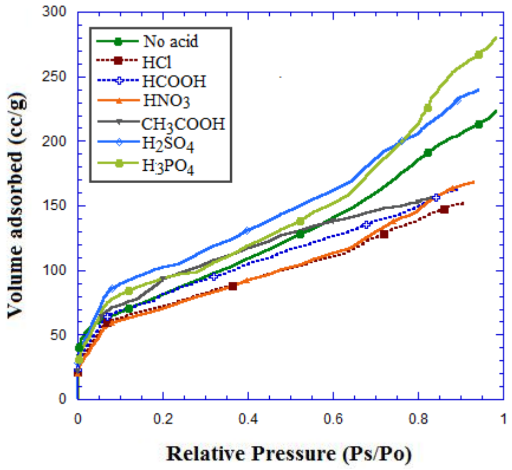

Figure 79. N_2 adsorption isotherm of P123-TiO_2_$TiOSO_4$ samples: a) effect of reaction temperature, b) effect of Ti content, and c) effect of acid catalyst.

a) Effect of reaction temperature

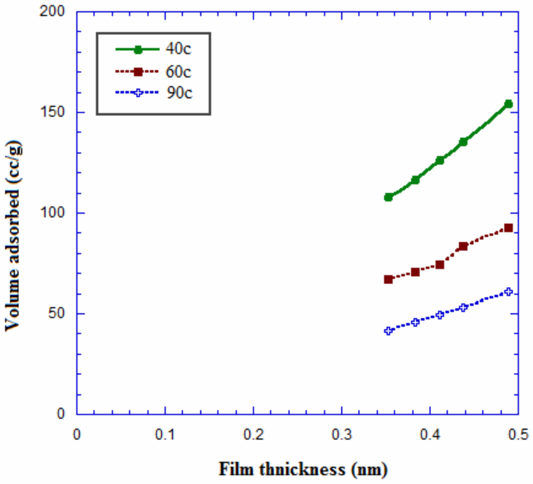

a) Effect of water content

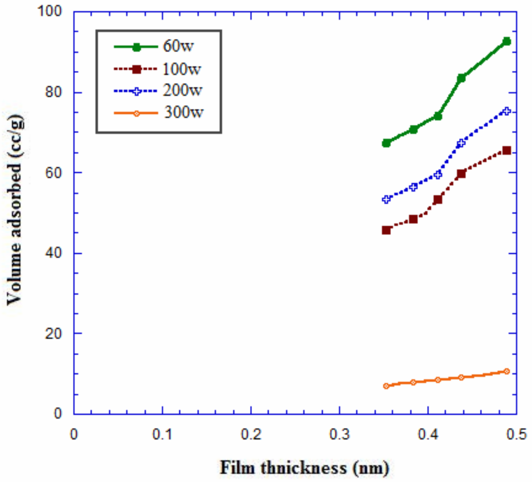

b) Effect of acid

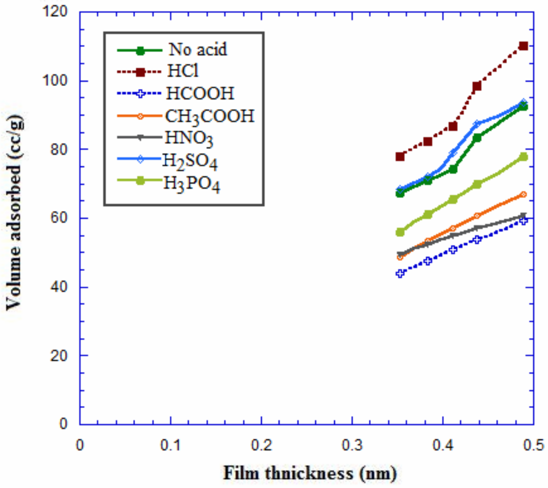

Figure 80. *t*-plot of P123-TiO_2_$TiCl_4$ samples: a) effect of reaction temperature, b) effect of water content, and c) effect of acid catalyst.

a) Effect of reaction temperature

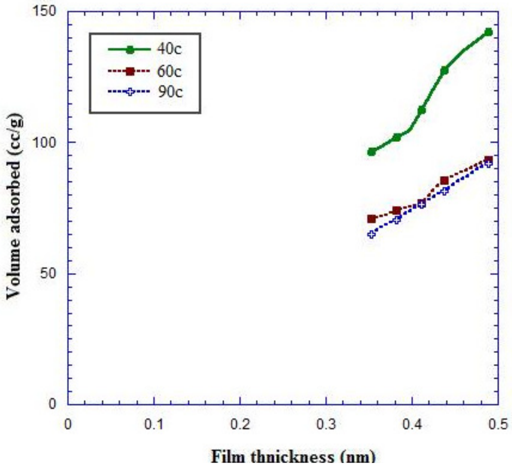

b) Effect of Ti content

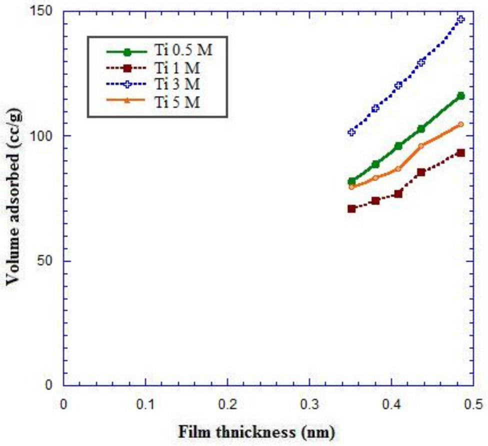

c) Effect of acid

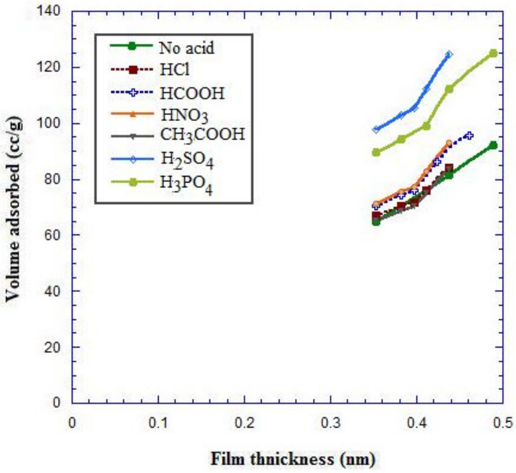

Figure 81. *t*-plot of P123-TiO_2_$TiOSO_4$ samples: a) effect of reaction temperature, b) effect of Ti content, and c) effect of acid catalyst.

a) Effect of reaction temperature

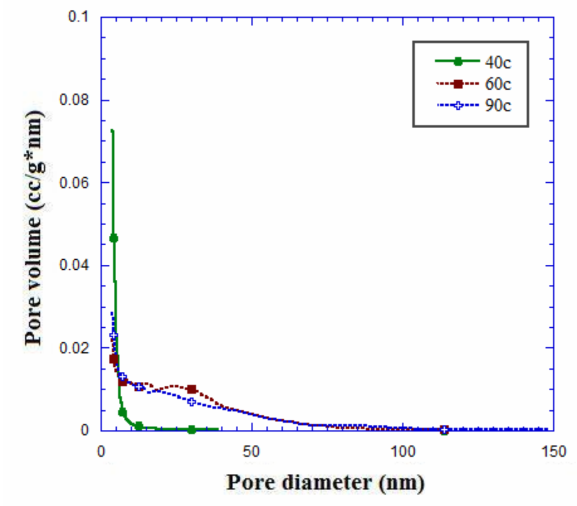

b) Effect of water content

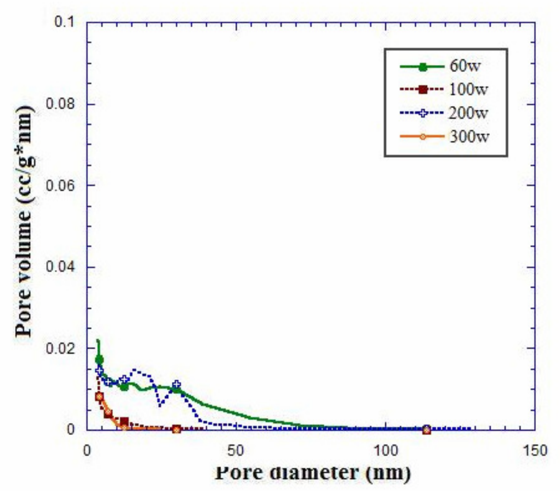

c) Effect of acid

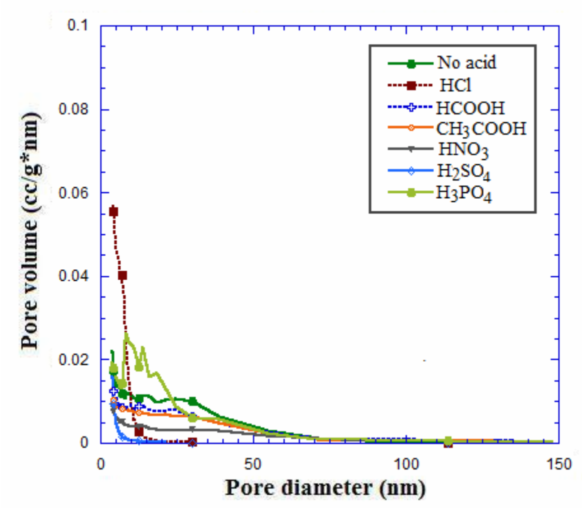

Figure 82. Pore size distribution of P123-TiO_2_$TiCl_4$ samples: a) effect of reaction temperature, b) effect of water content, and c) effect of acid catalyst.

a) Effect of reaction temperature

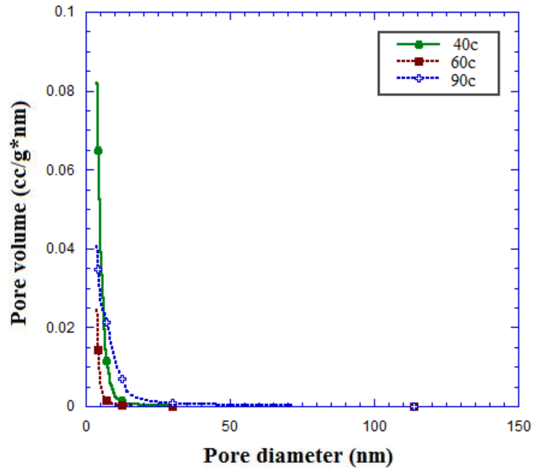

b) Effect of Ti content

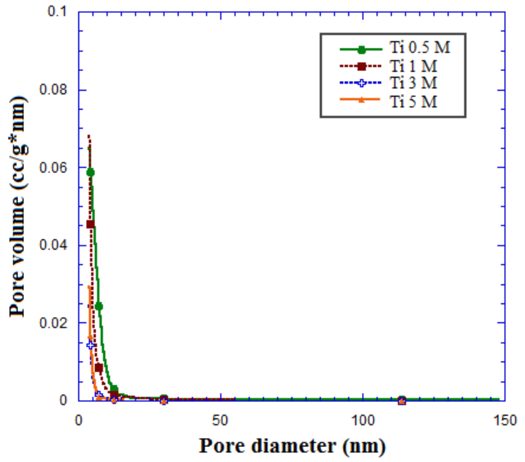

c) Effect of acid

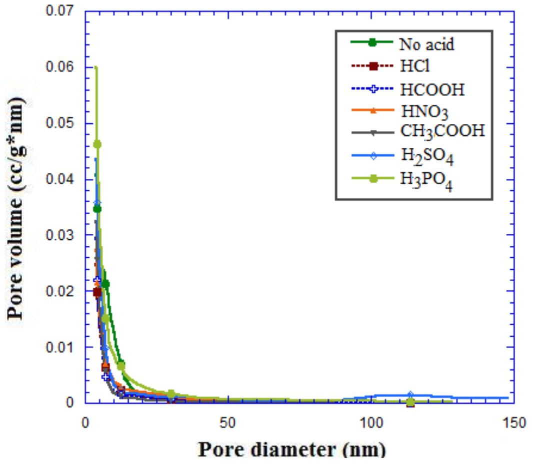

Figure 83. Pore size distribution of P123-TiO_2_$TiOSO_4$ samples: a) effect of reaction temperature, b) effect of Ti content, and c) effect of acid catalyst.

Table 21. The specific surface area, pore volume, pore size of P123-TiO_2_$TiCl_4$ samples.

P123/TiO_2 sample	Surface area (m^2/g)	Type of isotherm	BJH pore volume (cm^3/g)
Effect of reaction temperature			
40c	492	Type I	0.134
60c	306	Type I and IV	0.503
90c	194	Type I and IV	0.491
Effect of water content			
60w	306	Type I and IV	0.503
100w	205	Type I and IV	0.066
200w	240	Type I and IV	0.405
300w	33	Type III	0.048
Effect of acid			
No acid	306	Type I and IV	0.503
HCl	354	Type I and IV	0.274
HCOOH	195	Type I and IV	0.419
CH_3COOH	221	Type I and IV	0.369
HNO_3	202	Type I and IV	0.247
H_2SO_4	293	Type I and IV	0.035
H_3PO_4	253	Type I and IV	0.601

Table 22. The specific surface area, pore volume, pore size of P123-TiO_2_$TiOSO_4$ samples.

P123/TiO_2 sample	Surface area (m^2/g)	Type of isotherm	BJH pore volume (cm^3/g)
Effect of reaction temperature			
40c	438.54	Type I and IV	0.188
60c	305.76	Type I and IV	0.040
90c	295.12	Type I and IV	0.235
Effect of Ti concentration			
0.5 M	375.83	Type I and IV	0.272
1 M	470.12	Type I and IV	0.158
3 M	305.76	Type I and IV	0.040
5 M	346.69	Type I and IV	0.046
Effect of acid			
No acid	295.12	Type I and IV	0.235
HCl	281.65	Type I and IV	0.114
HCOOH	305.31	Type I and IV	0.114
CH_3COOH	308.83	Type I and IV	0.106
HNO_3	280.21	Type I and IV	0.142
H_2SO_4	420.42	Type I and IV	0.252
H_3PO_4	409.92	Type I and IV	0.286

UV-Vis diffused reflectance spectroscopy is used to probe the band structure or molecular energy levels in the materials since UV-Vis light excitation creates photo-generated electron and holes (Reddy, *et al.*, 2001). Figures 84-85 shows the UV-Vis absorption spectra of the P123-TiO_2_$TiCl_4$ samples and P123-TiO_2_$TiOSO_4$ samples, respectively. The strong broad band seen from 200 to 380 nm, indicates the existence of Ti-skeleton in the structure of the sample (Dai, *et al.*, 2002). The onset wavelengths (λ_{onset}) of as-prepared samples were in the range 378-420 nm corresponding to the electron transition from the valence band which composed of 2p atomic orbitals of oxygen (π bonding orbitals) to the conduction band originated from the 3d atomic orbitals of titanium (Sanchez, *et al.*, 1995). The absorption edge was determined by the linear extrapolation of the steep part of the UV adsorption toward the baseline and the band gap energy was calculated from Plank's equation ($E_g = hc/\lambda_{onset}$). The calculated band gap energy of P123-TiO_2_$TiCl_4$ samples and P123-TiO_2_$TiOSO_4$ samples are given in Tables 23-24.

To establish the type of band-to-band transition in the synthesized titanium dioxide particles, the absorption data were fitted to equations for both indirect or direct bandgap transitions. Figures 86 - 87 showed the plot of $(\alpha E_{phot})^{1/2}$ versus E_{phot} for an direct transition and Figures 88 - 89 showed the of $(\alpha E_{phot})^2$ versus E_{phot} for a indirect transition, respectively. The value of E_{phot} extrapolated to $\alpha = 0$ gives an absorption energy which corresponds to a band gap energy (E_g), as seen in Figures 86-89 for both direct and indirect transitiond of the synthesized P123-TiO_2 samples. The results appeared though not a perfect fit but line close to the direct transition assignment (Tables 23 and Table 24). Therefore, for this study, the band-to-band transitions in most of the synthesized titanium dioxide samples were fitted to the direct bandgap transitions. This result is in agreement with the work of Serpone *et al.*, (1995) who had established the mechanism believed being operatively in nanophase titanium dioxide. They had attributed the spectral blue shifts due to quantum size effects in titanium dioxide colloids as a result of direct transitions (Serpone, *et al.*, 1995).

Table 23. The band gap energy calculated from Plank's equation, direct and indirect band gap energy of P123-TiO_2_$TiCl_4$ samples.

P123/TiO_2 sample	λ_{onset} (nm)	E_g [a] (eV)	Direct E_g [b] (eV)	Indirect E_g [c] (eV)
Effect of reaction temperature				
40c	406	3.05	3.20	2.89
60c	408	3.04	3.16	2.94
90c	408	3.04	3.20	2.93
Effect of water content				
60w	408	3.04	3.15	2.92
100w	403	3.08	3.23	2.93
200w	405	3.06	3.16	2.96
300w	412	3.01	3.14	2.88
Effect of acid				
No acid	408	3.04	3.15	2.92
HCl	410	3.02	3.17	2.89
HCOOH	407	3.05	3.21	2.92
CH_3COOH	408	3.04	3.12	2.92
HNO_3	406	3.05	3.13	2.97
H_2SO_4	405	3.06	3.21	2.88
H_3PO_4	382	3.25	3.40	3.04

[a] Calculated from $E_g=1240/\lambda_{onset}$

[b] Estimated from plot of $(\alpha E_{phot})^{1/2}$ versus E_{phot} by extrapolating to $\alpha = 0$ give direct E_g

[c] Estimated from plot of $(\alpha E_{phot})^{2}$ versus E_{phot} by extrapolating to $\alpha = 0$ give indirect E_g

Table 24. The band gap energy calculated from Plank's equation, direct and indirect band gap energy of P123-TiO_2_$TiOSO_4$ samples.

P123/TiO_2 sample	λ_{onset} (nm)	E_g[a] (eV)	Direct E_g[b] (eV)	Indirect E_g[c] (eV)
Effect of reaction temperature				
40c	403	3.08	3.24	2.87
60c	402	3.08	3.20	2.86
90c	390	3.18	3.28	3.00
Effect of Ti concentration				
0.5 M	390	3.18	3.33	2.92
1 M	402	3.08	3.30	2.95
3 M	402	3.08	3.18	2.85
5 M	396	3.13	3.23	2.87
Effect of acid				
No acid	390	3.18	3.28	3.00
HCl	394	3.15	3.29	2.95
HCOOH	393	3.16	3.28	2.98
CH_3COOH	395	3.14	3.29	2.96
HNO_3	392	3.16	3.29	2.97
H_2SO_4	396	3.13	3.26	2.94
H_3PO_4	389	3.19	3.31	2.99

[a] Calculated from $E_g=1240/\lambda_{onset}$

[b] Estimated from plot of $(\alpha E_{phot})^{1/2}$ versus E_{phot} by extrapolating to $\alpha = 0$ give direct E_g

[c] Estimated from plot of $(\alpha E_{phot})^{2}$ versus E_{phot} by extrapolating to $\alpha = 0$ give indirect E_g

a) Effect of reaction temperature

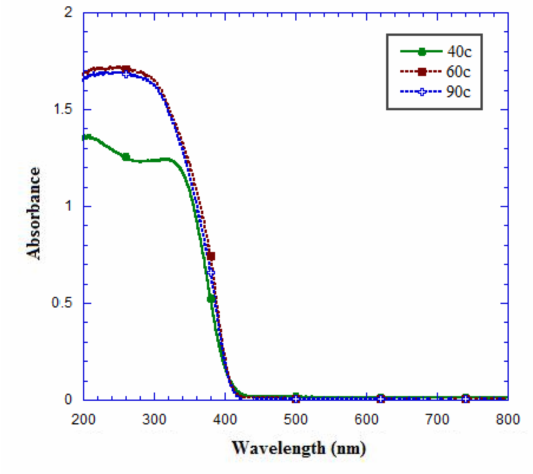

b) Effect of water content

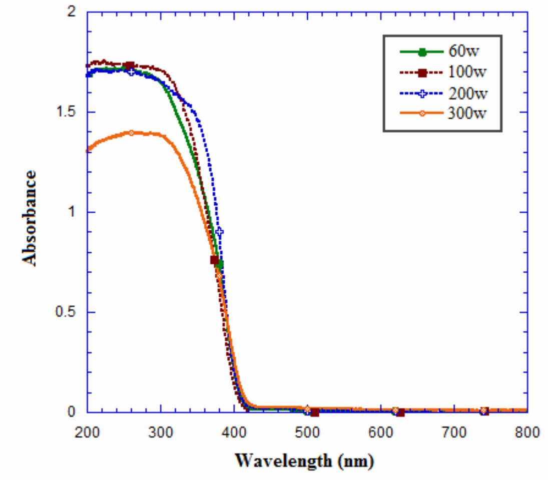

c) Effect of acid

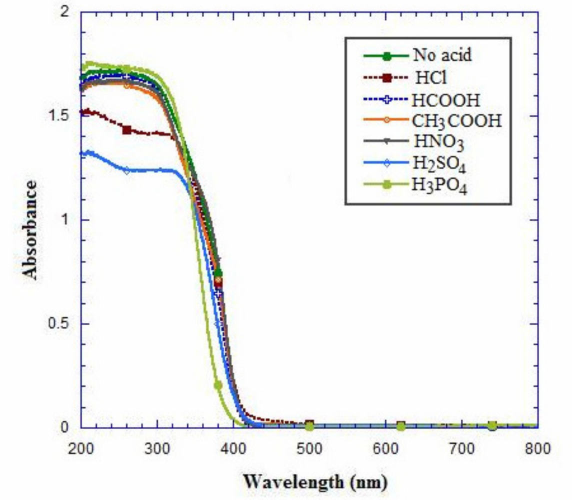

Figure 84. DRS spectra of P123-TiO_2_$TiCl_4$ samples: a) effect of reaction temperature, b) effect of water content, and c) effect of acid catalyst.

a) Effect of reaction temperature

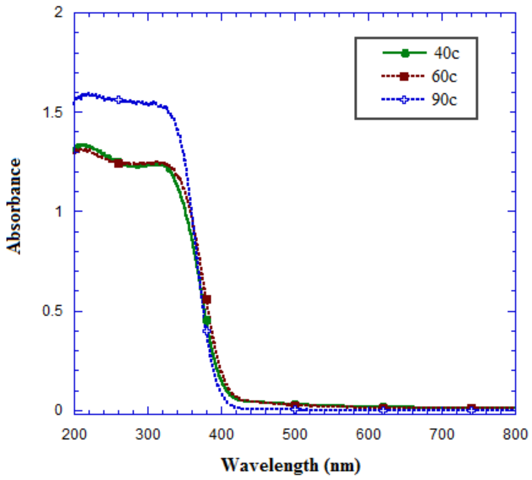

b) Effect of Ti content

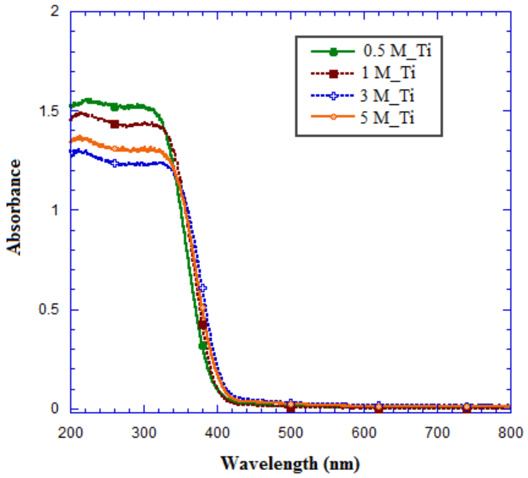

c) Effect of acid

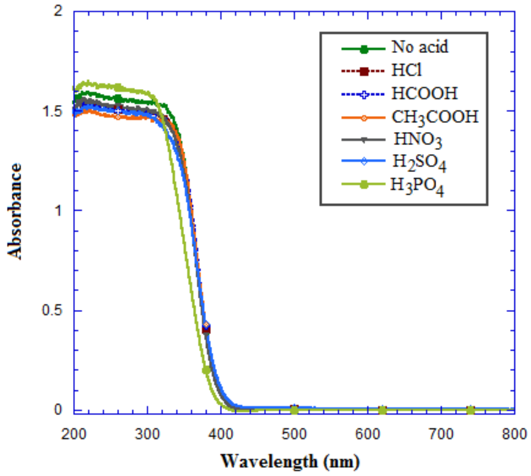

Figure 85. DRS spectra of P123-TiO_2_$TiOSO_4$ samples: a) effect of reaction temperature, b) effect of Ti content, and c) effect of acid catalyst.

a) Effect of reaction temperature

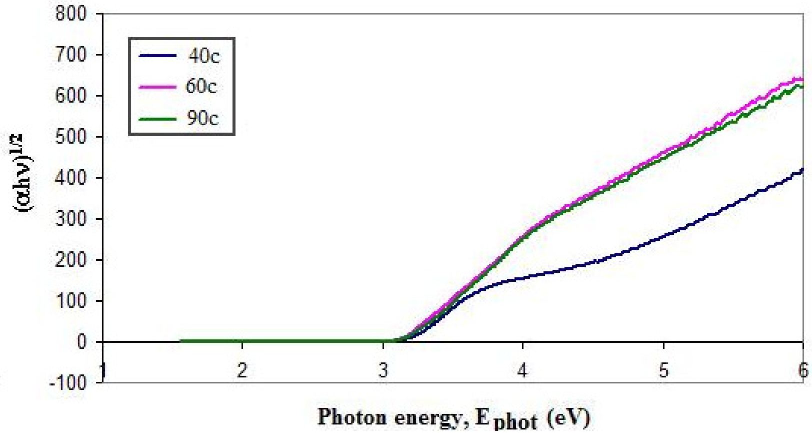

b) Effect of water content

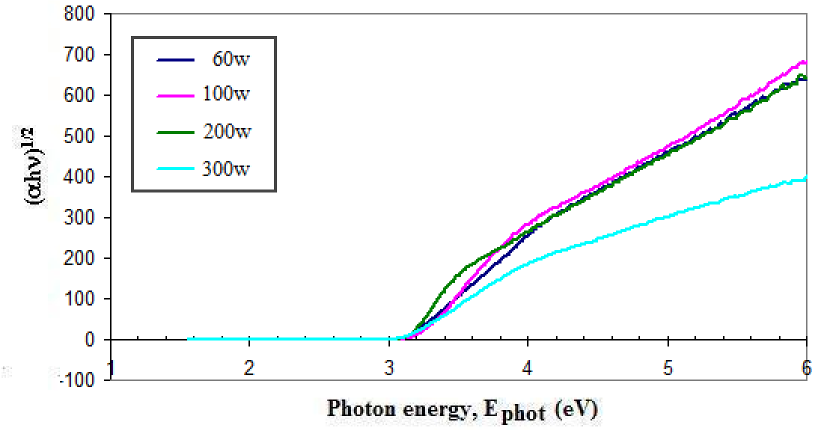

c) Effect of acid

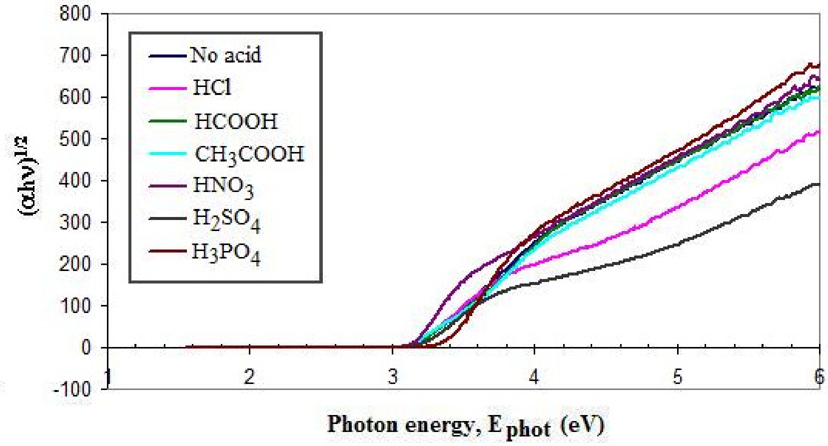

Figure 86. Plot of $(\alpha\ h\nu)^{1/2}$ versus E_{phot} for the direct transition of P123-TiO_2_$TiCl_4$ samples.

a) Effect of reaction temperature

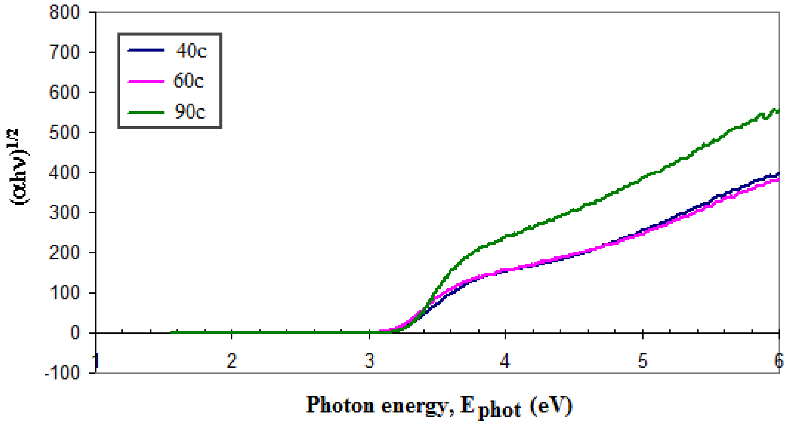

b) Effect of Ti content

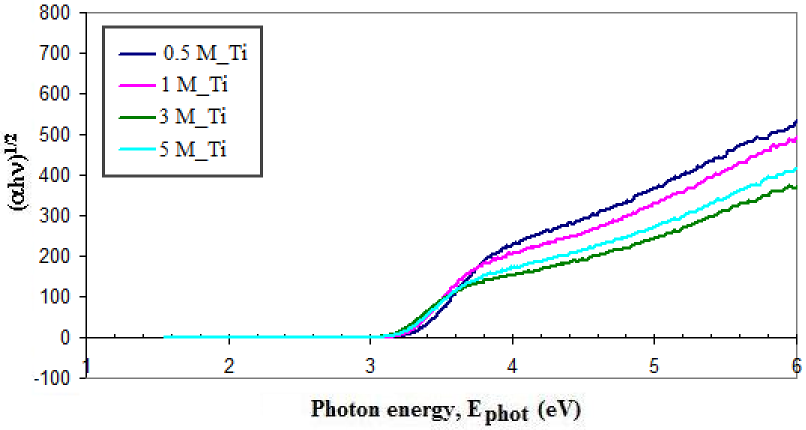

c) Effect of acid

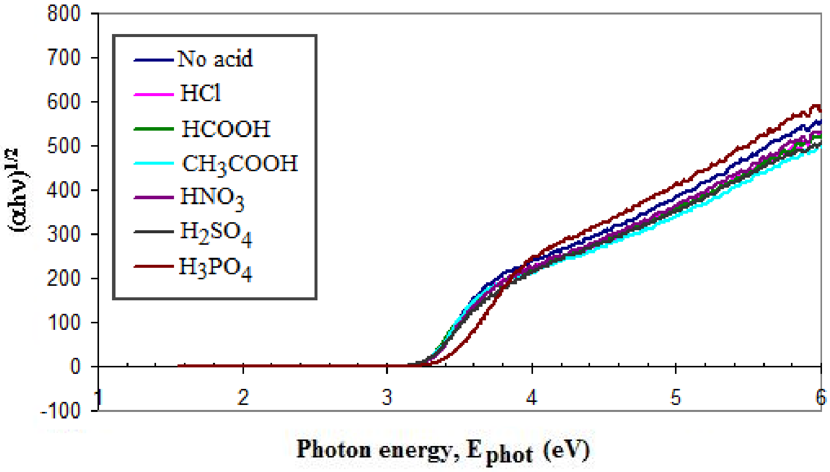

Figure 87. Plot of $(\alpha\ h\nu)^{1/2}$ versus E_{phot} for the direct transition of P123-TiO_2_$TiOSO_4$ samples.

a) Effect of reaction temperature

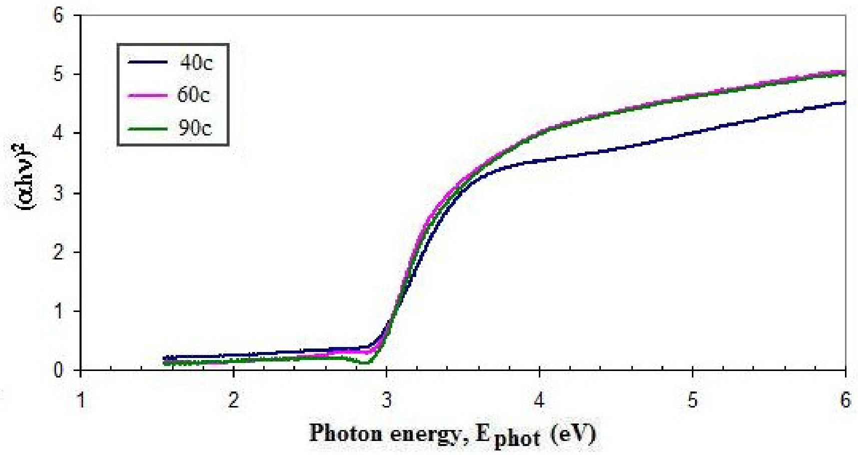

b) Effect of water content

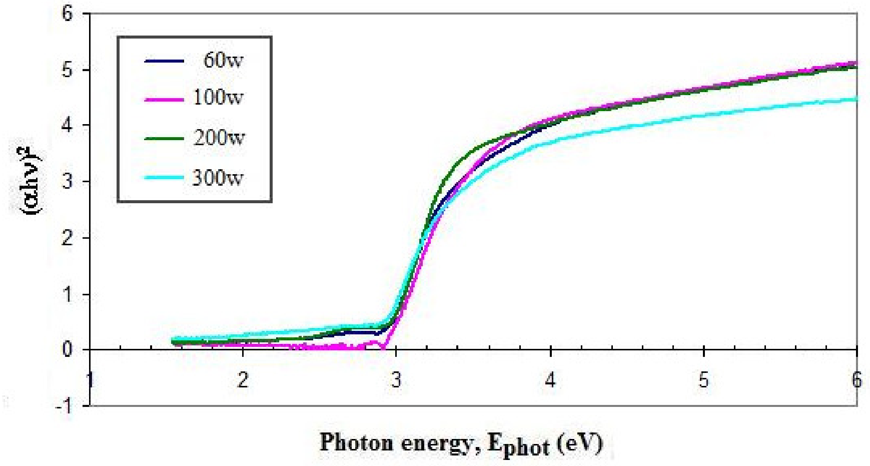

c) Effect of acid

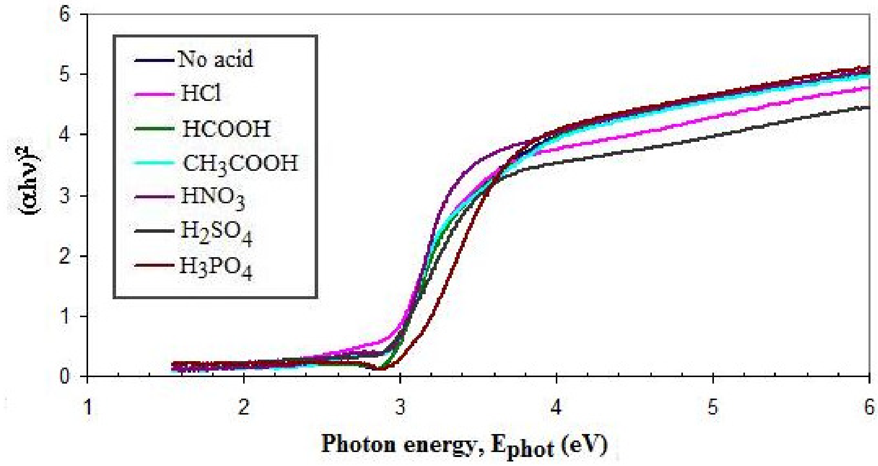

Figure 88. Plot of $(\alpha\ h\nu)^2$ versus E_{phot} for the indirect transition of P123-TiO_2_$TiCl_4$ samples.

a) Effect of reaction temperature

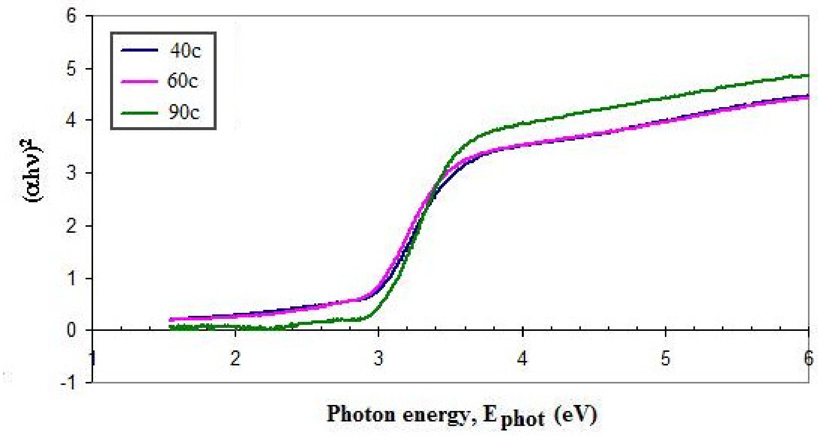

b) Effect of Ti content

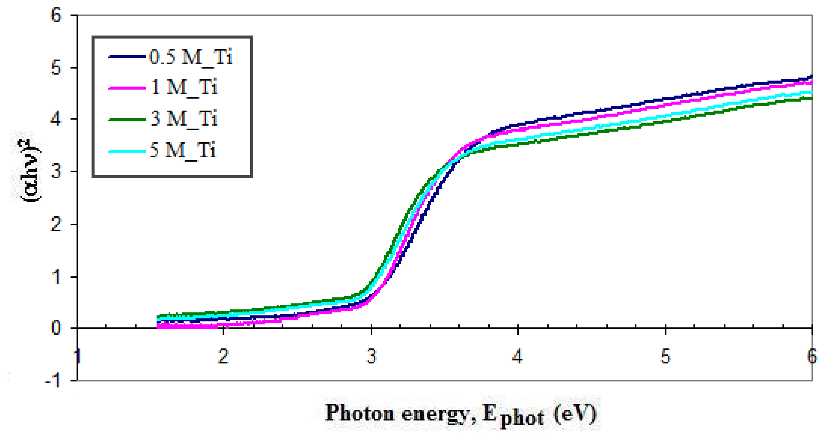

c) Effect of acid

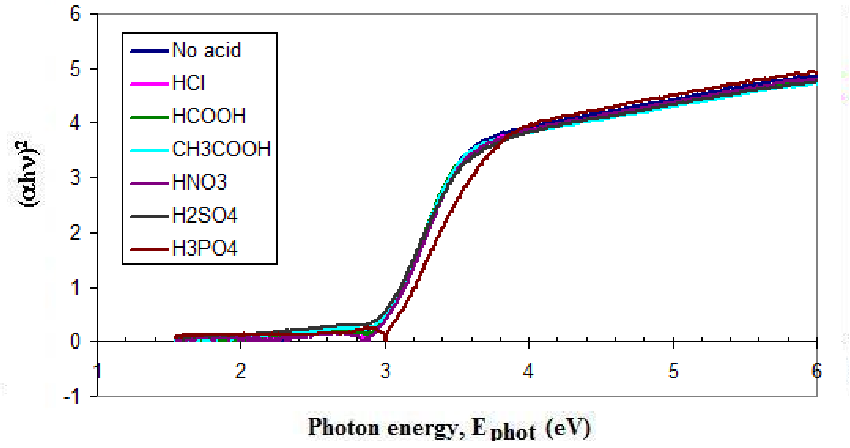

Figure 89. Plot of $(\alpha\ h\nu)^2$ versus E_{phot} for the indirect transition of P123-TiO_2_$TiOSO_4$ samples.

The morphology of the as-synthesized TiO_2 samples was investigated by SEM and TEM techniques as seen in Figures 90-93. Figures 90-91 show SEM images of P123-TiO_2_$TiCl_4$ and P123-TiO_2_$TiOSO_4$ samples at low and high magnification. Most of SEM images reveal dense and highly aggregated particles for the P123-TiO_2_$TiCl_4$ samples. It is interesting to see that only 100w P123-TiO_2_$TiCl_4$ sample shows uniform and spherical particles. TEM image consists of anatase and rutile phases with spherical and tenuous fibers shaped of anatase and rutile, respectively, as shown in Figure 96. TEM results reveal the aggregation of anatase crystallites coated on the fiber shape of rutile phase to form larger spherical particles in agreement with SEM image. The pore channels were found near the surface of sample where the pore was formed between the anatase crystallines.

A1) Effect of reaction temperature_low magnification

40c 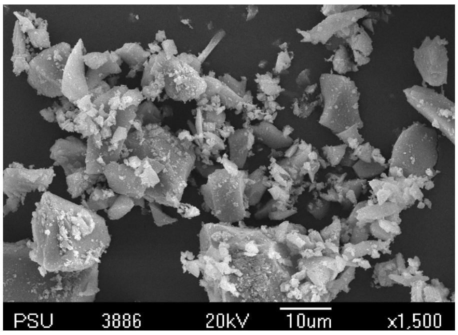 	60c 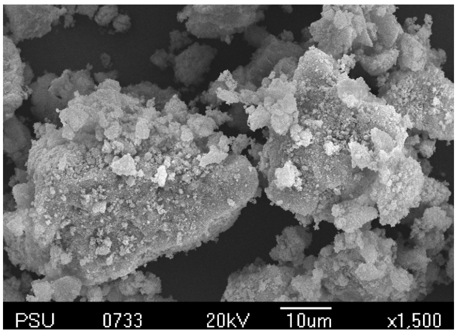
90c 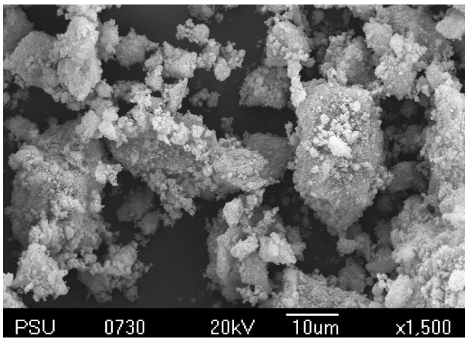 	

A2) Effect of reaction temperature_high magnification

40c

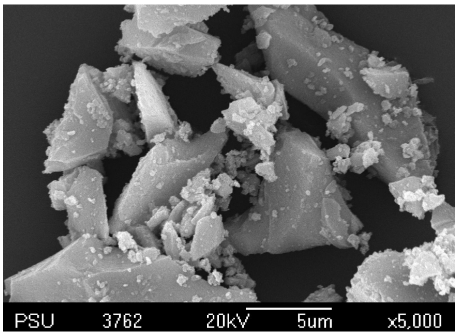

60c

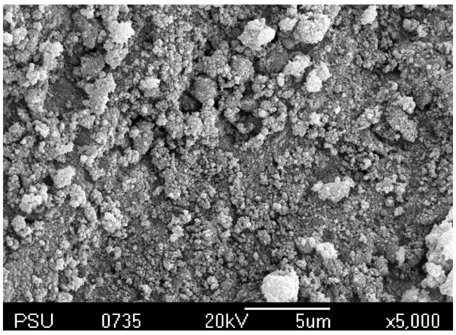

90c

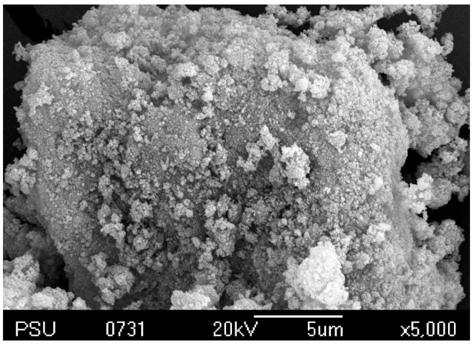

B1) Effect of water content_low magnification

60w

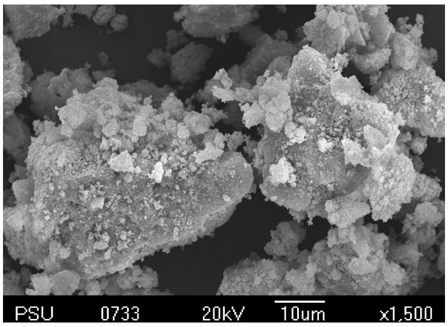

100w

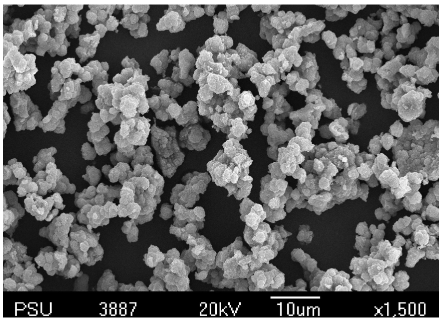

200w

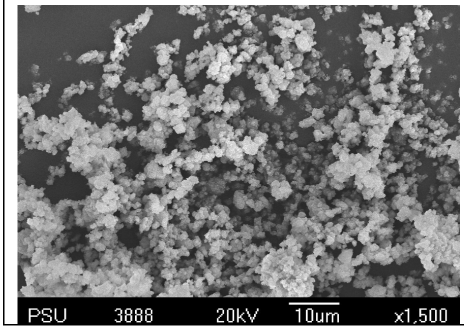

300w

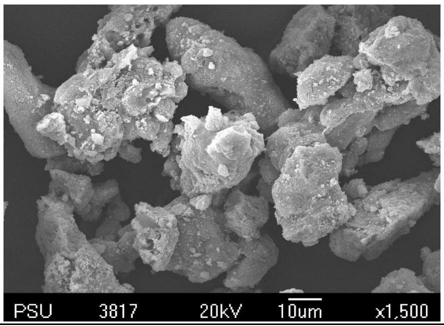

B2) Effect of water content_high magnification

60w 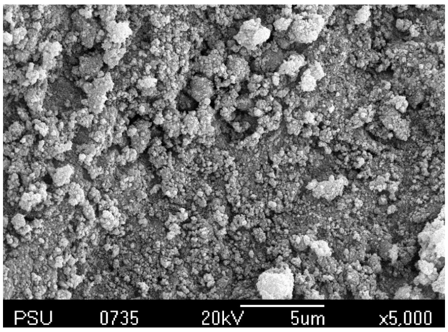 	100w 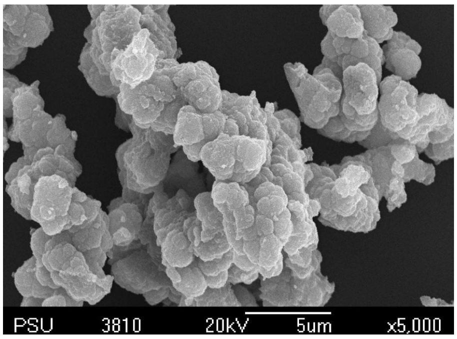
200w 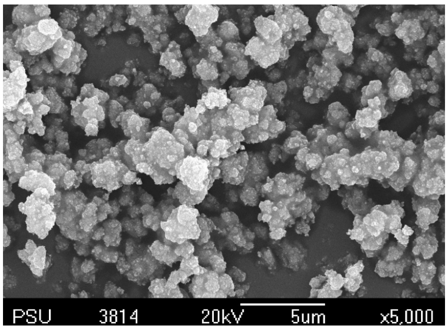 	300w 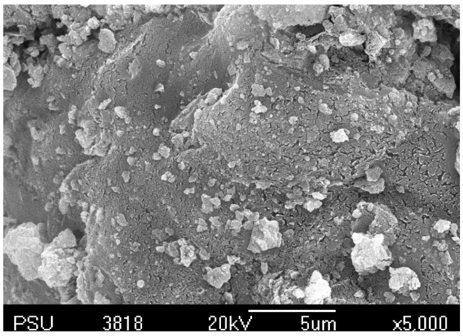

C1) Effect of acid_low magnification

HCl 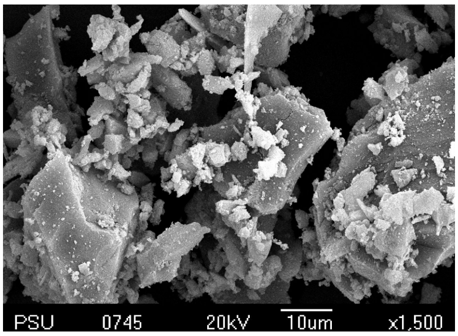 	HCOOH 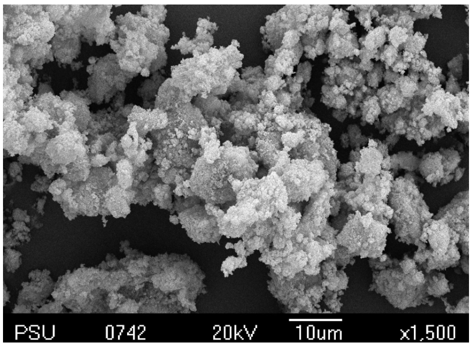

CH_3COOH

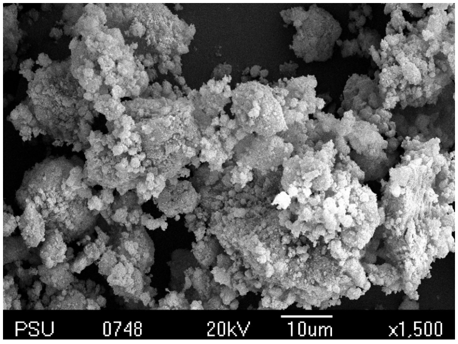

HNO_3

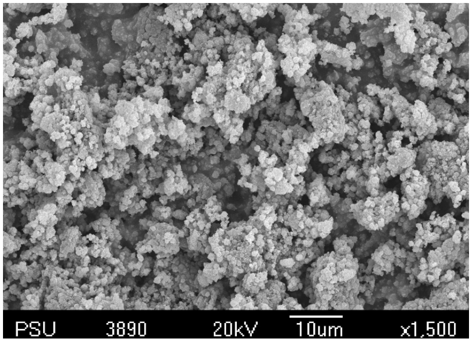

H_2SO_4

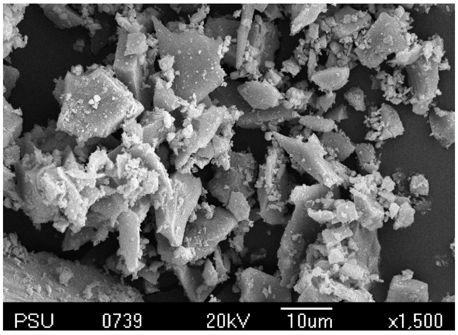

H_3PO_4

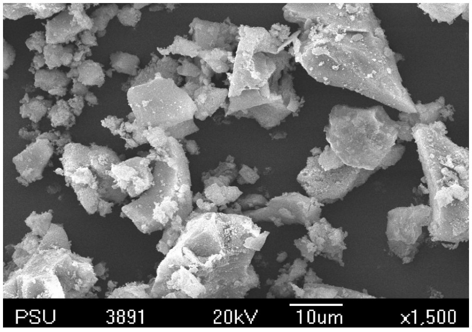

No acid

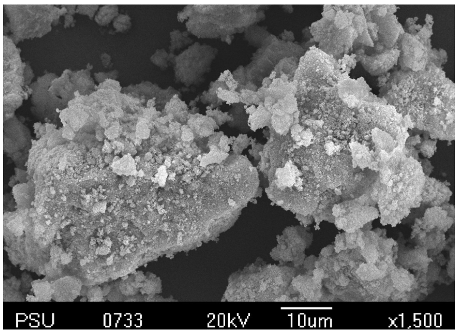

C2) Effect of acid_high magnification

HCl

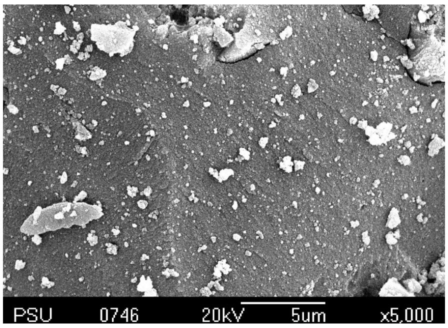

HCOOH

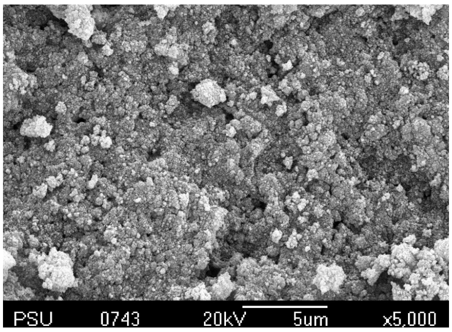

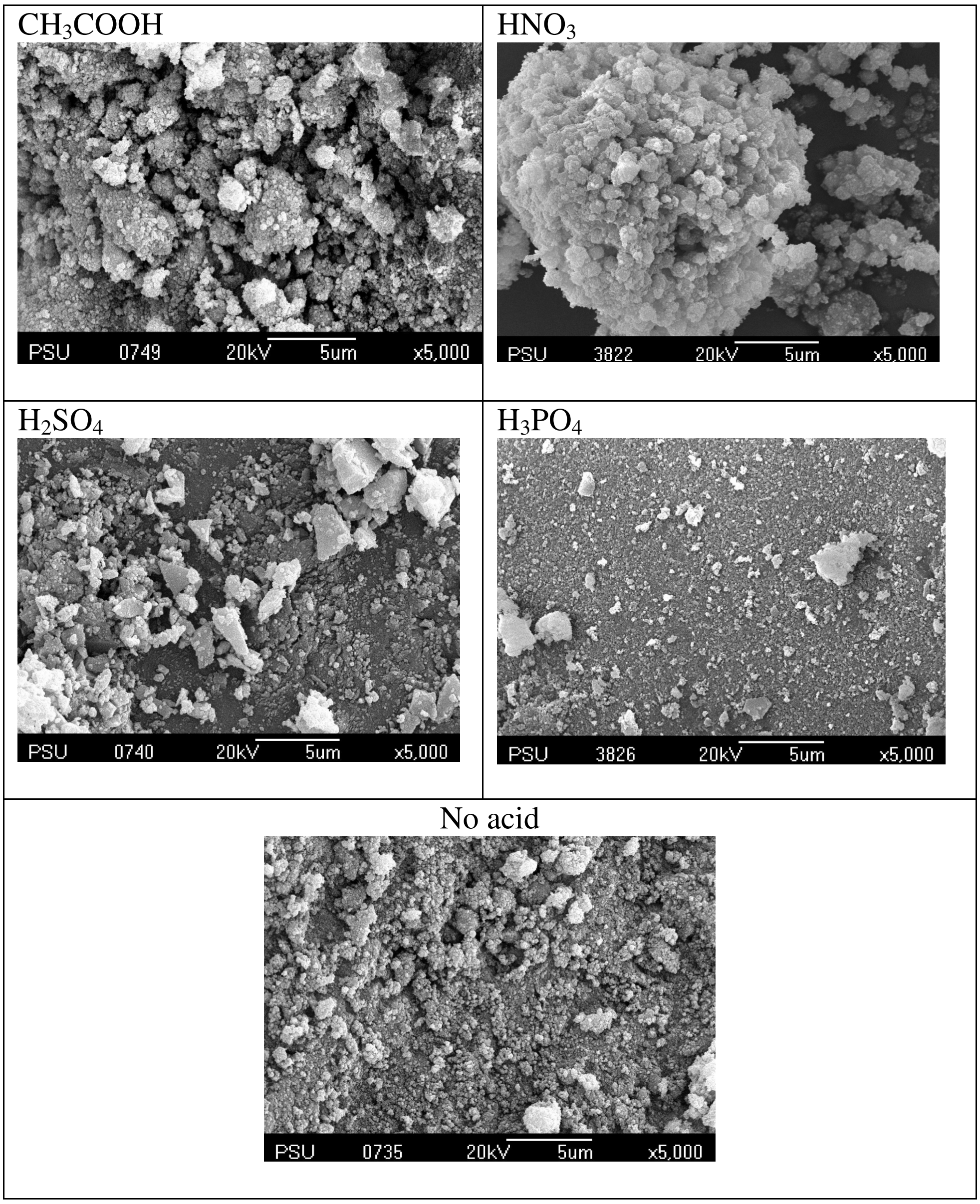

Figure 90. SEM images of P123-TiO_2_$TiCl_4$ samples: A) effect of reaction temperature, B) effect of water content, and C) effect of acid catalyst at low and high magnification.

A1) Effect of reaction temperature_low magnification

40c 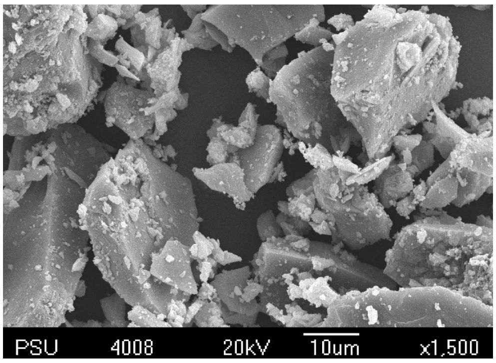 	60c 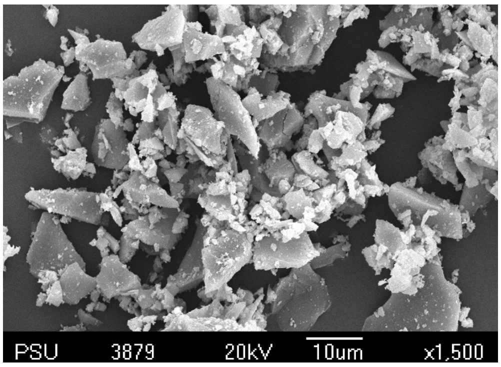
90c 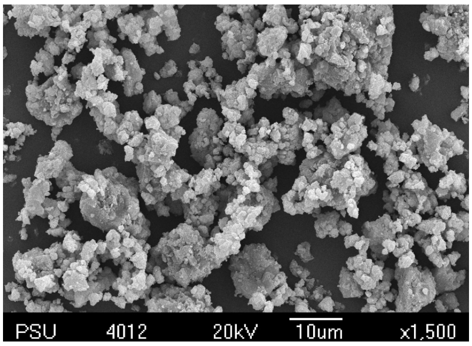 	

A2) Effect of reaction temperature_high magnification

40c 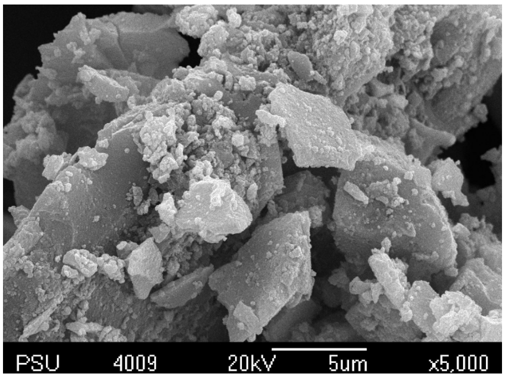 	60c 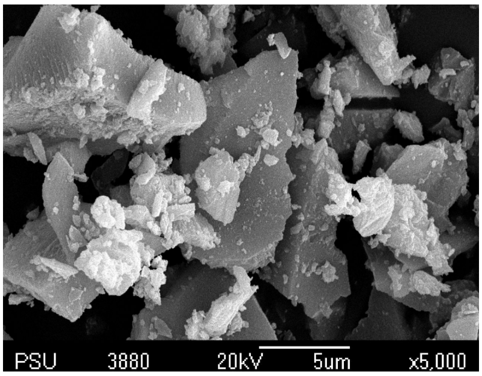

90c

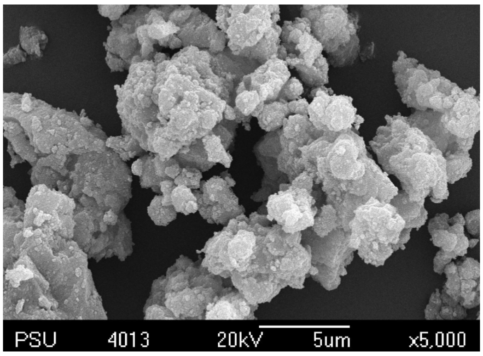

B1) Effect of Ti content_low magnification

0.5 M_Ti

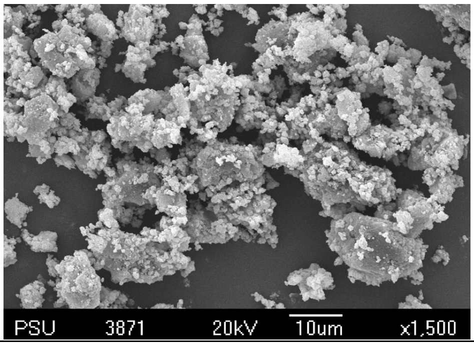

1 M_Ti

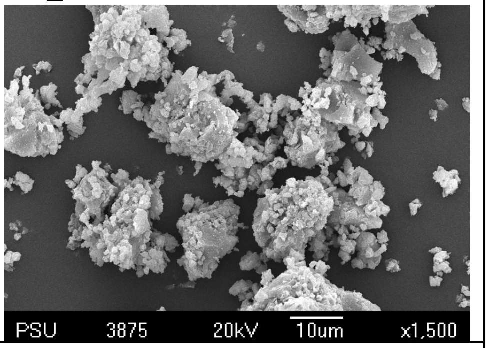

3 M_Ti

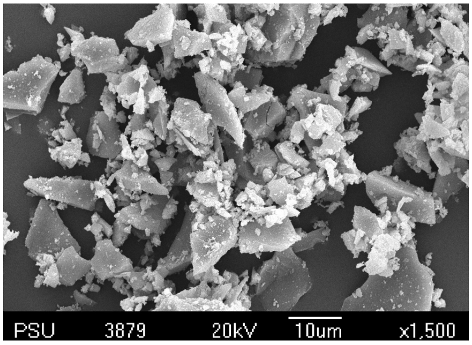

5 M_Ti

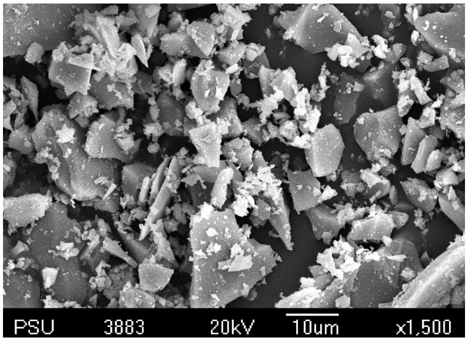

B2) Effect of Ti content_high magnification

0.5 M_Ti

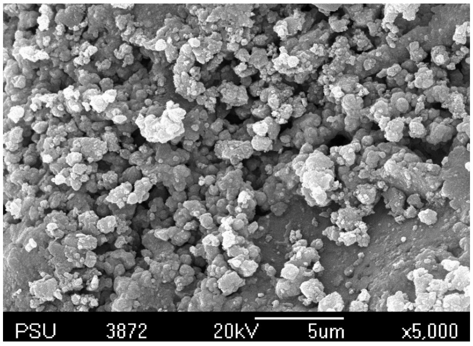

1 M_Ti

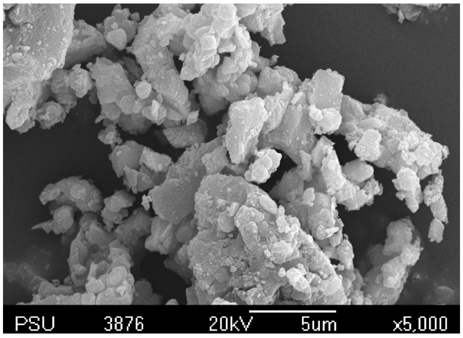

3 M_Ti

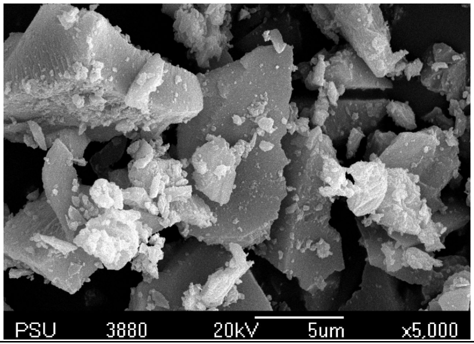

5 M_Ti

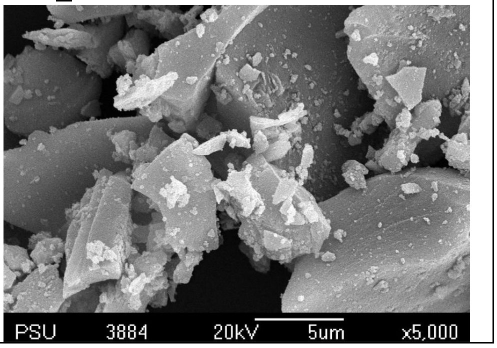

C1) Effect of acid_low magnification

HCl

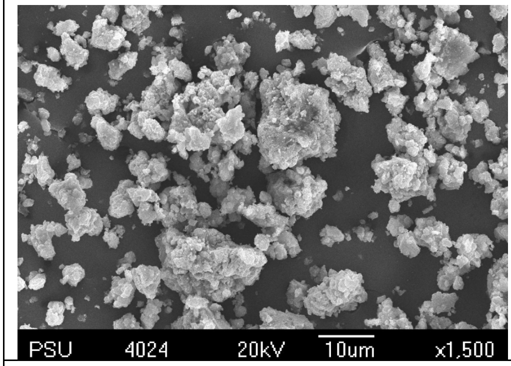

HCOOH

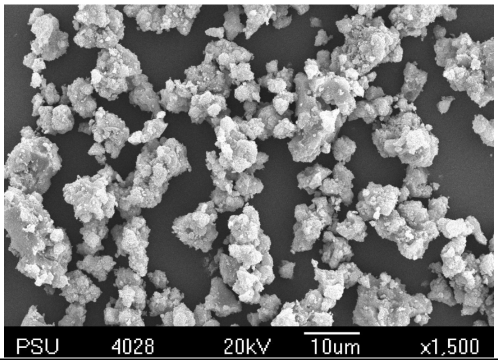

CH_3COOH

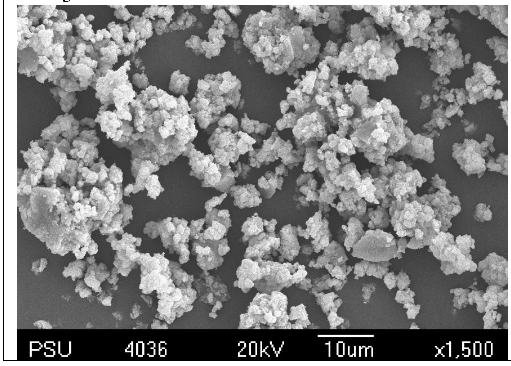

HNO_3

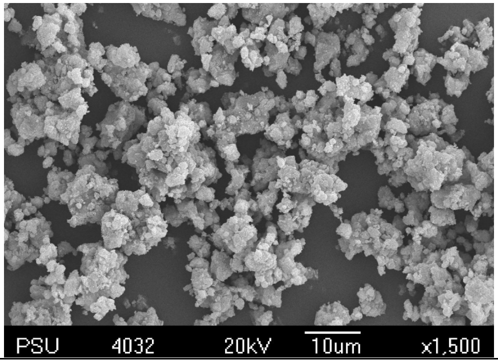

H_2SO_4

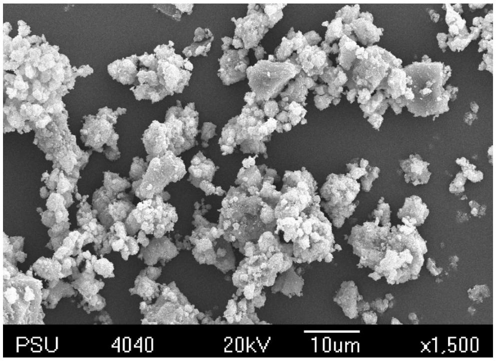

H_3PO_4

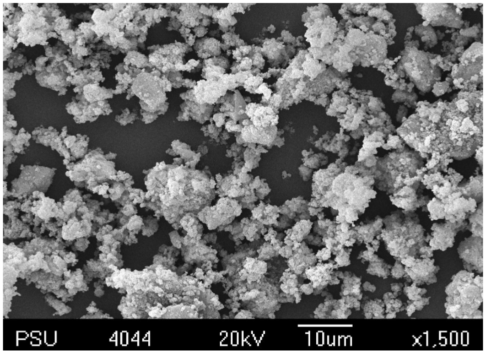

No acid

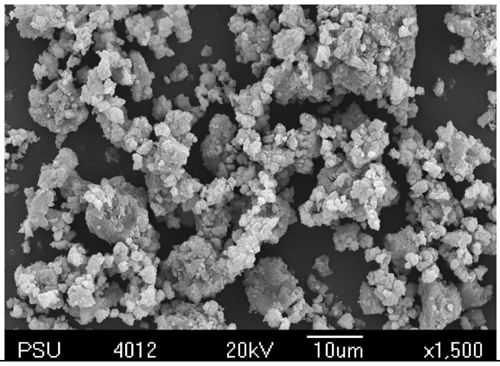

C2) Effect of acid_high magniffication

HCl

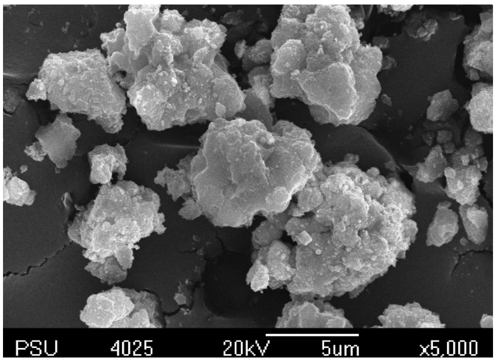

HCOOH

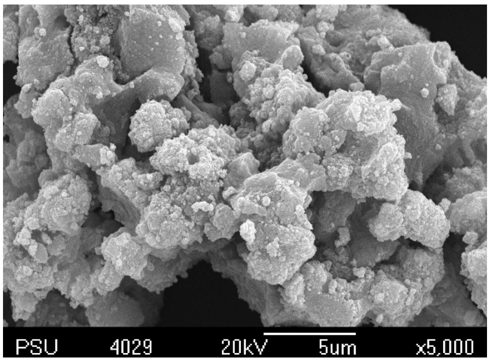

CH_3COOH

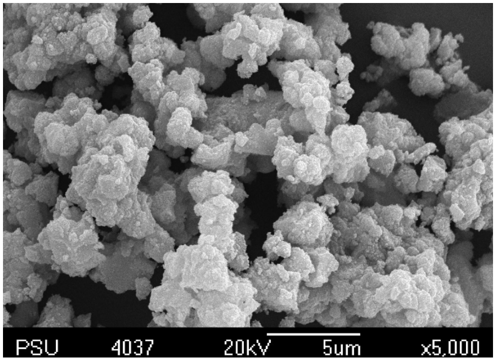

HNO_3

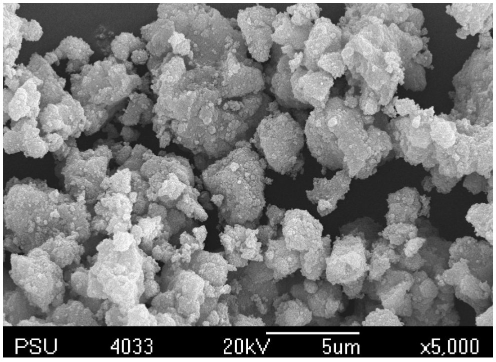

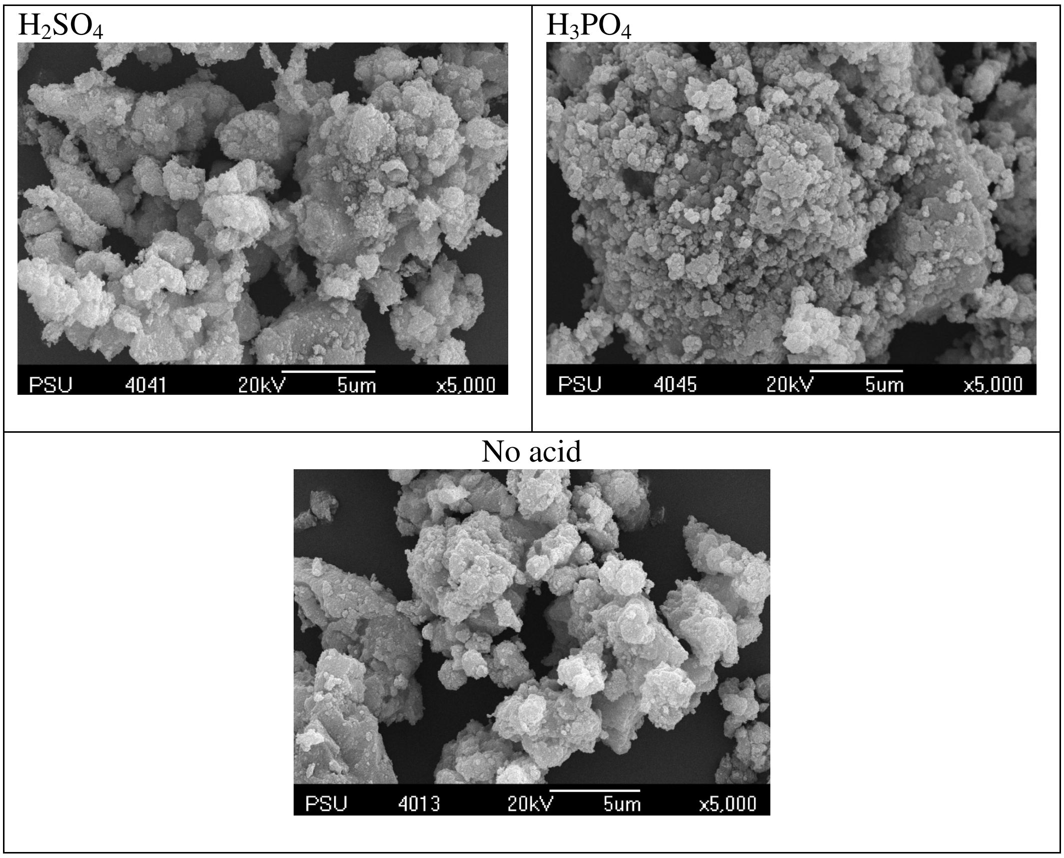

Figure 91. SEM images of P123-TiO_2_$TiOSO_4$ samples: A) effect of reaction temperature, B) effect of water content, and C) effect of acid catalyst at low and high magnification.

In varying the reaction temperatures of P123-TiO_2_$TiOSO_4$ samples, lower reaction temperature (40°C and 60°C) showed dense samples with highly growth to larger particles. At 90°C, the TiO_2 sample showed uniform spherical particle with lower agglomerated particles. In varying Ti concentrations, the low Ti concentrations (0.5 M Ti and 1.0 M Ti) gave spherical with lower agromerated particles while the dense sphere TiO_2 particles were obtained at higher Ti concentrations (3 M Ti and 5 M Ti). In varying the acid catalyst, the morphology of products from all types of acid catalyst appear as spherical with lower agglomerated particles like the TiO_2 particles without acid catalyst. TEM image consisted of anatase phase with spherical shaped of anatase, as shown in Figure 95. The TEM results revealed the aggregation of anatase crystallites to form larger spherical particles in agreement with SEM image. The pore channels were found near the surface of sample which pores were formed between the anatase crystallines. The pore channels also are helpful for chemical reactions to take place in the channels. The TEM result from this work agrees with the study of Zheng and coworkers (Zheng, *et al.*, 2001).

The difference in the morphology could be ascribed to different preparation conditions, especially, rection temperature, the volume of water, the amount of Ti content, the type of acid catalyst. These factors may affect the aggregation of each synthesized sample. The morphology of the dense synthesized sample is similar to the results of Yu, *et al.*, 2003 (Yu, *et al.*, 2003), Du, *et al.*, 2005 (Du, *et al.*, 2005), and Wang, *et al.*, 2005 (Wang, *et al.*, 2005) as shown in Figure 92. In case of the spherical synthesized TiO_2 samples, they appeared as lower aggregated samples with morphology similar to the results of Baiju, *et al.*, 2007 (Baiju, *et al.*, 2007), Tian, *et al.*, 2008 (Tian, *et al.*, 2008), and Huang, *et al.*, 2006 (Huang, *et al.*, 2006) as shown in Figure 93.

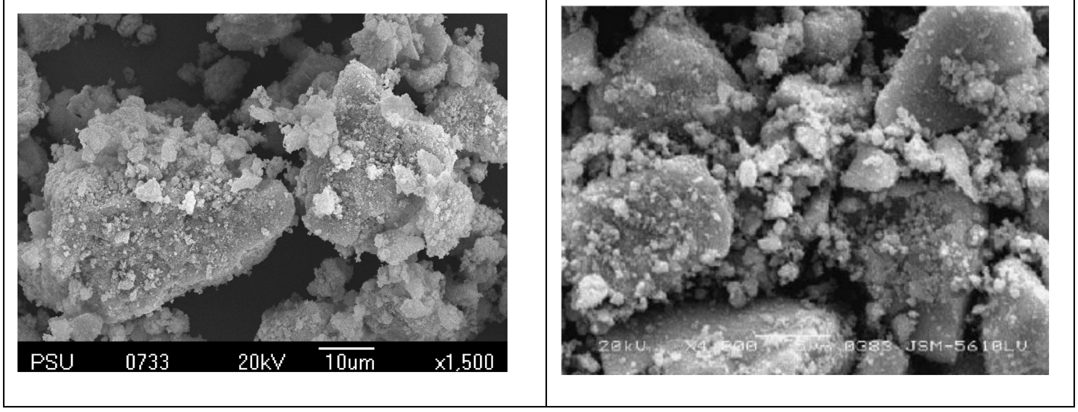

a) This work (No acid-$TiCl_4$)

b) Yu, *et al.*, 2003

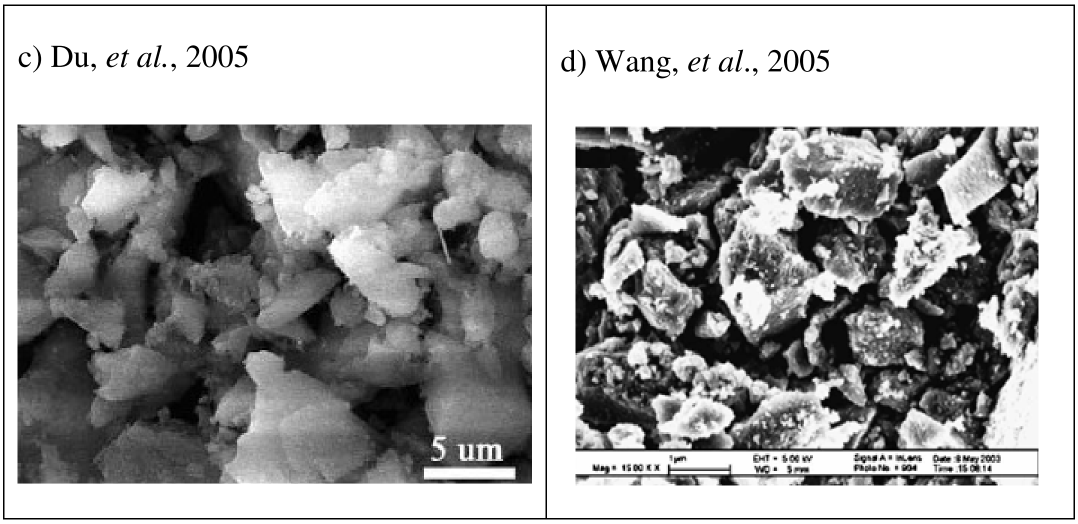
c) Du, *et al.*, 2005

d) Wang, *et al.*, 2005

Figure 92. SEM images of the highly aggregate TiO_2 samples.

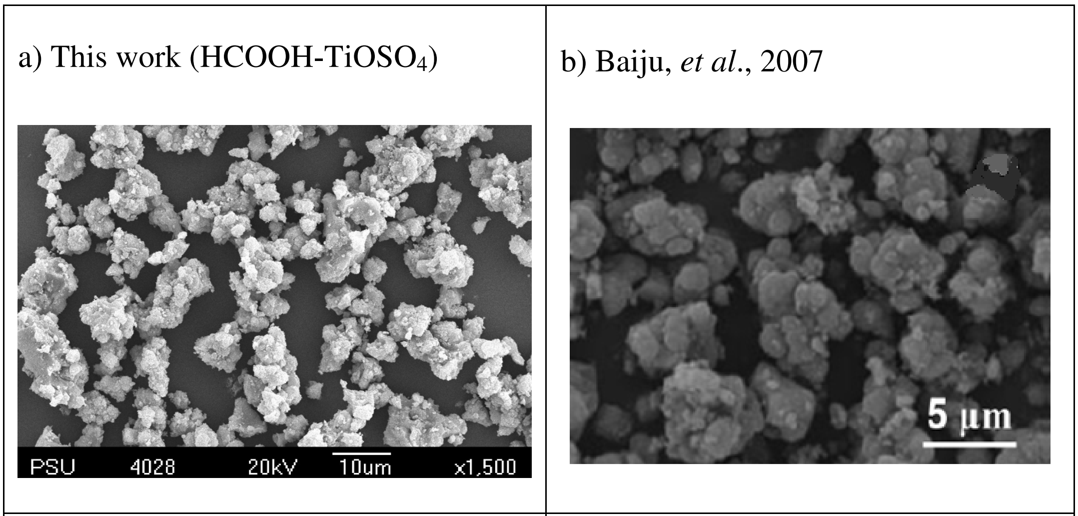
a) This work (HCOOH-$TiOSO_4$)

b) Baiju, *et al.*, 2007

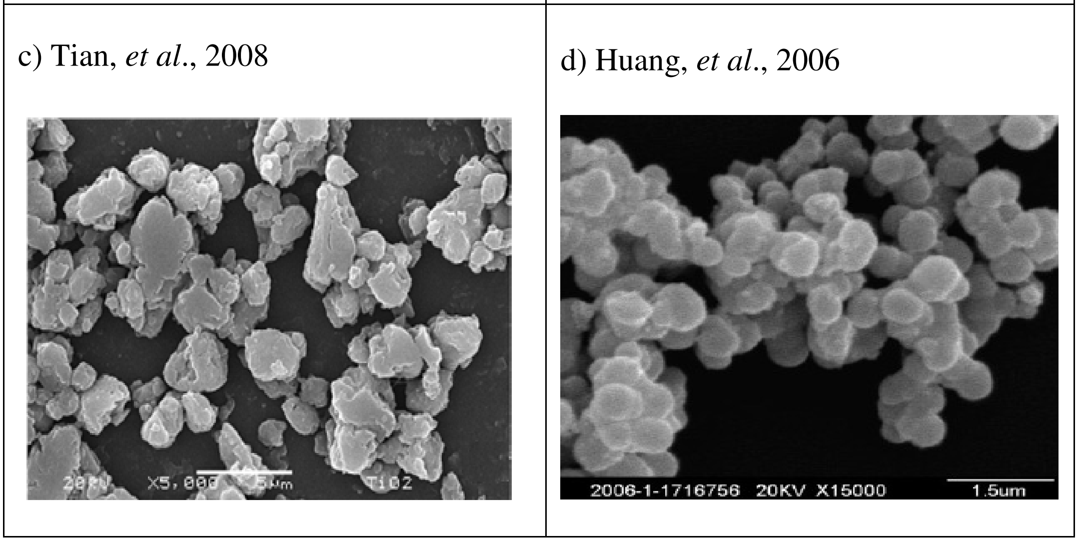
c) Tian, *et al.*, 2008

d) Huang, *et al.*, 2006

Figure 93. SEM images of the lower aggregate TiO_2 samples.

a) ×30 K magnification

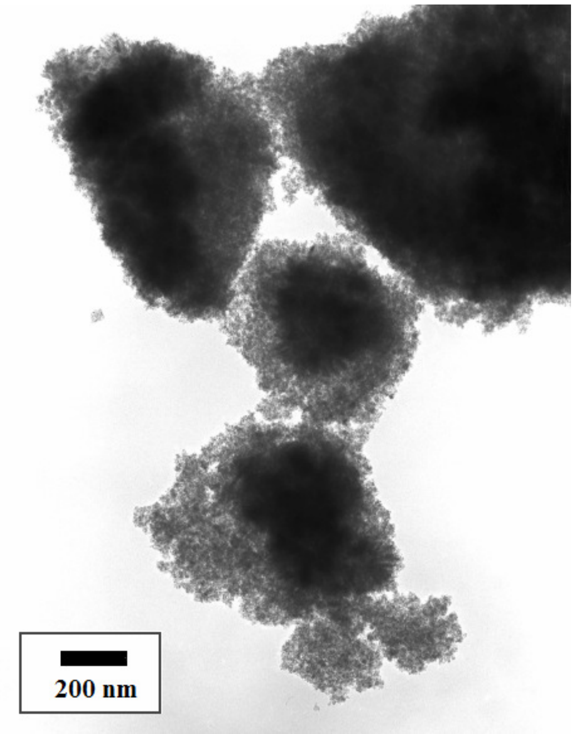

b) ×120 K magnification

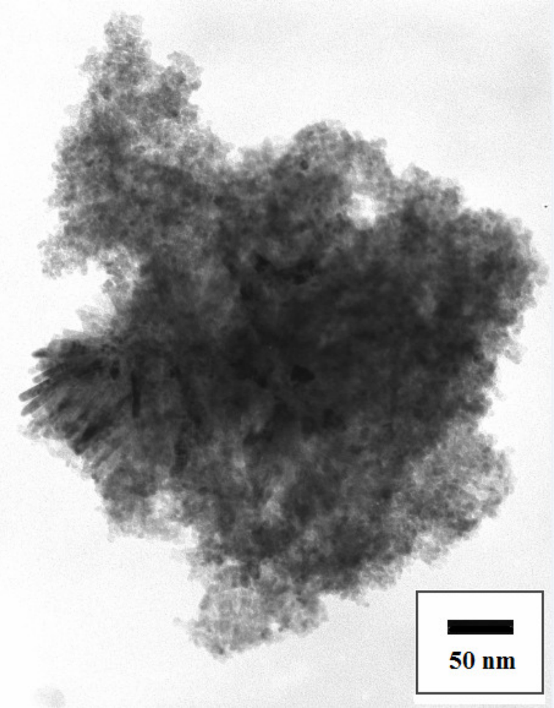

Figure 94. TEM images of 100w-P123-TiO_2_$TiCl_4$ sample at a) ×30 K magnification and ×120 K magnification.

a) ×120 K magnification

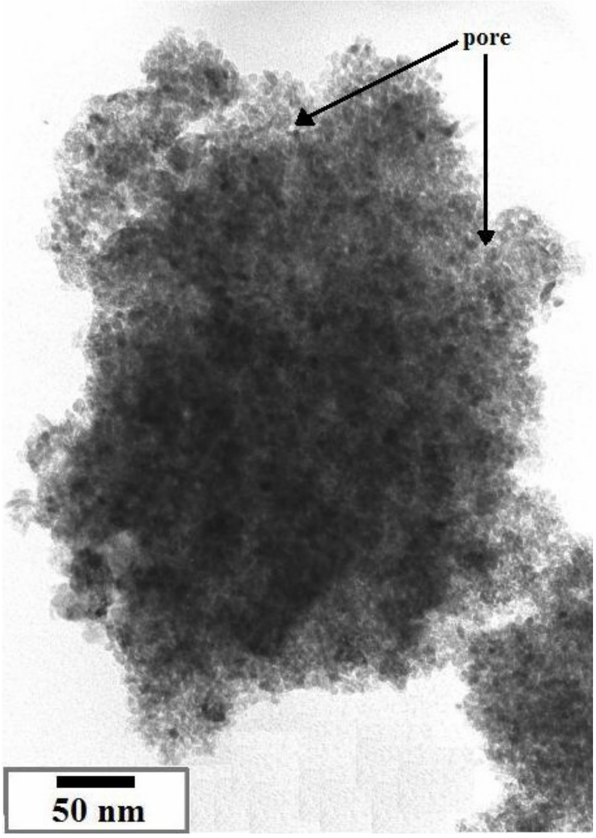

b) ×300 K magnification

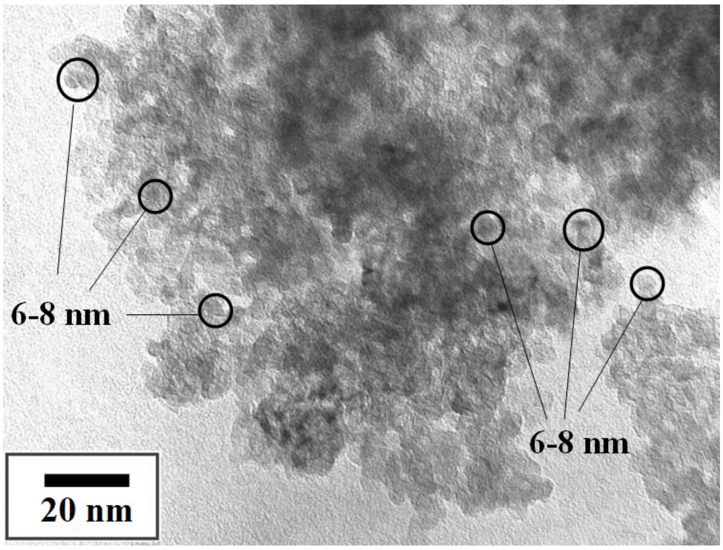

Figure 95. TEM images of 90c-P123-TiO_2_$TiOSO_4$ sample at a) ×30 K magnification and ×120 K magnification.

a) Anatase

b) Rutile

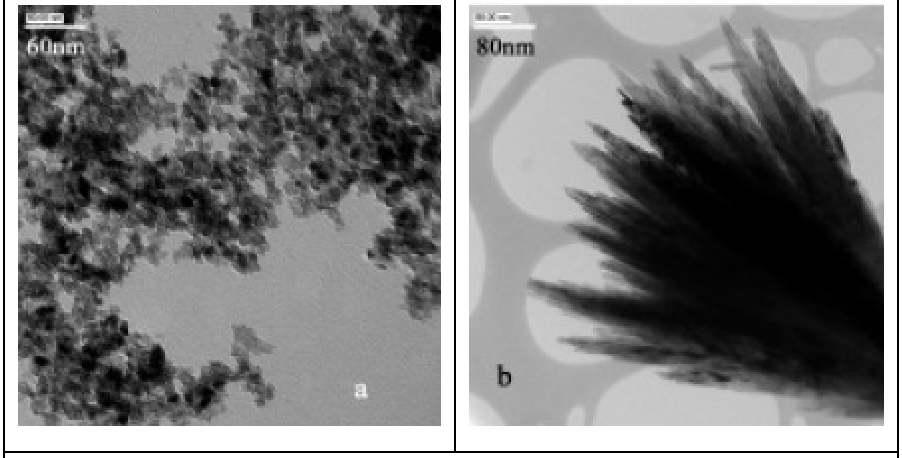

c) Mesoporous TiO$_2$

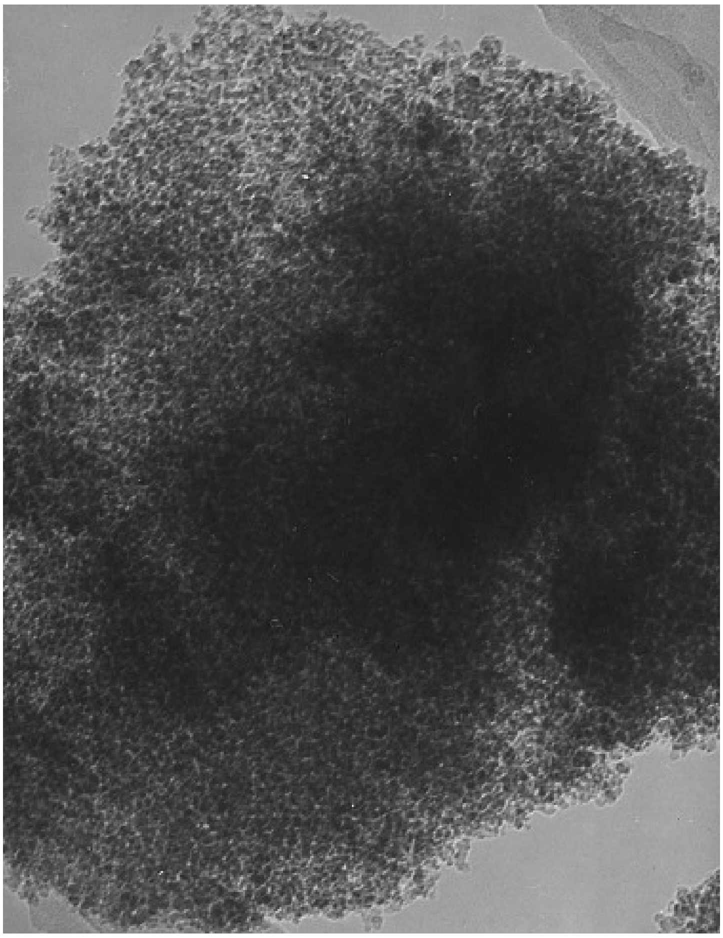

Figure 96. TEM images of a) anatase (Zhu, *et al.*, 2005), b) rutile (Zhu, *et al.*, 2005), and c) mesoporous-TiO$_2$ (Zheng, *et al.*, 2001).

When a nonionic surfactant is used as a template, it interacts with the inorganic skeleton based on hydrogen-bonding, a weaker force between molecules than statically electric force, so it is possible to remove it through a mild way such as solvent extraction instead of calcinations at high temperature (Wang, *et al.*, 2006). The template removal is a crucial procedure, since the pores of the mesostructures open up and become capable to adsorb the reactant molecules. Template removal by solvent extraction has a significant structural advantage, because it avoids the local damage caused in template removing by calcinations (Zhao, *et al.*, 2004). In this investigation, the Pluronic P123 was removed by solvent extraction. The removal of P123 was confirmed by using FT-IR technique. Figures 97-98 shows FT-IR spectra to evaluate the elimination of template of P123-TiO_2_$TiCl_4$ and P123-TiO_2_$TiOSO_4$ samples. Comparing Figure 97(a) with Figures 97(b)-97(d) and Figures 98(a)-98(c), the strong infrared absorption bands disappeared at around 2800-3000 cm^{-1} and 1150-1400 cm^{-1}, which are assigned to the C-H and C-O-C stretching vibration of P123, respectively (Zhao, *et al.*, 2004, Alapi, *et al.*, 2006). For the IR spectrum of TiO_2 samples, the vibration bands at 3428 and 1636 cm^{-1} are characteristic of the –OH group adsorbed to the surface of TiO_2. In addition, the band in the region 960–400 cm^{-1} indicated the characteristic vibrational modes of TiO_2 ($\nu_{Ti–O}$, stretching mode of Ti–O bond) is also detected (Zhang, *et al.*, 2002). Therefore, it is confirmed that the template P123 has been completely removed by dichloromethane extraction.

a) FT-IR spectrum of P123 as template

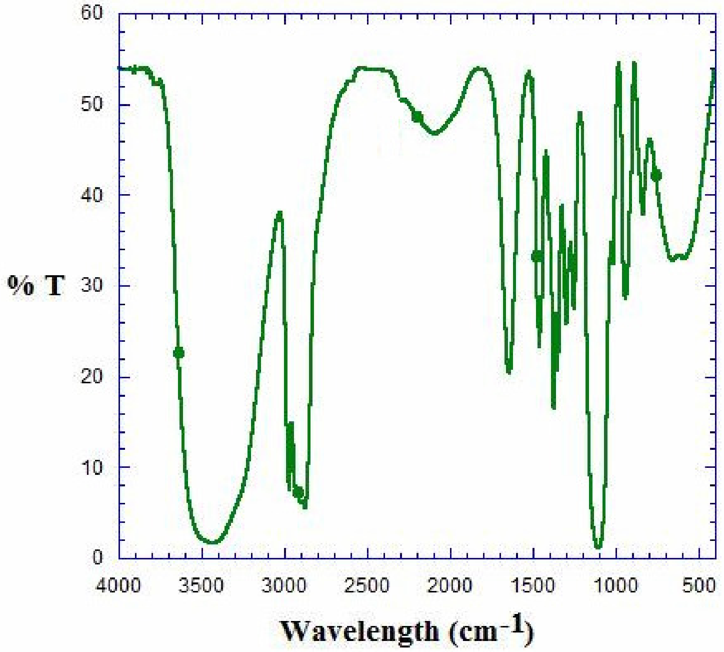

b) Effect of reaction temperature

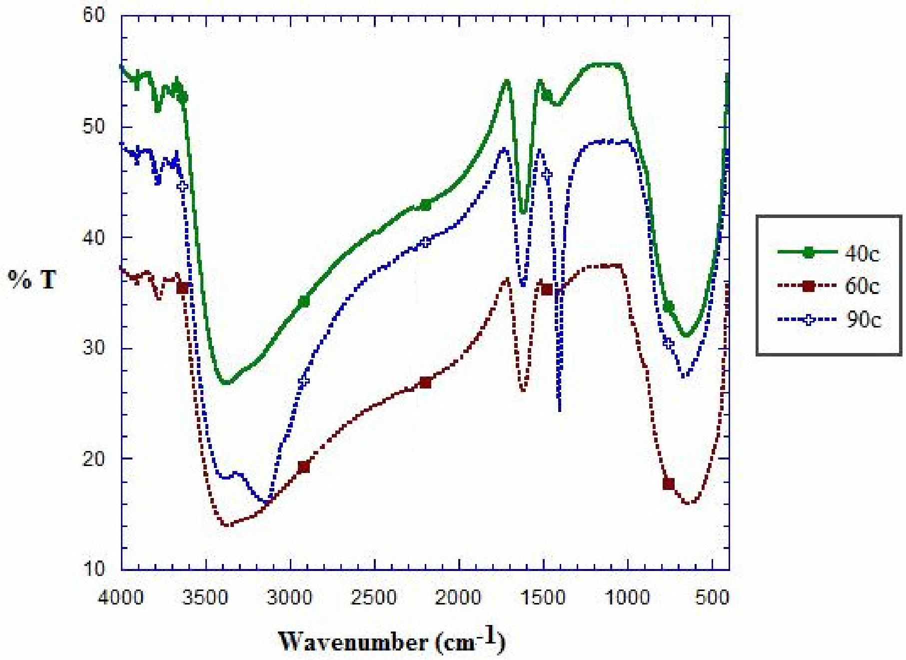

c) Effect of water content

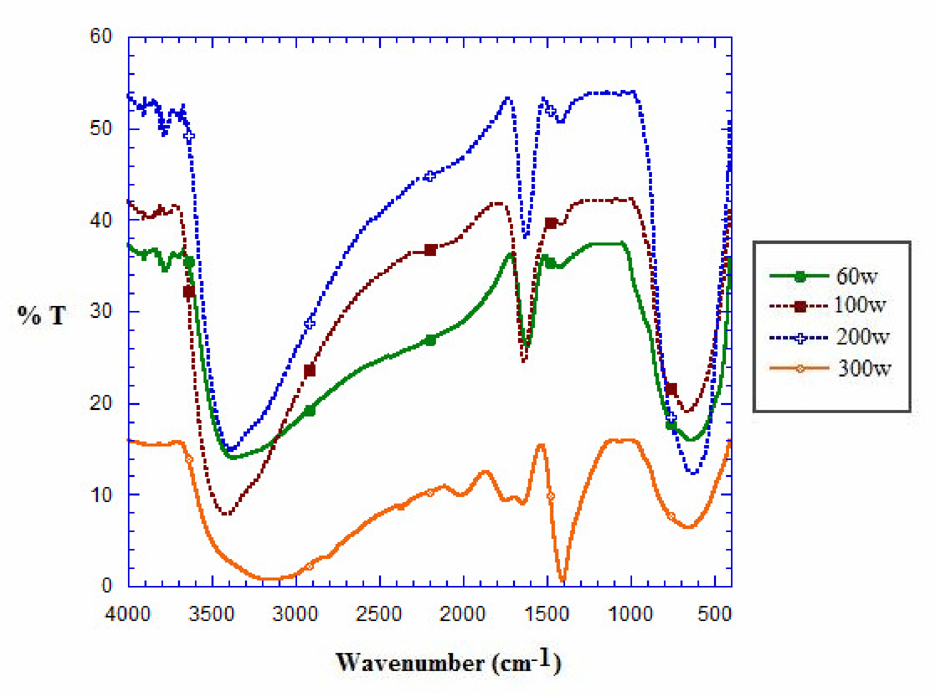

d) Effect of acid catalyst

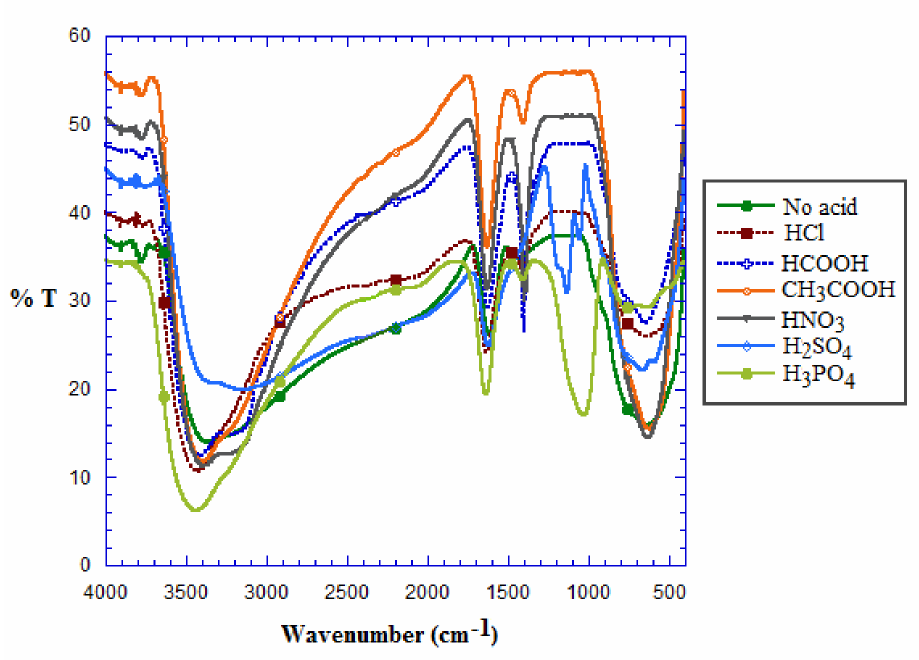

Figure 97. FT-IR spectra of P123-TiO_2_$TiCl_4$ samples: a) P123 as template, b) effect of reaction temperature, c) effect of water content, and d) effect of acid catalyst at low and high magnification.

a) Effect of Ti concentration

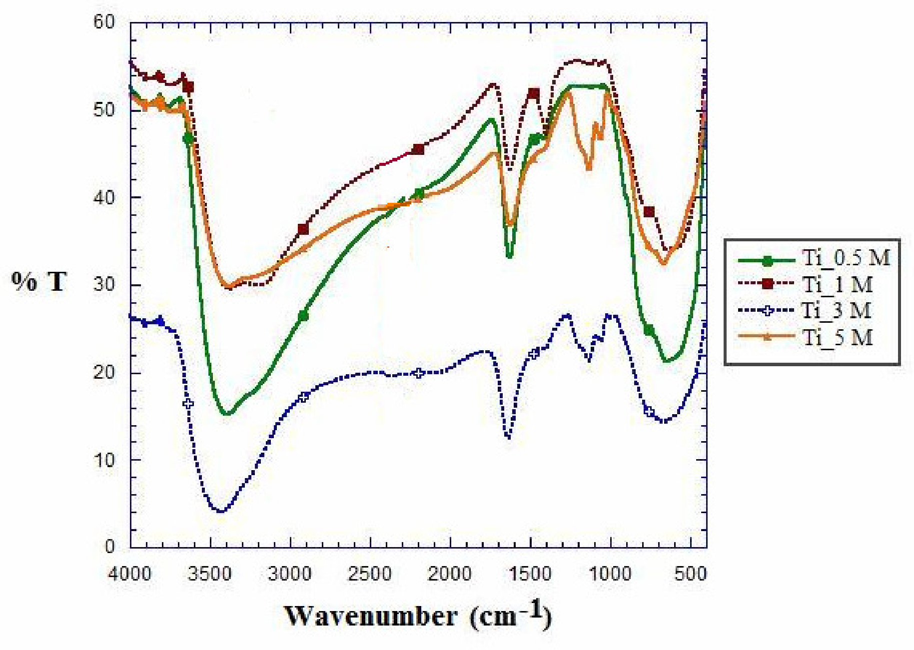

b) Effect of reaction temperature

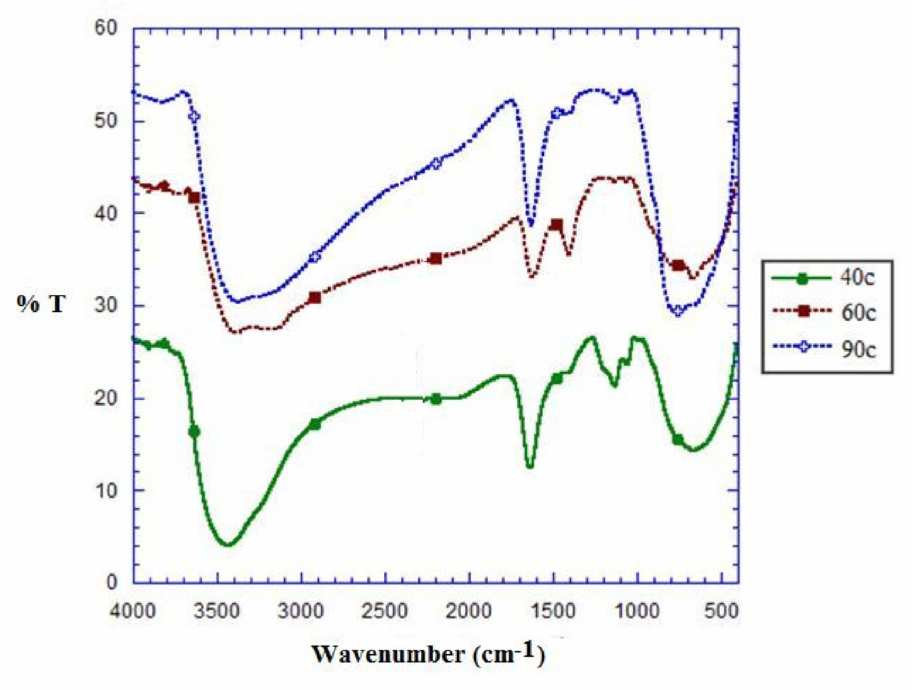

c) Effect of acid catalyst

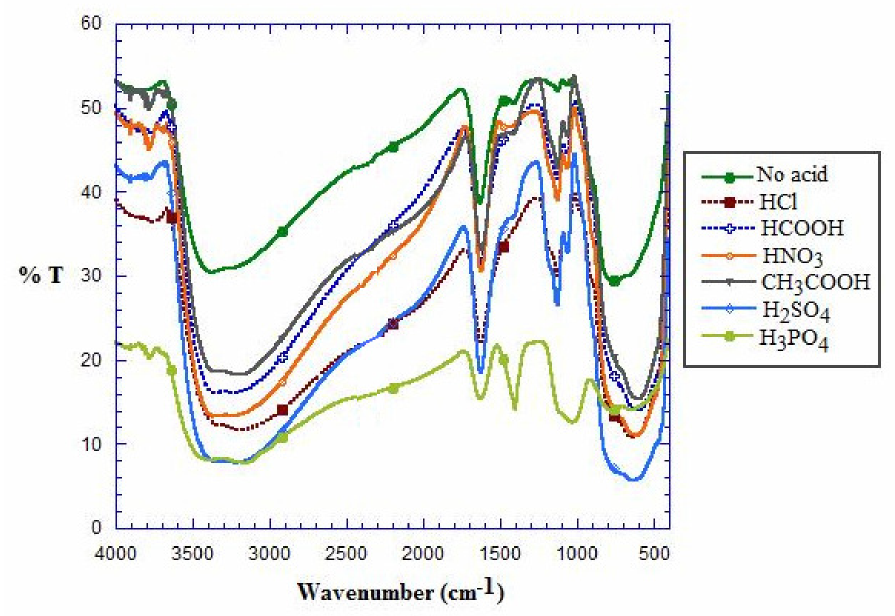

Figure 98. FT-IR spectra of P123-TiO_2_$TiOSO_4$ samples: a) effect of reaction temperature, c) effect of water content, and d) effect of acid catalyst at low and high magnification.

3.4.2 Formation mechanism of the mesoporous TiO_2 sample

Mesoporous TiO_2 was obtained for a range of reaction conditions produced by varying the concentration of surfactant, type of Ti precursor, acid catalyst, and the reaction temperature. In this work, the inorganic $TiCl_4$ was used as Ti precursor and triblock copolymer Pluronic P123 was used as templating agent. It is well known that surfactant organization into micelles take place when the critical micelle concentration (cmc) is reached. The cmc of Pluronic P123 is 0.4 g/L at 22°C in aqueous solution (Su, *et al.*, 2003). After cmc, the triblock copolymer forms micelles in aqueous solution. When the precursor $TiCl_4$ aqueous solution or $TiOSO_4$ aqueous solution was added in micelle solution, TiO_2 particles can only form at PEO block sites because only the PEO block is soluble in the aqueous solution (Zhao, *et al.*, 2004, Kim, *et al.*, 2007). The Pluronic P123 structure and its micelle are shown in Figure 99. It is well known that the interactions between inorganic skeleton and the hydrophilic (PEO) moieties based on the hydrogen bonding to direct mesostructure formation. After the pH of mixed P123 micelles and $TiCl_4$ aqueous solution was adjusted by NH_4OH solution, further hydrolysis and condensation of the titanium precursor leads to the growth of larger TiO_2 particles which slowly aggregate. As the TiO_2 particles aggregate further, the TiO_2 particles become microscopic, and form mesoporous TiO_2 particles with nearly spherical shapes. At this stage, it is supposed that micelle surrounds mesoporous TiO_2, helping the formation of spherical shape. Then the product was extracted by dichloromethane to remove the template. After solvent extraction, mesoporous TiO_2 particles with well-defined spherical shapes are obtained. The formation mechanism, base on the one proposed by Kim, et al. (Kim, *et al.*, 2007), of the mesostructured TiO_2 sample is shown in Figure 100. The TEM image in Figures 94 and 95 showed that the mesoporous TiO_2 is composed of TiO_2 particles, which confirms this mechanism.

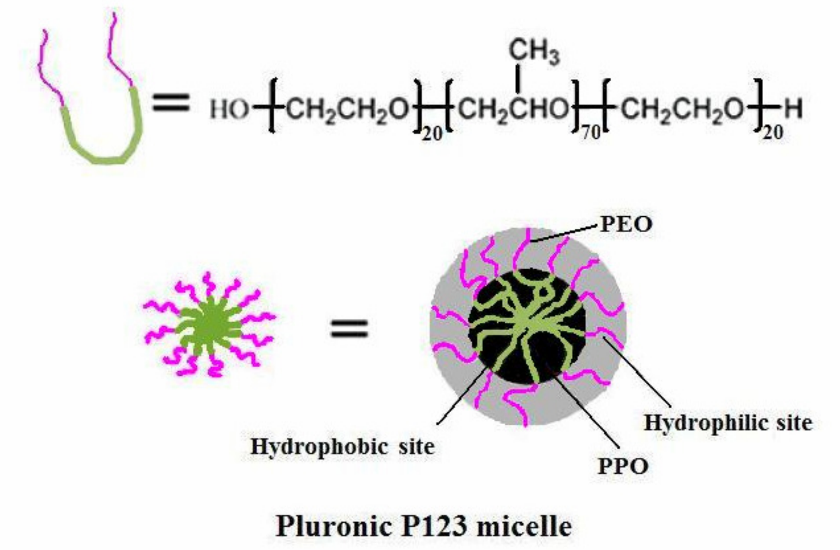

Figure 99. The Pluronic P123 molecular structure and its micelle structure. (Adapted from Wan, *et al.*, 2006 and Lettow, *et al.*, 2005)

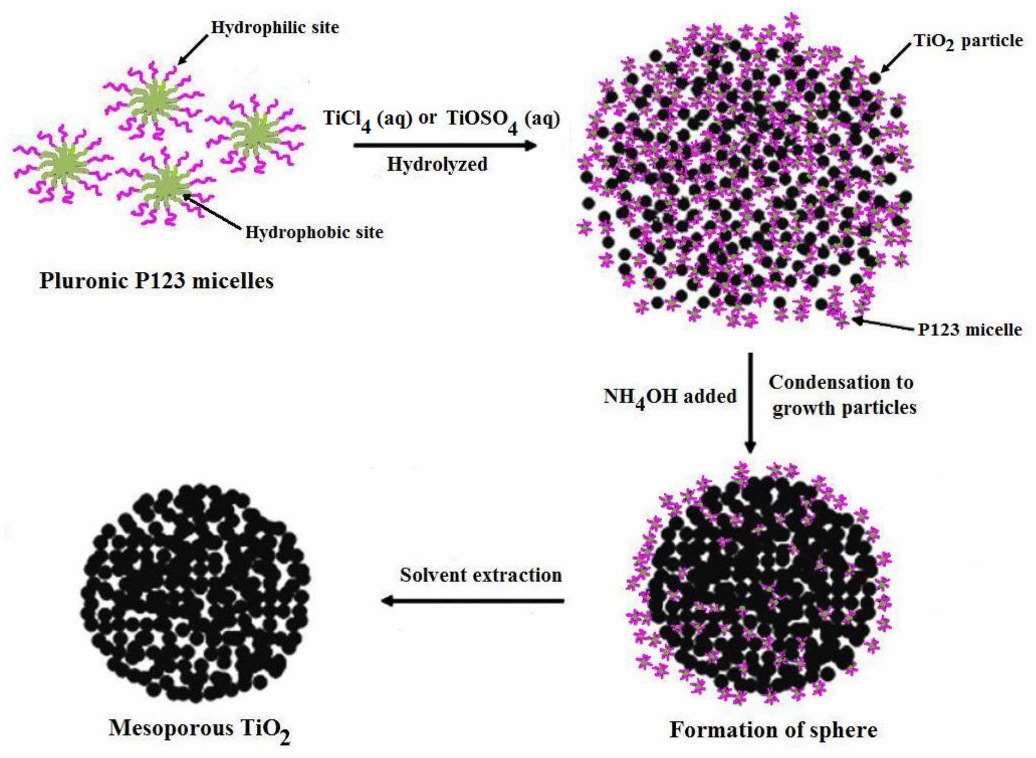

Figure 100. Possible mechanism for the formation of mesoporous TiO_2 particles (Adapted from Kim, *et al*., 2007).

In general, the sol-gel process consists of the hydrolysis and condensation reactions which are catalysed in the presence of acid. The hydrolysis reaction leads to the formation of original nuclei of titanium dioxide while the condensation reaction leads to the growth of network system of original nuclei (Kumar, *et al*., 1999). The possible reactions mechanisms for anatase and rutile TiO_2 formation when $TiCl_4$ was used as precursor are as follows.

The hydrolysis reaction:

$$TiCl_4 \quad + \quad 4\,H_2O \quad \xrightarrow{H^+} \quad Ti\,(OH)_4 \quad + \quad 4\,H^+ \quad + \quad 4\,Cl^- \tag{56}$$

The condensation reaction:

$$Ti\,(OH)_4 \quad \xrightarrow{OH^-} \quad TiO_2 \quad + \quad 2\,H_2O \tag{57}$$

The possible mechanism for anatase TiO_2 formation when $TiOSO_4$ was used as precursor is as follows.

The hydrolysis reaction:

$$2\,TiOSO_4 \;+\; 6\,H_2O \;\overset{H^+}{\rightarrow}\; 2\,Ti\,(OH)_4 \;+\; 4H^+ \;+\; 2\,SO_4^{2-} \qquad (23)$$

The condensation reaction:

$$Ti\,(OH)_4 \;\overset{OH^-}{\rightarrow}\; TiO_2 \;+\; 2\,H_2O \qquad (24)$$

Zhang *et al.*, (2000) suggested the equilibrium between the hydrolysis reaction (nucleation stage) and the condensation reaction (growth stage) made the formation of titanium dioxide particles in the rutile phase possible. After the neutralization of ammonia solution, the equilibrium between the hydrolysis and condensation was broken and the condensation reaction or the growth rate was possible to accelerate the formation of anatase phase (Zhang, *et al.*, 2000). According to Tang *et al.*, (2002), the formation of anatase and rutile titanium dioxide is determined by the hydrolysis and condensation reactions. If the condensation starts before completion of hydrolysis, either amorphous or anatase titanium dioxide will form. And also, in neutral and basic conditions, condensation starts before complete hydrolysis, while acid condition promotes the hydrolysis and decreases the condensation (Tang, *et al.*, 2002). At pH~7, the precipitation occurred quite rapidly resulting in low crystallinity, hence, the precipitate mostly appeared in this work were mixtures of dominant amorphous TiO_2, and small amount of anatase and rutile phase (see data in Table 19). This behavior had been earlier mentioned in other reports (Gopal, *et al.*, 1997; Bartlett, *et al.*, 1992; Wang, *et al.*, 1992). In this work, the amount of anatase was slightly higher than the rutile in most cases for the synthesized P123-TiO_2_$TiCl_4$ samples. This may reflect the statistical probability when the basic unit octahedral joined together, sharing other edges leading to anatase has more chances than joining the opposite edge to form rutile.

The anatase phase formation occurred on the synthesized P123-TiO_2_ $TiOSO_4$ samples might be the effect of SO_4^{2-} species. Yan and his coworkers found that bidentately bonding SO_4^{2-} species on the surface TiO_2, and the surface bidentately bonding SO_4^{2-} would be involved in the crystalline phase formation process of TiO_2

(Yan, *et al*., 2005). The bidentately bonding SO_4^{2-} species on the surface TiO_2 was confirmed by FT-IR spectra as shown in Figure 85 (a-c) around 1130 cm^{-1} corresponding to what Yan, et al., had pointed out (Yan, *et al*., 2005). The mechanism of forming anatase in the presence of SO_4^{2-} was proposed by Yan, et al., and is displayed in Figure 102. All TiO_2 crystal structures consist of TiO_6^{2-} octahedra which share edges and corners in different manners that result in forming different crystal phases. Octahedra in anatase share four edges and are arranged in zigzag chains along [221], while rutile octahedra share only two edges and form linear chains parallel to [001]. In brookite, the octahedra share both edges and corners, forming an orthorhombic structure. The crystal structures of anatase, brookite, and rutile are shown in Figure 101. For forming anatase and rutile nuclei, the placement of the third octahedron is very important and determines whether a rutile or an anatase nucleus is formed (Figure 102a). However, the presence of SO_4^{2-} would influence the orientation of the third octahedron. When SO_4^{2-} ions exist in the acid reaction media, the SO_4^{2-} ion would interact with octahedral hydroxyls by static electricity (Figure 102b). Because of the steric effect of SO_4^{2-}, the octahedron with SO_4^{2-} and another octahedron would polycondense along the converse direction in order to decrease the repulsion (Figure 102c), and the orientation of the third octahedron is more conducive to the formation of an anatase nucleus (Figure 102d). The more SO_4^{2-} there are, the more anatase nuclei can be formed. The TiO_2 clusters grow further on the nucleus and then form the anatase phase. It has been reported that the presence of SO_4^{2-} accelerated the growth of TiO_2 clusters to anatase (Yan, *et al*., 2005).

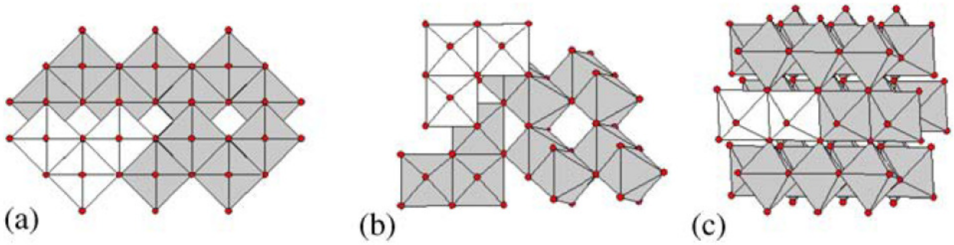

Figure 101. Crystal structure of (a) anatase, (b) brookite and (c) rutile showing the TiO_6 octahedral arrangement and emphasizing their fundamental octahedral cluster (unshaded octahedral) (Li, *et al*., 2004).

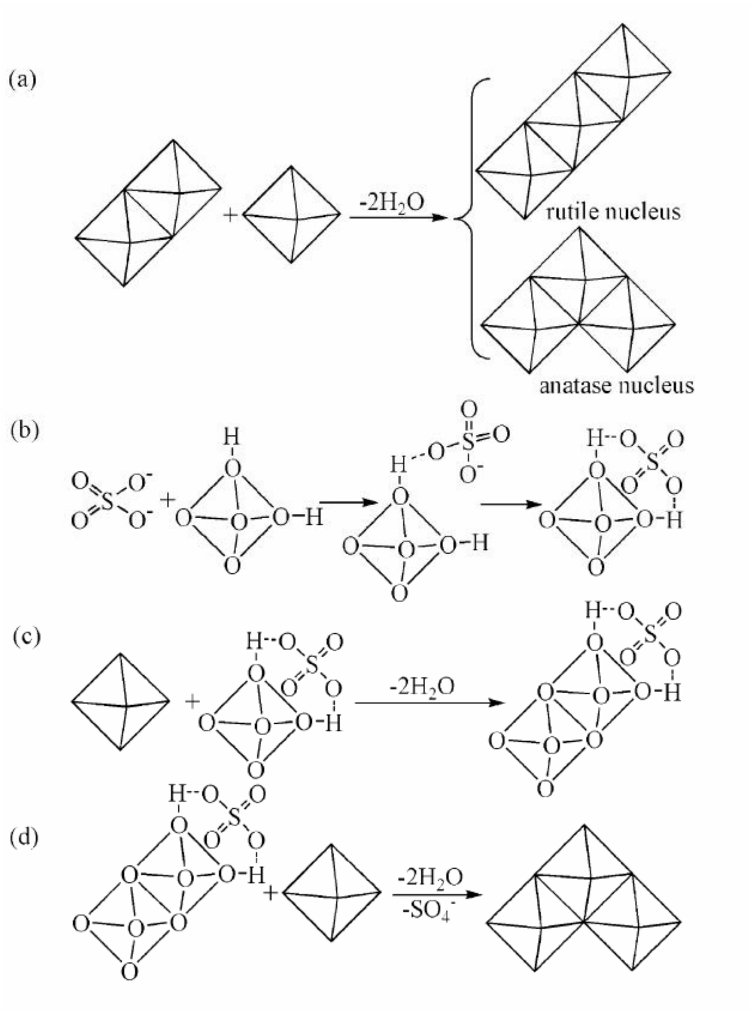

Figure 102. Proposed mechanism: (a) the orientation of the third octahedron determines whether a rutile or an anatase nucleus is formed; (b) interaction between SO_4^{2-} and TiO_6^{2-} octahedral hydroxyls; (c) two TiO_6^{2-} octahedra share edge in the presence of SO_4^{2-}; (d) formation of anatase in the presence of SO_4^{2-} (Yan, *et al.*, 2005).

It can be seen that all parameters studied (reaction temperature, concentration of Ti (or amount of water content), and type of acid catalyst added during hydrolysis) play an important role on the phase, composition, surface area, and texture of sol-gel prepared mesoporous TiO_2 products.

In the case of $TiCl_4$ as precursor it was found that increasing reaction temperature gave product of mixed amorphous, anatase and rutile. The crystallinity of product increase and surface area decrease. The Ti content also affected the amount of each phase: at low Ti content (300w-TiO_2) the product had low anatase and rutile content, high amorphous content, and highly aggromerated TiO_2 particles; at high Ti content (100w-TiO_2) the product had high anatase and rutile content, low amorphous, and a uniform lower aggromerated spherical TiO_2 particles. From acid catalyst studies it was found that each type of acid catalyst could affect the crystallinity, the phase content, and their morphologies.

In the case of $TiOSO_4$ as precursor it was found that increasing reaction temperature gave spherical particle with lower aggromerated spherical TiO_2 particles. The content of anatase and crystallinity increased but the surface area decreased. The effect of Ti content revealed that on increasing the Ti content, the size of anatase crystallinity decreased and gave highly aggromerated TiO_2 particles. In varying the acid catalyst it was found that all types of acid catalysts gave product of high surface area approximately 300-400 m^2/g, high amorphous content, and high anatase crystallinity.

3.4.3 Photocatalytic activity of the mesoporous TiO_2 sample

Indigo Carmine (IC), which belongs to acidic dyes group, was employed to evaluate the photocatalytic activity of as-prepared titania samples. In photo-degradation process, there are two factors resulting in the decreasing of the concentration of IC: the adsorption of IC onto the surface of photocatalyst, and the photooxidation of IC. In this experiment, the commercial reference material, Degussa P25-TiO_2, was used to compare the efficiency of decolorized IC solution of as-prepared TiO_2 samples. In the comparison test, the catalyst was used at fixed concentration (1.0 g/L) because in our experimental conditions, only material sample expected to show high photocatalytic efficiency. Controlled experiments without light and without TiO_2 were performed to ensure that degradation of the dye was dependent on the presence of light and TiO_2. The disappearance of IC was analyzed by UV–Vis spectrophotometer (Specord S100, Analytik Jena GmbH, Germany) over the 200–800 nm range as shown in Figure 103. Calibration plots based on Beer-Lamberts law were established relating the absorbance to the concentration. The decolorization was determined at the maximum 610 nm. % Removal efficiency of IC was measured by applying the following equation

$$\% \ \ Removal\ efficiency = \frac{C_0 - C}{C_0} \times 100 \qquad (16)$$

where C_o is the original indigo carmine (IC) content and C is the retained IC in solution. In the photocatalytic test, concentration of IC was generally used at 5.0×10^{-5} M. The photocatalytic results of as-synthesized P123-TiO_2_$TiCl_4$ samples and P123-TiO_2_$TiOSO_4$ samples are given in Figures 104-105.

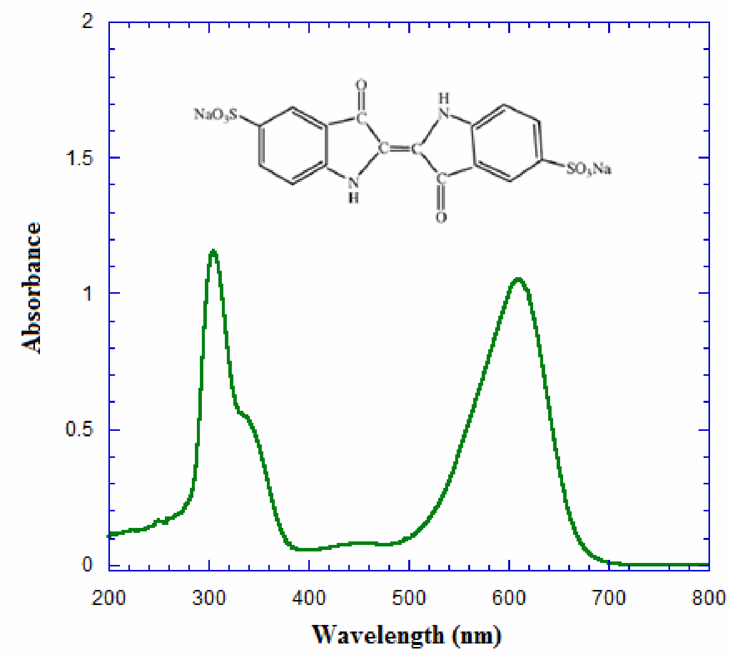

Figure 103. The molecular structure and characteristic absorption spectrum of indigo carmine.

The photocatalytic results, shown in Figure 104, of P123-TiO_2_$TiCl_4$ samples show that the 40c and 90c TiO_2 samples have high adsorption property but low photocatalytic activity, 60c TiO_2 sample has low adsorption property but high photocatalytic activity. In the varying water content for P123-TiO_2_$TiCl_4$ samples, the 300w-TiO_2 sample shows high adsorption property but the other samples have low adsorption property with rather good photocatalytic activity. The photocatalytic activity falls in order 100w > 200w > 60w > 300w. For varying of acids: P123-TiO_2_$TiCl_4$ samples, and samples with H_2SO_4, CH_3COOH, HCl have low adsorption property but high photocatalytic activity with the order of photocatalytic activity as H_2SO_4 > CH_3COOH > HCl. The samples with other acids have high adsorption property but low photocatalytic activity. From these results, it could be noticed that the 100w-TiO_2 sample has as good photocatalytic efficiency as the H_2SO_4-TiO_2 sample but the morphology of 100w-TiO_2 sample has more uniform spherical shape than the H_2SO_4-TiO_2 sample. Therefore, we chose the 100w-TiO_2 sample as the highest photocatalytic efficiency to represent the P123-TiO_2_$TiCl_4$ samples.

a) Effect of reaction temperature

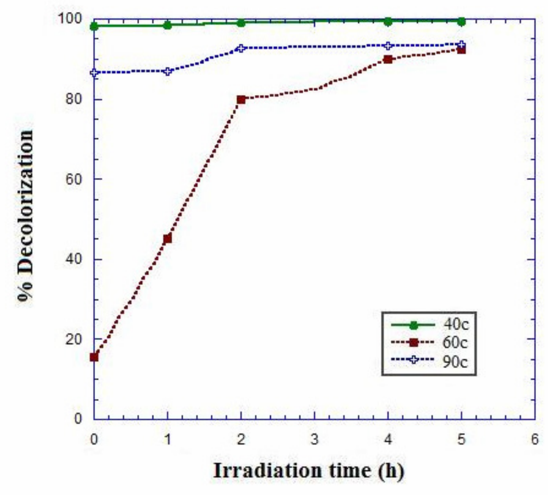

b) Effect of water content

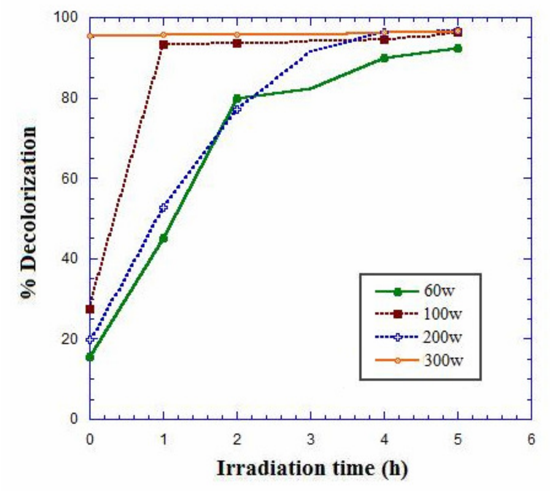

c) Effect of acid

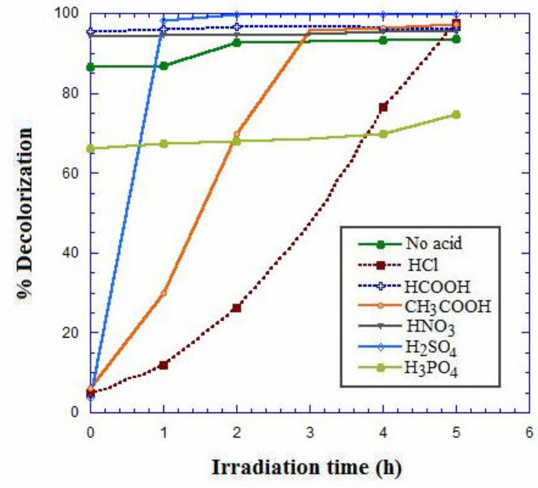

Figure 104. The decolorization of IC solution using P123-TiO_2_$TiCl_4$ samples: a) effect of reaction temperature, b) effect of water content, and c) effect of acid.

a) Effect of reaction temperature

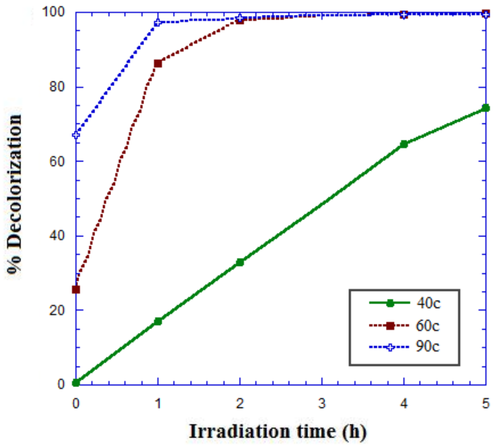

b) Effect of Ti content

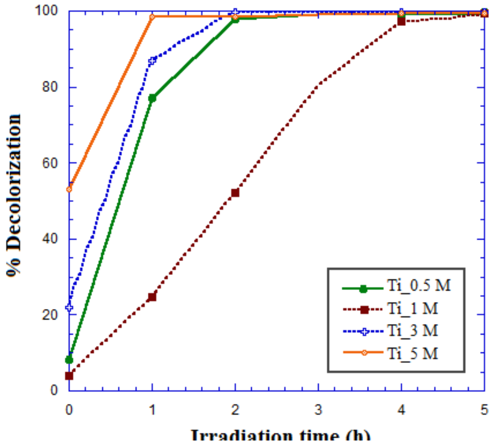

c) Effect of acid

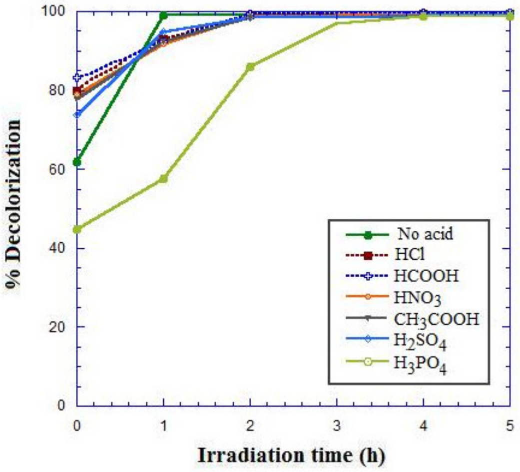

Figure 105. The decolorization of IC solution using P123-TiO_2_$TiOSO_4$ samples: a) effect of reaction temperature, b) effect of Ti content, and c) effect of acid.

For the P123-TiO_2_$TiOSO_4$ samples, the 40c and 60c TiO_2 samples have low adsorption property but showing some photocatalytic activity. The 90c TiO_2 sample has moderate adsorption property and high photocatalytic activity. For the varying Ti content: all samples of P123-TiO_2_$TiOSO_4$ samples have low adsorption property with good photocatalytic activity in the order as 0.5 M Ti ≈ 3 M Ti > 5 M Ti > 1 M Ti (photocatalytic order). For the type of acids: P123-TiO_2_$TiOSO_4$ samples and all types of acids-TiO_2 samples have high photocatalytic activity but low photocatalytic activity than when used no acid. From these results, it can be seen that the 0.5 M Ti-TiO_2 sample has as good photocatalytic efficiency as 3 M Ti-TiO_2 sample but % anatase in the 3 M Ti-TiO_2 sample is higher than the 0.5 M Ti-TiO_2 sample. Then, the 3 M Ti-TiO_2 was chosen to prepare sample at 90°C to give the 90c-TiO_2 having spherical morphology. Therefore, 90c-TiO_2 sample was chosen as a representative of P123-TiO_2_$TiOSO_4$ samples.

The synthesized 100w-TiO_2_$TiCl_4$ sample (denoted as P123-TiO_2_$TiCl_4$ sample) and 90c-TiO_2_$TiOSO_4$ sample (denoted as P123-TiO_2_$TiOSO_4$ sample) were selected to compare the photocatalytic activity with the commercial P25-TiO_2. The kinetics study, effect of pH, reclyclability were the parameters to be investigated. The experimental data from the comparision are shown in Figure 106. The results show that the synthesized mesoporous TiO_2 prepared from $TiOSO_4$ has higher photocatalytic efficiency than the commercial P25-TiO_2 and the one prepared from $TiCl_4$ as precursor. This may be attributed to two reasons, first, the as-synthesized P123-TiO_2_$TiOSO_4$ sample has much superior surface area to P25-TiO_2 and P123-TiO_2_$TiCl_4$ sample. The second reason is the presence of mesoporous channels which are favorable for the substance diffusion and thus accelerated the reaction rate.

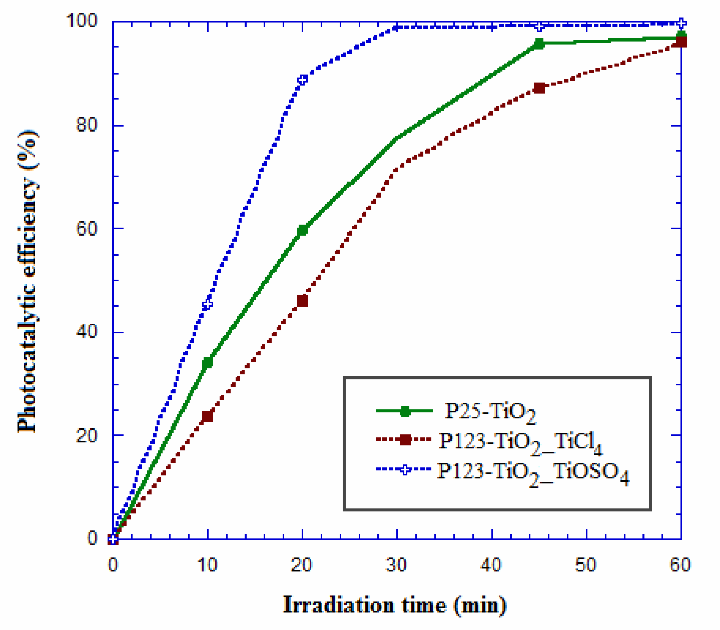

Figure 106. Decolorization efficiencies of IC solution (5.0×10^{-5} M) under UV irradiation in the presence of 1.0 g/L TiO_2 samples.

For kinetics study, a plot of ln (C_0/C) versus time represents a straight line, the slope of which upon linear regression equals the apparent first-order rate constant (Houas, *et al.*, 2001; Prevot, *et al.*, 2001) as shown in the equation (50);

$$\ln\left(\frac{C_0}{C}\right) = k.t \qquad (50)$$

In plots of ln (C_0/C) versus time (Figure 107), straight lines were found for all TiO_2 samples indicating that the degradation of indigo carmine by these samples is of a first order process. The rate constant values of as-synthesized P123-TiO_2_$TiCl_4$, P123-TiO_2_$TiOSO_4$, and P25-TiO_2 are 0.0479, 0.0966, and 0.0598 min^{-1}, respectively. Compared with P25-TiO_2, the mesoporous P123-TiO_2_$TiOSO_4$ sample exhibited a significantly faster degradation rate of indigo carmine.

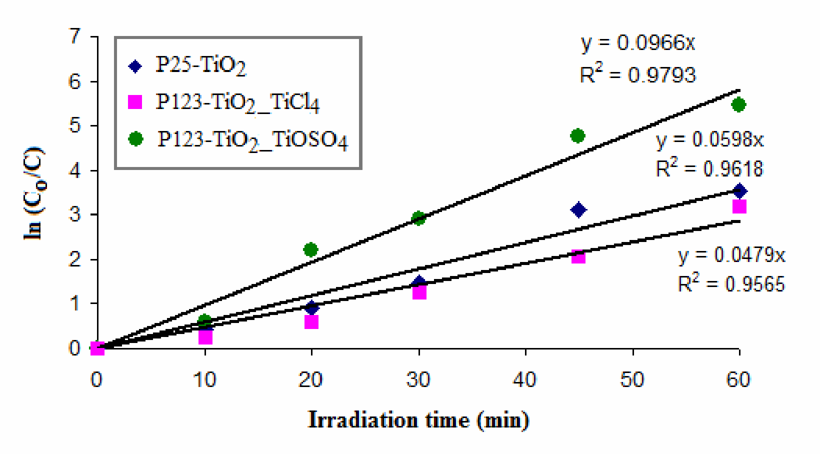

Figure 107. The kinetics of disappearance of indigo carmine using TiO_2 samples under UV irradiation in the presence of 1.0 g/L TiO_2 sample.

As the charge of the indigo carmine molecules and the surface of the TiO_2 photocatalyst are both pH-dependent, so we studied the influence of pH on the degradation of dye in the range from 3 to 11, including the natural pH of IC solution at 6.4. The pH was adjusted by adding aqueous solution of either HCl or NaOH, respectively. Figure 108 shows the effect of pH on the adsorption of dye on the surface of TiO_2 catalyst and the decomposition of dye in an aqueous TiO_2 suspension. It is well known that pH would influence both the surface state of titania and the ionization state of ionizable dye molecules. The point of zero charge (pzc) of the TiO_2 (Degussa P25) is at 6.8 (Konstantinou, *et al.*, 2004). Thus, the TiO_2 surface is positively charged in acidic media (pH<6.8), whereas it is negatively charged under alkaline condition (pH>6.8), according to the following reactions (Wen, *et al.*, 2005):

$$\text{pH} < \text{pzc:}\quad \text{Ti-OH} + H^+ \rightarrow TiOH_2^+ \qquad (51)$$

$$\text{pH} > \text{pzc:}\quad \text{Ti-OH} + OH^- \rightarrow TiO^- + H_2O \qquad (52)$$

a) Adsorption

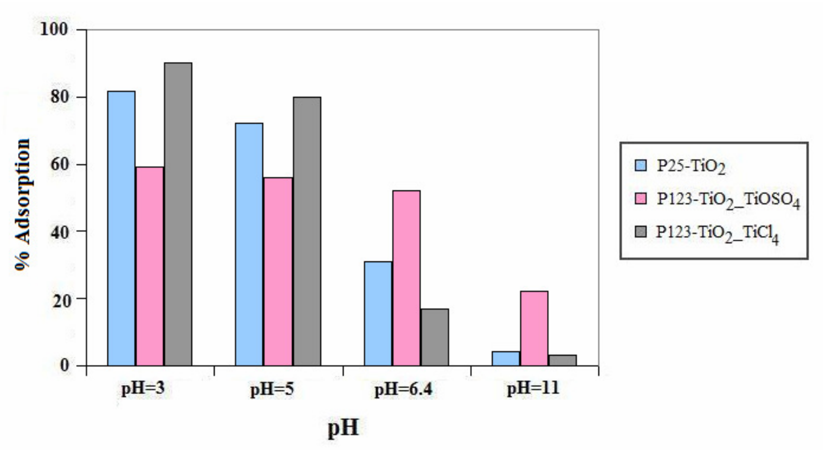

b) Photodegradation

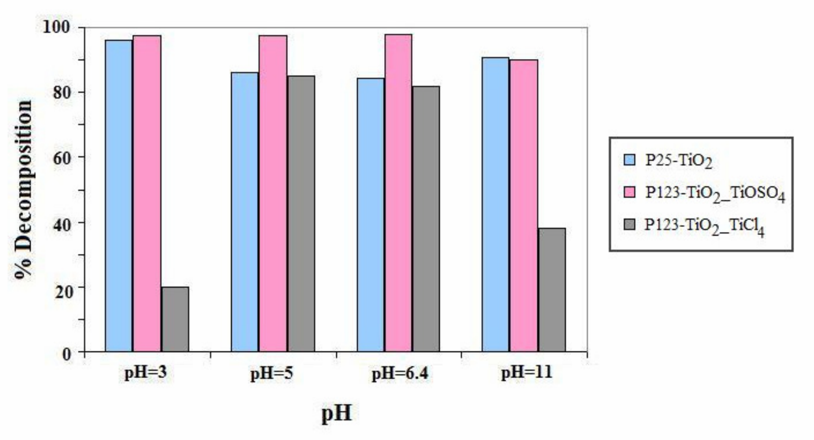

Figure 108. Effect of pH on a) adsorption of indigo carmine on the photocatalyst surface and b) the photocatalytic decomposition of indigo carmine. (Condition: TiO_2 1 g/L, 50 mL indigo carmine solution under adsorption in the dark 1 h (a) and under UV irradiation for 30 min (b)).

The adsorption results (from Figure 108a) shows that the adsorption of indigo carmine increase at low pH. Due to indigo carmine is an anionic dye, its adsorption on a positively charged surface of TiO_2 is favored. By contrast, at high pH, the adsorption is inhibited because of the opposite charged surface of TiO_2. The adsorption trend of all TiO_2 samples gradually decreased in adsorption capacity when the pH of indigo carmine solution was increased from 3 to 11. For the photocatalytic decomposition results, Figure 108b shows the high decomposition rate of both P25-TiO_2 and P123-TiO_2_$TiOSO_4$ samples indicating both TiO_2 samples can be used in wide pH conditions. In contrast, P123-TiO_2_$TiCl_4$ sample showed low decomposition efficiency at low (pH=3) and high pH (pH=11) while at medium pH it performed as good as P25. Therefore, the as-synthesized P123-TiO_2 samples could be a good candidate as photocatalyst for many applications of varying acidities.

To determine the recyclability of the prepared mesoporous-TiO_2 sample, the used TiO_2 samples was separated from the suspension by gravity sedimentation and used for further runs without any treatment. It was observed during the separation that the synthesized mesoporous-P123-TiO_2 samples could settle to the bottom faster than P25-TiO_2. The recycle results in Figure 109 show that the activity of prepared mesoporous-TiO_2_$TiCl_4$ and TiO_2_$TiOSO_4$ samples retained almost the same activity after seven uses as in the first use and almost no decline in efficiency were observed. In the eighth use the lowering in efficiency began to show up for TiO_2_$TiOSO_4$ with only 80% decomposition. However, if the irradiation time was extended, from 60 min to 90 min, the complete (100%) decomposition would result for the eighth run. This means the synthesized P123-TiO_2 samples prepared from both precursors can be brought back for reuse many times with some allowance of irradiation time appropriately adjusted. On the other hand, for P25-TiO_2 the photocatalytic activity gradually decreased until only 56% of indigo carmine could be decomposed after the eighth run. Complete decomposition by P25 could be obtained but the irradiation time had to be extended to 180 min. The used TiO_2 catalysts turned to pale yellow after the first run due to the organic compound chemisorbed on the active sites of TiO_2 surface (Cao, *et al.*, 1999). This color cast, however, seems to have no effect on the degradation efficiency. Therefore, the synthesized TiO_2 sample could be used many times which should be useful in practical uses.

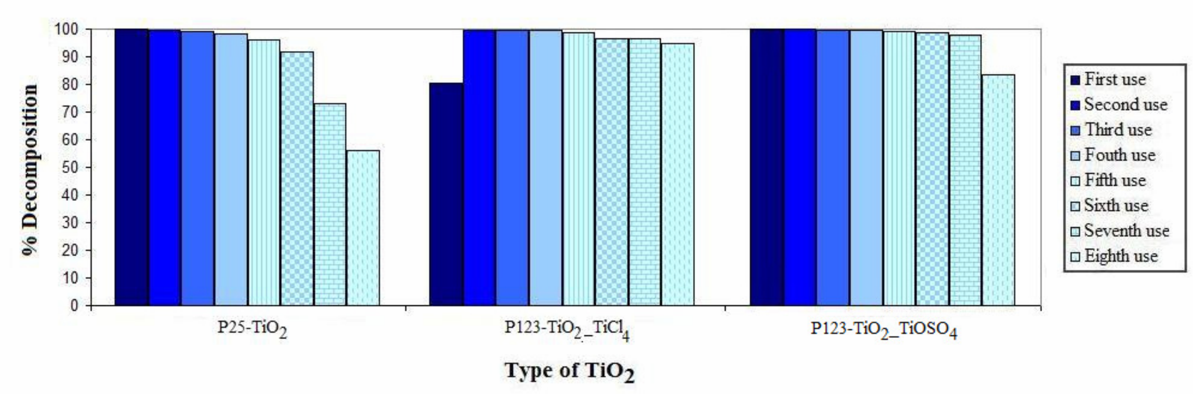

Figure 109. Comparisons of photocatalytic efficiency between P25-TiO_2 and synthesized P123-TiO_2 samples (prepared from $TiCl_4$ and $TiOSO_4$ as precursor) on the number of repeating uses (continuous uses without any regenerating treatment).

CHAPTER 4
CONCLUSIONS

This research is divided into four parts. Part 1: synthesis of potassium oxalate-doped TiO_2 powders and study on the effect of calcination on the morphology and their photocatalytic activity; part 2: preparation of TiO_2/rubber sheets and their photocatalytic activity; part 3: preparation of Chitosan/TiO_2 scaffolds and their photocatalytic activity; and part 4: synthesis of mesoporous TiO_2 powders with different precursors.

In part 1, potassium oxalate doped TiO_2 samples were prepared from $TiCl_4$ employing HMT to provide slow and controllable precipitation. The initial products had high specific surface area as a result of the ability of oxalate ion to form an open framework structure. In addition, the KOX doping could affect the phase composition, morphology, and retard the anatase to rutile transformation temperature of the TiO_2 products. The non-calcined samples (amorphous phase with small amount of anatase phase) showed very little photocatalytic activity but high adsorption capacity. Calcination changed the morphology, crystal structure, crystallite size, and photocatalytic activity of the as-prepared TiO_2 samples. The samples calcined at 400 and 600 °C still showed high adsorption capacity but decreasing as calcination temperature was increased. The photocatalytic activity also increased with increasing calcination temperature. When the calcination temperature was 800 °C, the photocatalytic activity of the calcined sample was comparable to that of Degussa P25. The non-calcined sample, due to its high adsorption property although low photocatalytic property, could decolorize high concentration MB solution, by adsorption, up to 2.5×10^{-4} M which is about ten fold of the normally used in other reports. At this high concentration, the decolorization could not be realized with P25. After use, the dye-covered powders could be regenerated. The regeneration method was carried out by using both H_2O_2 and UV irradiation. The regenerated TiO_2 samples could decolorize MB solution slightly better than the freshly prepared TiO_2 samples.

The high adsorption power combined with the recyclability should make this material an attractive candidate for an alternative method of dye-polluted water treatment.

In part 2, the rubber sheet impregnated with titanium dioxide particles (Imp-TiO_2) was prepared simply by directly mixing TiO_2 powders with rubber latex (60% HA) and distilled water. The used TiO_2 powders were two synthesized TiO_2 samples and two commercial TiO_2 samples. The synthesized TiO_2 samples were prepared by base-catalyzed sol-gel process. Degussa P25 and anatase were selected as commercial TiO_2 samples. The sheet impregnated with each TiO_2 samples were characterized for several techniques such as XRD, SEM, and DRS. Sheet impregnated with anatase (Imp-Ana) and K1-doped TiO_2 (Imp-K1) showed more uniform structure and better surface coverage than K2-doped TiO_2 (Imp-K2) and Degussa P25 (Imp-P25). Their photocatalytic activities were evaluated using methylene blue (MB) as a model dye pollutant. These impregnated sheets could degrade MB solution under UV-light irradiation. The efficiencies of decolorization of MB fell in the decreasing order as: Imp-K1 sheet > Imp-K2 sheet > Imp-Ana sheet > Imp-P25 sheet. Kinetic results indicated that the methylene blue degradation followed the pseudo-first order kinetics. For the recycle test, the Imp-K1 and Imp-K2 could decolorize MB with better performance than the two Imp-commercial TiO_2. More significantly, the dye adsorbed on surface of the used TiO_2 impregnated rubber sheet could be removed by treating with hydrogen peroxide solution under UV irradiation. The regenerated TiO_2 samples could be reused in the subsequent decolorization of MB solution without a decline in decolorization efficiency compared with freshly prepared TiO_2 samples.

In part 3, the 3D-macroporous CS/TiO_2 scaffolds were successfully prepared via ice-templating method. The parameters studied for preparing the ordered structure are ratio of TiO_2/chitosan, freezing rate, size of syringe, and type of TiO_2. The optimum condition to obtain the well-orderred structure is 1:1 ratio of TiO_2/chitosan, freezing rate of 5.9 mm/min, and 2 mL syringe size. Moreover, the unique properties of each type of TiO_2 could affect the morphologies of the scaffolds. The dialyzed-TiO_2 sol mixed well with crosslinked-chitosan to form the homogeneous gel, so the structure of its scaffold looked like the CS-scaffold. For P25-TiO_2 scaffold, the TiO_2 particles coated on the wall of scaffold. The KOX-TiO_2 scaffold showed the TiO_2 particles embeded on the walls. All types of CS/TiO_2 scaffolds could be used as photocatalyst. The photocatalytic efficiency of methylene blue degradation falls in the order: P25-TiO_2 > KOX-TiO_2 > dialyzed-TiO_2. In case of orange II degradation, the photocatalytic efficiency falls in the order: Dialyzed-TiO_2 > P25-TiO_2 > KOX-TiO_2. The ice-templating method can be used to fabricate the ordered macroporous structure materials which are expected to be used in various applications. Furthermore, this method can be easily applied to various precursor materials to obtain unique morphologies.

In part 4, mesoporous TiO_2 powders were successfully prepared using $TiCl_4$ and $TiOSO_4$ as inorganic precursors via sol-gel process. The nonionic triblock copolymer, Pluronic P123 was used as surfactant template. The as-synthesized materials were characterized by XRD, FT-IR, DRS, BET, SEM and TEM. The template could be easily removed by extracting with dichloromethane and confirmed by FT-IR. XRD pattern reveals that the as-synthesized product has a framework of anatase phase. From the N_2 adsorption–desorption analysis, the as-synthesized sample has a BET surface area of 285 m^2/g with narrow pore size distribution centered around 6 nm. It can be seen that all parameters studied (including reaction temperature, concentration of Ti, and type of acid catalyst added during hydrolysis of both precursors) play an important role on the phase composition, surface area, and texture of sol-gel made titania products. The photodegradation of indigo carmine including kinetics, pH, and deactivation were investigated. The photocatalytic results showed that the as-sythesized mesoporous titania could efficiently degrade indigo carmine under UV irradiation and showed a stronger photocatalytic activity than commercial Degussa P25-TiO_2. The formation mechanism of the mesostructured TiO_2 sample was also proposed.

References

Alapi, T.; Sipos, P.; Ilisz, I.; Wittmann, G.; Ambrus, Z.; Kiricsi, I.; Mogyorosi, K. and Dombi, A. 2006. Synthesis and Characterization of Titania Photocatalysts: The Influence of Pretreatment on The Activity. Appl. Catal. A: Gen. 303: 1-8.

An overview of products prepared by sol-gel methods from Science Technology: https://www.llnl.gov/str/May05/Satcher.html (accessed 31/03/09).

Andres, R.; Gruselle, M.; Malezieux, B.; Verdaguer, M. and Vaissermann, J. 1999 Enantioselective Synthesis of Optically Active Polymeric Homo- and Bimetallic Oxalate-Bridged Networks $[M_2(ox)_3]_n$ Inorg. Chem. 38: 4637-4646.

Antonelli, D.M. and Ying, J.Y. 1995. Synthesis of Hexagonally Packed Mesoporous TiO_2 by A Modified Sol-Gel Method. J. Angew. Chem., Int. Ed. Engl. 34: 2014-2017.

Antonelli, D.M. 1999. Synthesis of Phosphorus-Free Mesoporous Titania via Templating with Amine Surfactants. Microporous Mesoporous Mater. 30: 315–319.

Arroyo, R.; Cordoba, G.; Padilla, J. and Lara, V.H. 2003. Influence of Manganese Ions on The Anatase–Rutile Phase Transition of TiO_2 Prepared by The Sol–Gel Process. Mater. Lett. 54: 397-402.

Awati, P. S., Awate, S. V., Shah, P. P. and Ramaswamy, V. 2003. Photocatalytic Decomposition of Methylene Blue Using Nanocrystalline Anatase Titania Prepared by Ultrasonic Technique. Catal. Commun. 4: 393-400.

Azam, A. and Hamid, A. 2006. Effects of Gap Size and UV Dosage on Decolorization of C.I. Acid Orange 7 by UV/H_2O_2 Process. J. Hazardous Mater. B. 133: 167–171.

Baiju, K.V.; Shukla, S.; Sandhya, K.S.; James, J. and Warrier, K.G.K. 2007. Photocatalytic Activity of Sol-Gel Derived Nanocrystalline Titania. J. Phys. Chem. C 111: 7612-7622.

Bakardjieva, S.; Subrt, J.; Stengl, V.; Jesus Dianez, M. and Jesus Sayagues, M. 2005. Photoactivity of Anatase–Rutile TiO_2 Nanocrystalline Mixtures Obtained by Heat Treatment of Homogeneously Precipitated Anatase. Appl.Catal. B: Environ. 58: 193–202.

Bandara, J.; Mielczarski, J. A. and Kiwi, J. 1999. 2. Photosensitized Degradation of Azo Dyes on Fe, Ti, and Al Oxides: Mechanism of Charge Transfer during The Degradation. Langmuir. 15: 7680-7687.

Bartlett, J. R. and Woolfrey, J. L. 1992. Chemical Processing of Advanced Materials. John Wiley: New York.

Basic dye from dyes for paper: http://www.jagson.com/paper_dyes.htm Jacson Colorchem Limited (accessed 31/03/09).

Brunauer, S.; Emmett, P. H.; and Teller, E. 1938. Adsorption of Gases in Multimolecular Layers. J. Am. Chem. Soc. 60: 309-319.

Büchner, W.; Schliebs, S.; Winter, G., and Buchel. K. H. 1989. Industrial Inorganic Chemistry. New York : VCH. pp 526-528.

Calleja, G.; Serrano, D.P.; Sanz, R.; Pizarro, P. and Garcia, A. 2004. Study on The Synthesis of High-Surface-Area Mesoporous TiO_2 in The Presence of Nonionic Surfactants. Ind. Eng. Chem. Res. 43: 2485-2492.

Cao, L.; Huang, A.; Spiess, F.-J. and Suib, S. L. 1999. Gas-Phase Oxidation of 1-Butene Using Nanoscale TiO_2 Photocatalysts. J. Catal. 188: 48-57.

Carp, O; Huisman, C.L. and Reller, A. 2004. Photoinduced Reactivity of Titanium Dioxide. Progess in Solid State Chemistry. 32: 33-177.

Caruso, R.A. and Antonietti, M. 2001. Sol-Gel Nanocoating: An Approach to The Preparation of Structured Materials. Chem. Mater. 13: 3272-3282.

Chaiyapoom, L.; Wongnawa, S.; Pakawatchai, C.; Charmant, J. and Saithong, S. 2006. The Alexandrite-Like Cr-Doped Aluminum Oxalato Complexes. Inorg. Chem. Commun. 9: 316-318.

Chemat. 1998. Sol-Gel Technology. http://www.chemat.com/html/solgel.html Chemat Technology, Inc. (accessed 30/03/09).

Chen, L.; Zhu, J.; Liu, Y.M.; Cao, Y.; Li, H.X.; He, H.Y.; Dai, W.L. and Fan, K.N. Photocatalytic Activity of Epoxide Sol-Gel Derived Titanium Transformed into Nanocrystalline Aerogel Powders by Supercritical Drying. J. Mole. Catal. A: Chem. 225: 260-268.

Chen, L.-C.; Huang, C.-M. and Tsai, F.-R. 2007. Characterization and Photocatalytic Activity of K^+-Doped TiO_2 Photocatalysts. J. Mol. Catal. A: Chem., 265: 133-140.

Chen, Y.; Yang, S.; Wang, K. and Lou, L. 2005. Role of Primary Active Species and TiO_2 Surface Characteristic in UV-Illuminated Photodegradation of Acid Orange 7. J. Photochem. Photobiol. A: Chem. 172: 47-54.

Chiou, C.H.; Wu, C.Y. and Juang, R.S. 2008. Influence of Operating Parameters on Photocatalytic Degradation of Phenol in UV/TiO_2 Process. Chem. Eng. J.139: 322-329.

Clark, R. J. H. 1968. The Chemistry of Titanium and Vanadium. Amsterdam: Elsevier. pp 268-270.

Cooper, A.I. 2003. Porous Materials and Supercritical Fluids. Adv. Mater. 15: 1049-1059.

Cooper, C.D.; Clausen III, C.A.; Petty, L.; Collins, M.M. and de Fernandez, M.P. 2002. Investigation of Ultraviolet Light-Enhanced H_2O_2 Oxidation of NOx Emissions. J. Environ. Eng. 128: 68-72.

Coronado, E.; Galan-Mascaros, J.R. and Gomez-Garcia, C.J. 2000. Charge Transfer Salts of Tetrathiafulvalene Derivatives with Magnetic Iron(III) Oxalate Complexes: $[TTF]_7[Fe(ox)_3]_2.4H_2O$, $[TTF]_5[Fe_2(ox)_5]_2.2C_6H_5Me.2H_2O$ and $[TMTTF]_4[Fe_2(ox)_5]2.C_6H_5CN.4H_2O$ (TMTTF = Thetramethyltetrathiafulvalene. J. Chem. Soc. Dalton Trans. 205-210.

Crystal structures of TiO_2 from TiO_2 group: University of Colorado http://ruby.colorado.edu/~smyth/min/tio2.html (accessed 8/04/09).

Dabrowski, A. 2001. Adsorption_from Theory to Practice. Adv. Colloid Interf. Sci. 93: 135-224.

Dai, Q.; Shi, L.Y.; Luo, Y.G.; Blin, J.L.; Li, D.J.; Yuan, C.W. and Su, B.L. 2002. Effect of Templates on The structure, Stability and Photocatalytic Activity of Mesostructures TiO_2. J. Photochem. Photobiol. A: Chem. 148: 295-301.

Daneshvar, N.; Salari, D. and Khataee, A.R. 2003. Photocatalytic Degradation of azo Dye Acid Red 14 in Water: Investigation of The Effect of Operational Parameters. J. Photochem. Photobiol. A: Chem. 157: 111-116.

Decurtins, S.; Schmalle, H.W.; Pellaux, R.; Schneuwly, P. and Hauser, A. 1996. Chiral, Three-Dimensional Supramolecular Compounds: Homo- and

Bimetallic Oxalateand 1,2-Dithiooxalate-Bridged Networks. A Structural and Photophysical Study. Inorg. Chem. 35: 1451-1460.

Deville, S.; Saiz, E. and Tomsia, A.P. 2006. Freeze Casting of Hydroxyapatite Scaffolds for Bone Tissue Engineering. 27; 5480-5489.

Deville, S.; Saiz, E. and Tomsia, A.P. 2007. Ice-templated porous alumina structure. Acta Materialia. 55: 1965-1974.

Ding, Z.; Hu, X.; Yue, P.L.; Lu, G.Q. and Greenfield, P.F. 2001. Synthesis of Anatase TiO_2 Supported on Porous Solids by Chemical Vapor Deposition. Catal. Today. 68: 173-182.

Direct dye from all about hand dyeing: http://www.pburch.net/dyeing/directdye.shtml (accessed 31/03/09).

Djaoued, Y.; Thibodeau, M.; Robichaud, J.; Balaji, S.; Priya, S.; Tchoukanova, N. and Bates, S.S. 2008. Photocatalytic Degradation of Domoic Acid Using Nanocrystalline TiO_2 Thin Films. J. Photochem. Photobiol. A: Chem. 193: 271 –283.

Du, J.; Liu, Z.; Li, Z.; Han, B.; Huang, Y. and Gao, Y. 2005. Mesoporous TiO_2 with Wormlike Structure Synthesized via Interfacial Surfactant Assisted Route. Microporous Mesoporous Mater. 83: 19–24.

Dye from Wikipedia, the new world encyclopedia. http://www.newworldencyclopedia.org/entry/Dye (accessed 31/03/09).

Dye from Wikipedia, the free encyclopedia. http://en.wikipedia.org/wiki/Dye (accessed 30/03/09).

Electron microscopy from Wikipedia, the free encyclopedia. http://www.vcbio.science.ru.nl/en/image-gallery/electron/ (accessed 30/03/09).

Epling, G. A. and Lin, C. 2002. Photoassisted Bleaching of Dyes Utilizing TiO_2 and Visible Light. Chemosphere. 46: 561-570.

Evans, O.R. and Lin, W. 2001. Synthesis of Zinc Oxalate Coordination Polymers via Unprecedented Oxidative Coupling of Methanol to Oxalic Acid. Crystal Growth & Design. 1: 9-11.

Fernández, J., Kiwi, J., Lizama, C., Freer, J., Baeza, J. and Mansilla, H. D. 2002. Factorial Experimental Design of Orange II Photacatalytic Discolouration. J. Photochem. Photobiol. A: Chem. 151: 213-219.

Fernández, J.; Kiwi, J.; Baeza, J.; Freer, J.; Lizama, C. and Mansilla, H.D. 2004. Orange II Photocatalysis on Immobilised TiO_2 Effect of the pH and H_2O_2. Appl. Catal. B: Environ. 48: 205–211.

Foster, K.A.; J.E. House, Jr., 1983. Thermal studies on oxalate complexes. V. Potassium tris(oxalato)aluminate(III) trihydrate. Thermo. Chim. Acta. 60: 389-391.

Galindo, C.; Jacques, P. and Kalt, A. 2000. Photodegradation of The Aminoazobenzene Acid Orange 52 by Three Advanced Oxidation Processes: UV/H_2O_2, UV/TiO_2 and VIS/TiO_2 Comparative Mechanistic and Kinetic Investigations. J. Photochem.and Photobiol. A: Chem. 130: 35-47.

Gfroerer, T. H. 2000. Photoluminescence in Analysis of Surfaces and Interfaces. In: Encyclopedia of Analytical Chemistry, R.A. Mayers Ed. John Willey & Sons Ltd, Chichester. p. 9209-9231.

Gnaser, H.; Savina, M.R.; Galaway, W.F.; Tripa, C.E.; Veryovkin, I.V.; and Pellin, M.J. 2005. Photocatalytic Degradation of Methylene Blue on Nanocrystalline TiO_2: Surface Mass Spectrometry of Reaction Intermediates. Int. J. Mass Spectrom. 245: 61-67.

Gomes de Moraes, S.; Sanches Freire, R. and Duran, N. 2000. Degradation and Toxicity Reduction of Textile Effluent by Combined Photocatalytic and Ozonation Processes. Chemosphere. 40: 369-373.

Gome da Silva, C. and Faria, J.L. 2003. Photochemical and Photocatalytic Degradation of An Azo Dye in Aqueous Solution by UV Irradiation. J. Photochem. Photobiol. A: Chem. 155: 133-143.

Gopal, M., Chan, W. J. M. and De Jonghe, L. C. 1997. Room Temperature Synthesis of Crystalline Metal Oxides. J. Mater. Sci. 32: 6001-6008.

Grzechulska, J. and Morawski, A.W. 2002. Photocatalytic Decomposition of Azo-Dye Acid Black 1 in Water over Modified Titanium Dioxide. Appl. Catal. B: Environ. 36:45-51.

Guo, B.; Liu, Z.; Hong, L.; Jiang, H. and Lee, J.Y. 2005. Photocatalytic Effect of The Sol–Gel Derived Nanoporous TiO_2 Transparent Thin Films. Thin Solid Films. 479: 310-315.

Gutierrez, M.C.; Jobbagy, M.; Rapun, N.; Ferrer, M.L. and Monte, F.D. 2006. A Biocompatible Bottom-up Route for The Preparation of Hierarchical Biohybrid Material. Adv. Mater. 18: 1137-1140.

Gutierrez, M.C.; Hortiguela, M.J.; Amarilla, J. M.; Jimenez, R.; Ferrer, M.L. and Monte, F.D. 2007. Macroporous 3D Architectures of Self-Assembled MWCNT Surface Decorated with Pt Nanoparticles as Anodes for A Direct Methanol Fuel Cell. J. Phys. Chem. C. 11: 5557-5560.

Gutierrez, M.C.; Ferrer, M.L. and Monte, F.D. 2008. Ice-Templated Materials: Sophisticated Structure Exhibiting Enhanced Functionalities Obtained after Unidirectional Freezing and Ice-Segregation-Induced Self-Assembly. Chem. Mater. 20: 634-648.

Hachem, C.; Bocquillon, F.; Zahraa, O. and Bouchy, M. 2001. Decolourization of Textile Industry Wastewater by the Photocatalytic Degradation Process. Dyes and Pigments. 49: 117-125.

Hadjiinov, K.I. and Klissurski, D.G. 1996. Surface Chemistry of Titania (Anatase) and Titania-Supported Catalysts. Chem. Soc. Rev. 61-69.

Hammami, S.; Bellakhal, N.; Oturan, N.; Oturan, M. A. and Dachraoui, M. 2008. Degradation of Acid Orange 7 by Electrochemically Generated $^{\bullet}OH$ Radicals in Acidic Aqueous Medium using A Boron-Doped Diamond or Platinum Anode: A Mechanistic Study. Chemosphere 73: 678–684.

Hirakawa, T.; Yawata, K. and Nosaka, Y. 2007. Photocatalytic Reactivity for $O_2^{\bullet-}$ and $OH^{\bullet}$ Radical Formation in Anatase and Rutile TiO_2 Suspension as The Effect of H_2O_2 Addition. Appl. Catal. A: Gen, 325: 105-111.

Houas, A., Lachheb, H., Ksibi, M., Elaloui, E., Guillard, C. and Herrmann, J. –M. 2001. Photocatalytic Degradation Pathway of Methylene Blue in Water. Appl.Cat. B: Environ, 31: 145-147.

House, Jr., J.E. and Blumthal, T.G. 1980. Thermal Studies on Oxalate Complexes. II. Complexes of Iron (III) and Chromium (III). Thermo Chim. Acta, 36: 79-84.

Huang, D.; Wang, Y.J.; Yang, L.M. and Luo, G.S. 2006. Direct Synthesis of Mesoporous TiO_2 Modified with Phosphotungstic Acid under Template-Free Condition. Microporous Mesoporous Mater. 96: 301–306.

Huheey, J.E. 1978. Inorganic Chemistry: Principles of Structure and Reactivity, 2^{nd} edn., Harper International Edition, New York, 1978, p.78 and p.253.

Hurum, D.C.; Agrios, A.G.; Crist, S.E.; Gray, K.A.; Rajh, T. and Thurnauer, M.C. 2006. Probing reaction mechanisms in mixed phase TiO_2 by EPR. J. Electron Scopy and Related Phenomena. 150: 155-163.

Ibhadon, A.O.; Greenway, G.M.; Yue, Y.; Falaras, P. and Tsoukleris, D. 2008. The Photocatalytic Activity of TiO_2 Foam and Surface Modified Binary Oxide Titania Nanoparticles. J. Photochem. Photobiol. A: Chem., 197: 321-328.

Jameela, S.R. and Jayakrishnan, A. 1995. Glutaraldehyde Crosslinked Chitosan as a Long Ccting Biodegradable Drug Delivery Vehicle: Studies on The in Vitro Release of Mitoxantrone and in Vivo Degradation of Microspheres in Rat Muscle. Biomaterials. 16: 769–775.

Jiang, Z.; Yu, Y. and Wu, H. 2006. Preparation of CS/GPTMS Hybrid Molecularly Imprinted Membrane for Efficient Chiral Resolution of Phenylalanine Isomers. J. Membrane Sci. 280: 876–882.

Kabra, K.; Chaudhary, R. and Sawhney, R. L. 2004. Treatment of Hazardous Organic and Inorganic Compounds through Aqueous-Phase Photocatalysis: A Review. Ind. Eng. Chem. Res. 43: 7683-7696.

Khalil, T.; Abou El-Nour, F.; El-Gammal, B. and Boccaccini. 2001. Determination of Surface Area and Porosity of Sol-Gel Derived Ceramic Powders in The System TiO_2-SiO_2-Al_2O_3. Powder Technology. 114: 106-111.

Kim, D.S. and Kwak, S.-Y. 2007. The Hydrothermal Synthesis of Mesoporous TiO_2 with High Crystallinity, Thermal stability, Large Surface Area, and Enhanced Photocatalytic Activity. Appl. Catal. A: Gen. 323: 110–118.

Kiriakidou, F.; Kondarides, D. I. and Verykios, X. E. 1999. The Effect of Operational Parameters and TiO_2-Doping on the Photocatalytic Degradation of Azo-Dyes. Catal. Today. 54: 119-130.

Kluson, P.; Kacer, P.; Cajthaml, T. and Kalaji, M. 2001. Preparation of Titania Mesoporous Materials Using A Surfactant-Mediated Sol-Gel Method. J. Mater. Chem. 11: 644-651.

Konstantinou, I.K. and Albanis, T.A. 2004. TiO_2-Assisted Photocatalytic Degradation of Azo Dyes in Aqueous Solution: Kinetic and Mechanistic Investigations: A Review. Appl. Catal. B: Environ. 49: 1-14.

Kwon, C.H.; Shin, H.; Kim, J.H.; Choi, W.S. and Yoon, K.H. 2004. Degradation of Methylene Blue Via Photocatalysis of Titanium Dioxide. Mater.Chem. Phys. 86: 78-82.

Kumar, S. R.; Suresh, C.; Vasudevan, A. K.; Suja, N. R. and Mukundan, P. 1999. Phase Transformation in Sol-Gel Titania Containing Silica. Mater. Lett. 38: 161-166.

Kumar, P. M.; Barinarayanan, S. and Saatry, M. 2000. Nanocrystalline TiO_2 Studied by Optical, FT-IR and X-ray Photoelectron Spectroscopy: Correlation to Presence of Surface States. Thin Solid Films. 358: 122-130.

Legrini, O.; Oliveros, E.; Braun, A.M. 1993. Photochemical Processes for Water Treatment. Chem. Rev. 93; 671-698.

Lethbridge, Z.A.D.; Congreve, A.F.; Esslemont, E.; Slawin, A.M.Z. and Lightfoot, P. 2003. Synthesis and Structure of Three Manganese Oxalates: $MnC_2O_4.2H_2O$, $[C_4H_8(NH_2)_2][Mn_2(C_2O_4)_3]$ and $Mn_2(C_2O_4)(OH)_2$. J. Solid State Chem. 172: 212-218.

Li, J.-G.; Wang, Y.; Ikegami, T.; Mori, T. and Ishigaki, T. 2005. Reactive 10 mol% RE_2O_3 (RE =Gd and Sm) doped CeO_2 nanopowders: Synthesis, Characterization, and low-temperature sintering into dense ceramics. Mater. Sci. Eng. B. 121: 54-59.

Li, Y.; White, T.J. and Lim, S.H. 2004. Low-Temperature Synthesis and Microstructural Control of Titania Nano-Particles. J. Solid State Chem. 177: 1372–1381.

Linsebigler, A.L.; Lu, G.; Yates, J.T. 1995. Photocatalysis on TiO_2 Surfaces: Principles, Mechanisms, and Selected Results. Chem. Rev. 95: 735-758.

Liqiang, J.; Xiaojun,S.; Weimin, C.; Zili, X.; Yaoguo, D. and Honggang, F. 2003. The Preparation and Characterization of Nanoparticle TiO_2/Ti Films and Their Photocatalytic Activity. J. Phys. Chem. Solid. 64: 615–623.

Liqiang, J.; Yichun, Q.; Baiqi, W.; Shudan, L.; Baojiang, J.; Libin, Y.; Wei, F.; Honggang, F. and Jiazhong, S. 2006. Review of Photoluminescence Performance of Nano-Sized Semiconductor Materials and Its Relationships with Photocatalytic Activity. Sol. Energy Mater. Sol. Cells, 90: 1773-1787.

Liu, Y.L.; Su, Y.H. and Lai, J.Y. 2004. In Situ Crosslinking of Chitosan and Formation of Chitosan-Silica Hybrid Membranes with using γ-Glycidoxypropyltrimethoxy-Silane as a Crosslinking Agent. Polymer. 45: 6831–6837.

Liu, Y.L.; Su, Y.H.; Lee, K.R. and Lai, J.Y. 2005. Crosslinked Organic–Inorganic Hybrid Chitosan Membranes for Pervaporation Dehydration of Isopropanol–Water Mixtures with A Long-Term Stability, J. Membr. Sci. 251: 233–238.

Liu, Z.; Jin, Z.; Li, W. and Qiu, J. 2005. Preparation of ZnO Porous Thin Films by Sol-Gel Method using PEG Template. Mater. Lett. 59: 3620-3625.

Liu, Z.; Ma, R.; Osada, M.; Takada, K. and Sasaki, T. 2005. Selective and Controlled Synthesis of α- and β-Cobalt Hydroxides in Highly Developed Hexagonal Platelets. J. Am. Chem. Soc. 127: 13869-13874.

Losito, I.; Amorisco, A.; Palmisano, F. and Zambonin, P.G. 2005. X-ray Photoelectron Spectroscopy Characterization of Composite TiO_2–Poly(vinylidenefluoride) Films Synthesised for Applications in Pesticide Photocatalytic Degradation. Appl. Surf. Sci. 240: 180-188.

Mills, A. and Wang, J. 1999. Photobleaching of Methylene Blue Sensitised by TiO_2: An Ambiguous System? J. Photochem. Photobiol. A. 127: 123-134.

Mordant dye from Mordant dyes: http://www.jagson.com/mordant_dyes.htm Jacson Colorchem Limited (accessed 31/03/09).

Mukai, S.R.; Nishihara, H. and Tamon, H. 2006. Porous Microfibers and Microhoneycombs Synthesized by Ice Templating. Catalysis Survey from Asia. 10: 161-171.

Mukai, S. R.; Nishihara, H. and Tamon, H. 2008. Morphology Maps of Ice-Templated Silica Gels Derived from Silica Hydrogels and Hydrosols. Microporous Mesoporous Mater. 116: 166–170.

Mukoma, P.; Jooste, B.R. and Vosloo, H.C.M. 2004. Synthesis and Characterization of Cross-Linked Chitosan Membranes for Application as Alternative Proton Exchange Membrane Materials in Fuel Cells, J. Power Sources 136: 16–23.

Nagaveni, K.; Sivalingam, G. and Heged, M.S. 2004. Solar Photocatalytic Degradation of Dyes: High Activity of Combustion Synthesized Nano TiO_2. Appl. Catal. B: Environ. 48: 83-93.

Neppolian, H.C.; Choi, B.; Sakthivel, S.; Arabindoo, B. and Murugesan, V. 2002. Solar Light Induced and TiO_2 Assisted Degradation of Textile Dye Reactive Blue 4. Chemosphere, 46: 1173-1181.

Neppolian, B.; Sakthivel, S.; Phalanichamy, M. and Arabindoo, B. 2002. Solar/UV-Induced Photocatalytic Degradation of Three Commercial Textile Dyes J. Hazardous Mater. B. 89: 303-317.

Niemantsverdriet, J.W. 1993. Spectroscopy in catalysis: An Introduction. VCH Publishers.

Nishihara, H.; Mukai, S.R.; Yamashita, D. and Tamon, H. 2005. Ordered Macroporous Silica by Ice Templating. Chem. Mater. 17: 683-689.

Nishihara, H.; Mukai, S.R.; Fujii, Y.; Tago, T.; Masuda, T. and Tamon, H. 2006. Preparation of Monolithic SiO_2-Al_2O_3 Cryogel with Inter-connected Macroporous Through Ice Templating. J. Mater. Chem.16: 3231-3236.

Ohno, T.; Tokieda, K.; Higashida, S. and Matsumura, M. 2003. Synergism between Rutile and Anatase TiO_2 Particles in Photocatalytic Oxidation of Naphthalene. Appl. Catal. A: Gen. 244: 383-391.

Ohtani, B.; Ogawa, Y. and Nishimoto S. 1997. Photocatalytic Activity of Amorphous-Anatase Mixture of Titanium (IV) Oxide Particles Suspended in Aqueous Solutions. J. Phys. Chem. B. 101: 3746-3752.

Partsinis, S.E. 1996. Flame Synthesis of Nanosize Particles: Precise Control of Particle Size. J. Aerosol Sci. 27: s153-s154.

Patil, A.J.; Shinde, M.H.; Potdar, H.S.; Deshpande, S.B.; Sainkar, S.R.; Mayadevi, S. and Date, S.K. 2001. Chemical Synthesis of Titania (TiO_2) Powder via Mixed Precursor Route for Membrane Applications. Mater. Chem. Phys. 68: 7-16.

Peng, T.; Zhao, D.; Dai, K.; Shi, W. and Hirao, K. 2005. Synthesis of Titanium Dioxide Nanoparticles with Mesoporous Anatase Wall and High Photocatalytic Activity. J. Phys. Chem. B. 109: 4947-4952.

Potdar, H.S.; Deshpande, S.B.; Deshpande, A.S.; Khollam, Y.B.; Patil, A.J. and Pradham, S.D. 2001. Simplified Chemical Route for The Synthesis of Barium Titanyl Oxalate (BTO). Int. J. Inorg. Mater., 3: 613-623.

Prevot, A.B.; Baiocchi, C.; Brussino, M.C.; Pramauro, E.; Savarino, P.; Augugliaro, V.; Marc, G. and Palmisano, L. 2001. Photocatalytic Degradation of Acid Blue 80 in Aqueous Solutions Containing TiO_2 Suspensions. Environ. Sci. Technol. 35: 971-976.

Randorn, C., Wongnawa, S. and Boonsin, P. 2004. Bleaching of Methylene Blue by Hydrated Titanium Dioxide. ScienceAsia. 30: 149-156.

Reactive dye from Wikipedia, the free encyclopedia. http://en.wikipedia.org/wiki/Reactive_dye (accessed 31/03/09).

Reddy, K. M.; Reddy, R. C. V. and Manorama, S. V. 2001. Preparation, Characterization, and Spectra Studies on Nanocrystalline Anatase TiO_2. J. Solid State Chem. 158: 180-186.

Rouquerol, F.; Rouquerol, J. and Sing, K. 1999. Adsorption by Powders and Porous Solids: Principles, Methodology and Applications. Acadimic press.

Ryu, Z.; Zheng, J.; Wang, M. and Zhang, B. 1999. Characterization of pore size Distributions on Carbonaceous Adsorbents by DFT. Carbon. 37: 1257-1264.

Saien, J. and Khezrianjoo, S. 2008. Degradation of the Fungicide Carbendazim in Aqueous Solutions with UV/TiO_2 Process: Optimization, Kinetics and Toxicity Studies. J. Hazardous Mater. 157: 269-276.

Sanchez, E. and Lopez, T. 1995. Effects of Preparation Method on the Band Gap of Titania and Platinum-Titania Sol-Gel Materials. Mater. Lett. 25: 271-275.

Sankapal, S.B.; Steiner, M.Ch. and Ennaoui, A. 2005. Synthesis and Characterization of Anatase-TiO_2 Thin Films. Appl. Surf. Sci. 239: 165-170.

Sauer, T.; Neto, C.; José, H. J. and Moreira, R. F. P. M. 2002. Kinetics of Photocatalytic Degradation of Reactive Dyes in a TiO_2 Slurry Reactor. J. Photochem. Photobiol. A. 149: 147-154.

Scanning electron microscope from Wikipedia, the free encyclopedia. http://en.wikipedia.org/wiki/Scanning_electron_microscope (accessed 30/03/09).

Sen, S.; Mahanty, S.; Roy, S.; Heintz, O.; Bourgeois, S. and Chaumont, D. 2005. Investigation on Sol–Gel Synthesized Ag-Doped TiO_2 Cermet Thin Films. Thin Solid Films. 474: 245-249.

Senthikumaar, S.; Porkodi, K.; Gomathi, R.; Maheswari, A.G. and Manonmani, N. 2006. Sol-gel Derived Silver Doped Nanocrystalline Titania Catalysed Photodegradation of Methylene Blue from Aqueous Solution. Dyes and Pigments. 69: 22-30.

Serpone, N.; Lawless, D.and Khairutdinov, R. 1995. Size Effects on the Photophysical Properties of Colloidal Anatase TiO_2 Particles: Size Quantization or Direct Transition in This Indirect Semiconductor. J. Phys. Chem. 99: 16646-16654.

Shirosaki, Y.; Tsuru, K.; Hayakawa, S.; Osaka, A.; Lopes, M.A.; Santos, J.D. and Fernandes, M.H. 2005. In Vitro Cytocompatibility of MG63 Cells on Chitosan–Organosiloxane Hybrid Membranes, Biomater. 26: 485–493.

Shirosaki, Y.; Okayama, T.; Tsuru, K.; Hayakawa, S. and Osaka, A. 2008. Synthesis and Cytocompatibility of Porous Chitosan–Silicate Hybrids for Tissue Engineering Scaffold Application. Chem. Eng. J. 137: 122–128.

Shu, H.-Y. and Chang, M.-C. 2005. Decolorization and Mineralization of a Phthalocyanine Dye C.I. Direct Blue 199 Using UV/H_2O_2 Process. J. Hazard. Mater. B125: 96-101.

Shu, H.-Y. and Chang, M.-C. 2005. Pilot Scale Annular Plug Flow Photoreactor by UV/H_2O_2 for the Decolorization of Azo Dye Wastewater. J. Hazard. Mater., B125: 244-251.

Smatt, J.H.; Schunk, S. and Linden, M. 2003. Versatile Double-Templating Synthesis Route to Silica Monoliths Exhibiting a Multimodal Hierarchical Porosity. Chem. Mater. 15: 2354-2361.

Sreethawong, T.; Suzuki, Y. and Yoshikawa, S. 2005. Synthesis, Characterization, and Photocatalytic Activity for Hydrogen Evolution of Nanocrystalline Mesoporous Titania Prepared by Surfactant-Assisted Templating Sol–Gel Process. J. Solid State Chem. 178: 329-338.

Sriwong, C.; Wongnawa, S. and Patarapaiboolchai, O. 2008. Photocatalytic Activity of Rubber Sheet Impregnated with TiO_2 Particles and Its Recyclability.

Catal. Comm. 9: 213-218.

Stone, V.F. and Davis, R.J. 1998. Synthesis, Characterization, and Photocatalytic Activity of Titania and Niobia Mesoporous Molecular Sieves. Chem. Mater. 10: 1468-1474.

Stylidi, M.; Kondarides, D. I. and Verykios, X. E. 2003. Pathways of Solar Light-Induced Photocatalytic Degradation of Azo Dyes in Aqueous TiO_2 Suspensions. Appl. Catal. B: Environ. 40: 271–286.

Su, Y.I. and Liu, H.Z. 2003. Temperature-Dependent Solubilization of PEO-PPO-PEO Block Copolymers and Their Application for Extraction Trace Organics from Aqueous Solutions. Koren J. Chem. Eng. 20(2): 343-346.

Sulfur dye from dye summary. http://www.dyeman.com/Dye%20summary.html Thames and Hudson manual of Dyes and Fabrics - Joyce Storey (accessed 31/03/09).

Sun, C.; Wang, N.; Zhou, S.; Hu, X.; Zhou, S. and Chen, P. 2008. Preparation of Self-Supporting Hierarchical Nanostructured Anatase/Rutile Composite TiO_2 Film. Chem. Commun. 3293–3295.

Suwanchawalit, C. and Wongnawa, S. 2008. Influence of Calcination on the Microstructures and Photocatalytic Activity of Potassium Oxalate-Doped TiO_2 Powders. Appl.Catal. A: Gen. 338: 87-99.

Tan, T.W.; He, X.J. and Du, W.X. 2001. Adsorption Behaviour of Metal Ions on Imprinted Chitosan Resin, J. Chem. Technol. Biotechnol. 76: 191–195.

Tan, H.; Wu, J.; Lao, L. and Gao, C. 2009. Gelatin/Chitosan/Hyaluronan Scaffold Integrated with PLGA Microspheres for Cartilage Tissue Engineering. Acta Biomater. 5: 328-337.

Tanaka, K.; Padermpole, K. and Hisanaga, T. 2000. Photocatalytic Degradation of Commercial Azo Dyes. Wat. Res. 34: 327-333.

Tang, Z.; Zhang, J.; Cheng, Z. and Zhang, Z. 2002. Synthesis of Nanosized Rutile TiO_2 Powder at Low Temperature. Mater. Chem. Phys. 9319: 1-4.

Tian, C.; Zhang, Z.; Hou, J. and Luo, N. 2008. Surfactant/Co-Polymer Template Hydrothermal Synthesis of Thermally Stable, Mesoporous TiO_2 from $TiOSO_4$. Mater. Lett. 62: 77–80.

Thongprachana, N.; Nakagawab, K.; Sanoc, N.; Charinpanitkula, T. and Tanthapanichakoon, W. 2008. Preparation of Macroporous Solid Foam from Multi-Walled Carbon Nanotubes by Freeze-Drying Technique. Mater. Chem. Phys.112: 262–269.

Transmission electron microscope from Wikipedia, the free encyclopedia. http://en.wikipedia.org/wiki/Transmission_electron_microscope (accessed 30/03/09).

Trotman, E.R. 1975. Dyeing and Chemical Technology of Texile Fibres. Fifth edition, Charles Griffin & Co. Ltd. p318; p470.

Tryba, B.; Toyoda, M.; Morawski, A.W.; Nonaka, R. and Inagaki, M. 2007. Photocatalytic Activity and OH Radical Formation on TiO_2 in the Relation to Crystallinity. Appl. Catal. B: Environ. 71: 163-168.

Vat dye from Wikipedia, the free encyclopedia. http://en.wikipedia.org/wiki/Vat_dye (accessed 31/03/09).

Vat dye from dye summary. http://www.dyeman.com/Dye%20summary.html Thames and Hudson manual of Dyes and Fabrics - Joyce Storey (accessed 31/03/09).

Vaidhyanathan, R.; Natarajan, S.; Cheetham, A.K. and Rao, C.N.R. 1999. New Open-Framework Zinc Oxalates Synthesized in the Presence of Structure-Directing Organic Amines. Chem. Mater. 11: 3636-3642.

Velardi, S.A.; Barresi, A.A. 2008. Development of Simplified Models for the Freeze-Drying Process and Investigation of the Optimal Operating Conditions. Chem. Eng. Des. 86: 9-22.

Velev, O. D. and Kaler, E. W. 2000. Structured Porous Materials via Colloidal Crystal Templating: From Inorganic Oxides to Metals. Adv. Mater.12: 531-534.

Venkatachalam, N.; Palanichamy, M. and Murugesan, V. 2007. Sol-gel Preparation and Characterization of Nanosize TiO_2: Its Photocatalytic Performance. Mater. Chem. Phys. 104: 454-459.

Wang, K.; Zhang, J.; Lou, L.; Yang, S. and Chen. Y. 2004. UV or Visible Light Induced Photodegradation of AO7 on TiO_2 Particles: the Influence of Inorganic Anions. J. Photochem. Photobiol. A: Chem. 165: 201-207.

Wang, O. J.; Moss, S. C.; Shalz, M. L.; Glaeser, A. M.; Zandbergen, H. W. and Zschack, P. 1992. In Physics and Chemistry of Finite Systems: from Clusters to Crystals, vol. II, edited by Jena, P.; Khanna, S. N. and Rao, B. K. Kluwer Academic Publishers, Boston, pp. 1287.

Wang, Y.; Jiang, Z.H. and Yang, F.J. 2006. Preparation and Photocatalytic Activity of Mesoporous TiO_2 Derived from Hydrolysis Condensation with TX-100 as Template. Mater. Sci. Eng. B. 128: 229-233.

Wang, Z.; Cai, W.; Hong, X.; Zhao, X.; Xu, F. and Cai, C. 2005. Photocatalytic Degradation of Phenol in Aqueous Nitrogen-Doped TiO_2 Suspensions with Various Light Sources. Appl. Catal. B: Environ. 57: 223–231.

Wang, Z. C.; Chen, J. F. and Hu, X. F. 2000. Preparation of Nanocrystalline TiO_2 Powder at near Room Temperature from Peroxo-Polytitanic Acid Gel. Mater. Lett. 43: 87-90.

Wen, B.; Liu, C. and Liu, Y. 2005. Optimization of the Preparation Methods Synthesis of Mesostructured TiO_2 with High Photocatalytic Activities. J. Photochem. Photobiol. A: Chem. 173: 7-12.

Weng, W.; Ma, M.; Du, P.; Zhao, G.; Shen, G.; Wang, J. and Han, G. 2005. Superhydrophilic Fe Doped Titanium Dioxide Thin Films Prepared by a Spray Pyrolysis Deposition. Surf. Coat. Technol. 198: 340-344.

West, A.R. 1987. Solid State Chemistry and Its Application. John Wiley & Sons Ltd.

Wu, M.; Lin, G.; Chen, D.; Wang, G.; He, D.; Feng, S. and Xu, R. 2002. Sol-Hydrothermal Synthesis and Hydrothermally Structural Evolution of Nanocrystal Titanium Dioxide. Chem. Mater. 14: 1974-1980.

Xu, N.; Shi, Z.; Fan, Y.; Dong, J.; Shi, J. and Hu, M. Z.-C. 1999. Effects of Particle Size of TiO_2 on Photocatalytic Degradation of Methylene Blue in Aqueous Suspensions. Ind. Eng. Chem. Res. 38: 373-379.

Yan, M.; Chen, F.; Zhang, J. and Anpo, M. 2005. Preparation of Controllable Crystalline Titania and Study on the Photocatalytic Properties. J. Phys. Chem. B. 109: 8673-8678.

Yang, J.; Zhang, J.; Zhu, L.; Chen, S.; Zhang, Y.; Tang, Y.; Zhu, Y. and Li. Y. 2006. Synthesis of Nano Titania Particles Embedded in Mesoporous SBA-15: Characterization and Photocatalytic Activity. J. Hazardous Mater. B. 137: 952-958.

Yang, J.H.; Han, Y.S. and Choy, J.H. 2006. TiO_2 Thin-Films on Polymer Substrates and Their Photocatalytic Activity. Thin Solid Films. 495: 266-271.

Yanqing, Z.; Erwei, S.; Zhizhan, C.; Wenjun, L. and Xingfang, H. 2001. Influence of Solution Concentration on the Hydrothermal Preparation of Titania Crystallites. J. Mater. Chem. 11: 1547-1551.

Yoo, K.S.; Choi, H. and Dionysiou, D.D. 2005. Synthesis of Anatase Nanostructured TiO_2 Particles at Low Temperature Using Ionic Liquid for Photocatalysis. Catal. Comm., 6: 259-262.

Yoo, K.S.; Lee, T.G. and Kim, J. 2005. Preparation and Characterization of Mesoporous TiO_2 Particles by Modified Sol-Gel Method Using Ionic Liquids", Microporous Mesoporous Mater. 84: 211-217.

Yu, C.; Yu, Y.; Miao, L. and Zhao, D. 2001. Highly Ordered Mesoporous Silica Structures Templated by Poly(butylene oxide) Segment Di- and Tri-Block Copolymers. Microporous Mesoporous Mater. 44-45: 65-72.

Yu, H.-F. and Wang, S.-M. 2000. Effects of Water Content and pH on Gel-Derived TiO_2-SiO_2. J. Non-Crystalline Solid. 261: 260-267.

Yu, J.; Yu, H.; Cheng, B. and Trapalis, C. 2006. Effects of Calcination Temperature on the Microstructures and Photocatalytic Activity of Titanate Nanotubes. J. Mol. Cat. A: Chem. 249: 135-142.

Yu, J.C.; Zhang, L.; Zheng, Z. and Zhao, J. 2003. Synthesis and Characterization of Phosphated Mesoporous Titanium Dioxide with High Photocatalytic Activity. Chem. Mater. 15: 2280-2286.

Yu, J. G. Y.; Yu, J. C.; Cheng, B.; Hark, S. K. and Ju, K. 2003. The Effect of F-Doping and Temperature on the Structural and Textural Evolution of

Mesoporous TiO_2 Powders. J.Solid State Chem. 174: 372-380.

Zarur, A. J.; Mehenti, N. Z.; Heibel, A. T. and Ying, J. Y. 2000. Phase Behavior, Structure, and Applications of Reverse Microemulsions Stabilized by Nonionic Surfactants. Langmuir. 16: 9168-9176.

Zhang, B.J.; Davis, S. A. and Mann, S. 2002. Starch Gel Templating of Spongelike Macroporous Silicalite Monoliths and Mesoporous Films. Chem. Mater. 14: 1369-1375.

Zhang, F., Zhao, J., Shen, T., Hidaka, H., Pelizzetti, E. and Serpone, N. 1998. TiO_2-Assisted Photodegradation of Dye Pollutants II. Adsorption and Degradation Kinetics of Eosin in TiO_2 Dispersions under Visible Light Irradiation. Appl.Catal. B. 45: 147-156.

Zhang, H. and Cooper, A.I. 2007. Aligned Porous Structures by Directional Freezing. Adv. Mater. 19: 1529-1533.

Zhang, J.; Li, M.; Feng, Z.; Chen, J. and Li, C. 2006. UV Raman Spectroscopic Study on TiO_2. I. Phase Transformation at the Surface and in the Bulk. J. Phys. Chem. B. 110: 297-935.

Zhang, J.; Minagawa, M.; Matsuoka, M.; Yamashita, H. and Anpo, M. 2000. Photocatalytic Decomposition of NO on Ti-HMS Mesoporous Zeolite Catalysts”, Catal. Lett. 66, 241–243.

Zhang, Q.; Gao, L. and Guo, J. 2000. Effects of Hydrolysis Conditions on Morphology and Crystallization of Nanosized TiO_2 Powders. J. Eur. Ceram. Soc. 20: 2153-2158.

Zhang, X.; Zhang, F. and Chan, K.-Y. 2006. The Synthesis of Pt-Modified Titanium Dioxide Thin Films by Microemulsion Templating, Their Characterization and Visible-Light Photocatalytic Properties. Mater. Chem. Phys. 97: 384-389.

Zhang, X.; Sun, D.D.; Li, G.; Wang, Y. 2008. Investigation of the Roles of Active Oxygen Species in Photodegradation of Azo Dye AO7 in TiO_2 Photocatalysis Illuminated by Microwave Electrodeless Lamp. J. Photochem. Photobiol. A: Chem. 199: 311–315.

Zhang, Y.; Weidenkaff, A. and Reller, A. 2002. Mesoporous Structure and Phase Transition of Nanocrystalline TiO_2.. Mater. Lett. 54: 375-381.

Zhang, Y.; Li, G.; Wu, Y.; Luo, Y. and Zhang L. 2005. The Formation of the Mesoporous TiO_2 Spheres via a Facile Chemical Process. J. Phys. Chem. B. 109: 5478-5481.

Zhang, Y. and Mu, J. 2007. One-pot Synthesis, Photoluminescence, and Photocatalysis of Ag/ZnO Composites. J. Colloid Interface. Sci., 309: 478-484.

Zheng, J.Y.; Pang, J.B.; Qiu, K.Y. and Wei, Y. 2001. Synthesis and Characterization of Mesoporous Titania and Silica-Titania Materials by Urea Templated Sol-Gel Reactions. Microporous Mesoporous Mater. 49: 189-195.

Zhiyong, Y.; Laub, D.; Bensimon, M. and Kiwi, J. 2008. Flexible Polymer TiO_2 Modified Film Photocatalysts Active in the Photodegradation of Azo-Dyes in Solution. Inorg. Chim. Acta. 361: 589 –594.

Zhiyong, Y.; Keppner, H.; Laub, D.; Mielczarski, E.; Mielczarski, J.; Kiwi-Minsker, L.; Renken, A. and Kiwi, J. 2008. Photocatalytic Discoloration of Methyl Orange on Innovative Parylene–TiO_2 Flexible Thin Films under Simulated Sunlight. Appl. Catal. B: Environ, 79: 63-71.

Zhao, L.; Yu, Y.; Song, L.; Ruan, M.; Hu, X. and Larbot, A. 2004. Preparation of Mesoporous Titania Film Using Nonionic Triblock Copolymer as Surfactant Template. Appl. Catal. A: Gen. 263: 171–177.

Zhao, X. K. and Fendler, J. H. 1991. Size Quantization in Semiconductor Particulate Films. J. Phys. Chem. 95: 3716-3723.

Zhu, C.; Wang, L.; Kong, L.; Yang, X.; Wang, L.; Zheng, S.; Chen, F.; MaiZhi, F. and Zong, H. 2000. Photocatalytic Degradation of AZO Dyes by Supported TiO_2 + UV in Aqueous Solution. Chemosphere. 41: 303-309.

Zhu, H. Y.; Lan, Y.; Gao, X. P.; Ringer, S. P.; Zheng, Z. F.; Song, D. Y. and Zhao, J. C. 2005. Phase Transition between Nanostructures of Titanate and Titanium Dioxides via Simple Wet-Chemical Reactions J. Am. Chem. Soc. 127: 6730-6736.

Appendices

ELSEVIER

Available online at www.sciencedirect.com
ScienceDirect

Applied Catalysis A: General 338 (2008) 87–99

APPLIED CATALYSIS
A: GENERAL

www.elsevier.com/locate/apcata

Influence of calcination on the microstructures and photocatalytic activity of potassium oxalate-doped TiO_2 powders

Cheewita Suwanchawalit, Sumpun Wongnawa *

Department of Chemistry, Faculty of Science, Prince of Songkhla University, Hat Yai, Songkhla 90112, Thailand

Received 2 October 2007; received in revised form 14 December 2007; accepted 21 December 2007
Available online 15 January 2008

Abstract

Potassium oxalate-doped TiO_2 powders were prepared by the base-catalyzed sol–gel process with $TiCl_4$ as a precursor and hexamethylenetetramine as basic agent. The influence of calcination on the structure and photocatalytic activity of the as-prepared TiO_2 samples was investigated. The physical properties of the pre- and post-calcined materials were studied by X-ray diffraction spectroscopy, scanning electron microscopy, specific surface area, Fourier-transformed infrared spectroscopy, photoluminescence spectroscopy, and diffuse reflectance ultraviolet-visible spectroscopy. The photocatalytic activity of the products was evaluated by decolorizing methylene blue solutions and comparing them with a commercial TiO_2 powder (Degussa P25). The optimum calcination temperature of 800 °C yielded samples with enhanced photocatalytic activity comparable to Degussa P25. On the other hand, the non-calcined TiO_2 sample (amorphous phase with small amount of anatase phase) produced a better decolorization efficiency than did commercial P25, due to its excellent adsorptive properties with high concentrations of methylene blue solutions. More significantly, the dye adsorbed onto the surface of the non-calcined TiO_2 sample could be removed by treating with hydrogen peroxide solution under UV irradiation. The regenerated TiO_2 samples could be reused in the subsequent decolorization of methylene blue solution without a decline in decolorization efficiency compared with freshly prepared TiO_2 samples, with even slightly better efficiency.

Keywords: Titanium dioxide; Amorphous titanium dioxide; Sol–gel process; Calcinations; Methylene blue; Dye decolorization

1. Introduction

Titanium dioxide (TiO_2) has been the prevailing photocatalyst for the removal of organic contaminants from wastewater in recent years. It has many advantages over other semiconductor photocatalysts: chemical stability, strong oxidizing power, nontoxicity, inexpensive, and commercially available [1–3]. Some of its drawbacks are, low photocatalytic efficiency and problems of recovery after use [4–7]. To date commercially available products are the Degussa P25 and anatase. The latter is produced by many manufacturers. Many research workers have focused on the synthesis of variations of TiO_2 to improve its photocatalytic property and its applicability to wastewater treatment. These results demonstrate that the effective performance of the TiO_2 photocatalyst depends on many factors such as its crystal structure, crystallinity, crystallite size, surface functionality, and surface area of the catalyst [8–11].

The very convenient and practical sol–gel method is usually used for the preparation of TiO_2 mesostructures to achieve a high surface area with sizes ranging from nanometers to several micrometers. Among the advantages of this technique are molecular-scale mixing of the components, high purity of the precursor, and homogeneity of the sol–gel products with high uniformity of physical, morphological and chemical properties [11–13]. This method is mainly based on the hydrolysis and polycondensation of a metal alkoxide that will ultimately yield a hydroxide or oxide under certain conditions. However, in the traditional sol–gel method for TiO_2 preparation, it is often difficult to control the rate of hydrolysis as titanium precursors are highly reactive towards water [14]. As a result, the physicochemical properties of TiO_2 can be practically uncontrollable. Several attempts have been made to solve this problem by modifying various aspects of the reaction conditions: adding strong acid or base to retard the reaction rate of both hydrolysis and the condensation reactions [15,16],

---

* Corresponding author. Fax: +66 7421 2918.
E-mail address: sumpun.w@psu.ac.th (S. Wongnawa).

0926-860X/$ – see front matter © 2008 Elsevier B.V. All rights reserved.
doi:10.1016/j.apcata.2007.12.029

and using polymers as surfactant to obstruct the contact between the titanium precursor and water molecules [17,18].

In the present study, TiO_2 powders were prepared by the sol–gel method, using $TiCl_4$ as starting material for its low cost but high content of titanium. Hexamethylenetetramine was used as the basic reagent to control the rate of hydrolysis and condensation reactions. Potassium oxalate (KOX) was used as the doping agent to enhance surface area by forming an open framework structure. Furthermore, the oxalate group when bonded to metal ion will exert a ligand field strength similar to the oxide ion (O^{2-}) in TiO_2, therefore, the intrinsic energy levels within the material bulk is almost unchanged. The use of potassium oxalate creates another advantage over using oxalic acid as acid causes the solution to become too acid. Potassium oxalate was added in varying amounts: 0.5, 1.0, 2.0, and 4.0% by mass. Only the 0.5% concentration will be discussed in this report since it has some interesting properties that make it stand out from the rest. The oxalate anion is a good multidentate ligand that usually interlinks the metal ions into a two- or three-dimensional network [19–26]. This property of the oxalate anion may help form aggregates of TiO_2 with a framework with a large specific surface area which is one important parameter in the photocatalytic study. Hexamethylenetetramine (HMT) was used as a homogeneous hydrolyzing agent. The advantage of this reagent lies in its slow hydrolysis that introduces OH^- uniformly and homogeneously into the system, thereby, causing the metal hydroxide to precipitate. The slow precipitation means that morphology, size, and crystallinity of the product can be controlled [27,28]. The effect of the calcination temperature on the phase structure, crystallite size, morphology, specific surface area, pore structure, and photocatalytic activity of the as-prepared TiO_2 samples were investigated. Their photocatalytic properties were tested using the decolorization of methylene blue and results were compared with properties of commercial Degussa P25 TiO_2. The regeneration of the used catalyst and its reuse were also studied.

2. Experimental

2.1. Synthesis of the TiO_2 powders

All chemicals used in this work were of analytical grade and were used without further purification. The titanium tetrachloride ($TiCl_4$, Merck) was the starting material to produce titanium dioxide particles by the sol–gel method. For the preparation, 20 mL of $TiCl_4$ was added slowly to 100 mL of cold distilled water to obtain the titanium tetrachloride aqueous solution. Then 70 mL of potassium oxalate ($(COOK)_2 \cdot H_2O$, Ajax Finechem, 1.3 M) was added into this solution and refluxed at 90 °C for 13 h with vigorous stirring. The resulting solution was then treated with hexamethylenetetramine ($C_6H_{12}N_4$, Fluka) until the pH value was 7 and maintained at the same temperature for 13 h. The white precipitate formed was filtered and then washed with distilled water until no chloride ion was found by the $AgNO_3$ solution test. The washed samples were dried at 105 °C for a day and ground to a fine powder to give final product designated as 0.5KOX–TiO_2–*n*c. Then the resulting sample was calcined at 400, 600, 800, and 1000 °C for 3 h and designated as 0.5KOX–TiO_2–*x*c, where *x* is the calcination temperature.

2.2. Characterization of samples

The crystallization and phase formation of the resulting TiO_2 samples were studied with the Philips PW 3710 powder diffractometer (PHILIPS X'Pert MPD, The Netherlands) using Cu Kα radiation and equipped with a Ni filter in the range 5–90° (2θ). The specific surface area and pore size distribution of TiO_2 samples were characterized by analyzing the N_2 adsorption isotherms obtained at 77 K using the SA 3100 (Coulter, U.S.A.) equipment. The surface features and morphologies of the as-prepared TiO_2 samples were investigated by using a scanning electron microscope (SEM) model JSM-5800 LV (Jeol Apparatus, Japan). The infrared spectra were recorded using Fourier-transformed infrared (FT-IR) spectroscopy (EQUINOX55, Bruker, Germany) in the diffused reflectance mode at 400–4000 cm^{-1} with KBr as the reference material. The band gap energies of the TiO_2 samples were determined using two methods: UV–vis and photoluminescence (PL) spectroscopies. For the UV–vis method, a Shimadzu UV-2401 spectrophotometer (Shimadzu, Japan) was used. The spectra were recorded in the diffused reflectance mode using $BaSO_4$ as a reference. For the PL method, the samples were analyzed with a luminescence spectrometer (LS 55, PerkinElmer Instrument, U.K.). The band gap energies (E_g) of the catalyst were calculated according to the equation:

$$E_g = h\frac{c}{\lambda} \quad (1)$$

where E_g is the band gap energy (eV), *h* the Planck's constant, *c* the light velocity (m/s), and λ is the wavelength (nm).

2.3. Evaluation of photocatalytic activity of TiO_2 samples

The photocatalytic activity of TiO_2 samples were tested based on the degradation of methylene blue solution. The experiments were performed in a closed compartment (0.9 m × 0.9 m × 0.9 m) containing five fluorescence blacklight (20 W) tubes. The 1.0 g/L TiO_2 sample was dispersed in 75 mL methylene blue solution (2.5×10^{-4} M) in each experiment. Prior to the illumination, the suspension was stirred for 1 h to reach the adsorption equilibrium. Then the mixture was irradiated using five tubes of fluorescence blacklight 20 W (λ_{max} 366 nm) [29]. In all studies, the mixture was magnetically stirred, before and during illumination. At given irradiation time intervals (every 1 h), 5 mL of the sample was collected and centrifuged to separate TiO_2 powders prior to the absorbance measurement. The residual concentration of MB was monitored by observing the change in absorbance at 665 nm using a UV–vis spectrophotometer (Specord S100, Analytik Jena GmbH, Germany). Controlled experiments, without light or without TiO_2, were performed to demonstrate that degradation of the dye was dependent on the presence of both light and TiO_2.

3. Results and discussion

3.1. Characterization of the synthesized TiO_2 powders

The potassium oxalate-doped TiO_2 powders reported in this study were prepared by the sol–gel process, using $TiCl_4$ as the titanium source. In general, the sol–gel process consists of hydrolysis and condensation reactions: the former leads to the formation of the original nuclei of titanium dioxide while the latter leads to the growth of a network system of the original nuclei. When $TiCl_4$ was dissolved in water an exothermic reaction took place with the formation of orthotitanic acid [$Ti(OH)_4$], Eq. (2). When potassium oxalate was added a ''titanium oxalate complex'' was formed in the same hydrolysis solution, Eq. (3).

The hydrolysis reaction :

$$TiCl_4 + 4H_2O \rightarrow Ti(OH)_4 + 4H^+ + 4Cl^- \quad (2)$$

$$yTi(OH)_4 + yK_2C_2O_4 \rightarrow yK_2[Ti(OH)_4(C_2O_4)] \quad (3)$$

The coefficient y is used in Eq. (3) to mean that only a small amount of $K_2C_2O_4$ was used ($y \ll 1$). The hypothetical ''titanium oxalate complex'' is loosely represented by $K_2[Ti(OH)_4(C_2O_4)]$. Upon addition of HMT and at 90 °C, NH_3 and formaldehyde were produced, Eq. (4) [30]. The presence of NH_3 rendered the solution basic, Eq. (5), and catalyzed the condensation reaction to yield the products, Eqs. (6) and (7).

$$(CH_2)_6N_4 + H_2O \rightarrow 4NH_3 + 6HCHO \quad (4)$$

$$NH_3 + H_2O \rightarrow NH_4{}^+ + OH^- \quad (5)$$

The condensation reaction:

$$(1-y)Ti(OH)_4 \xrightarrow{OH^-} (1-y)TiO_2 + 2(1-y)H_2O \quad (6)$$

$$yK_2[Ti(OH)_4(C_2O_4)] \xrightarrow{OH^-} yTiO(C_2O_4) + yK_2O + 2yH_2O \quad (7)$$

The precipitated product obtained should be the mixture of $TiO_2 + y\ TiO(C_2O_4) + yK_2O$. The occurrence of $TiO(C_2O_4)$ was supported by the studies of titanium-oxalate systems [31,32].

The X-ray diffraction spectra of the as-prepared samples are illustrated in Fig. 1. The XRD pattern at $2\theta = 25.50°$ (1 0 1) in the spectrum of TiO_2 is identified as the crystal of the anatase form (denoted as "A") whereas the peak at $2\theta = 27.50°$ (1 1 0) arises from the crystal of the rutile form (denoted as "R"). The patterns apparently revealed the effect of the calcination temperature on the phase change of TiO_2 samples. It can be seen that the 0.5KOX–TiO_2–*nc* sample is composed of an amorphous phase as the main component and only a trace of anatase. When the samples were calcined at 400–800 °C they changed to the anatase phase, and as the calcination temperature rose to 1000 °C the crystals completely turned to rutile. According to many reports, the anatase–rutile transformation temperature was usually observed around 700–800 °C [33–38]. The result in this study indicated that the anatase–rutile transformation was significantly retarded. It has been reported that the phase transformation temperature mainly depends on the particles sizes, morphology of crystals, and the addition of additives [39]. In this study, the transformation was retarded as indicated by the transformation temperature being raised to 1000 °C and this may be attributed to the addition of potassium oxalate during the sol–gel reaction. TiO_2 that was treated with K^+ ion or prepared in the ionic liquid medium exhibited a higher anatase–rutile transformation temperature [35,40] while the treatment with Na^+ appeared

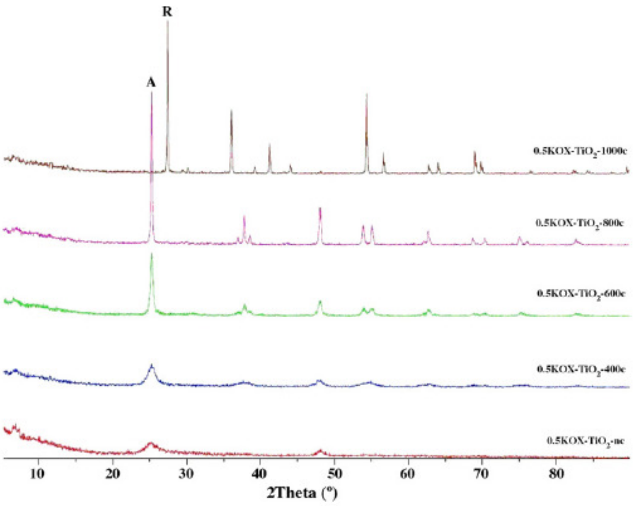

Fig. 1. XRD patterns of the as-prepared 0.5KOX–TiO_2 samples at different calcination temperatures (A = anatase, R = rutile).

Table 1
Effect of calcination temperature on the phase structure and average crystallite size (nm) of TiO_2 samples

Sample	Crystallite phase	Crystallite size (nm)[a]
0.5KOX–TiO_2–*nc*	Amorphous	–
0.5KOX–TiO_2–400c	Anatase	8
0.5KOX–TiO_2–600c	Anatase	24
0.5KOX–TiO_2–800c	Anatase	37
0.5KOX–TiO_2–1000c	Rutile	36

[a] Calculated from the Scherrer's formula.

to have no effect on the transformation temperature [36]. The oxalate group in many complexes usually decomposes at temperature <500 °C or at the most <650 °C [41,42]. Therefore, when the temperature reached 700–800 °C all the oxalate ions should have been destroyed leaving the final product in the form of TiO_2 with a trace of K_2O. In the sample bulk, the K^+ ion will be surrounded by the oxide ions, its own O^{2-} and also O^{2-} from TiO_2. This is, in fact, the ionic solid and its stability is governed by the lattice energy. The size of the K^+ ion is almost equal to that of the O^{2-} ion, 133 pm for the former and 140 pm for the latter [43]. Theoretically, the comparable sizes of cation and anion produce a more favorable lattice energy [43]. The product at this stage is presumably in the anatase phase, hence, it will be quite stable with K_2O and to transform it to the rutile phase would need a higher temperature. (In the presence of Na^+ ion, the effect is less favorable due to the smaller size of Na^+ ion which is only 95 pm, hence it is slightly mismatched with the O^{2-} ion and has a less favorable lattice energy when compared with the K^+ case.) The phase structure and average crystallite size of the calcined TiO_2 samples calculated using the Scherrer's equation for the main diffraction peak are given in Table 1.

The N_2 adsorption isotherms and pore size distributions before and after calcination at different temperatures are shown in Figs. 2 and 3, respectively. The isotherms of types I and IV (BDDT classification) were observed for 0.5KOX–TiO_2–*nc* and 0.5KOX–TiO_2–400c samples indicating the presence of a microporous and mesoporous structure. The samples calcined at higher temperatures showed the isotherm of type IV and almost had no hysteresis loop indicating that all the pores collapsed during calcination and the total pore volumes were very small. (The Coulter SA 3100 is not equipped to measure the desorption process, hence, the hysteresis loop could not be determined.)

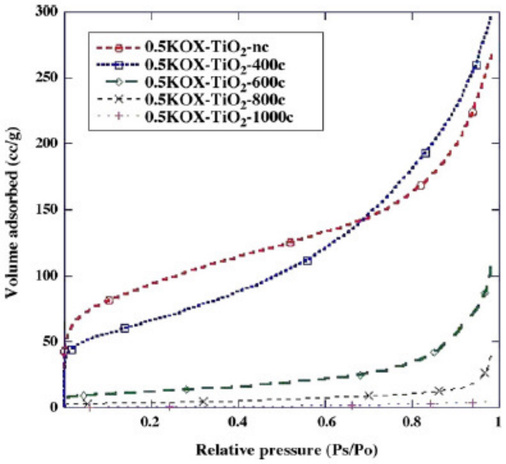

Fig. 2. N_2 adsorption isotherms for calcined TiO_2 samples.

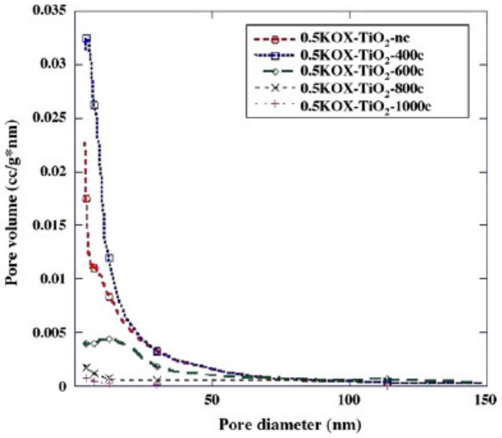

Fig. 3. Pore size distributions for calcined TiO_2 samples.

It could be seen from Fig. 3 that 0.5KOX–TiO_2–*nc* and 0.5KOX–TiO_2–400c samples had a wide pore size distribution from microporous to mesoporous. The 0.5KOX–TiO_2–600c sample had a mesopore size in the range 20–80 nm. However, the pore size distribution curve of 0.5KOX–TiO_2–800c and 0.5KOX–TiO_2–1000c samples turned into a line, indicating the disappearance of pores. The specific surface areas, pore volumes, and pore diameters are summarized in Table 2. It is obvious that the BET surface area and pore volume decreased with increasing calcination temperatures. As the calcination temperature increased the crystallity also increased, however, the specific surface area decreased due to the collapse of the pore structure and the growth of TiO_2 crystallites.

The agglomerated particle size of 0.5KOX–TiO_2–*nc* sample is rather large, about 3–5 μm, and had an almost spherical shape with a rough surface. Some of these agglomerated lumps were hollow as detected by the SEM and TEM techniques (Fig. 4). In addition, the TiO_2 modified with potassium oxalate has a different morphology compared with the unmodified TiO_2

Table 2
Effect of calcination temperature on the BET specific surface area (S_{BET}) and pore parameters of TiO_2 samples

Sample	S_{BET} (m^2/g)	Pore volume (cm^3/g)	Pore diameter (nm)
0.5KOX–TiO_2–*nc*	337	0.29	4
0.5KOX–TiO_2–400c	236	0.41	5
0.5KOX–TiO_2–600c	43	0.18	12
0.5KOX–TiO_2–800c	14	0.08	5
0.5KOX–TiO_2–1000c	2	0.01	6

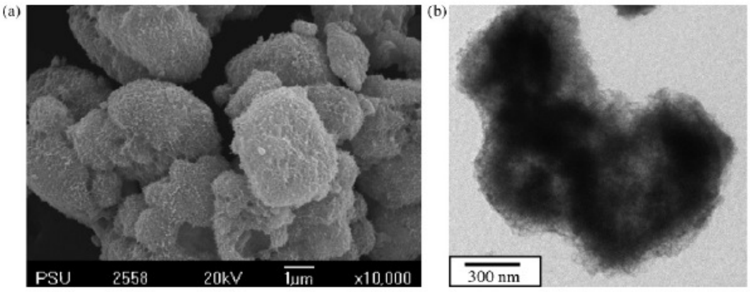

Fig. 4. The morphologies of 0.5KOX–TiO_2–*nc* sample: (a) SEM image and (b) TEM image.

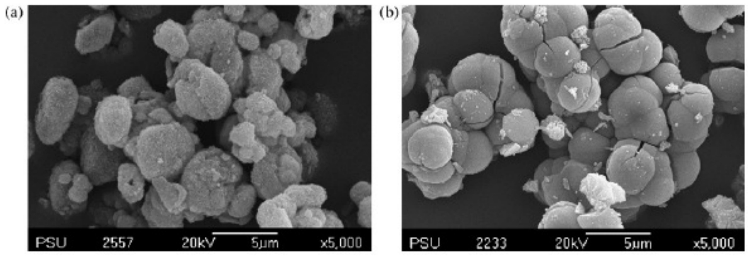

Fig. 5. The SEM images of non-calcined samples: (a) 0.5KOX–TiO_2–*nc* and (b) undoped TiO_2.

sample as shown in Fig. 5. This result provides evidence that potassium oxalate really affects the surface morphology of the TiO_2 sample.

Fig. 6 shows the SEM images of the samples after calcination. With increasing calcination temperatures the crystals began to grow and form larger agglomerated particles. The morphologies of the non-calcined sample (Fig. 5a) and the one calcined at 400 °C (Fig. 6a) were very similar both in shapes and surface textures. This result agreed with the XRD that both samples consisted mainly of an amorphous phase and,

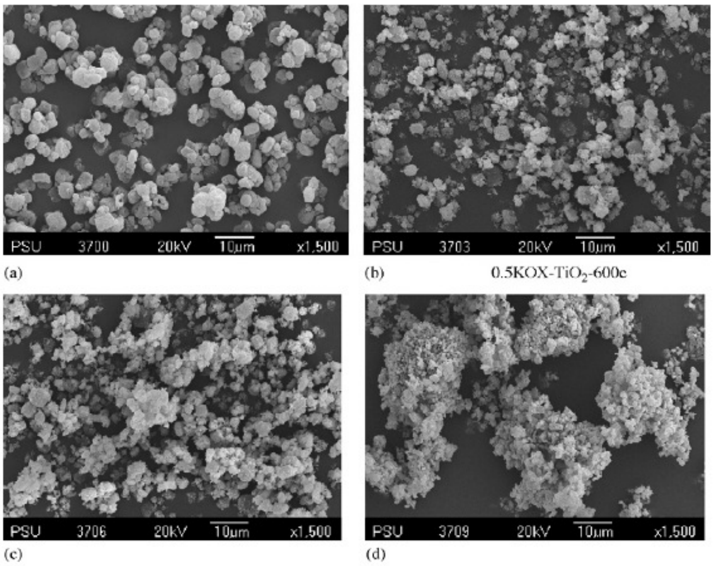

Fig. 6. SEM images of calcined 0.5KOX–TiO_2 samples at different temperatures: (a) 0.5KOX–TiO_2–400c, (b) 0.5KOX–TiO_2–600c, (c) 0.5KOX–TiO_2–800c, and (d) 0.5KOX–TiO_2–1000c.

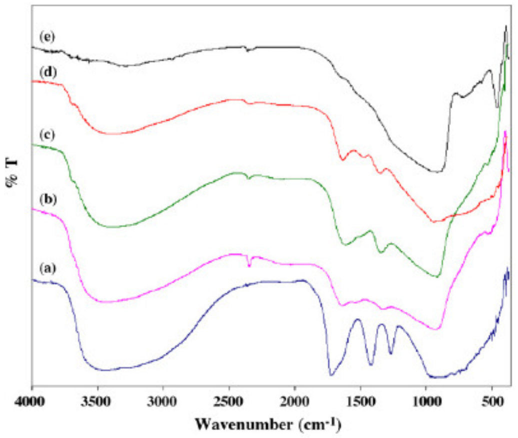

Fig. 7. FT-IR spectra of (a) 0.5KOX-TiO_2–*nc*, (b) 0.5KOX–TiO_2–400c, (c) 0.5KOX–TiO_2–600c, (d) 0.5KOX–TiO_2–800c, and (e) 0.5KOX–TiO_2–1000c samples. [A small sharp band at 2400 cm^{-1} is due to the atmospheric CO_2].

thus, had a large surface area as evidenced from the BET results. As the calcination temperature rose the amorphous phase completely transformed to the anatase phase at 600 °C which in turn transformed into the rutile phase at 1000 °C. As the calcination temperature was increased, the sample bulk became denser and more aggregation was observed (Figs. 6a–d). The very high degree of crystallinity could be seen in the sample calcined at 1000 °C (Fig. 6d) which is the rutile phase. At higher magnification (not shown) the sample of Fig. 6d appears as compact and well-formed crystals with rounded edges/corners and smooth surfaces.

Fig. 7 shows the FT-IR spectra of TiO_2 samples in the range of 4000–400 cm^{-1}. From these spectra, regions of strong bands appear at 3313 cm^{-1}, 1752–1627 cm^{-1}, 1413 cm^{-1}, 1217 cm^{-1}, and in the regions of low energy (960–420 cm^{-1}) can be clearly observed. The band at 3313 cm^{-1} can be assigned to both ν_{OH} and ν_{NH} (stretching modes) indicating the presence of the hydroxyl groups of water in the samples. In the case of 0.5KOX–TiO_2–*nc* sample, the C═O and C–O stretching modes show up as intense bands in the range 1752–1627 cm^{-1} and 1413–1217 cm^{-1}, respectively. These bands indicate the presence of the oxalate ligand resulting from addition of potassium oxalate during the sol–gel process. The bands in the region 960–420 cm^{-1} associate with the characteristic vibrational modes of TiO_2 ($\nu_{Ti–O}$, stretching mode of Ti–O bond) [44]. In this study, the Ti–O stretching mode of rutile appears at 450 cm^{-1}, however, the characteristic bands of anatase at 475 and 528 cm^{-1} are not clearly seen. With regards to calcination, the characteristic bands of the hydroxyl group of water and of the oxalate ligand decreased with increasing calcination temperature. The results from FT-IR spectra, hence, confirmed the presence of the oxalate ligand and impurities such as NH_4^+ and H_2O on the surface of the synthesized TiO_2.

Table 3
Data from the DRS and PL techniques of TiO_2 samples before and after calcinations

Sample	DRS		PL	
	λ_{onset} (nm)	E_g (eV)	λ_{emis}(nm)	E_g (eV)
0.5KOX–TiO_2–*nc*	385	3.22	390	3.18
0.5KOX–TiO_2–400c	387	3.20	390	3.18
0.5KOX–TiO_2–600c	388	3.19	390	3.18
0.5KOX–TiO_2–800c	389	3.18	390	3.18
0.5KOX–TiO_2–1000c	416	2.98	416	2.98

UV–vis diffuse reflectance and photoluminescence spectra were obtained in order to characterize the band gap energy including the nature of electronic transition in the materials. The absorption edge in the UV–vis DRS and the emission peak in the PL spectra were used to calculate the band gap energy by the Eq. (1). The position of the absorption edge (λ_{onset}) and the PL emission peak (λ_{emis}), however, remained rather unchanged, except that of the rutile. The λ_{onset}, the λ_{emis}, and the calculated band gap energy of the synthesized samples are shown in Table 3. All the PL spectra are not much different in that they show one sharp UV emission peak at 390 nm and one broad peak with high intensity at 650 nm. The UV band peaking at 390 nm has been attributed to the electronic transition from the conduction band (CB) to the valence band (VB) for the anatase crystal and the band at 415 nm for the rutile crystal, respectively. Since they are very similar, only some of the representative UV–vis absorption and PL spectra are shown in Fig. 8. The intensity of both UV–vis DRS and PL decreased steadily as the calcination temperature increased due to high crystallinity, low surface defect, and less oxygen vacancies in these calcined samples. This is because the PL signals of semiconductor materials relate to the recombination rate of electron-hole pairs in the material bulk produced after irradiation [45]. The recombination rate is high for poor crystallinity with high surface defect materials, and vice versa.

3.2. *Photocatalytic activity and regeneration studies*

Methylene blue (MB) was employed to evaluate the photocatalytic activity of the as-prepared TiO_2 samples. Generally, MB could be mineralized into harmless gaseous CO_2, inorganic SO_4^{2-}, NH_4^+, and NO_3^-. The degradation reaction is proposed to start with the cleavage of the $C–S^+{=}C$ component of the MB molecule leading to formation of sulfate ions. Other species were also detected such as leucomethylene blue, sulfoxides, and sulfones. However, at the end of reaction these species vanished and MB appeared to be completely mineralized [46,47].

In the photodegradation process, the most likely scenario is that the MB molecule is first adsorbed onto the catalyst surface followed by photo-oxidation to complete the mineralization. The adsorption stage is favored by the attraction force between the positive charge on the MB molecule and the negative charge at the oxygen atom attached to titanium at the catalyst surface. In this experiment, commercial Degussa P25 was used to compare the efficiency of the decolorization of MB solution with the as-prepared TiO_2 samples. Fig. 9 shows a typical

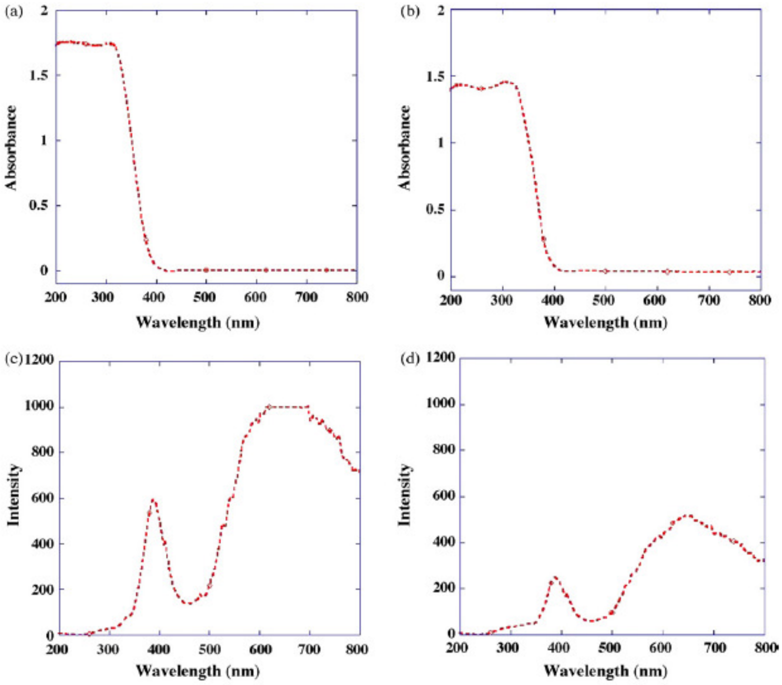

Fig. 8. The representative UV–vis DRS spectra (a) 0.5KOX–TiO_2–*nc*, (b) 0.5KOX–TiO_2–800c; and PL spectra (c) 0.5KOX–TiO_2–*nc*, (d) 0.5KOX–TiO_2–800c.

absorption spectra of methylene blue (2.5×10^{-5} M) solution that decreased with increasing irradiation time.

Figs. 10 and 11 show the efficiencies of decolorization of MB by the commercial TiO_2 sample and the as-prepared TiO_2 samples before and after being calcined at different calcination temperatures. Fig. 10 shows the results when a low concentration of MB was used (2.5×10^{-5} M). At this low concentration, P25 and four of the as-prepared TiO_2 (non-calcined, 400c, 600c, and 800c) showed 100% decolorization by the combined adsorption and photocatalytic processes. The one calcined at 1000 °C, which was converted to rutile, showed only 80% decolorization. The decolorization by P25 (Fig. 10a) was mainly by the photocatalytic process. In the dark, P25 could decolorize by only *ca.* 30% which is presumably by the adsorption process. The non-calcined sample showed very high adsorptive power and by adsorption alone could completely decolorize the solution leaving no trace of color to test for the photocatalytic power. As the samples were calcined at higher temperatures, the adsorptive power decreased significantly with an increase of the calcination temperature (Fig. 10c–f). When the adsorption was low the photocatalytic power became dominant and the decolorization could be further increased by the photocatalytic process. In Fig. 10f the decolorization was not complete even with help from the photocatalytic process. This sample was composed mainly of rutile which is known for its low efficiency of degradation by the photocatalytic process. However, in other samples (Figs. 10c–e), the decolorizations were all completed by the photocatalytic process. The composition of these samples were mainly amorphous (Fig. 10c), mixed amorphous and anatase (Fig. 10d), and anatase (Fig. 10e). At this concentration, the non-calcined sample and those calcined at 400, 600, and 800 °C could

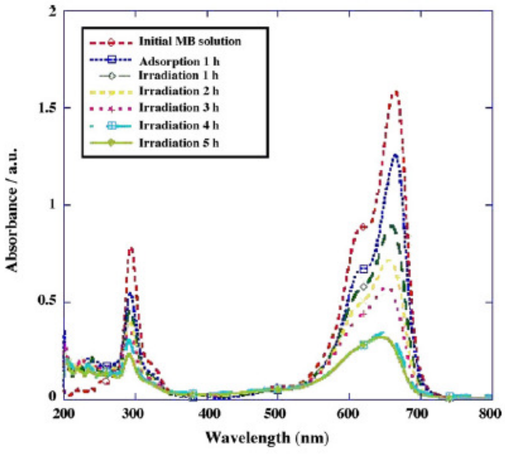

Fig. 9. Typical absorption spectra of methylene blue solutions containing the as-prepared TiO_2 samples during irradiation with UV light at different time intervals.

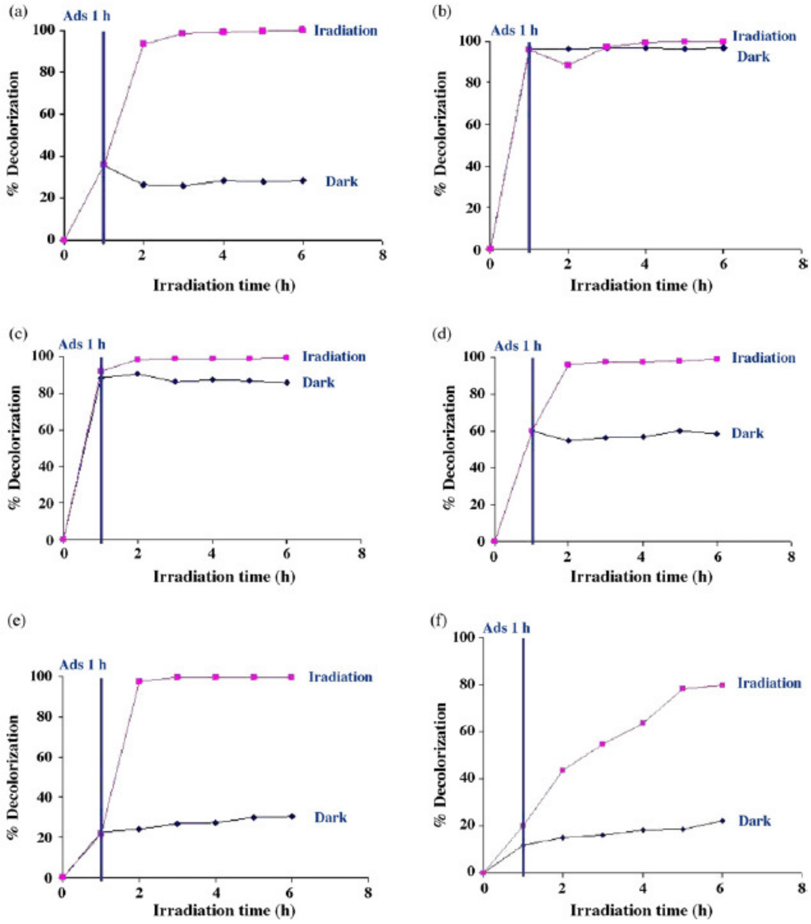

Fig. 10. The efficiencies of decolorization of MB solution (2.5×10^{-5} M) during irradiation with UV light in the presence of 1.0 g/L TiO_2 sample: (a) P25–TiO_2, (b) 0.5KOX–TiO_2–*n*c, (c) 0.5KOX–TiO_2–400c, (d) 0.5KOX–TiO_2–600c, (e) 0.5KOX–TiO_2–800c, and (f) 0.5KOX–TiO_2–1000c.

decolorize the dye solution as well as did P25. The non-calcined and the low-temperature calcined-samples decolorized the dye mainly by the adsorption process while the samples calcined at the higher temperature did by the combined adsorption and photocatalytic processes. Degradation of the sample calcined at the highest temperature occurred mainly by the photocatalytic process. This result agrees with other reports of studies on the effect of calcination temperature on the efficiency of the photocatalytic effect [36–38]. The high adsorption power of the non-calcined and low temperature calcined samples stems from the large surface area in these samples. As might be expected the added oxalate group should chelate with the titanium ion as well as causing the interlinking of a few units of titanium moieties together to form some open framework, hence producing a large surface area. The framework, however, should be rather small as evidenced by the low crystallinity of the samples. Furthermore, the oxalate group is rich in oxygen atoms that bear partial negative charges. This is another factor that gives rise to the strong adsorptive power besides the large surface area. Upon calcination, decomposition of the oxalate group took place and, hence, the framework collapsed. The particle aggregation increased with higher crystallinity of the bulk resulting in a lower surface area (Table 2). Therefore, the decrease in adsorptive ability can be observed with the samples that were calcined at high temperatures. This trend is clearly demonstrated by the data in Figs. 10 and 11. At low temperatures of calcination (400 °C) the collapse of the oxalate framework was not complete as evidenced by the still high surface area and the FT-IR spectrum showing the characteristic bands of oxalate (the region 1752–1627 cm^{-1} in Fig. 7b), therefore, the adsorption power was still considerably high.

Results from Figs. 10 and 11 shows that the as-prepared 0.5KOX–TiO_2–*n*c sample could decolorize MB solution completely during the adsorption of MB in the dark for concentrations up to 1.25×10^{-4} M. Eventhough, the photocatalytic experiments were performed, no conclusion could be drawn as to whether this complete decolorization resulted from adsorption alone or the combination of both processes. Therefore, further investigations for 0.5KOX–TiO$_2$–*nc* were carried out by using higher concentrations of MB solutions in order to study the photocatalytic activity. At low concentrations up to 2.5×10^{-4} M, the non-calcined sample could completely decolorize the MB solutions—mainly by adsorption (Fig. 12a). At higher concentrations, 5.0×10^{-4} M (Fig. 12b) and 7.5×10^{-4} M (Fig. 12c), the non-calcined sample began to show its limitation by causing only *ca.* 70–80% and *ca.* 50–60% decolorization, respectively. It is important to point out the very low, barely detectable, photocatalytic activity exhibited by the non-calcined samples. The decrease in adsorption of MB at higher concentrations (5.0×10^{-4} and 7.5×10^{-4} M) resulted solely from its adsorption saturation point being reached. The saturation point should lie between 2.5×10^{-4} and 5.0×10^{-4} M. At the concentration of 5.0×10^{-4} M the sample exhibited *ca.* 65% adsorption, so the approximate saturation point would be *ca.* 3.8×10^{-4} M. This corresponds well with the *ca.* 55% adsorption exhibited by the concentration of 7.5×10^{-4} M. (This simple explanation fits with this case where the adsorption is dominant. In other system where the photocatalytic activity is dominant, the decrease of % decolorization with increasing the dye concentrations is usually observed.

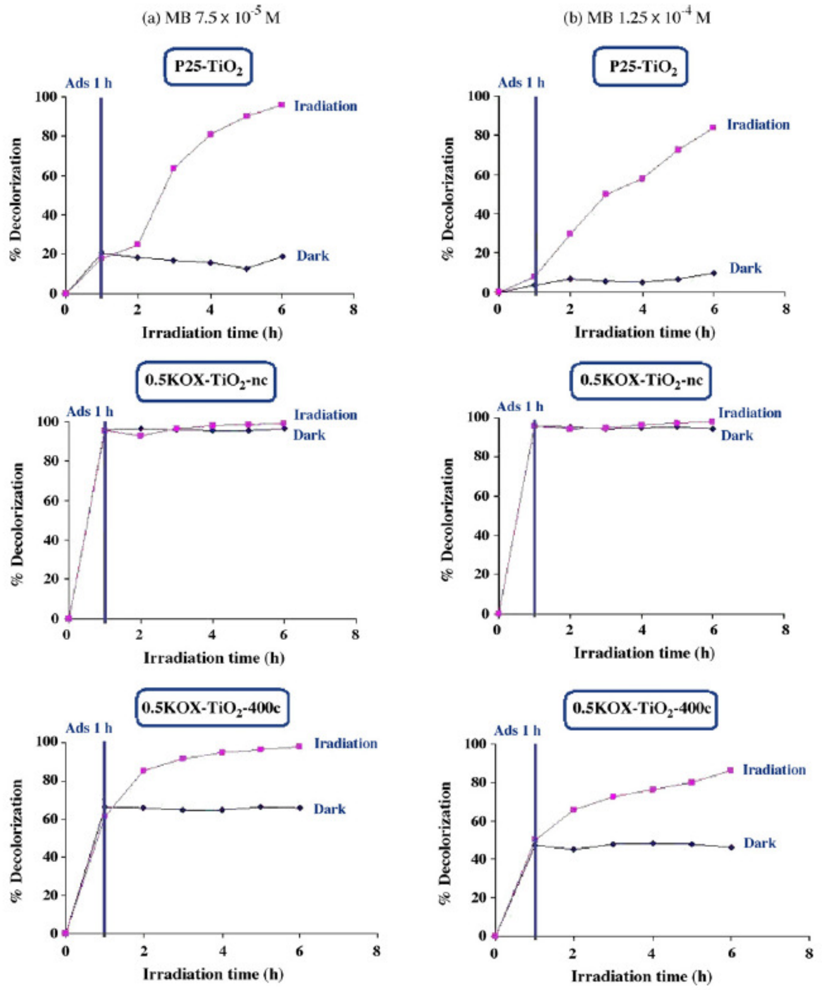

Fig. 11. The efficiencies of decolorization of higher concentrations of MB solution: (a) 7.5×10^{-5} M and (b) 1.25×10^{-4} M with irradiation by UV light in the presence of 1.0 g/L TiO$_2$ sample.

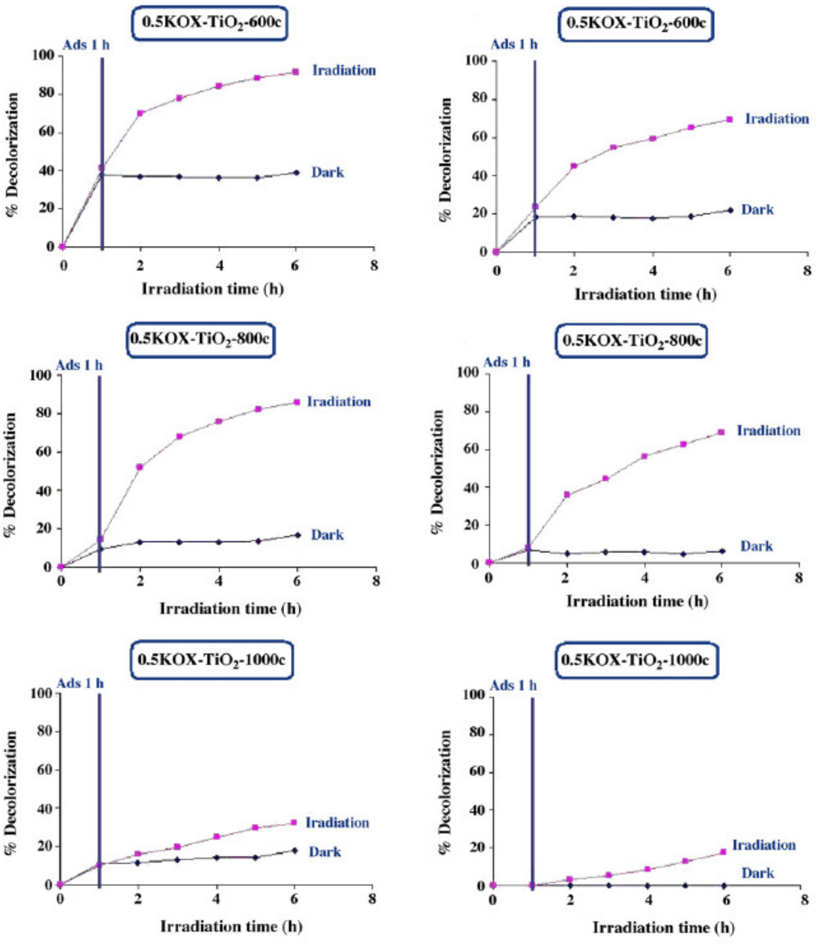

Fig. 11. (*Continued*).

The explanation in such system will be slightly different from that given above, see for example Ref. [48].)

The non-calcined sample has a large amount of –OH functional groups on its surface as evidenced by the very strong absorption band at 3300–3400 cm^{-1} in the FT-IR spectrum. This band decreased as the sample was calcined at higher temperatures due to the loss of –OH functional group in the form of H_2O. The >Ti–OH group at the surface acts like a surface-charge carrier that traps both the conduction band electron and the valence band hole as shown in Eqs. (8) and (9).

$$e^- + >Ti^{IV}{-}OH \rightarrow (>Ti^{III}{-}OH) \tag{8}$$

$$h^+ + >Ti^{IV}{-}OH \rightarrow (>Ti^{IV}{-}{}^{\bullet}OH)^+ \tag{9}$$

where $>Ti^{IV}{-}OH$ is the hydrated surface functional group ($>Ti^{III}{-}OH$) is the surface-trapped conduction band electron, and $(>Ti^{IV}{-}{}^{\bullet}OH)^+$ is the surface-trapped valence band hole [37]. The crystallite size of the samples increases with the calcination temperatures and the reverse is true when the crystallite size of the non-calcined samples are the smallest in the series. (As shown in Table 1, the non-calcined sample existed in its amorphous phase. The lack of diffraction peaks in the XRD prevented calculation of the crystallite size by the Scherrer's equation.) The effect of a small crystallite size means that the two surface-charge carrier traps in Eqs. (8) and (9) will be close together on the surface leading to recombination. This is called the surface-charge carrier recombination and probably is the main factor for the inactivity of the amorphous or low crystallinity form of TiO_2. For the calcined samples, the one calcined at 800 °C showed the best photocatalytic activity, approximately equal to that of P25. This could be due to its high crystallinity and the presence of only a small amount of rutile. There has been a prevailing presumption that a small amount of rutile mixed with anatase seems to provide a

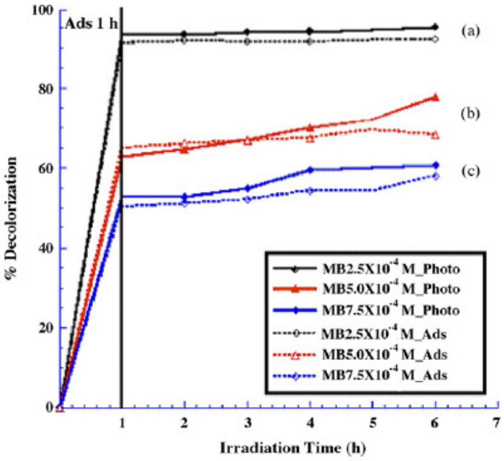

Fig. 12. Comparison of decolorization efficiencies at low (a) and high (b and c) concentrations by the non-calcined sample.

synergistic effect on the photocatalytic process [49]. In the most recent report by Hirakawa et al. [50], it was shown that pure anatase and a mixture of anatase and a small amount of rutile efficiently generated $^{\bullet}OH$ radicals in the photocatalytic process while the amount of OH-radicals generated was extremely low with pure rutile. This indicates that anatase is the active phase in the photocatalytic process. The general trend for the calcined samples, on comparing data from several reports, is that the higher the calcination temperature the better is the photocatalytic activity as long as the anatase phase is still present and once the calcination temperature surpasses the anatase–rutile transformation temperature, the photocatalytic activity drops [35–38,40]. This is because at that temperature the main composition is anatase of high crystallinity with only very small amounts of rutile beginning to form and being mixed with the anatase. Beyond this temperature, the content of rutile increases and the photocatalytic activity decreases.

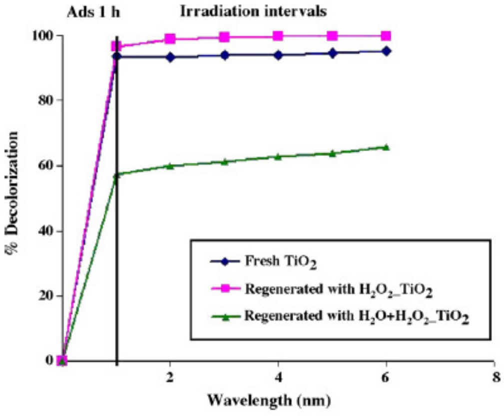

Fig. 13. Comparison of the decolorization efficiencies of MB solution (2.5×10^{-4} M) using fresh and regenerated TiO_2 samples.

After the decolorization experiments, the powders were covered with dye molecules due to their high adsorptive power. The clean surface, however, could be regenerated for further use. Two methods of regeneration were attempted. The first was by mixing the used powder in 50 mL of distilled water and 5 mL of H_2O_2 solution (1 M) with stirring overnight under UV light irradiation. The second was by using the same method but with only 50 mL hydrogen peroxide (H_2O_2, 1 M) solution and UV light. The regenerated TiO_2 powders were obtained and separated for reuse in the next cycle. The regenerated TiO_2 powders were off-white instead of being “snow” white after they were freshly prepared. The performance of the two regenerated TiO_2 samples were compared to the freshly prepared TiO_2 sample as shown in Fig. 13. It can be seen that the sample regenerated with H_2O_2 showed higher decolorization ability than the freshly prepared sample and much better than the one regenerated with mixed H_2O and H_2O_2 solution. In the regeneration process, the presence of both H_2O_2 and UV light were necessary. In the presence of UV light alone no regeneration was observed. In the presence of H_2O_2 alone regeneration occurred but it took a long time. These observations could be rationalized based on the increase of the reactive $^{\bullet}OH$ radical in the regeneration setup.

It appears that in the regeneration process, H_2O_2 played the major role to destroy any dye molecules previously adsorbed at the TiO_2 surface. This resulted from the increasing concentration of the $^{\bullet}OH$ radical according to the following equations [51].

$$H_2O_2 \rightarrow 2^{\bullet}OH \tag{10}$$

$$H_2O_2 + e^- \rightarrow OH^- + {}^{\bullet}OH \tag{11}$$

$$H_2O_2 + O_2^{\bullet -} \rightarrow OH^- + {}^{\bullet}OH + O_2 \tag{12}$$

Eq. (10) represents the homolytic cleavage of H_2O_2 by light while Eqs. (11) and (12) are associated with the photocatalytic reaction of TiO_2. Comparing Eqs. (11) and (12), the main source of $^{\bullet}OH$ comes from Eq. (11) where H_2O_2 is reduced by the conduction band electron. The production of $^{\bullet}OH$ from Eq. (12) is negligible as only a small amount of $O_2^{\bullet -}$ anion was produced [50]. In a separate controlled experiment, without TiO_2, the MB pigment was also slowly decomposed by H_2O_2 and UV light. This observation plus the very low photocatalytic property exhibited by the non-calcined sample, as depicted in Fig. 12, we therefore, concluded that the regeneration was driven by Eq. (10). The combined use of UV/H_2O_2 to decolorize and mineralize dyes has been demonstrated recently by using UV light with a major wavelength of 254 nm [52,53]. In another study to investigate the UV/H_2O_2 oxidation of NO_x emissions, a UV lamp with a spectral output range from 200 to 320 nm was used (with an additional spike at 365–370 nm) [54]. However, a small amount of the UV spectrum in solar light, *ca.* 5%, could also initiate the $^{\bullet}OH$ production from H_2O_2 and this accounted for 20–25% degradation of dye by H_2O_2 in the absence of TiO_2 [51]. In our system, the emission wavelength from the fluorescent UV light was 366 nm which should be sufficient to initiate the $^{\bullet}$OH radical in the regeneration process.

4. Conclusions

Potassium oxalate-doped TiO_2 samples were prepared from $TiCl_4$ employing HMT for the slow and controllable precipitation. The initial products had a high specific surface area as a result of the ability of oxalate ion to form an open framework structure. The non-calcined samples (amorphous phase with small amount of anatase phase) showed very little photocatalytic activity but high adsorptive capacity. Calcination changed the morphology, crystal structure, crystallite size, and photocatalytic activity of the as-prepared TiO_2 samples. The samples calcined at 400 and 600 °C still showed high adsorption capacity but decreasing as calcination temperature was increased. The photocatalytic activity was also increased with increasing calcination temperature. When the calcination temperature was 800 °C, the photocatalytic activity of the calcined sample was comparable to that of Degussa P25. The non-calcined sample, due to its high adsorptive property although with low photocatalytic property, could decolorize high concentrations of MB solutions, by adsorption, up to 2.5×10^{-4} M which is about ten times the normal concentration used in other reports. At this high concentration, the decolorization with P25 did not occur. After use, the dye-covered powders could be regenerated. The regeneration method required both H_2O_2 and UV irradiation. The regenerated TiO_2 samples could decolorize MB solution slightly better than the freshly prepared TiO_2 samples. The high adsorptive power combined with the recyclability should make this material an attractive candidate for an alternative method to treat dye-polluted waters.

Acknowledgements

Financial support from the Thailand Research Fund through the Royal Golden Jubilee Ph.D. Program (Grant No. PHD/0197/2548), the Center for Innovation in Chemistry: Postgraduate Education and Research Program in Chemistry (PERCH-CIC), Commission on Higher Education, Ministry of Education, and the Graduate School-PSU through the Thesis Research Fund are gratefully acknowledged. Valuable suggestions from an anonymous reviewer on how to improve the manuscript is much appreciated. The authors also thank Dr. Brian Hodgson, Faculty of Science, PSU, for his assistant on checking and correcting the manuscript. Sample of Degussa P25 used throughout this work was donated by Degussa AG, Frankfurt, Germany, through its agency in Bankok, Thailand.

References

[1] O. Legrini, E. Oliveros, A.M. Braun, Chem. Rev. 93 (1993) 671.
[2] A.L. Linsebigler, G. Lu, J.T. Yates, Chem. Rev. 95 (1995) 735.
[3] I.K. Konstantinou, T.A. Albanis, Appl. Catal. B: Environ. 49 (2004) 1.
[4] J. Lin, J.G. Yu, J. Photochem. Photobiol. A: Chem. 116 (1998) 63.
[5] S. Horikoshi, A. Saitou, H. Hidaka, Environ. Sci. Technol. 37 (2003) 5813.
[6] S.X. Liu, X.Y. Chen, X. Chen, J. Hazard. Mater. 143 (2007) 257.
[7] C. Sriwong, S. Wongnawa, O. Patarapaiboolchai, Catal. Commun. 9 (2008) 213.
[8] H. Zhang, J.F. Banfield, J. Non-Cryst. Solids 261 (2000) 260.
[9] A.C. Pierre, G.M. Pajonk, Chem. Rev. 102 (2002) 4243.
[10] T. Peng, D. Zhao, K. Dai, W. Shi, K. Hirao, J. Phys. Chem. B 109 (2005) 4947.
[11] L. Chen, J. Zhu, Y.-M. Liu, Y. Cao, H.-X. Li, H.-Y. He, W.-L. Dai, K.-N. Fan, J. Mol. Catal. A: Chem. 255 (2006) 260.
[12] J.-M. Wu, T.-W. Zhang, Langmuir 21 (2005) 6995.
[13] Z. Liu, Z. Jin, W. Li, J. Qiu, Mater. Lett. 59 (2005) 3620.
[14] S.-T. Oh, J.-S. Choi, H.-S. Lee, L. Lu, H.-H. Kwon, I.K. Song, J.J. Kim, H.-I. Lee, J. Mol. Cat. A: Chem. 267 (2007) 112.
[15] Y. Wang, C.S. Hong, Wat. Res. 33 (1999) 2031.
[16] H.-F. Yu, S.-M. Wang, J. Non-Cryst. Solids. 261 (2000) 260.
[17] X. Liu, J. Yang, L. Wang, X. Yang, L. Lu, X. Wang, Mater. Sci. Eng. A. 289 (2000) 241.
[18] J.-Y. Zheng, J.-B. Pang, K.-Y. Qui, Y.J. Wei, Mater. Chem. 11 (2001) 3367.
[19] R. Andres, M. Gruselle, B. Malezieux, M. Verdaguer, J. Vaissermann, Inorg. Chem. 38 (1999) 4637.
[20] R. Vaidhyanathan, S. Natarajan, A.K. Cheetham, C.N.R. Rao, Chem. Mater. 11 (1999) 3636.
[21] C. Boudaren, T. Bataille, J.-P. Auffredic, D. Louer, Solid State Sci. 5 (2003) 175.
[22] Z.A.D. Lethbridge, A.F. Congreve, E. Esslemont, A.M.Z. Slawin, P. Lightfoot, J. Solid State Chem. 172 (2003) 212.
[23] S. Decurtins, H.W. Schmalle, R. Pellaux, P. Schneuwly, A. Hauser, Inorg. Chem. 35 (1996) 1451.
[24] E. Coronado, J.R. Galan-Mascaros, C.J. Gomez-Garcia, J. Chem. Soc. Dalton Trans. (2000) 205.
[25] O.R. Evans, W. Lin, Cryst. Growth Des. 1 (2001) 9.
[26] L. Chaiyapoom, S. Wongnawa, C. Pakawatchai, J. Charmant, S. Saithong, Inorg. Chem. Commun. 9 (2006) 316.
[27] J.-G. Li, Y. Wang, T. Ikegami, T. Mori, T. Ishigaki, Mater. Sci. Eng. B 121 (2005) 54.
[28] Z. Liu, R. Ma, M. Osada, K. Takada, T. Sasaki, J. Am. Chem. Soc. 127 (2005) 13869.
[29] C. Random, S. Wongnawa, P. Boonsin, ScienceAsia 30 (2004) 149.
[30] Y. Zhang, J. Mu, J. Colloid Interf. Sci. 309 (2007) 478.
[31] H.S. Potdar, S.B. Deshpande, A.S. Deshpande, Y.B. Khollam, A.J. Patil, S.D. Pradham, Int. J. Inorg. Mater. 3 (2001) 613.
[32] A.J. Patil, M.H. Shinde, H.S. Potdar, S.B. Deshpande, S.R. Sainkar, S. Mayadevi, S.K. Date, Mater. Chem. Phys. 68 (2001) 7.
[33] R. Arroyo, G. Cordoba, J. Padilla, V.H. Lara, Mater. Lett. 54 (2003) 397.
[34] T. Sreethawong, Y. Suzuki, S. Yoshikawa, J. Solid State Chem. 178 (2005) 329.
[35] K.S. Yoo, H. Choi, D.D. Dionysiou, Catal. Commun. 6 (2005) 259.
[36] J. Yu, H. Yu, B. Cheng, C. Trapalis, J. Mol. Cat. A: Chem. 249 (2006) 135.
[37] K.V. Baiju, S. Shukla, K.S. Sandhya, J. James, K.G.K. Warrier, J. Phys. Chem. C 111 (2007) 7612.
[38] B. Tryba, M. Toyoda, A.W. Morawski, R. Nonaka, M. Inagaki, Appl. Catal. B: Environ. 71 (2007) 163.
[39] M. Wu, G. Lin, D. Chen, G. Wang, D. He, S. Feng, R. Xu, Chem. Mater. 14 (2002) 1974.
[40] L.-C. Chen, C.-M. Huang, F.-R. Tsai, J. Mol. Catal. A: Chem. 265 (2007) 133.
[41] J.E. House Jr., T.G. Blumthal, Thermo Chim. Acta 36 (1980) 79.
[42] K.A. Foster, J.E. House Jr., Thermo Chim. Acta 60 (1983) 389.
[43] J.E. Huheey, Inorganic Chemistry: Principles of Structure and Reactivity, 2nd ed., Harper International Edition, New York, 1978, p. 78 and p. 253.
[44] Y. Zhang, A. Weidenkaff, A. Reller, Mater. Lett. 54 (2002) 375.
[45] J. Liqiang, Q. Yichun, W. Baiqi, L. Shudan, J. Baojiang, Y. Libin, F. Wei, F. Honggang, S. Jiazhong, Sol. Energy Mater. Sol. Cells 90 (2006) 177.
[46] A. Houas, H. Lachheb, M. Ksibi, E. Elaloui, C. Guillard, J.-M. Herrmann, Appl. Catal. B: Environ. 31 (2001) 145.

[47] H. Gnaser, M.R. Savina, W.F. Galaway, C.E. Tripa, I.V. Veryovkin, M.J. Pellin, Int. J. Mass Spectrom. 245 (2005) 61.
[48] J. Grzechulska, A.W. Morawski, Appl. Catal. B: Environ. 36 (2002) 45.
[49] T. Ohno, K. Tokieda, S. Higashida, M. Matsumura, Appl. Catal. A: Gen. 244 (2003) 383.
[50] T. Hirakawa, K. Yawata, Y. Nosaka, Appl. Catal. A: Gen. 325 (2007) 105.
[51] B. Neppolian, H.C. Choi, S. Sakthivel, B. Arabindoo, V. Murugesan, Chemosphere 46 (2002) 1173.
[52] H.-Y. Shu, M.-C. Chang, J. Hazard. Mater. B 125 (2005) 96.
[53] H.-Y. Shu, M.-C. Chang, J. Hazard. Mater. B 125 (2005) 244.
[54] C.D. Cooper, C.A. Clausen III, L. Petty, M.M. Collins, M.P. de Fernandez, J. Environ. Eng. 128 (2002) 68.

Vitae

Name	Miss Cheewita Suwanchawalit
Student ID	4823025

Education Attainment

Degree	**Name of Institution**	**Year of Graduation**
B. Sc. (Chemistry)	Prince of Songkla University	2002
M. Sc. (Inorganic Chemistry)	Prince of Songkla University	2005

Scholarship Awards during Enrolment

1. The Royal Golden Jubilee Ph.D. Program (RGJ) Grant No. PHD/0197/2548 of the Thailand Research Fund (TRF)
2. The Center for Innovation in Chemistry: Post Graduate Education and Research Program in Chemistry (PERCH-CIC), Commission on Higher Education, Ministry of Education
3. Graduate School, Prince of Songkla University

List of Publications and Proceedings

Publications

1. Suwanchawalit, C. and Wongnawa, S. 2008. Influence of calcination on the microstructures and photocatalytic activity of potassium oxalate-doped TiO_2 powders, *Applied Catalysis A: General* **338**: 87–99.

2. Suwanchawalit, C. and Wongnawa, S. 2008. Preparation and photocatalytic activity of mesoporous TiO_2 derived from sol-gel process with nonionic triblock copolymer (Pluronic P123) as template, *Material Chemical and Physic* (submitted)

Presentations

Oral presentations

1. Cheewita Suwanchawalit, Sumpun Wongnawa, Orawan Sirichote, and Phadoong Bunsin, **“**The effect of metal-doping on the physical and photocatalytic properties of nanosized TiO_2 powder**”** PERCH Congress IV. Jomtein Palm Beach, Pattaya, Chonburi, Thailand. 8-11 May 2005.
2. Cheewita Suwanchawalit, Sumpun Wongnawa, **“**Syntheses and Characterization of Al and B doped TiO_2Nanocrystallines**”** The 4th PSU Symposium on Graduate Research. Faculty of science, Prince of Songkla University, Hat Yai, Songkhla, Thailand. 31 March 2006.
3. Cheewita Suwanchawalit, Sumpun Wongnawa, “Improving photocatalytic activity of TiO_2 powders via calcinations” Pure and Applied Chemistry International Conference. Sofitel Centara Grand, Bangkok, Thailand. 30 January-1 Febury, 2008.

Poster presentations

1. Cheewita Suwanchawalit, Orawan Sirichote, Sumpun Wongnawa, “Preparation, characterization, and photocatalytic activities of nano-sized metal oxide-doped TiO_2 photocatalysts” The 3rd PSU Symposium on Graduate Research. Faculty of science, Prince of Songkla University, Hat Yai, Songkhla, Thailand. 11 March 2005.
2. Cheewita Suwanchawalit, Sumpun Wongnawa, “The effect of trivalent element-doping on the physical and photocatalytic properties of nanocrystalline TiO_2”. 1st Penang International Conference for Young Chemists. Universiti Sains Malaysia, Penang, Malaysia. 24-27 May 2006.
3. Cheewita Suwanchawalit, Sumpun Wongnawa, **“**Adsorption study of methylene blue at high concentration on hydrated titania**”** PERCH-CIC Conference V. Jomtein Palm Beach Resort, Pattaya, Chonburi Thailand. 6-9 May 2007.
4. Cheewita Suwanchawalit, Sumpun Wongnawa, **“**Influence of calcination on the microstructures and photocatalytic activity of TiO_2 powders**”** RGJ-Ph.D. Congress X. Jomtein Palm Beach Resort, Pattaya, Chonburi Thailand. 3-5 Apirl 2009.

5. Cheewita Suwanchawalit, Avinash Patil, Stephen Mann, Sumpun Wongnawa, "Preparation of the ordered macroporous structure of chitosan/TiO_2 scaffolds and their photocatalytic activity" PERCH-CIC Conference VI. Jomtein Palm Beach Resort, Pattaya, Chonburi Thailand. 3-6 May 2009.